IMPROVEMENTS IN PULSE PARAMETER SELECTION FOR ELECTROPORATION-BASED THERAPIES

Kenneth Nolen Aycock

Dissertation submitted to the faculties of
Virginia Polytechnic Institute and State University
in partial fulfillment of the requirements for the degree of

Doctor of Philosophy
in
Biomedical Engineering

Rafael V. Davalos, Chair
Christopher B. Arena
Iain H. McKillop
John L. Robertson
Joanne L. Tuohy
Scott S. Verbridge

February 13th, 2023
Blacksburg, VA

Keywords: tissue ablation, pulsed electric fields, nerve stimulation, thermal damage, irreversible electroporation, treatment planning, minimally invasive surgery, electropermeabilization

Copyright © 2023 Kenneth N. Aycock

Improvements in Pulse Parameter Selection for Electroporation-Based Therapies

Kenneth N. Aycock

ABSTRACT

Irreversible electroporation (IRE) is a non-thermal tissue ablation modality in which electrical pulses are used to generate targeted disruption of cellular membranes. Clinically, IRE is administered by inserting one or more needles within or around a region of interest, then applying a series of short, high amplitude pulsed electric fields (PEFs). The treatment effect is dictated by the local field magnitude, which is quite high near the electrodes but dissipates exponentially. When cells are exposed to fields of sufficient strength, nanoscale "pores" form in the membrane, allowing ions and macromolecules to rapidly travel into and out of the cell. If enough pores are generated for a substantial amount of time, cell homeostasis is disrupted beyond recovery and cells eventually die. Due to this unique non-thermal mechanism, IRE generates targeted cell death without injury to extracellular proteins, preserving tissue integrity. Thus, IRE can be used to treat tumors precariously positioned near major vessels, ducts, and nerves. Since its introduction in the late 2000s, IRE has been used successfully to treat thousands of patients with focal, unresectable malignancies of the pancreas, prostate, liver, and kidney. It has also been used to decellularize tissue and is gaining attention as a cardiac ablation technique.

Though IRE opened the door to treating previously inoperable tumors, it is not without limitation. One drawback of IRE is that pulse delivery results in intense muscle contractions, which can be painful for patients and causes electrodes to move during treatment. To prevent contractions

in the clinic, patients must undergo general anesthesia and temporary pharmacological paralysis. To alleviate these concerns, high-frequency irreversible electroporation (H-FIRE) was introduced. H-FIRE improves upon IRE by substituting the long (~100 µs) monopolar pulses with bursts of short (~1 µs) bipolar pulses. These pulse waveforms substantially reduce the extent of muscle excitation and electrochemical effects. Within a burst, each pulse is separated from its neighboring pulses by a short delay, generally between 1 and 5 µs. Since its introduction, H-FIRE burst waveforms have generally been constructed simply by choosing the duration of constitutive pulses within the burst, with little attention given to this delay. This is quite reasonable, as it has been well documented that pulse duration plays a critical role in determining ablation size. In this dissertation, we explore the role of these latent periods within burst waveforms as well as their interaction with other pulse parameters. Our central hypothesis is that tuning the latent periods will allow for improved ablation size with reduced muscle contractions over traditional waveforms.

After gaining a simple understanding of how pulse width and delay interact *in vitro*, we demonstrate theoretically that careful tuning of the delay within (interphase) and between (interpulse) bipolar pulses in a burst can substantially reduce nerve excitation. We then analyze how pulse duration, polarity, and delays affect the lethality of burst waveforms toward determining the most optimal parameters from a clinical perspective. Knowing that even the most ideal waveform will require slightly increased voltages over what is currently used clinically, we compare the clinical efficacy of two engineered thermal mitigation strategies to determine what probe design modifications will be needed to successfully translate H-FIRE to the clinic while maintaining large, non-thermal ablation volumes. Finally, we translate these findings in two studies. First, we demonstrate that burst waveforms with an improved delay structure allow for enhanced safety and larger ablation volumes *in vivo*. And finally, we examine the efficacy of H-

FIRE in spontaneous canine liver tumors while also comparing the ablative effect of H-FIRE in tumor and non-neoplastic tissue in a veterinary clinical setting.

Improvements in Pulse Parameter Selection for Electroporation-Based Therapies

Kenneth N. Aycock

(GENERAL AUDIENCE ABSTRACT)

Cancer is soon to become the most common cause of death in the United States. In 2023, approximately 2 million new cases of cancer will be diagnosed, leading to roughly 650 thousand lost lives. Interestingly, about half of newly diagnosed cancers are caught in the early stages before the disease has spread throughout the body. With effective local intervention, these patients could potentially be cured of their malignancy. Surgical removal of the tumor is the gold standard, but it is often not possible due to tumor location, patient comorbidities, or organ health status. In some instances, focal thermal ablation with radiofrequency or microwave energy can be performed when resection is not possible. These treatments entail the delivery of thermal energy through a needle electrode, which causes local tissue damage through coagulation (cooking) of the tissue. However, thermal ablation destroys tissue indiscriminately, meaning that any nearby blood vessels or neural components will also be damaged, which precludes thousands of patients from treatment each year.

Irreversible electroporation (IRE) was introduced to overcome these challenges and provide a treatment option for patients diagnosed with otherwise untreatable tumors. IRE uses pulsed electric fields to generate nanoscale pores in cell membranes, which lead to a homeostatic imbalance and cell death. Because IRE is a membrane-based effect, it does not rely on thermal effects to generate cellular injury, which allows it to be administered to tumors that are adjacent to critical tissue structures such as major nerves and vasculature.

Though IRE opened the door to treating otherwise inoperable tumors, procedures are technically challenging and require specialized anesthesia protocols. High-frequency irreversible electroporation (H-FIRE) was introduced by our group roughly a decade ago to simplify the procedure through the use of an alternate pulsing strategy. These higher frequency pulses offer several advantages such as limiting muscle contractions and reducing the risk of cardiac interference, both of which were concerns with IRE. However, H-FIRE ablations have been limited in size, and there is limited knowledge regarding the optimal pulsing strategy needed in order to maximize the ratio of therapeutic benefits to undesirable side effects like muscle stimulation and Joule heating. In this dissertation, we sought to understand how different pulse parameters affect these outcomes. Using a combination of computational, benchtop, and *in vivo* experiments, we comprehensively characterized the behavior of user-tunable pulse parameters and identified optimal methods for constructing H-FIRE protocols. We then translated our findings in a proof-of-principle study to demonstrate the ability of newly introduced waveform designs to increase ablation size with H-FIRE. Overall, this dissertation improves our understanding of how H-FIRE waveform selection affects clinical outcomes, introduces a new strategy for maximizing therapeutic outcomes with minimal side effects, and provides a framework for selecting parameters for specific applications.

Acknowledgements

First, I would like to thank my advisor, Dr. Rafael Davalos, for giving me the opportunity to join the lab, and for all your guidance along the way. You provided the framework for me to experience all phases of translational research, and your mentorship has given me the confidence to independently pursue new questions and ideas. I am very grateful to have been a part of this lab, and to be involved in so many collaborative and unique projects; I could not have gotten to this point in my graduate career without your support. Thank you for always providing the perfectly timed (gentle) nudges and the motivation to help me finish what I started.

I am also deeply grateful to each of my committee members; your unique perspectives and ideas have helped me view my work from new angles and with deeper insight. Dr. Arena, I cannot thank you enough for helping me get off the ground with my modeling skills in my first couple of years. Without your advice and willingness to help me troubleshoot and expand my ideas, none of this work would have been successful. Dr. McKillop, you have helped me become a better writer and have provided a truly invaluable clinical perspective of my work. I also appreciate you always making sure our trips to Charlotte went as smoothly as possible despite the long hours and massive efforts on behalf of the animal husbandry team, surgeons, and numerous other support staff. Dr. Tuohy, it has been wonderful getting to work with you and your team. I appreciate you always providing objectivity to our team as well as to your patients, and for allowing us the chance to help treat dogs with few other options. I also appreciate you motivating me to ride my bike on more than one occasion, and for helping me become more confident in that regard. Dr. Bob, thank you for always being a source of encouragement and positivity. You have helped keep morale high even through difficult times, and your regular reminders that our work is part of a bigger picture have helped me stay motivated and excited throughout this work. I also appreciate your generosity

with the perfused organ system and for helping me gain the tools to perform ex vivo experiments successfully. Dr. Verbridge, your deep curiosity into the mechanisms behind the biophysical effects of H-FIRE has been inspiring. I appreciate your willingness to pose thoughtful theories and lines of questioning to help direct this work, especially when working on the projects with AngioDynamics. Your ability to reason through seemingly trivial results and to build on them has helped me give more credit and respect to even the most basic experiments.

To my fellow lab mates: you have been instrumental in my development as both a researcher and as an engineer. I am deeply indebted to each of you for teaching me how to use countless instruments and software, helping with experiments, and for the amazing, collaborative atmosphere you have helped create in our lab. To the senior students and post-docs that devoted hours upon hours to help me gain the skills necessary to work independently in the lab – I cannot thank you enough for your generosity; you set the bar extremely high from not only a research perspective, but your leadership played a huge role in my success. I would also like to thank the many students, professors, and staff in all of the labs we have collaborated with who have helped me along the way – each of you has played an important role in the completion of this work.

Mom and Dad, I am amazingly blessed to have you as parents. Your unconditional support has provided me with the opportunity to pursue my dreams. Thank you for always being there for me and for being a source of perpetual motivation. Emma – thank you for being such a great sister, and for regularly making the effort to come see us in Blacksburg, despite being super busy as a teacher and a new mother. You have always inspired me and have been such a great role model my entire life. To the rest of my family and friends, thank you for providing support to Tessa and me throughout the past few years. This has been quite the team effort; we could not have gotten through it without the amazing people in our life.

Finally, to my wife, Tessa, you are an absolutely incredible human. Thank you for putting up with the long hours, stress, and irrationality that has come with my time in graduate school, and for doing it all with a smile. I am truly unsure of where I would be without you, but I am certain I would not have been successful over the past five years. I cannot thank you enough for always being there for me and for putting things into perspective.

Table of Contents

List of Figures

List of Tables

1 – Overview

1.1 – Contemporary Challenges in Oncology

Cancer needs little introduction – it is the second most common cause of death worldwide and maybe the most enigmatic. Perhaps the most unsettling trait of cancer is that it does not discriminate. While there are well-understood risk factors, cancer can afflict anyone –rich or poor, young or old, healthy or obese. Despite the prominence of cancer in our daily lives and extensive research spending by the U.S. government, progress in treating the disease has been relatively slow. In fact, the most substantial improvements in cancer mortality have come by way of improved public awareness and reduction of known risk factors rather than medical breakthroughs. In the past three decades, cancer deaths have increased by over 250 thousand per year in the United States. In the same timeframe, modern advancements in medicine have helped reduce cardiac-related deaths by over 100 thousand annually, and experts predict that cancer will soon overcome cardiovascular disease as the prevailing cause of death in the U.S (Weir et al., 2019).

The first line of treatment for solid malignant neoplasms – which comprise roughly 91% of all cancers (Siegel et al., 2021) – is surgical resection, or the physical removal of the tumor. Ideally, the resected volume would contain the entire tumor, along with a margin of non-neoplastic tissue to increase the odds that all malignant cells are removed. However, tumors arising in many organ systems are often difficult to access due to their location and/or proximity to other sensitive structures. Focal ablation was first introduced in the clinic in the 1980s to provide patients with an interventional option other than resection. Clinical reports indicating the use of high-intensity focused ultrasound as well as radiofrequency, microwave, laser, and cryoablation skyrocketed at the turn of the century, and it appeared that major breakthroughs in the targeted treatment of cancer were just around the corner.

However, though being introduced over two decades ago, none of these modalities have established themselves as a first-line therapy for non-resectable tumors. This is likely in part due to their cell death mechanism, which is based on denaturation of proteins through drastic manipulations in local temperature. Because proteins are highly prevalent both intra- and extracellularly, thermal therapies generate "indiscriminate" damage within a certain distance of the probes, meaning that both parenchymal and stromal tissue components are destroyed.

In 2005, irreversible electroporation (IRE) was introduced as a non-thermal tissue ablation technique (Davalos et al., 2005a). Unlike other energy directed therapies, IRE utilizes high intensity pulsed electric fields to generate nanoscale "pores" within the membranes of targeted cells. Owing to this unique cell death mechanism, IRE has garnered significant attention for the treatment of surgically inaccessible tumors in the liver, pancreas, prostate, and brain (Geboers et al., 2020; Jiang et al., 2015; Yarmush et al., 2014a).

1.2 – Research Aims and Approach

High-frequency irreversible electroporation (H-FIRE) presents several improvements over conventional IRE such as reduced muscle stimulation and electrochemical effects, more predictable, homogeneous ablation volumes, and reduced risk of cardiac arrhythmia. However, H-FIRE waveforms suffer from reduced ablation volumes in comparison to IRE. In this dissertation, we test the hypothesis that modifications to the latent periods within H-FIRE bursts can improve therapeutic outcomes (i.e., ablation volume) while mitigating potential side effects such as nerve stimulation, thermal damage, and electrical arcing. We address this hypothesis with multiple tools from computational modeling and benchtop testing to *in vivo* treatments in laboratory animals as well as clinical canine patients.

1.3 – Document Organization

Each chapter in this PhD dissertation is organized in a manuscript format, with the cumulative body of work encompassing multiple scientific papers that each contribute to the common theme. Chapter 2 provides an overview of pre-clinical and clinical investigations of IRE and introduces H-FIRE prior to discussing its potential benefits. Chapter 3 presents an initial parametric study of parameters affecting H-FIRE burst lethality, exploring the dynamics of pulse duration and delay on three prostate cell lines. Chapter 4 builds on these results by showing theoretically that interphase and interpulse delays can be specifically tuned to improve ablation volumes while simultaneously reducing nerve stimulation. Chapter 5 takes these findings a step further by assessing the feasibility of designing a monopolar waveform with reduced muscle stimulation prior to analyzing the mechanistic effects that polarity and delay play on ablative capacity and nerve stimulation. Toward translating the discoveries from Chapters 3 through 5, Chapter 6 examines the clinical efficacy of engineered thermal mitigation modalities which will be necessary to achieve relevant ablation volumes with H-FIRE while maintaining acceptable levels of thermal damage. Chapter 7 then employs the prior findings *in vivo*, utilizing actively cooled single-insertion electrodes and novel H-FIRE waveforms to generate large, non-thermal hepatic ablation volumes. And finally, Chapter 8 demonstrates the translative capacity of these results by demonstrating that H-FIRE generates substantial non-thermal, targeted ablations in canine patients with spontaneous tumors, but spares peripheral non-neoplastic tissue. Chapter 9 provides a conclusion of the present dissertation along with recommendations for future work.

2 – Background [1]

2.1 – Introduction

Electroporation is a biophysical phenomenon in which cellular membranes exhibit increased permeability to ions and macromolecules when exposed to external electric fields. Although the exact mechanisms of electroporation have not been fully elucidated, the scientific community has mostly come to agreement that permeabilizing nanoscale defects or “nanopores” are formed in cellular membranes upon exposure to high amplitude electric fields of sufficient duration (Weaver & Chizmadzhev, 1996). This phenomenon is manifested in two distinct forms: reversible electroporation, in which permeabilizing structures are transient and membrane integrity is quickly recovered; and irreversible electroporation (IRE), in which permeabilization disrupts cellular homeostasis and leads to cell death.

2.1.1 – *The discovery of reversible electroporation*

The earliest reports of electroporation date back over two centuries, but the most widely recognized initial discoveries originate in the 1950s when Stampfli and colleagues studied the “electrical breakdown” of nodes of Ranvier extracted from frogs (Stampfli, 1958; Stampfli & Willi, 1957). A decade later, intense electric fields were used to non-thermally kill microorganisms and to induce changes in permeability of vesicular membranes, leading to release of catecholamines (Neumann & Rosenheck, 1972; Sale & Hamilton, 1967). A series of investigations by Kinosita and Tsong in the 1970s showed that high-amplitude pulsed electric fields (PEFs) could be tuned to generate pores of different sizes in erythrocyte membranes, allowing for selective internalization of normally impermeable molecules (Kinosita & Tsong, 1977a, 1978). They also

---

[1] Chapter 2 is adapted and reprinted with permission granted under Creative Commons Attribution 4.0 International License. © Kenneth N. Aycock and Rafael V. Davalos; Published by Mary Ann. Liebert, Inc. Aycock, K. N., & Davalos, R. V. (2019). Irreversible Electroporation: Background, Theory, and Review of Recent Developments in Clinical Oncology. Bioelectricity, 1(4), 214–234.

demonstrated the increase in conductivity that follows the application of high voltage pulses and the ability to directly cause hemolysis with induced electric fields (Kinosita & Tsong, 1977b, 1979). These early contributions provided a mass of evidence supporting the theory of aqueous pore formation, which was first published in 1979 (Abidor et al., 1979). We acknowledge the perpetuity of this work as the fundamental principles introduced still underly our current understanding of electroporation.

Within the next decade, seminal investigations established the ability of PEFs to increase uptake of genes and chemotherapeutics, leading to development of the prominent fields now known as electrochemotherapy (ECT) and electrogene transfer (EGT) (Mir et al., 1991; Neumann et al., 1982; Okino & Mohri, 1987). As its name implies, ECT utilizes reversible electroporation to locally increase cellular uptake of chemotherapeutics, namely bleomycin or cisplatin, which allows for lower drug concentrations and can limit off-target toxicity. EGT employs similar techniques to introduce plasmid DNA into cells. This technique is now widely used for laboratory transfection assays, but its clinical utility is still being developed.

The aforementioned studies, along with many others, laid the framework for clinical applications of electroporation, which focused exclusively on enhancing transmembrane transport of existing biologic and pharmaceutical agents until the 21st century. During these two decades, electroporation was not used directly to injure cells, and IRE was largely viewed as an undesirable side effect of over-treatment.

2.1.2 – IRE as a Tissue Ablation Modality

In 2005, however, Davalos *et al.* proposed IRE as a standalone soft tissue ablation technique (Davalos et al., 2005a). Their original work showed numerically that electric fields capable of non-thermal IRE exist and are capable of destroying clinically- relevant volumes of tissue. Unlike existing focal ablation techniques that indiscriminately eliminate all biomolecules within a certain proximity, IRE allows for preservation of collagenous and other protein and/or lipid- based structures including vasculature and ductal networks (Maor et al., 2007; Ueshima et al., 2018). It has also been shown that carefully-planned IRE treatments cause minimal long-term damage to myelinated neurons, but that overtreatment or direct physical penetration can injure these structures (W. Li et al., 2011). The inherent advantages of IRE compared to other focal cancer therapies, such as reduced treatment time, reduced vascular complications, decreased risk of overtreatment, and minimized heat-sink effect when administered near vessels, led to an array of early publications evaluating the efficacy and feasibility of IRE to non-thermally ablate healthy and malignant soft tissues including liver (Edd et al., 2006; E. W. Lee et al., 2007; B. Rubinsky et al., 2007), prostate (Onik et al., 2007; J. Rubinsky et al., 2008), pancreas (Bower et al., 2011), kidney (Pech et al., 2011), lung (Deodhar, Monette, et al., 2011; Dupuy et al., 2011), and brain (Ellis et al., 2011; Garcia et al., 2009; Garcia, Neal, et al., 2010; Garcia, Rossmeisl, et al., 2010). Hundreds of follow-up studies have scrutinized the application of IRE in these tissues and others. Importantly, a large number of pre-clinical and clinical reports have been published in recent years. This review will serve to present these results in an organized manner to serve as a comprehensive reference for the interested reader. To maintain brevity, our discussion will focus on treatments in the prostate, pancreas and liver, as tumors in these tissues present obvious difficulties that IRE has the potential to address.

2.2 – *Mechanisms of Electroporation and IRE*

2.2.1 – *A brief overview of Pore Formation Theory*

Although fundamentals of pore formation are not the focus of this review, we provide a brief summary. A number of exceptional publications have examined the mechanistic events leading to permeabilization in much more detail than offered here (Böckmann et al., 2008; C. Chen et al., 2006; Kotnik et al., 2012; Levine & Vernier, 2010; Tieleman, 2004).

Biological membranes are organized into lipid bilayers (**Figure 2.1a**). In aqueous solution, the amphiphilic fatty acids spontaneously form a membrane composed of two identical leaflets with opposite orientations, as this is the most energetically favorable configuration. The outer face of either leaflet is composed of hydrophilic head groups that interact with the aqueous solution, whereas the innermost core is formed of hydrophobic tails. Physiologically, the lipid bilayer serves as a semipermeable barrier that separates the cytosol from extracellular fluid, only allowing diffusion of certain small uncharged and/or hydrophobic molecules. Large or charged molecules are transported through discrete trans-membrane proteins organized into channels or pumps. Although the cell membrane is structurally stable, the fatty acids are held together by weak van der Waals forces, creating a ‘‘fluid-like’’ structure in which each fatty acid is constantly moving

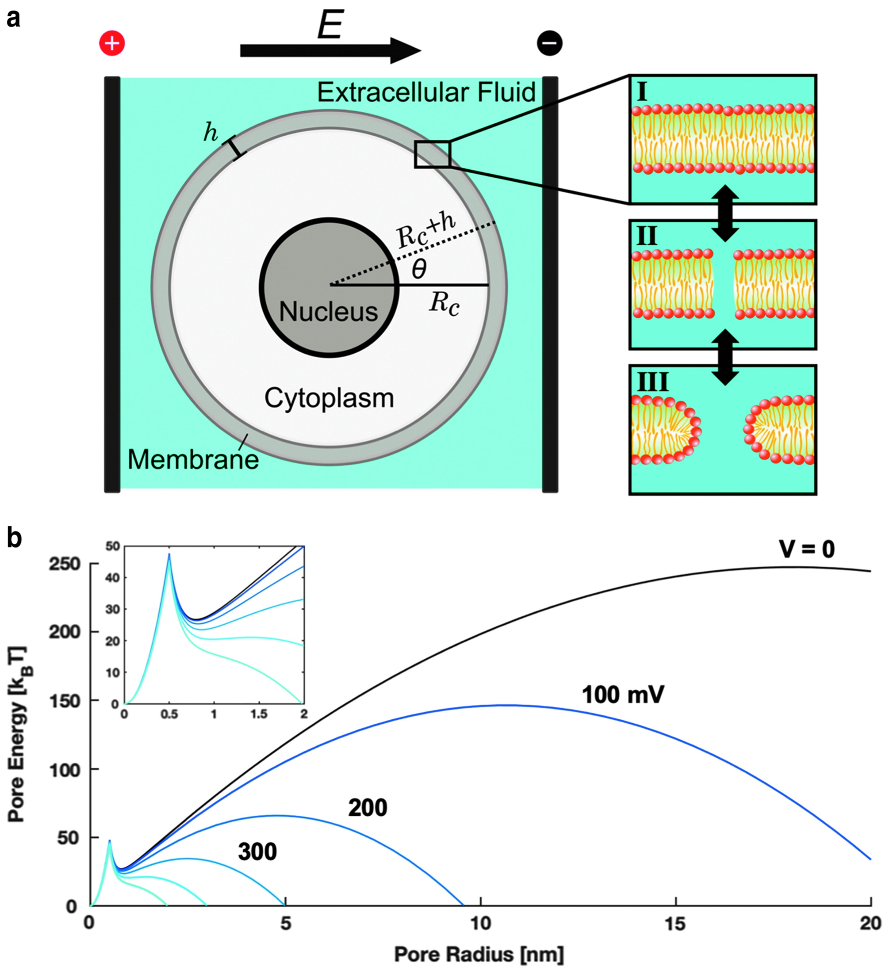

Figure 2.1 – Pore formation is a stochastic process manifested in the lipid bilayer. The behavior of a cell exposed to an external electrical stimulus (a) depends on the amplitude and temporal characteristics of the field. Under physiological conditions (I), the lipid bilayer is a stable barrier exhibiting permeability only to select molecules. After exposure to an intense electric field, hydrophobic pores appear immediately (II) and stabilize after reorientation of lipid head groups (III), allowing for passage of previously impermeable molecules. The asymptotic model proposed by Neu and Krassowska shows that (b) the free energy of induced pores decreases with increasing transmembrane potential beyond a critical radius.

within the bilayer, mostly laterally within the same leaflet. This property gives the membrane the ability to allow passage of small molecules, to externalize proteins and waste, and to internalize molecules critical to intracellular processes.

The unique properties of the cell membrane allow aqueous pores to spontaneously form due to strong interactions between water molecules on either side, especially under environmental influences such as thermal fluctuations (Deamer & Bramhall, 1986; Jansen & Blume, 1995) or mechanical insult (Akinlaja & Sachs, 1998). Although these nanopores can appear spontaneously, external electric fields (**Figure 2.1a**) lower the activation energy necessary for the stochastic pore formation process, resulting in the production of pores at a higher rate (Kotnik et al., 2012).

When the electrical stimulus is of sufficient strength, water dipoles on either side of the bilayer reorient to the field and their interaction becomes favorable (Tokman et al., 2013). Initially, the water column spanning the membrane is highly unstable, forming hydrophobic pores or ''water wires'' (**Figure 2.1a I-II**) (Kramar et al., 2012). As electrical energy is delivered to the system and water molecules penetrate the membrane, many of the initial structures evolve into long-lived hydrophilic pores (Pavlin & Miklavčič, 2008). This transition is mediated by reorientation of the polar fatty acid head groups into a more energetically favorable alignment, thereby stabilizing the pore (Abidor et al., 1979; Kramar et al., 2012; Tieleman, 2004). Simulations predict that hydrophobic pores are <1 nm in diameter and reseal within milliseconds, whereas hydrophilic pores are roughly 1–10 nm in diameter and reseal within minutes to hours (Böckmann et al., 2008; Pavlin & Miklavčič, 2008; Tieleman, 2004).

2.2.2 – Mathematical Determinants of Pore Formation

Under physiological conditions, a biological cell will maintain an endogenous transmembrane potential, or resting potential, in which the inside of the cell has a slightly negative charge (-50 to -90 mV) relative to its environment. Under an applied field, an induced transmembrane potential (TMP), $\Delta\Psi_m$, also arises across the membrane. Herman P. Schwan was among the first to develop a mathematical description for $\Delta\Psi_m$ (Schwan, 1957). Now bearing his name, this intuitive analytical equation assumes the cell is isolated and has a spherical geometry with radius R_c and membrane thickness h (**Figure 2.1**). The steady-state equation is relevant for low-frequency pulses (pulse widths >>1 μs) after the induced TMP has reached its maximum:

$$\Delta\Psi_m(r,\theta) = \Delta\Psi_m(R_c,\theta) - \Delta\Psi_m(R_c+h,\theta) = f_s E R_c cos\theta \tag{2.1}$$

where E is the magnitude of the homogenous applied field, θ is the polar angle between the normal vector of the applied field and the site on the membrane at which $\Delta\Psi_m$ is evaluated, and f_s is a dimensionless term relating the properties of each component:

$$f_s = \frac{2\sigma_e[3hR_c^2\,\sigma_i + (3h^2R_c - h^3)(\sigma_m - \sigma_i)]}{2R_c^3(\sigma_m + 2\sigma_i)\left(\sigma_m + \frac{1}{2}\sigma_i\right) - 2(R_c - h)^3(\sigma_e - \sigma_m)(\sigma_i - \sigma_m)} \qquad (2.2)$$

In this equation, σ_i, σ_m and σ_e represent the conductivity of the cytosol, membrane and extracellular fluid, respectively. To evaluate the transient behavior of the induced TMP, dielectric permittivity of the lipid bilayer (ε_m) must be considered, and the equation is written as:

$$\Delta\Psi_m(r,\theta,t) = f_s E R_c cos\theta\left(1 - e^{-t/\tau_m}\right) \qquad (2.3)$$

This equation assumes the intracellular and extracellular fluid permittivity are negligible. It is valid for sinusoidal fields with frequencies below 1 MHz and rectangular pulses longer than 1 µs (Kotnik & Pucihar, 2010). In equation (2.3), τ_m is the membrane charging constant given by:

$$\tau_m = \frac{R_c\varepsilon_m}{2h\left(\frac{\sigma_i\sigma_e}{\sigma_i+2\sigma_e}\right) + R_c\sigma_m} \qquad (2.4)$$

In many *in vitro* experiments, f_s simplifies to 1.5 by assuming the lipid bilayer is completely insulative (i.e., $\sigma_m \approx 0$), allowing one to easily estimate $\Delta\Psi_m$ for a specific experiment or treatment. The dependence of the TMP on θ results in a potential gradient with a maximum near $\theta = 0$ and minima at the poles.

Mathematical descriptions of pore formation following the induced TMP have also been reported. The Smoluchowski diffusion equation provided the original framework for pore formation (Pastushenko et al., 1979). This partial differential equation describes the flux, S, of pores into and out of the membrane as a function of time and pore radius:

$$S(t,r) = \frac{dN}{dt} - D\left(\frac{\partial N}{\partial r} + \frac{N}{k_B T}\frac{\partial U}{\partial r}\right) \tag{2.5}$$

where N is the pore density distribution function, D is the diffusion constant of the pores, U is the pore energy, k_B is Boltzmann's constant and T is the absolute temperature. In 1999, Neu and Krassowska derived an asymptotic reduction of equation (2.5) to an easily solvable ordinary differential equation (Neu & Krassowska, 1999). Briefly, a quadratic term was introduced to describe the formation of hydrophilic pores beyond a critical radius. For small hydrophilic pores, a Bessel function is used to explain expansion. The intercept of these two curves represents a local energy minimum indicated by the sharp peak at $r = 0.5$ nm in **Figure 2.1b**. In summary, the pore energy can be described as:

$$U(r) = \begin{cases} U_* \left(\frac{r}{r_*}\right)^2 - \pi a_p r^2 \Delta\Psi_m^2, & 0 \le r \le r_* \\ 2\pi r\gamma - \pi r^2 \Gamma - \pi a_p r^2 \Delta\Psi_m^2 + \left(\frac{C}{r}\right)^4, & r_* \le r \le h \end{cases} \tag{2.6}$$

where U_* and r_* are the critical energy and pore radius at the hydrophobic-hydrophilic transition, respectively; γ is the line tension per unit length of pore perimeter and Γ is the surface tension per unit area of the intact membrane. The final quadratic term accounts for the steric repulsion between lipid heads lining the pore, where C is a constant chosen to match empirical data (Debruin & Krassowska, 1999; Glaser et al., 1988; Neu & Krassowska, 1999). The term $\pi a_p r^2 \Delta\Psi_m^2$ represents the capacitive contribution to the transition in which a_p defines the dielectric permittivity of the porous membrane and is given as $\epsilon_0\,(\kappa_w - \kappa_m)/2h$. Here, ϵ_0 is the dielectric permittivity of free space, and κ_w and κ_m are dielectric constants of water and the membrane, respectively. **Figure 2.1b** illustrates the behavior of this system for different values of $\Delta\Psi_m$. Substituting equation (2.6) into (2.5), rearranging, and simplifying with several assumptions, pore density $N(t)$ is approximated by:

$$\frac{dN}{dt} = \alpha e^{\beta^2}\left(1 - \frac{N}{N_0} e^{-q\beta^2}\right) \tag{2.7}$$

in which α and q are fitting parameters, β is the ratio of $\Delta\Psi_m$ to the electroporation threshold $\Delta\Psi_{ep}$, and N_0 is the pore density when $\Delta\Psi_m = 0$ (Debruin & Krassowska, 1998). A summary of the parameters presented in these equations can be found in **Table 2.1**. Importantly, a significant body of work has shown agreement between these equations and experimental observations. Further, researchers are now able to directly utilize these simplified equations via analytical or numerical methods for experiment planning, protocol optimization and data analysis.

2.2.3 – *Electric field intensity, duration, and IRE*

Permeability increase, pore formation, and induced biological effects depend on applied parameters such as the amplitude, number, and length of pulses. ECT treatments typically use eight pulses with electric field magnitudes near 1 kV/cm (Sersa et al., 2008). However, when a high number of pulses (60-100) of sufficient amplitude (0.5 – 1.0 kV/cm) are delivered, treated cells lose homeostatic equilibrium and die within minutes to hours (Al-Sakere, André, et al., 2007). The exact mechanisms through which IRE causes cell death have not been fully elucidated, but a number of possible pathways such as direct electro-conformational denaturation of macromolecules (W. Chen et al., 2006; R. C. Lee et al., 2000), induced depletion of adenosine triphosphate (ATP) (Frandsen et al., 2012), local vascular disruptions (Kanthou et al., 2006; Sersa

Table 2.1 – Summary of parameters used in basic transmembrane potential and pore formation equations.

Symbol	*Definition*	*Value or Range*	*Units*	*Source*
R_c	Radius of a mammalian cell	5 - 50	μm	–
k_B	Boltzmann constant	1.380649 x 10^{-23}	J/K	–
T	Temperature	295	K	–
σ_e	Extracellular fluid conductivity (saline)	1.6	S/m	–
ϵ_0	Dielectric permittivity of vacuum	8.85 x 10^{-12}	F/m	–
h	Lipid bilayer thickness	3-15	nm	–
σ_i	Cytosol conductivity	0.1-1	S/m	a, b
σ_m	Lipid bilayer conductivity	10^{-10} - 8.7 x 10^{-6}	S/m	a, b
ε_m	Lipid bilayer dielectric permittivity	4.4 x 10^{-11}	F/m	c, d, e
τ_m	Membrane charging constant	0.1-1	μs	e, f
D	Diffusion constant of pores	5 x 10^{-14}	m^2/s	g, h
U_*	Pore energy at transition	45	k T	i
r_*	Pore radius at transition	0.5-0.8	nm	i
γ	Normalized line tension of pore perimeter	1.8 x 10^{-11}	J/m	i, e
Γ	Normalized surface tension of membrane	10^{-3}	J/m^2	i
C	Quadratic fitting parameter	9.67 x 10^{-15}	$J^{1/4}$ m	i
a_p	Permittivity constant	6.9 x 10^{-2}	F/m^2	i
κ_w	Dielectric constant of water	80	–	i
κ_m	Dielectric constant of membrane	2	–	i
N_0	Equilibrium pore density	1.5 x 10^5	cm^{-2}	a
$\Delta\Psi_{ep}$	Characteristic voltage of electroporation	258	mV	a
α	Fitting parameter	100	cm^{-2} ms^{-1}	a
q	Fitting parameter	2.46	–	a

a – Debruin and Krassowska, 1999; b – Kotnik and Miklavcic, 2006; c – Glascoyne et al., 1993; d – Hu et al., 2009; e – Smith et al., 2006; f – Ye et al., 2010; g – Weaver and Chizmadzhev, 1996; h – Vasilkoski et al., 2006; i – Neu and Krassowska, 1999.

a – Debruin and Krassowska, 1999; b – Kotnik and Miklavcic, 2006; c – Glascoyne et al., 1993; d – Hu et al., 2009; e – Smith et al., 2006; f – Ye et al., 2010; g – Weaver and Chizmadzhev, 1996; h – Vasilkoski et al., 2006; i – Neu and Krassowska, 1999.

et al., 2008) or electrolytic pH changes (L. Rubinsky et al., 2016) could contribute to cell injury. Further, it has been shown that Na^+/K^+ pumps play a major role in restoring contractility after electroporation of skeletal muscle, supporting the theory that chemical imbalances mediate eventual cell death (Clausen & Gissel, 2005). Ultimately, high amounts of ATP are required to restore disrupted chemical concentration gradients; depending on the number and lifespan of the pores, this ATP demand can outweigh what can be generated by the cell, leading to high levels of intracellular Ca^{2+} and eventual cell death (Gissel et al., 2011). Notably, the temporal scale in which IRE lesions appear seems to vary depending on the tissue type, suggesting a moiety of death mechanisms (Vogel et al., 2016). Future work evaluating these mechanisms more rigorously will be vital to our understanding of IRE-induced cell death.

Importantly, the application of an electric field across a dielectric material – such as biological matter (cells/tissue) – results in resistive losses and subsequent generation of heat. Thus, supplying excessive electrical energy within a given time frame can cause thermal damage (Davalos et al., 2005a; Davalos & Rubinsky, 2008; O'Brien et al., 2017). This side effect can be alleviated by referencing the literature to use previously determined non-thermal parameters for specific tissues, by incorporating thermal mitigation strategies, or by modeling treatment beforehand to select pulse paradigms capable of non-thermal IRE (O'Brien, Lorenzo, et al., 2019).

2.2.4 – *Basics of Tissue Ablation with IRE*

IRE is typically performed as a minimally invasive percutaneous or laparoscopic procedure. Patients are sedated with general anesthesia and neuromuscular blocking agents are prophylactically administered to mitigate muscle contractions that can occur due to electrical stimulation of nearby neurons. Though flat plate and endoscopic electrodes have been used, electrical energy is typically supplied through parallel needle electrodes (∅~1 mm) inserted directly into the tissue of interest (**Figure 2.2**). Depending on the size of the lesion, IRE is performed with as little as two or up to 6 monopolar probes. Additionally, a single-insertion bipolar probe has been reported for certain small tumors in precarious locations. After insertion, probe locations can be verified via intraoperative imaging (ultrasound or computed tomography (CT)), and 50-100 pulses on the order of 100 μs in length are sequentially delivered between each electrode pair. IRE is synchronized with the absolute refractory period of the electrocardiogram (ECG) to mitigate the risk of electrical interference with cardiac myocytes and potential arrhythmia (Deodhar, Dickfeld, et al., 2011).

The electric field distribution in the tissue drives treatment outcome – this is dictated by a variety of factors including electrode geometry/configuration, pulse parameters and tissue properties. Important tissue-specific parameters pertaining to the production of non-thermal ablation are the dynamic electrical conductivity and lethal electric field threshold. Dynamic conductivity describes the evolution of the tissue's electrical conductivity when exposed to electric fields of increasing amplitude and can be determined through carefully planned experiments (Miklavcic et al., 2005; Neal et al., 2012). The lethal threshold is a metric of the susceptibility of a certain tissue or cell type to IRE-induced cell death. It is dependent upon the shape and amplitude of the characteristic waveform, number of pulses, and duration of the applied field, but for most

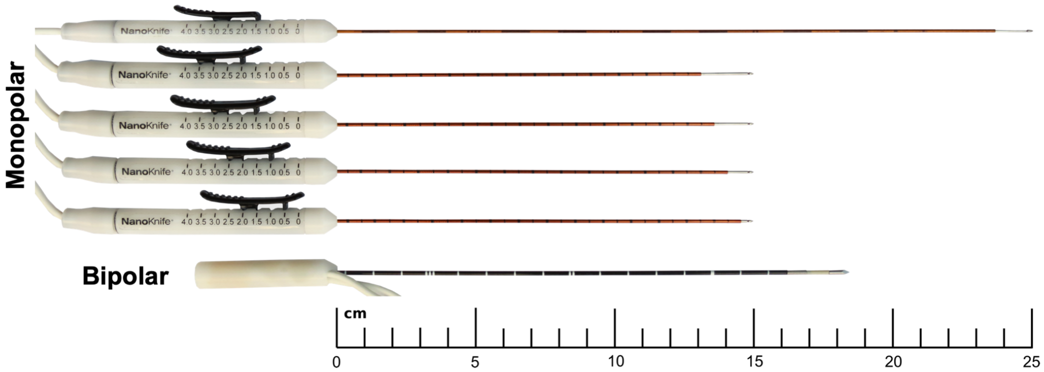

Figure 2.2 – IRE is delivered through 25- or 15-cm long monopolar electrodes with varying degrees of exposure. In some cases, a bipolar electrode with fixed exposure and electrode separation is also used.

tissues this threshold is between 300 – 1000 V/cm when 100 pulses are applied (Jiang et al., 2015). It is critical to note that the electric field threshold for a given tissue decreases as more pulses are applied but saturates after a certain number of pulses. Moreover, because minor Joule heating effects occur during treatment, increased pulse numbers result in local increases in conductivity at a rate of 1-3% per degree Celsius, which can also propagate the electric field and increase ablation volume. However, because IRE outcomes are heavily dependent on user inputs as well as characteristic properties of the tissue under study, the framework by which lethal thresholds are calculated must be taken into careful consideration. The minimum parameters that should be reported after IRE treatment are the number of pulses, pulse width (μs), frequency (Hz), and voltage-to-distance ratio (VDR, V/cm) – defined as the quotient of the applied potential (V) and electrode separation (cm). These allow one to gauge the intensity of treatment and provide a basic level of standardized reporting.

Pre-clinical investigations of IRE often employ pre-treatment planning tools to study the outcomes of certain pulse paradigms. Such models allow for the development of personal treatment plans for each patient, ensuring accurate probe placement, complete tumor coverage and minimal temperature rise (Kos et al., 2015; Latouche et al., 2017). A brief example of the treatment planning process can be seen in **Figure 2.3**. In the future, such planning modules will likely become a mainstay of human treatments, but no clinically accepted modeling procedure/algorithm has been introduced thus far.

2.3 – Irreversible Electroporation as a Monotherapy

Since its introduction in 2005, over 50 clinical trials have been organized to study IRE (**Figure 2.4**) and hundreds of papers demonstrating clinical outcomes have been published. IRE has helped over 5,500 patients with unresectable cancer, many of whom have participated in these trials. In subsequent sections, we review the major *in vivo* work and clinical studies that provide insight regarding the uses and outcomes of IRE. While we acknowledge the many studies that have investigated IRE in the lung, kidney, brain, and other organ systems, we maintain a focus on the prostate, pancreas, and liver, as cancers in these locations pose specific opportunities that IRE can potentially address.

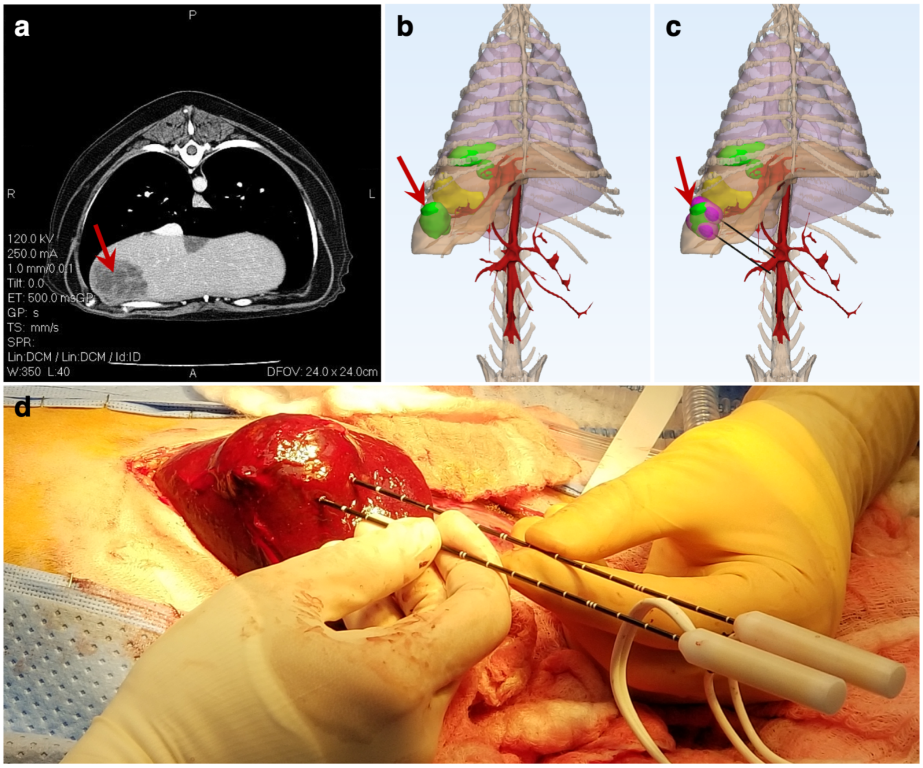

Figure 2.3 – Pretreatment planning allows for prediction of ablation outcomes. For a canine case of multifocal liver cancer, this consists of (a) locating malignant tissue (red arrow) on diagnostic imaging, (b) reconstructing patient anatomy to assess tumor proximity to relevant structures, (c) identifying suitable electrode insertion pathway and estimating ablation volume (pink), and (d) using the pretreatment planning model to inform insertion tracts for optimal ablation outcomes.

2.3.1 – Prostate

Prostate cancer (PCa) is the most common neoplasm in men, accounting for 1 in 5 new cancer cases (Siegel et al., 2019). Though patients diagnosed with PCa have 5-year survival rates of nearly 100%, this disease is the second-most deadly cancer in the male population (Heidenreich et al., 2008). Available interventions including radical prostatectomy and radiotherapy tend to have negative consequences on sexual and urinary function (Nam et al., 2014); thus, focal ablation has emerged as a viable alternative. IRE is particularly promising for patients with PCa due to fact that roughly 80% of these patients exhibit localized disease (J. Li et al., 2012). Additionally, IRE may improve functional outcomes for PCa patients due to the presence of protein-rich structures near the prostate including the neurovascular bundle, lower urinary sphincter, ejaculatory vesicles, and urethra – all of which are at risk when patients undergo resection or thermal ablation.

The first evaluation of IRE in prostate was performed by Onik and colleagues in 2007 (Onik et al., 2007). In this initial study, 6 healthy canine prostates were treated with IRE using voltage-to-distance ratios (VDRs) up to 3,000 V/cm. The urethra was spared even when purposefully ablated, and although necrosis was noted on directly ablated vessels, patency was maintained without evidence of thrombosis. In a follow-up study, Onik and Rubinsky evaluated early safety and efficacy of IRE in 16 human patients (Onik & Rubinsky, 2010). At 3 weeks post-

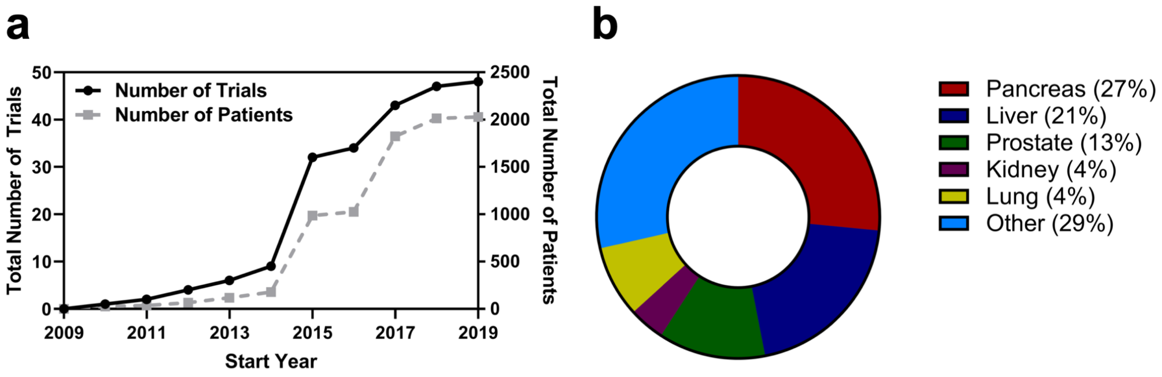

Figure 2.4 – (a) Temporal trends in the cumulative number of interventional clinical trials investigating IRE and the corresponding number of patients associated with them. (b) Distribution of clinical trials based on cancer location. Data acquired from ClinicalTrials.org on August 31, 2019.

IRE, 93% of biopsies were negative and potency was preserved in all men potent before treatment. Subsequent reports sought to elaborate on these early findings. In 2013, Tsivian and Polascik performed bilateral ablations in the healthy prostate of 12 dogs and confirmed the ability of IRE to spare the urethra, rectum, and capsule when probes were placed in close vicinity (~7 mm) to these structures (Tsivian & Polascik, 2013). Additionally, no clinically significant side effects were observed and erectile function was maintained in all dogs. The first report evaluating intermediate-term safety and feasibility in humans was published shortly thereafter (Valerio et al., 2014). In this study, IRE was performed in 34 men with localized PCa. At a median follow-up of 6 months, potency and continence were preserved in 95% and 100% of men potent/continent a priori. From an oncological perspective, 6 patients had suspicious residual disease and 1 local failure was recorded. In 2015, a series of investigations evaluating quality of life (QoL) (van den Bos et al., 2015), histopathological outcomes (van den Bos, Jurhill, et al., 2016), and effects of electrode configuration (van den Bos, de Bruin, et al., 2016) on ablation outcomes were published on a 16-patient cohort that underwent IRE treatment followed by radical prostatectomy 4 weeks later. Here, it was shown that the mild adverse events resulting from IRE were mostly resolved by the 4-week timepoint. Slight declines were noted in urinary QoL while functional outcomes were retained. Histologically, sharp demarcations between ablated and viable tissue were noted and correlated well with the hypointense region seen on transrectal ultrasound (Error! Reference source not found.). Lastly, it was found that a higher number of electrodes produced a larger ablation relative to the area circumscribed by the electrode configuration (van den Bos, de Bruin, et al., 2016).

A number of other clinical studies have since evaluated IRE outcomes for the ablation of PCa (**Table 2.2**). Recently, two larger patient cohorts have been assessed. In the first, safety, QoL, and short-term oncological outcomes were evaluated by van den Bos et al (van den Bos et al., 2018). Safety was again demonstrated while oncological control was 84% in-field and 76% whole-gland. The authors noted that after gaining experience with the procedure, margins were increased and Nanoknife® operation became more efficient; oncological control with increased margins in the absence of system errors increased to 97% and 87%, respectively. The latter study by Guenther et al was a retrospective analysis of longer-term outcomes for 429 patients (Guenther et al., 2019). This cohort was made up of patients with high-risk disease (73%), but 5-year recurrence rates were similar to that of radical prostatectomy at roughly 10%. Further, IRE maintained urogenital function, including complete preservation of urinary continence while only 3% of patients experienced erectile dysfunction 12 months after treatment. Though further randomized

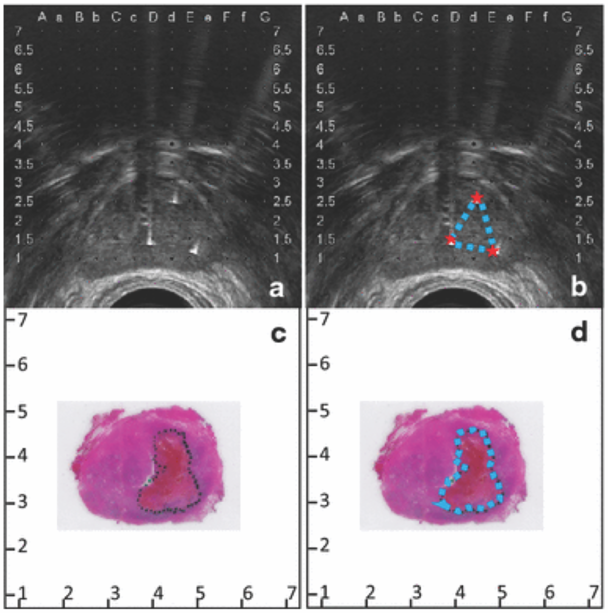

Figure 2.5 – Ablation regions visualized on transrectal ultrasound correlate with those quantified histologically. (a) Perioperative ultrasound shows (b) the area circumscribed by the electrode configuration within the hypoechoic prostatic tissue. (c) Histology obtained after radical prostatectomy 4 weeks post-treatment shows (d) the area of ablation, which closely resembles the size, shape, and location of that visualized intraoperatively. Image reprinted under Creative Commons Attribution 4.0 International License from van den Bos et al., 2016.

evaluations are necessary, these results support the safety and feasibility for treatment of patients with localized PCa, especially those with disease that is recurrent and/or not amenable to surgery/radiation.

2.3.2 – Pancreas

So far, unresectable pancreatic tumors present perhaps the largest window of opportunity for IRE as a technique capable of drastically improving clinical outcomes. Patients with pancreatic cancer have extremely low 5-year survival (9%) and less than 20% are candidates for surgery (Howlader et al., 2018; Siegel et al., 2019). The pancreas is situated near the celiac trunk, hepatic artery, and superior mesenteric vein, contributing to its surgical inaccessibility (**Figure 2.6**). Thermal ablation is associated with high morbidity when applied to pancreatic tumors due to the presence of these fragile structures (Pandya & Shelat, 2015). Thus, IRE is an emerging tool that could play a critical role in the future management of patients with locally advanced disease.

To date, roughly 30 manuscripts have evaluated IRE in vivo for focal ablation of pancreatic tissue. The first of these was performed by Charpentier et al. in swine (Charpentier et al., 2010). The authors of this study used two monopolar needle electrodes with an induced voltage of 1500 V and spacing of 10 to 15 mm to ablate healthy pancreas. All pigs tolerated the procedure without complication and pancreatic ducts were preserved. Bower et al. published a similar study shortly thereafter, confirming preservation of vascular structures and reporting the feasibility of both monopolar and bipolar IRE probes for pancreatic ablations (Bower et al., 2011). The first clinical study of pancreatic IRE was performed by Martin and colleagues in 2012 (R. C. G. Martin et al., 2012). Here, 27 patients with locally advanced pancreatic adenocarcinoma (LAPC) were treated with IRE at a target VDR of 1500 V/cm. 100% ablation success was achieved with only 4 potential IRE-related adverse events, and no evidence of recurrence was observed within the 90-day follow-up period. In a similar study, Narayanan et al. performed the first percutaneous IRE treatments in a cohort of patients with unresectable or metastatic disease under computed tomography (CT) guidance (Narayanan et al., 2012). Of the 15 patients, 2 were downstaged and underwent margin-negative resection. In the remaining 13 patients, 46% had stable disease at last follow-up. In 2015, Martin and colleagues published a study evaluating IRE in 150 patients with LAPC (R. C. G. Martin et al., 2015). Patients receiving treatment with IRE had an overall survival of 18 months and local progression-free survival of 10.7 months. Including another 50 patients in which IRE was used for margin accentuation, overall survival for the 200-patient cohort was 24.9 months. In recent years, IRE has been associated with overall survival of up to 27 months for patients with unresectable LAPC (Leen et al., 2018) and response rates commonly exceed 70% (Belfiore et al., 2017; R. C. G. Martin et al., 2013; Paiella et al., 2018). In addition to potential survival improvements, some patients have been able to lower narcotic intake after treatment and others have shown major improvements in quality of life (Belfiore et al., 2017; R. C. G. Martin et al., 2012). Depending on the extent of vascular involvement, downstaging occurs in 5-10% of cases, allowing for follow-up resection (Flak et al., 2019; Leen et al., 2018; Månsson et al., 2016). Despite the promising results reported in some studies, a limited number of institutions have adopted IRE. This could be due to inherent difficulties in treating advanced pancreatic tumors, discrepancies in patient selection, and differences in institutional protocols for IRE application. Moreover, post-operative imaging has proven more difficult for assessing ablation outcomes for pancreatic lesions, which could contribute to these inconsistent findings (Akinwande et al., 2015). Though many investigators have reported prolonged survival after IRE, future randomized studies are critically needed to directly compare the safety and efficacy of IRE against alternative treatments.

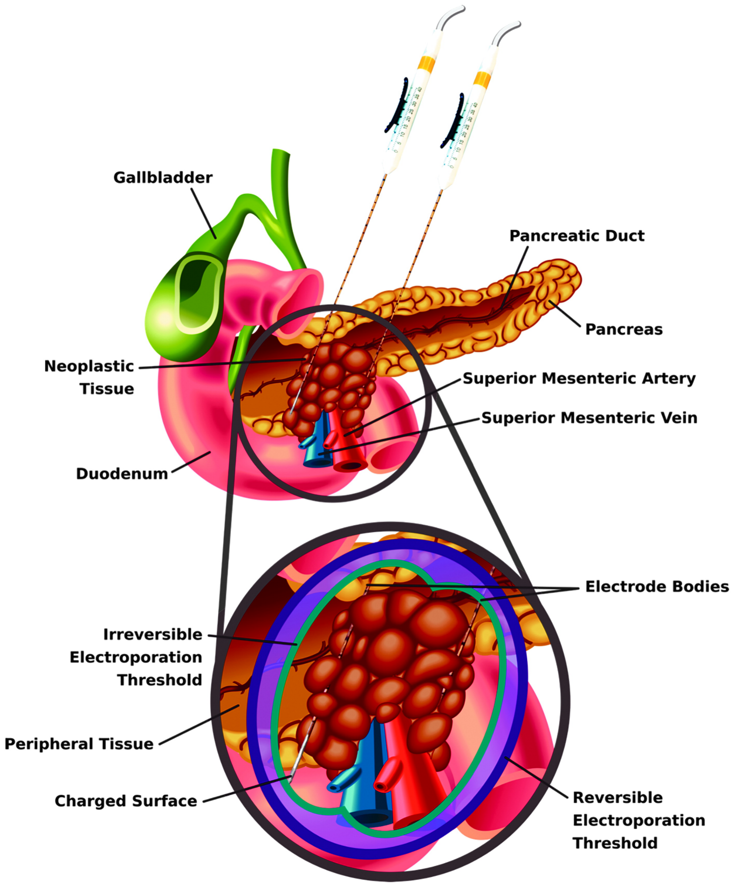

Figure 2.6 – Schematic depicting generalized electrode placement and resulting treatment zone for a pancreatic tumor encasing the superior mesenteric vessels. The proximity of the pancreas to these vessels and other vasculature limits interventional options for a large number of patients. In such cases, IRE has shown promise as it allows for focal ablation of the tumor without long-term injury to these critical proteinaceous structures. Additionally, the zone of reversible electroporation could be used to increase uptake of adjuvant molecules and/or chemotherapeutics in the periphery of the ablation, further increasing efficacy.

2.3.3 – *Liver*

Hepatocellular carcinoma (HCC) represents the vast majority of liver malignancies and is the third most common cause of cancer-related mortality (Altekruse et al., 2014). When detected early, curative treatment for HCC can be achieved with resection or transplantation, but less than 15% of patients fall into this category (Iavarone & Colombo, 2014). The liver is also frequently a site of metastasis, especially for primary tumors of the gastrointestinal (GI) tract. Focal thermal ablation has become a mainstay in the management of liver lesions and has shown similar oncological outcomes to resection with limited complications and without reducing transplant exception points (Niemeyer et al., 2014a; M. Zhang et al., 2017a). Despite this, thermal ablation is often not an option due to the presence of tumors on or near hepatic blood vessels or biliary structures, and patients with underlying liver dysfunction have increased rates of post-treatment abscess formation after thermal ablation (Kim & Thomas, 2014). The non-thermal nature of IRE allows it to overcome many of these limitations, and its role in the management of hepatic masses is still being fully established.

The first in vivo study of IRE for liver ablation used flat plate electrodes and a single, 20 ms monopolar pulse with 1 kV/cm amplitude to create reproduceable regions of "endothelial necrosis, thrombus formation, vascular compromise, and vacuolar degeneration" within 3 hours of treatment in rats (Edd et al., 2006). Shortly after this publication, needle electrodes were used to generate ablations in a large animal model (B. Rubinsky et al., 2007) and the ability to perform percutaneous IRE in the liver and observe ablation in real-time via ultrasound was demonstrated (E. W. Lee et al., 2007). These early findings were first translated to the clinic when Thomson et al. found IRE to have an acceptable safety profile for the ablation of liver, kidney and lung tumors, including metastases from primary tumors elsewhere in the body (Thomson et al., 2011). In several subsequent studies, IRE was shown to be suitable for ablating tumors near vital hepatic structures (Cannon et al., 2013; Dollinger et al., 2015; Kingham et al., 2012; Narayanan et al., 2014; Silk et al., 2014). The ability to treat these tumors has opened the door to many clinical investigations. Some of these reports have investigated functional deficits following IRE and have found that biomarkers of hepatic function tend to rise transiently (1-2 days) but return to baseline within a few days, verifying safety (Alnaggar et al., 2018; Silk et al., 2014). Notably, Bhutiani et al. found that IRE had a similar 6-month success rate but was more tolerable than microwave ablation

(MWA) for patients with compromised liver function (Child-Pugh B) (Bhutiani et al., 2016). IRE-treated patients also had shorter hospital stays and lower rates of re-admission, likely due to lower indiscriminate effects on hepatic tissue. In recent years, reports with intermediate to long-term follow-up have shown that IRE produces acceptable oncological outcomes for patients with unresectable disease, especially for small tumors (Mafeld et al., 2019; Schicho et al., 2019). For tumors larger than 2-4 cm, overall and recurrence-free survival tend to decline, but modifications to the treatment paradigm in the future may allow for higher efficacy in larger lesions (Appelbaum et al., 2014). Besides large tumors, the only other major contraindication for performing hepatic IRE is the presence of metallic implants in close proximity to the tumor, which has been shown to adversely affect progression-free survival (Cornelis et al., 2019). Varying degrees of complication have been observed with IRE in liver tumors (Kingham et al., 2012; Mafeld et al., 2019; Silk et al., 2014), likely due to the learning curve inherent in the adoption of this new treatment modality (Philips et al., 2013). In recent retrospective analyses, however, the overall complication rate of hepatic IRE was similar to thermal ablation despite being used as a salvage therapy in many cases of advanced disease (Scheffer et al., 2014; Verloh et al., 2019). In summary, IRE appears to be a promising option for precarious, central hepatic tumors abutting proteinaceous structures such as the biliary tree or portal vein, but again, randomized studies are needed to further delineate its oncological outcomes in comparison to existing focal therapies.

2.4 – *Alternative Applications and Future Directions*

2.4.1 – *Cardiovascular*

IRE may be a useful addition to the technological repertoire for cardiac ablation and other vascular applications where focal destruction of aberrant cells is desired, namely in conditions such as atrial fibrillation, restenosis and resistant hypertension. Though it was first noted that intense electric fields arising during defibrillation may create “sarcolemmal microlesions” in 1987,114 IRE was not intentionally pursued for clinical cardiovascular applications until the pioneering work of Maor and Rubinsky appeared in the late 2000s (Maor et al., 2007, 2008; Maor & Rubinsky, 2010).

Early investigations applied IRE to rat carotid arteries and demonstrated ablation of vascular smooth muscle cells (VSMCs) without complication and without macroscopic damage to acellular vascular architecture (Maor et al., 2007) using a wide range of pulse parameters (Maor et al., 2009). Later reports showed that VSMCs are eliminated over the course of 72 hours without injury to elastic lamella, collagen fibers or proteoglycans, and endothelial cells regenerated by 7 days (Maor, Phillips, et al., 2010). IRE has also been shown to mitigate restenosis following angioplasty (Maor et al., 2008) and custom devices capable of endovascular pulse delivery have been developed (Maor, Ivorra, et al., 2010). Although not covered in depth here, these findings led to a series of papers investigating the use of IRE as a tissue decellularization technique, which was initially demonstrated both in situ and ex vivo (Maor, Phillips, et al., 2010; Sano et al., 2010).

Lavee and colleagues were the first to use IRE to correct arrhythmogenic regions of the heart. Schemes using between 8 and 32 pulses generated completely transmural, epicardial atrial ablations in swine (Lavee et al., 2007). Circular ablation catheters were introduced by Wittkampf et al. and were shown to safely generate clinically-relevant lesions in pulmonary vein (PV) ostia (Wittkampf et al., 2011) and ventricles (Neven et al., 2014). Van Driel and colleagues demonstrated a reduction in PV stenosis after catheter-based IRE versus radiofrequency ablation (Van Driel et al., 2014), and a later study demonstrated similar PV ablations with a commercially-available catheter in canines (Witt et al., 2018). Other relevant work has shown *ex vivo* that IRE can be used to ablate Purkinje fibers and reduce vulnerability to ventricular fibrillation (Livia et al., 2018). Lastly, one human study has been performed in which IRE was used successfully to electrically isolate PVs in 22 patients (Reddy et al., 2018). Ablation times were less than one minute, and 1-month follow-up visits indicated uneventful recovery. These emerging data support the further exploration of IRE for cardiovascular implications.

2.4.2 – Immune Modulation and Synergy with Immunotherapy

Recently, the ability of focal tumor therapies to elicit systemic immune activation has garnered much attention. Immune modulation in response to IRE treatment has been investigated in a number of in vitro and in vivo studies. The first of these showed a decline in immune cell populations – CD4+ and CD8+ T lymphocytes, antigen-presenting cells, macrophages and natural killer cells – over the course of 6 hours after IRE treatment, indicating the ability of IRE to form substantial ablations without relying on antitumor immunity (Al-Sakere, Bernat, et al., 2007). A more comprehensive study evaluating immune cell populations and cytokines produced up to 21 days after treatment in an immune-competent rat osteosarcoma model found significantly increased CD3+ and CD4+ T lymphocytes, a higher CD4+/CD8+ ratio, and modified cytokine expression in IRE versus sham and surgery control groups (X. Li et al., 2012).

It was later shown that immunocompetent mice have a better local response to IRE and improved survival versus their immunodeficient counterparts (Neal et al., 2013). Further, recent in vitro work has shown that melanoma cells ablated with IRE release substantially more protein and TRP-2 antigen than those treated with thermal ablation (heating and cryoablation) (Shao et al., 2019a). Additional analyses showed that protein released from IRE-treated cells was more efficient at inducing T cell proliferation than that released from heat or cryotherapy-treated cells, supporting the observation that IRE reduces the rate of metastases in a rabbit VX2 model (E. W. Lee et al., 2012) and exhibits a stronger abscopal effect than thermal ablation (Bulvik et al., 2016). Improved immune response versus other modalities could be due to release of intracellular contents or direct modulation of cell signaling, but further investigation is warranted (Goswami et al., 2017).

To assess the translational potential of these early findings, Lin et al. used IRE alone or alongside allogenic natural killer (NK) cell therapy in 71 patients with stage III or IV pancreatic cancer (M. Lin et al., 2017). IRE with NK therapy increased survival for patients with either stage III or IV disease and produced substantial increases in CD4+ and CD8+ T lymphocytes, NK cells, and B cells for stage III patients. Interestingly, Th2 cytokine (IL-4, IL-10) levels remained relatively unchanged while Th1 cytokines (IL-2 and IFN-γ) increased in response to both treatments, consistent with pre-clinical findings (X. Li et al., 2012). This initial study, along with a similar investigation for patients with unresectable liver cancer, indicates that IRE could play a "priming" role by preparing the tumor microenvironment for effective exploitation by immunotherapy (Yang et al., 2019). Further clinical examination has shown that immune modulation occurs quickly after IRE and that attenuation of the highly immunosuppressive environment, as seen by a reduction in regulatory T cells, can be achieved for at least two weeks (He et al., 2019; Scheffer et al., 2019). These results are supported by the finding that IRE and anti-PD1 immunotherapy work synergistically to improve survival in a murine model of pancreatic cancer (J. Zhao et al., 2019). This study again showed the presence of immune memory that was able to address tumor rechallenge. Similar to the findings of He et al., infiltrating CD8+ T lymphocytes were associated with improved survival. These results are paving the way toward the clinical translation of combinatorial treatment strategies that capitalize on the ability of IRE to create an immunostimulatory microenvironment.

2.4.3 – High-Frequency Irreversible Electroporation

In 2011, Arena and colleagues numerically showed that short pulses (500 ns – 2 µs) of alternating polarity may be more favorable for predictable tissue ablation in heterogeneous tissues than long monopolar pulses (Arena, Sano, Rylander, et al., 2011). In this initial computational analysis, a tissue domain consisting of an external layer of skin surrounding a cylinder of fat was modeled to study the extent of electroporation induced by pulsatile voltage waveforms with different characteristic frequencies between 250 kHz and 2 MHz. High-frequency voltage waveforms were shown to penetrate the heterogeneous system more uniformly. A follow-up study introduced the term high-frequency irreversible electroporation (H-FIRE, **Figure 2.7a**) and showed the ability of these waveforms to generate non-thermal ablations in rat brain without muscle contractions (Arena, Sano, Rossmeisl, et al., 2011). H-FIRE has since been used to treat intracranial malignancies in canines and low-amplitude H-FIRE waveforms have been used to transiently disrupt the blood-brain barrier (BBB) (Arena et al., 2014).

In addition to the aforementioned advantages, in vitro work has shown that H-FIRE may exhibit selectivity towards malignant phenotypes (**Figure 2.7**) (Ivey et al., 2015). Further, H-FIRE ablation in a 4T1 murine mammary tumor model stimulated a local inflammatory response and resulted in systemic immune activation capable of reducing distant metastases, suggesting this technology is well suited for both standalone and combinatorial treatment strategies (Ringel-Scaia et al., 2019). In its first clinical evaluation, H-FIRE was used to treat prostate cancer in 40 men without ECG synchronization (Dong, Wang, et al., 2018). Four weeks after treatment, evaluated patients had complete preservation of urinary (40/40) and sexual (14/14) function. Additionally, no cardiac-related side effects were noted. These emerging data support the notion that H-FIRE

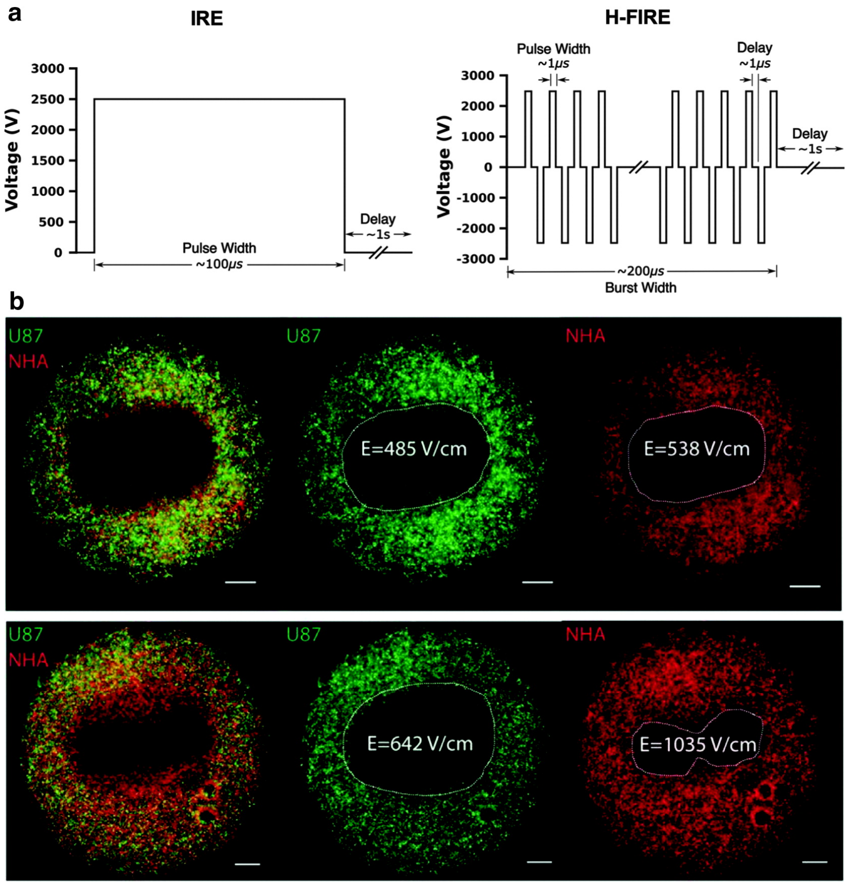

Figure 2.7 – H-FIRE selectively targets malignant cells. IRE and H-FIRE employ voltage waveforms (a) with different characteristic frequencies, which result in unique biological effects. IRE-treated malignant (U251) and healthy (NHA) astrocytes (b, top) exhibit similar electric field thresholds for cell death. However, lethal electric field thresholds for H-FIRE (b, bottom) are much lower for U251 cells than NHAs, demonstrating the capacity of H-FIRE to target malignant phe- notypes. (b) Published in Ivey et al.144 reprinted under Creative Commons Attribution 4.0 International License. H-FIRE, high-frequency irreversible electroporation. Scale bar represents 1 mm.

will likely augment the clinical efficacy of high voltage pulsed electric fields in the coming years. Future studies investigating oncological outcomes in larger, randomized patient cohorts are warranted and will be critical to this development.

2.5 – *Concluding Remarks*

IRE has an array of potential advantages over existing technologies. Though promising results have been demonstrated, dissemination of knowledge and training is critical to the widespread adoption of IRE. Differences in physician experience, patient inclusion criteria, and reporting have led to inconsistencies in the application of IRE. Additionally, studies thus far have primarily evaluated IRE in patients with advanced disease and with numerous comorbidities. Despite this, IRE has shown to be a viable option for certain patients diagnosed with tumors of the prostate, liver, kidney, and pancreas. With proper patient selection and choice of pulse paradigms, IRE can improve outcomes as demonstrated by the *in vivo* and clinical results provided herein. Future developments involving combinatorial therapeutic regimens and alternate waveforms have shown exciting early results, and further evaluation will likely expand the clinical impact of IRE in the coming years.

3 – Experimental and Numerical Study of Parameters affecting High-Frequency Irreversible Electroporation[2]

3.1 – Introduction

Prostate cancer (PCa) is the most commonly diagnosed and second most deadly cancer in males, accounting for one in five new cancer cases globally (Litwin & Tan, 2017; Seraphin et al., 2021; Siegel et al., 2021). Despite its prevalence, diagnosis and treatment of PCa presents a challenge for patients and clinicians. Because PCa is insidious in nature and often does not threaten life expectancy, early detection has led to unnecessary overtreatment, reducing quality of life (QoL) for countless patients (Ferrer et al., 2013). The 2012 guidelines of the US Preventative Services Task Force even recommended against prostate-specific antigen (PSA) screening with the hopes of preventing overtreatment (Cancer et al., 2012), but recent evidence suggests this recommendation may be partly responsible for the recent plateau in PCa mortality, which had been in steady decline for over two decades (Jemal et al., 2021). Declining QoL after treatment of local-stage low-risk PCa is perhaps the most salient motive behind recommendations against prostate-specific antigen screening. Standard-of-care options like radical prostatectomy (RP) and radiotherapy can damage critical stromal neurovasculature, diminishing QoL by creating urinary and sexual problems for patients (Ferrer et al., 2013). More specifically, ~20% of men who undergo RP experience long-term urinary incontinence, while both RP and radiotherapy cause long-term erectile dysfunction in over half of men treated (Fenton et al., 2018). For these reasons and due to improved diagnostics allowing for regional localization of disease, focal therapy has garnered attention as a low-risk treatment option that can prevent or delay the transition of low-

---

[2] Chapter 3 is adapted and reprinted with kind permission from The American Society of Mechanical Engineers. © 2022 by ASME. Aycock, K. N., Vadlamani, R. A., Jacobs, E. J., Imran, K. M., Verbridge, S. S., Allen, I. C., Manuchehrabadi, N., & Davalos, R. V. (2022). Experimental and Numerical Investigation of Parameters Affecting High-Frequency Irreversible Electroporation for Prostate Cancer Ablation. *Journal of Biomechanical Engineering*, *144*(6), 1–11.

grade PCa to a more aggressive state (Schmid et al., 2020). The main goal of these modalities is to treat tumor (index) foci without injury to the urethra, ejaculatory vesicles, neurovascular bundle, rectum, and other sensitive structures within and adjacent to the treatment region. Cryotherapy, high-intensity focused ultrasound, and laser ablation are currently the most widely utilized local interventions for treating prostate tumors (Perera et al., 2016). However, these therapies rely on thermal mechanisms that cause indiscriminate and sometimes extensive stromal damage within the treatment region (Roberts et al., 2011; Schmid et al., 2020).

Irreversible electroporation (IRE) is an emerging nonthermal pulsed field ablation modality with the potential to overcome these limitations. IRE treatment is performed by delivering several high-amplitude electric pulses through pairs of needle electrodes inserted directly into the treatment region. The induced electric field increases the transmembrane potential of targeted cells, forming nanoscale membrane defects (pores) that cumulatively lead to cell death. Unlike the aforementioned focal therapies, IRE's unique nonthermal mechanism allows it to be administered near critical structures such as nerves and vasculature. Preclinical work has demonstrated the ability of IRE to ablate malignant tissue immediately adjacent to the urethra while preserving microvasculature (Onik et al., 2007; Onik & Rubinsky, 2010), with clinical studies showing that the 5-yr survival rate with IRE is comparable to radical prostatectomy (Guenther et al., 2019). However, the long monopolar pulses used during IRE can stimulate excitable cells including cardiomyocytes, skeletal muscle fibers, and peripheral nerves; if ignored, this can lead to the potential for cardiac arrhythmias, intense muscle contractions, and pain. Thus, patients must undergo general anesthesia, pulses are electrocardiogram synchronized, and neuromuscular blocking agents are administered to limit skeletal muscle contractions (Deodhar, Dickfeld, et al., 2011; Fusco et al., 2021; Yao, Dong, Zhao, Lv, et al., 2017).

High-frequency irreversible electroporation (H-FIRE), or next-generation IRE, was introduced to provide the benefits of IRE while mitigating its disadvantages. While IRE employs 70–100 ls monopolar pulses, H-FIRE uses bursts of short (1–10 µs), bipolar pulses repeated with small delays (1–10 µs) between them. These short pulses enable current flow through both intracellular and extracellular spaces prior to electroporation (Ibey et al., 2014), so the electric field distribution is not as reliant on cell morphology or tissue architecture as compared to IRE (S. P. Bhonsle et al., 2015; Murovec et al., 2016; Yao, Zhao, Liu, et al., 2017). This simplifies treatment planning and improves predictability of ablation geometries. The alternating polarity of H-FIRE also reduces muscle contractions, obviating the need for neuroparalytics and reducing the risk of cardiac arrhythmias. H-FIRE has been examined *in vitro* and in preclinical *in vivo* studies for a range of visceral cancers (Z. Fang et al., 2021; Fesmire, Petrella, Fogle, et al., 2020; Fusco et al., 2021; Latouche et al., 2018; Rolong et al., 2017). Additionally, several recent works have reported the use of H-FIRE waveforms for the treatment of cardiac arrhythmias (Maor et al., 2019; Verma et al., 2021). Despite these generally promising results, aside from an initial clinical trial assessing feasibility, H-FIRE has not been evaluated for ablation of prostate cancer (Dong, Wang, et al., 2018).

It is generally unknown which H-FIRE waveforms are best for ablating large tissue volumes while maintaining acceptable levels of nerve stimulation and thermal damage. It is well established that pulse width is the dominant waveform parameter affecting the size of H-FIRE ablations. Longer pulse durations lead to improved ablation volumes (H. Liu et al., 2021; Vižintin et al., 2020; Yao, Dong, Zhao, Lv, et al., 2017), but these also increase the likelihood of muscle contractions. Short pulse widths theoretically favor selective ablation of malignant cells (Ivey et al., 2015) but require higher electric field strengths to generate cell death (Yao, Zhao, Liu, et al., 2017), making it difficult to generate the targeted lesion size while avoiding thermal damage (Agnass et al., 2020; Aycock et al., 2021; Yao, Liu, Zhao, Mi, et al., 2017). A second waveform parameter that may impact treatment outcomes is the delay between subsequent pulses. Pilot *in vitro* cuvette studies have demonstrated that inclusion of longer delays can reduce lethal ablation thresholds for "continuous" H-FIRE bursts (Vižintin et al., 2020). However, theoretical work has shown that waveforms with longer symmetric delays could cause more intense nerve stimulation (Aycock et al., 2021). Thus, waveform choice is not a trivial task, and specifically for PCa, little progress has been made toward determining the optimal combination of pulse width and interpulse delay.

In this chapter, we use immortalized and primary malignant prostate cells as well as a non-neoplastic prostate cell line to examine the ablative electric field thresholds (EFTs) for nine H-FIRE waveforms (three pulse widths × three interpulse delays) as well as conventional IRE. In parallel, we develop a numerical approach to objectively compare the risk of muscle contractions and heat generation for different waveforms. Experimentally, we characterize lethal EFTs for each cell type in a well-established three-dimensional (3D) culture platform that preserves cellular morphology, which is thought to play an important role in mediating waveform efficacy (Arena, Szot, et al., 2012; Ivey et al., 2019). Computationally, we use a modified spatially extended nonlinear node nerve fiber model to estimate stimulation thresholds for each waveform. These two thresholds, along with waveform-specific dynamic electrical conductivity, are then used to predict the volumes of tissue undergoing ablation, nerve stimulation, and thermal damage with standard dose-matched protocols. Finally, voltage is adjusted for each waveform such that ablation volume is consistent across each H-FIRE waveform, and at this *equivalent voltage*, we examine the extent of thermal damage and nerve stimulation.

3.2 – Methods

3.2.1 – Experimental Approach

Cells were seeded in 3D tumor mimics and incubated for 24 hours prior to treatment using the waveform parameters shown in **Table 3.1**. Cell size and morphology were assessed by confocal microscopy, and ablated lesions were visualized through live-dead fluorescence microscopy 24 hours after treatment. A numerical model of pulse delivery to the tumor mimics was constructed as previously described, allowing us to correlate lesion areas to the electric field distribution and calculate a lethal threshold (Arena, Szot, et al., 2012).

3.2.2 – Cell Lines

Three cell lines were tested in this study. The non-neoplastic immortalized prostate epithelial cell line RWPE-1 (CRL-11609, ATCC) was cultured in keratinocyte serum-free medium (K-SFM, 17005-042, Life Technologies, Carlsbad, CA) supplemented with 0.05 mg/ml bovine pituitary extract (BPE, Life Technologies) and 5 ng/mL human recombinant epidermal growth factor (EGF, Life Technologies). The prostate carcinoma cell line 22Rv1 (CRL-2505, ATCC) was cultured in Roswell Park Memorial Institute (RPMI) 1640 medium with 10% FBS (ATCC) and 1% penicillin-

Table 3.1 – Lethal electric field thresholds and nerve stimulation thresholds determined for the H-FIRE and IRE waveforms examined in this study, with conductivity curve data from Beitel-White et al., 2022.

Waveform	*Tissue Represented*	*Cell Type*	*NST (V/cm)*	*EFT (V/cm)*	*Conductivity Curve Origin*
2-5-2	Non-neoplastic Prostate	RWPE-1	57.0	1358.5	Estimated
	Prostate Tumor	22Rv1		1297.3	Estimated
		PDX		997.8	
5-5-5	Non-neoplastic Prostate	RWPE-1	25.4	873	Experimental Data
	Prostate Tumor	22Rv1		815.7	Experimental Data
		PDX		893.7	
10-1-10	Non-neoplastic Prostate	RWPE-1	16.0	761.3	Experimental Data
	Prostate Tumor	22Rv1		750	Estimated
		PDX		835.3	
IRE	Non-neoplastic Prostate	RWPE-1	1.2	635.2	Experimental Data
	Prostate Tumor	22Rv1		602.9	Experimental Data
		PDX		546.4	

NST – Nerve stimulation threshold; EFT – Electric field threshold streptomycin (Fisher Scientific). Finally, primary human prostate tumor cells were isolated from mice bearing patient-derived xenografts (PDX). These xenograft cells were extracted using common techniques (Pei et al., 2012) and cultured in complete F medium (X. Liu et al., 2017) containing Rho-associated kinase (ROCK) inhibitor Y-27632. This formulation has been introduced to allow the indefinite proliferation of primary epithelial cells derived from heterogenous tissue samples. PDX prostate cells were confirmed by flow cytometry analysis using FITC-conjugated PSCA antibody (Santa Cruz Biotechnology) as a human prostate cell marker and PE-conjugated CD140a (BioLegend, San Diego, CA) as a mouse cell marker. Human PDX prostate cells were used at early passage numbers (3 to 7). Flow cytometry analysis showed that at higher passage number (8+), mouse feeder cells (L929) become overgrown. All cells were incubated at 37°C and 5% CO_2 and passaged regularly at ~80% confluency.

3.2.3 – Hydrogel Platform

Collagen was extracted from rat tails and stored as a lyophilized solid as previously described (Rajan et al., 2007). Working stocks of 10 mg/mL were prepared by dissolution in sterile 0.1% acetic acid. Dissolved collagen was mixed with 10× DMEM (10% v/v) and 1N NaOH was used to adjust pH to ~ 7.4 to arrive at a final collagen concentration of 5 mg/mL. Cells suspended in their respective culture medium were introduced into the collagen mixture, which was homogenized and injected into prefabricated cylindrical PDMS wells ($\emptyset = 1$ cm, $h = 1$ mm) within a 24-well tissue culture plate. Cylindrical polydimethylsiloxane (PDMS) lids were placed on each well to ensure uniform cylindrical geometries. Culture plates were incubated at 37 °C for 25 minutes to allow the collagen to fully polymerize. PDMS lids were removed and 600 µl of complete media was added to each well. Hydrogels were incubated for 24 hours prior to treatment.

3.2.4 – Pulse Delivery

Electrical treatment and recording equipment were set up according to the schematic in **Figure 3.1a.** Conventional IRE (100 µs monopolar pulses, **Figure 3.1b**) was delivered using a BTX ECM 830 (Harvard Apparatus, Cambridge, MA) pulse generator. H-FIRE waveforms (**Figure 3.1b)** were generated using an EPULSUS FBM1-5 solid state Marx generator (Energy Pulse Systems, Lisbon, Portugal) with digital triggering. Bursts consisted of a series of bipolar pulses with pulse widths of 2, 5, or 10 µs and interpulse delays of 1, 5, or 10 µs. Within a single burst, pulses of alternating polarity were repeated until a total energized time of 100 µs was achieved. For both IRE and H-FIRE, 100 pulses/bursts were delivered at a rate of 1 Hz using a two-needle electrode setup (∅ = 0.9144 mm) with center-to-center separation of 4 mm and a voltage-to-distance ratio of 1500 V/cm (**Figure 3.1**). Treatments were performed within a sterile, humidified incubator at 37 °C to increase physiologic relevance of the data (Fesmire, Petrella, Fogle, et al., 2020; Fesmire, Petrella, Kaufman, et al., 2020).

3.2.5 – Confocal Imaging of Tumor Mimics

Approximately 24 hours after pulsing, cell-laden hydrogels were incubated for 30 min with 2 µM Calcein green AM (Life Technologies, Carlsbad, CA) and 15 µM propidium iodide (Life Technologies) in Dulbecco's phosphate buffered saline (DPBS, Fisher Scientific). This timepoint is informed by prior studies showing that H-FIRE lesions develop over the course of 24 hours (Mercadal et al., 2020). Images were taken using a confocal microscope (Carl Zeiss LSM 800) with a 5× objective and a 10× eyepiece. Lesion areas were measured using FIJI (National Institutes of Health, Bethesda, MD). The green filter channel was used to measure the ablation region (live cells). For morphology staining, hydrogels were fixed with 10% neutral buffered formalin, permeabilized by incubation with 0.5% Triton X-100 for 10 minutes and blocked with 1% bovine serum albumin (BSA) for 60 minutes. We used an Alexa Fluor^{TM} 568 Phalloidin (ThermoFisher Scientific) stain to mark F-actin and DAPI (ThermoFisher Scientific) to stain nuclei. Cell morphology was visualized via confocal microscopy. We computed cell and nuclear areas as well as nucleus-to-cell area (NCR) ratio to determine if morphology had a bearing on cell death thresholds. Z-stack images acquired by a confocal microscope were projected onto a 2-dimensional plane, then the spline function in Zen Blue (Carl Zeiss®, Geneva) was used to determine the cell and nuclear areas ($n \geq 20$).

3.2.6 – Numerical Estimation of Lethal Electric Field Thresholds

The hydrogel geometry (**Figure 3.1a**) was constructed in COMSOL Multiphysics® software (v5.6, COMSOL Inc., Burlington, MA) to model the electric field distribution, as previously described (Arena, Szot, et al., 2012). The hydrogel domain was assigned an initial

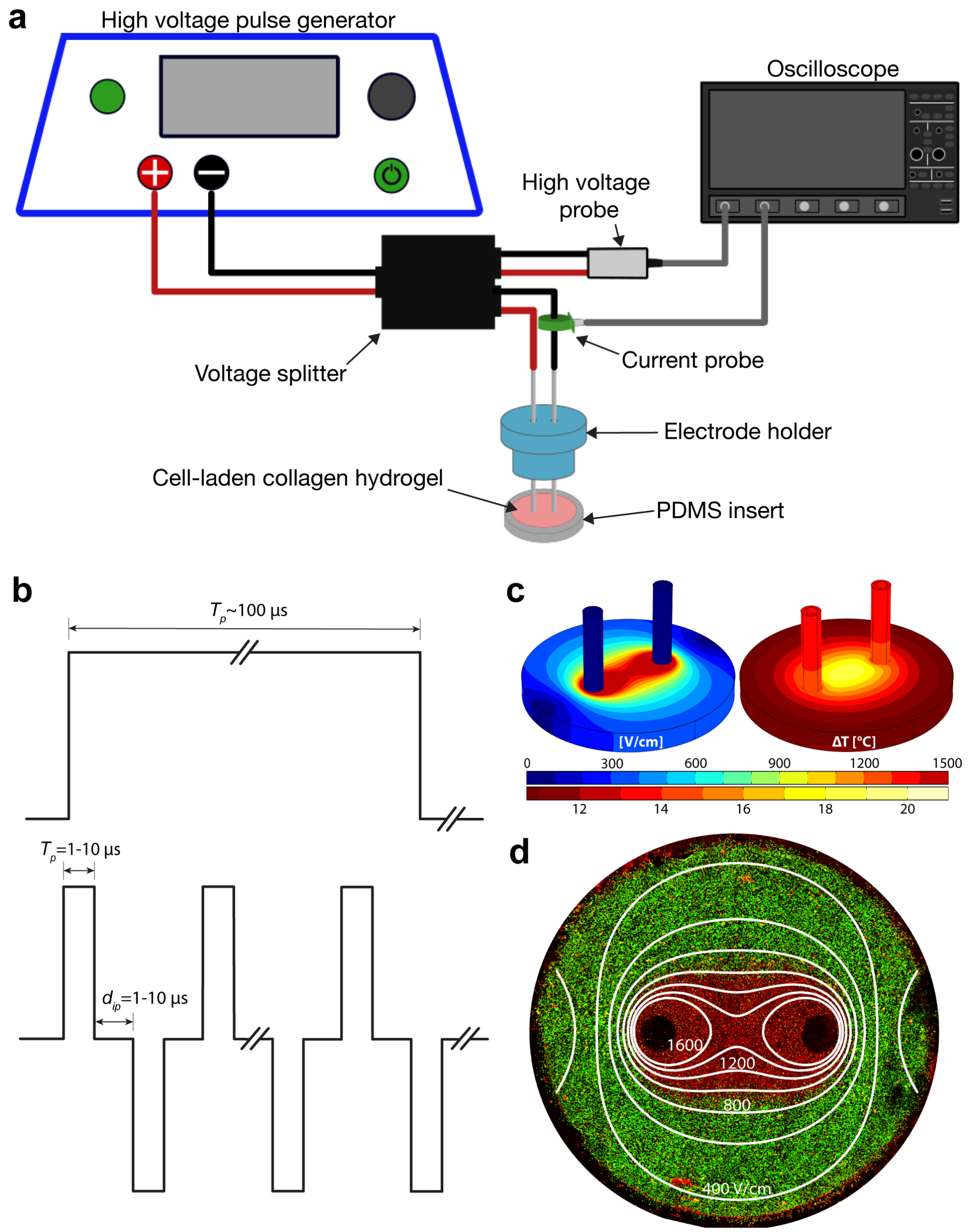

Figure 3.1 – Overview of methodology employed to derive lethal EFTs from hydrogel IRE/H-FIRE treatment. Electrical connections and recording equipment (a) were used to deliver (b) IRE (top) or H-FIRE (bottom) waveforms to collagen hydrogels. Numerical modeling was used to estimate the electric field and temperature distribution within the hydrogel (c). Lethal EFTs are determined by overlaying the field distribution on live/dead confocal images (d).

electrical conductivity of 1.25 S/m, which was experimentally determined using a conductivity meter (data not shown). Changes in gel conductivity due to heating were captured through the thermal coefficient of conductivity (α), which was set to 2 % per °C. An electric potential of 600 V was applied to one electrode boundary while the other was set to zero. A time-dependent simulation was used to account for Joule heating due to the application of multiple pulses. During the last (100th) pulse, electric field contours at varying magnitudes were plotted, and the surface area contained within each contour was integrated. The curve fitting tool in MATLAB® (Mathworks, Natick, MA) was used to fit a two-term exponential equation to the resulting area versus electric field data (**Figure 3.1d**). Finally, measured cell areas were used as inputs in this equation to compute thresholds.

3.2.7 – Predictive Modeling of Clinical Prostate Treatments

To estimate the efficacy of each waveform, outcomes of clinical treatment protocols were numerically computed. First, the SENN model proposed in (Mercadal et al., 2017) was constructed in MATLAB® and used to approximate the electric field magnitude required to stimulate a nerve fiber terminus in the vicinity of the electrodes for a given waveform. Next, this threshold and the lethal field threshold determined *in vitro* were used as inputs into a clinically representative numerical simulation to determine volumes of tissue undergoing ablation, thermal damage, and nerve stimulation.

SENN model construction and boundary conditions followed well-established approaches (Mercadal et al., 2017). An externally applied electric field with the given temporal characteristics was constructed in MATLAB® with 5 ns time resolution and applied in parallel to a 6-node myelinated nerve terminus. Waveforms were modeled with 100 µs of energized time and rise/fall times of 100 ns each. The electric field was sequentially increased by 0.25% until an action potential was detected, and this field was considered the field required for stimulation.

Using the experimentally determined lethal EFTs and numerically computed nerve stimulation thresholds, outcomes of a typical clinical procedure were estimated. A representative domain was constructed in COMSOL Multiphysics. Prostate tissue was modeled as a sphere with a radius of 10 cm to avoid boundary effects, and COMSOL's default "extra fine" meshing option was employed for all simulations. Two needle electrodes with center-to-center spacing of 1.5 cm, exposure of 1.0 cm, and diameter of 1 mm were centered in the domain (**Figure 3.2**). Models considered treatment with 100 bursts (or 100 pulses for IRE), each with 100 μs on-time, delivered at the desired repetition rate. To accurately account for the capacitors recharging, a 3.5 second delay was included after every set of 10 bursts/pulses. Computation of the electric potential, temperature, and thermal damage within the domain followed well described methods (Davalos et al., 2005a; Sano, DeWitt, et al., 2018). Dynamic conductivity due to electroporation was considered by using the sigmoidal dynamic conductivity functions from Beitel-White *et al.* at 37 °C (Beitel-White et al., 2022). In some cases, dynamic conductivity curves were estimated (**Figure 3.3**). For non-neoplastic prostate models, conductivity curves were from normal porcine prostate and RWPE-1 thresholds were used to compute ablation volumes. In prostate tumor models, conductivity curves originated from primary human tumor tissue propagated in mice, and ablation volumes were calculated using lethal EFT data from either 22Rv1 cells or PDX cells (**Table 3.1**). Electrical conductivity was assumed to increase at a rate 2 % per °C increase in temperature (Beitel-White et al., 2020). Material properties of the electrodes and other thermal properties of prostate tissue can be found in **Table 3.2**.

Volumes of tissue exposed to values of Ω equal to or above 1 were considered thermally damaged. Similarly, at the end of treatment, tissue exposed to fields above the thresholds for ablation and nerve stimulation were considered ablated and stimulated, respectively. Initially, models representative of three H-FIRE waveforms (2-5-2, 5-5-5, 10-1-10) as well as IRE were performed assuming an applied voltage of 3 kV, as this is representative of current clinical IRE treatments in prostate. Subsequently, a parametric sweep of V_0 was performed at values of 3.5 kV, 4 kV, 4.5 kV, and 5 kV, providing trends in ablation volume versus V_0 for each H-FIRE waveform. An exponential curve was fit to the dataset for each waveform with the form:

$$Q_{PEF} = a \cdot (V_0)^b \tag{3.1}$$

where Q_{PEF} is the volume of tissue undergoing (non-thermal) ablation due to the applied treatment, and a and b are fitting terms. For a given repetition rate and cell line, Q_{PEF} achieved with conventional IRE applied at 3 kV was inserted into equation (3.1), which was then solved for V_0. This was considered the *equivalent voltage* for that waveform, or in other words, the voltage needed with a given H-FIRE treatment to match the ablation volume achieved with a standard IRE procedure. Finally, for each H-FIRE waveform, one final simulation was performed in which V_0 was set to the equivalent voltage, allowing for examination of thermal effects, energy deposition, and nerve stimulation with equivalent ablation volumes across waveforms.

3.2.8 – Statistical Methods

Prism version 9 (GraphPad Software, San Diego, CA) was employed for all statistical analyses with α = 0.05. Cellular morphology data were analyzed using a one-way analysis of variance (ANOVA) with post-hoc Tukey's test. For comparison of ablation areas and EFT data, a two-way ANOVA was used. Šídák's multiple comparison's test was used to examine the effect of temperature across different waveforms. Tukey's HSD test was used to compare ablation sizes and EFTs across different cell types, while Dunnett's test was employed to compare each waveform to IRE.

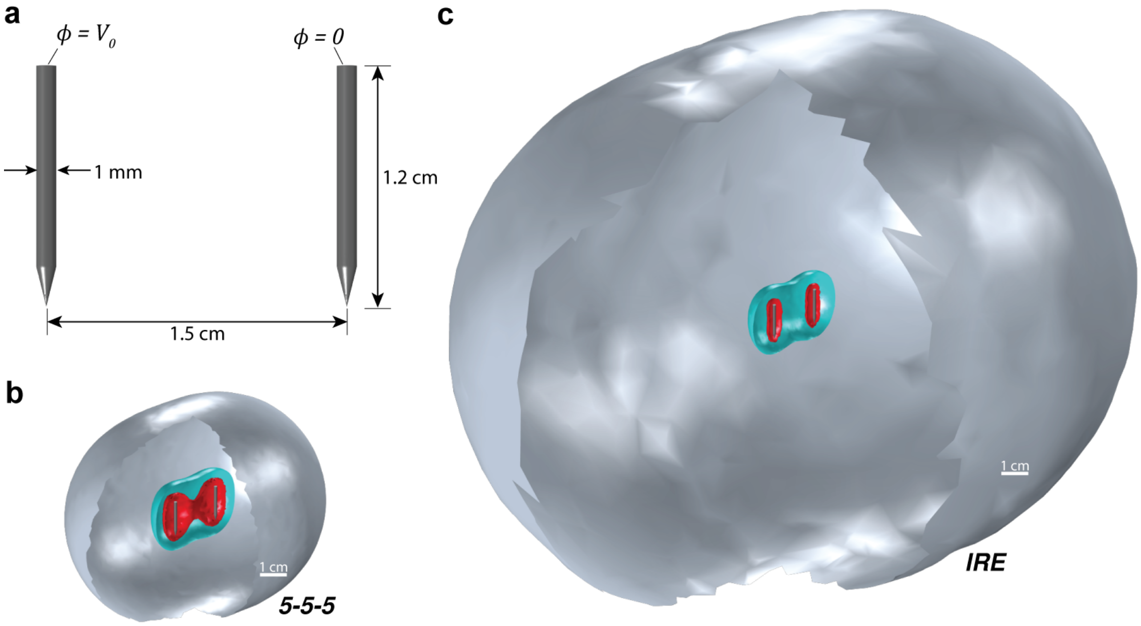

Figure 3.2 – (a) Geometric setup of clinical two-needle electrode models and representative volumes of ablation (teal), thermal damage (red), and nerve stimulation (gray) for prostate tumor treated with (b) H-FIRE (5-5-5) and (c) conventional IRE assuming ablation thresholds of 22Rv1 cells. Conventional IRE treatment simulated with V_0 = 3 kV; 5-5-5 simulation performed with V_0 = 3.83 kV (*equivalent voltage*).

<u>3.3 – *Results*</u>

3.3.1 – Cellular Morphology

Measured cytoplasmic and nuclear areas for each cell type under study are shown in **Figure 3.4**. The calculated nucleus-cell area ratio (NCR) is shown in in **Figure 3.4b**, and representative confocal images are shown in in **Figure 3.4c-e**. Qualitatively, all three cell types appeared relatively elliptical with large nuclei and 22Rv1 cells exhibited a wide array of cell sizes. From a quantitative perspective, RWPE-1 cells appeared larger than PDX and 22Rv1 cells but were only significantly larger than PDX cells. All three cell types exhibited similar nuclear areas and thus, RWPE-1 cells had the lowest NCR. While measured areas were relatively consistent across PDX and RWPE-1 cells, 22Rv1 cells demonstrated significant heterogeneity in terms of cell and nuclear size.

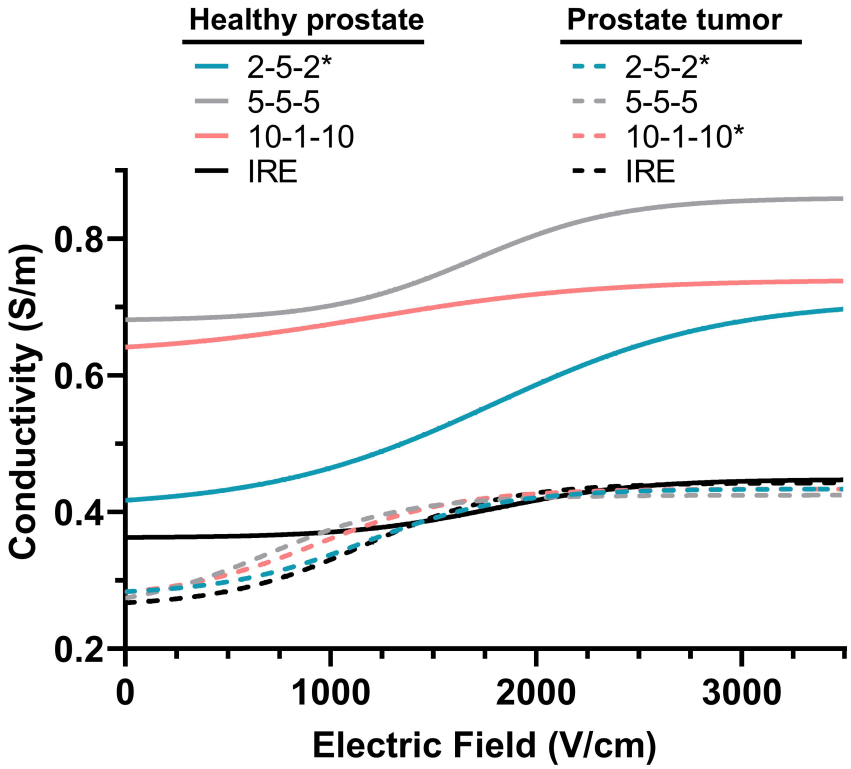

Figure 3.3 – Dynamic conductivity curves employed for each waveform in either normal or malignant prostate simulations. Asterisks indicate conductivity curves that were estimated.

3.3.2 – *Malignant prostate cells are more sensitive to treatment temperature than non-neoplastic cells*

Recent work has revealed that H-FIRE lethal thresholds may be temperature dependent, and some studies have used mild hyperthermia within the treatment region to enhance lesion sizes (Edelblute et al., 2017; Fesmire, Petrella, Kaufman, et al., 2020; Wei et al., 2010). To study the extent to which treatment temperature may impact effectiveness of H-FIRE in prostate cancer ablations, RWPE-1 and 22Rv1 cells were treated with each waveform at room temperature (~23 °C) as well as physiologic temperature (37 °C) using a benchtop incubator (**Figure 3.5**). For non-neoplastic prostate cells (RWPE-1), ablation areas were relatively unaffected by treatment temperature. Statistically relevant differences in lesion size were observed only for the 10-1-10 H-FIRE waveform as well as IRE. These did not translate into significant differences in lethal EFT, however, as none of the H-FIRE waveforms nor IRE showed a statistically significant difference in EFT as a function of temperature. On the other hand, most H-FIRE waveforms generated significantly larger ablations in 22Rv1 cells when treated at 37 °C compared to 23 °C. Specifically, all H-FIRE waveforms apart from the 2-5-2 and 2-10-2 exhibited lower EFTs when applied at

Table 3.2 – Material properties for electrodes and tissues utilized in the numerical model.

Material	*Symbol*	*Description*	*Value*	*Units*	*Ref.*
Stainless Steel					
	ρ	Mass density	7850	kg/m^3	COMSOL
	σ	Electrical conductivity	4.032×10^6	S/m	COMSOL
	k	Thermal conductivity	44.5	W/(m K)	COMSOL
	c_p	Heat capacity	475	J/(kg K)	COMSOL
Prostate Tissue					
	ρ	Mass density	1045	kg/m^3	(Hasgall et al., 2018)
	α	Conductivity thermal coefficient	2	%/°C	(Beitel-White et al., 2020)
	k	Thermal conductivity	0.51	W/(m K)	(Hasgall et al., 2018)
	c_p	Heat capacity	3760	J/(kg K)	(Hasgall et al., 2018)
	ω_b	Average blood perfusion rate	6.86×10^{-3}	1/s	(Hasgall et al., 2018)
	ρ_b	Blood density	1050	kg/m^3	(Hasgall et al., 2018)
	c_b	Blood heat capacity	3617	J/(kg K)	(Hasgall et al., 2018)

physiologic temperature. Like the RWPE-1 cells, IRE lesion areas were different at the two temperatures, but lethal EFTs were similar.

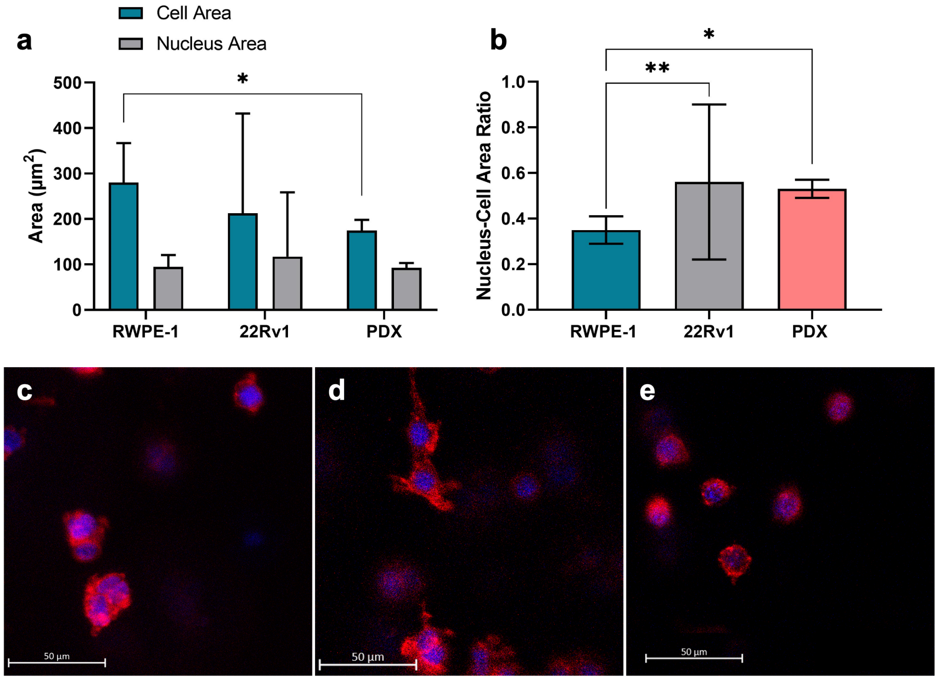

Figure 3.4 – RWPE-1 non-neoplastic prostate cells exhibit unique cellular morphology compared to immortalized or patient-derived prostate cancer cells. Confocal microscopy was used to quantify (a) cell and nuclear areas as well as the (b) nucleus-cell area ratio. Representative images are shown for (c) RWPE-1, (d) 22Rv1 and (e) PDX cells (40× objective). F-actin stained by Alexa Fluor 568 phalloidin; nuclei stained with DAPI ($n \geq 20$ cells each). **$p < 0.01$, *$p < 0.05$.

3.3.3 – High-Frequency Irreversible Electroporation Waveforms with Longer Pulse Durations and Interpulse Delays are Similarly Lethal to Irreversible Electroporation

Lesion areas as well as lethal electric field thresholds as a function of H-FIRE waveform are shown in Fig. 3. Pulse widths of 5 µs were more effective at generating lesions that 2 µs pulse durations for all cell types, as anticipated (**Figure 3.6a**). Increasing the pulse width further, to 10 µs, however, produced a smaller effect which could be dependent upon the interpulse delay. While differences are seen between 5–1–5 and 10–1–10 lethal EFTs for all three cell types, with inter-pulse delays of 5 or 10 µs, lethal EFTs are nearly identical regardless of pulse width (**Figure 3.6b**). Notably, the 5–10–5 waveform exhibited similar lethality in cancer cells (22Rv1 and PDX) as compared to conventional IRE. Waveforms with 10 µs pulse durations also exhibited lethal EFTs

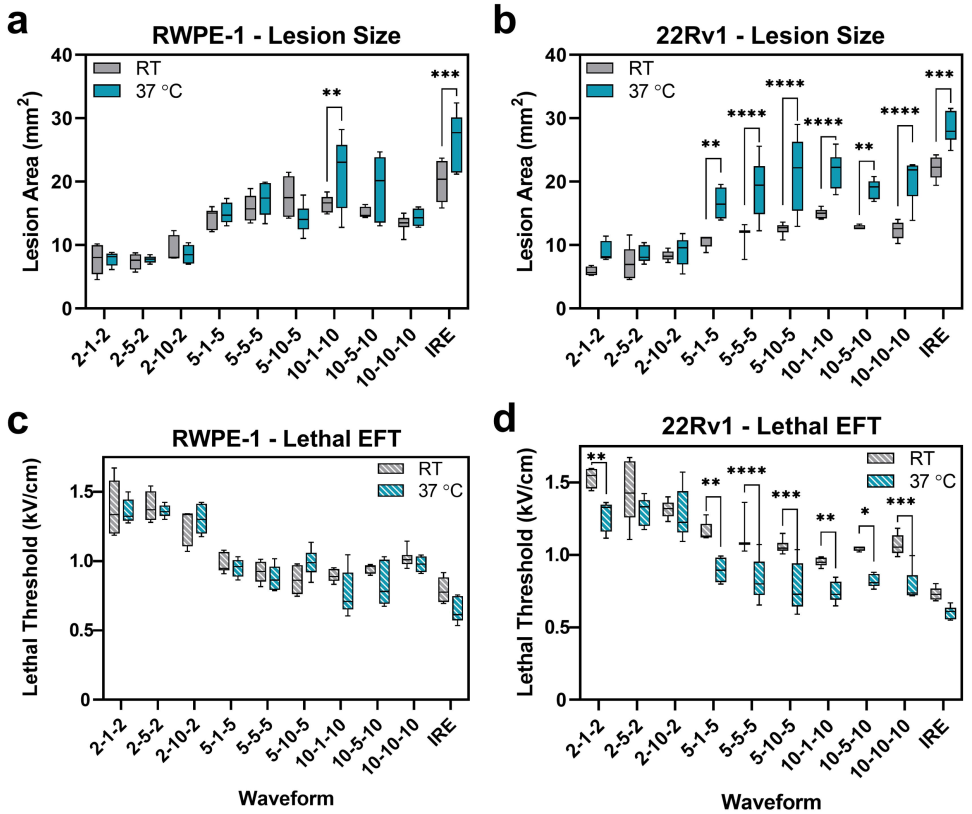

Figure 3.5 – Vulnerability of immortalized prostate cancer cells to H-FIRE pulse waveforms is more dependent on thermal mechanisms than non-neoplastic cells. Lesion areas (a, b) and (c, d) lethal electric field thresholds after treatment with the given waveform and conventional IRE are given for (a, c) RWPE-1 and (b, d) 22Rv1 cells, respectively ($n \geq 4$). Box boundaries represent standard deviations, line inside box is the sample mean, and whiskers indicate sample minimum and maximum. ****$p < 0.0001$, ***$p < 0.001$, **$p < 0.01$, *$p < 0.05$.

similar to IRE, but no other single waveform was particularly efficient across both cancer cell types. H-FIRE lethal thresholds in RWPE-1 cells were consistently higher than those achieved with IRE except for with the 10–1–10 waveform (**Figure 3.6b**). This suggests that non-neoplastic prostate cells are more resistant to H-FIRE waveforms than to IRE, regardless of waveform composition.

3.3.4 – High-Frequency Irreversible Electroporation Waveforms with short Pulse Widths display signs of selectivity in heterogeneous Patient-Derived (Xenograft) Primary Cells

With 2 µs pulse durations, PDX cells were significantly more vulnerable to H-FIRE treatment than non-neoplastic RWPE-1 cells. Patient-derived cells treated with these waveforms exhibited EFTs approximately 400 V/cm lower than immortalized non-neoplastic prostate cells (**Figure 3.6b**). The separation in EFTs between non-neoplastic and patient-derived cells was no longer significant for 5 µs and 10 µs pulse durations, save the 5–10–5 (**Figure 3.6b**). Interestingly, 22Rv1 cells were also slightly more susceptible to 2 µs duration H-FIRE waveforms than RWPE-1 cells, but not significantly. Across all H-FIRE waveforms, malignant cells consistently showed a lower EFT than the normal cell line, while PDX cells trended toward lower EFTs than the 22Rv1 cell line (**Figure 3.6b**). Both the 5–10–5 and 10–10–10 exhibited significantly lower EFTs in immortalized cancer cells compared to their non-neoplastic counterpart, suggesting the interpulse delay may be an important mediator of selectivity (**Figure 3.6b**). Finally, despite the trends noted for different H-FIRE waveforms, IRE demonstrated similar lethal EFTs across all cell types (**Figure 3.6b**).

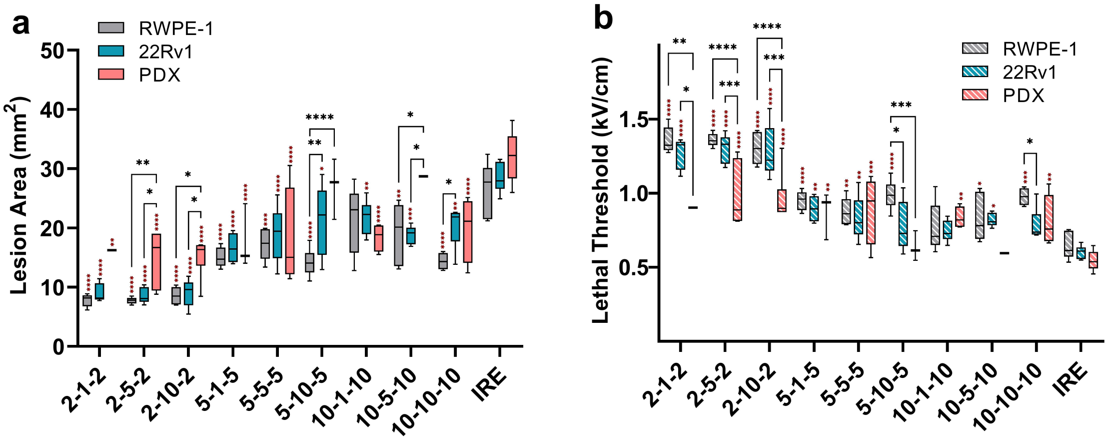

Figure 3.6 – Dependence of H-FIRE waveform lethality on pulse width, interpulse delay, and prostate cell type. The effect of H-FIRE or IRE voltage waveforms on (a) lesion area and (b) lethal EFTs is shown for RWPE-1, 22Rv1 and PDX cells. Black asterisks represent differences between cell lines treated with the same waveform; red asterisks represent differences between the given waveform and IRE within the cell line indicated. Box boundaries represent standard deviations, line inside box is the sample mean, and whiskers indicate sample minimum and maximum. ****$p < 0.0001$, ***$p < 0.001$, **$p < 0.01$, *$p < 0.05$.

3.3.5 – Modeled Outcomes of standard clinical treatment with Irreversible Electroporation and High-Frequency Irreversible Electroporation

Clinical prostate ablations were numerically modeled to estimate outcomes for each H-FIRE waveform as well as IRE when delivered with 3 kV applied across two-needle electrodes (**Figure 3.7**). Simulations considered ablations performed within either prostate tumor tissue or non-neoplastic prostate to understand the interplay of tissue-specific conductivity and lethal electric field thresholds. As anticipated, models predicted an increase in ablation volume as a function of pulse width, with IRE producing the largest ablation volumes. For a given waveform, relatively minor differences in ablation volume were predicted across different cell types. Further, the tissue-specific dynamic conductivity functions influenced the electric field distribution during treatment, so lethal EFT was not a direct predictor of ablation volume. Thermal damage was more pronounced in non-neoplastic prostate tissue, especially when treated with H-FIRE, presumably due to the increased electrical conductivity of normal prostate compared to prostate tumor (**Figure**

3.3). More specifically, thermal damage volumes in all tumor models and non-neoplastic prostate treated with IRE were ~0.4 cm^3, while thermal damage in non-neoplastic prostate was ~1cm^3 for 2–5–2 and just over 2 cm^3 for the 5–5–5 and 10–1–10 (**Figure 3.7b**). Modeled volumes of nerve stimulation were also heavily dependent upon applied waveform (**Figure 3.7c**). The 2–5–2 produced the least amount of nerve stimulation, with volumes hovering near 100 cm^3. The 5–5–5 gave volumes of ~200 cm^3 and the 10–1–10 produced volumes close to 300 cm^3, while predicted nerve stimulation volumes for IRE were just above 3000 cm^3 (**Figure 3.7c**).

For each waveform, predicted volumes were used to calculate a summary ratio – a dimensionless metric normalizing ablation volume by the predicted volumes of thermal damage and nerve stimulation (**Figure 3.7d**). This provides an objective measure of the efficacy of a given waveform. Overall, the summary ratio for each waveform was higher in tumor tissue (22Rv1 or PDX) than in non-neoplastic prostate (RWPE-1). For non-neoplastic tissue, summary ratios were low (~0.04) and nearly identical regardless of waveform. The highest summary ratio (0.41) was observed for the 2–5–2 using the lethal EFT of PDX cells, but both the 5–5–5 and 10–1–10 produced consistent values near 0.2 in tumor tissue represented by either cell type.

3.3.6 – Clinical Outcomes of ablation-matched High-Frequency Irreversible Electroporation Treatments

A final series of models was performed in which applied voltage was adjusted such that each H-FIRE waveform produced an ablation volume identical to IRE in either non-neoplastic prostate or tumor tissue (**Figure 3.8** and **Figure 3.2**). The equivalent voltage, or the voltage needed with a given H- FIRE waveform to match the ablation size achieved with the standard IRE protocol, is shown in **Figure 3.8a**. Waveforms with 2 ls pulse durations required the highest voltages to achieve this large ablation size (4.5–5 kV), while longer duration H-FIRE waveforms required only a few hundred volts more than IRE in RWPE-1 and 22Rv1 simulations. However, equivalent voltages for the 5–5–5 and 10–1–10 in PDX cells were just over 4 kV. The error between the targeted (IRE) ablation volume for a given H- FIRE waveform and the actual modeled

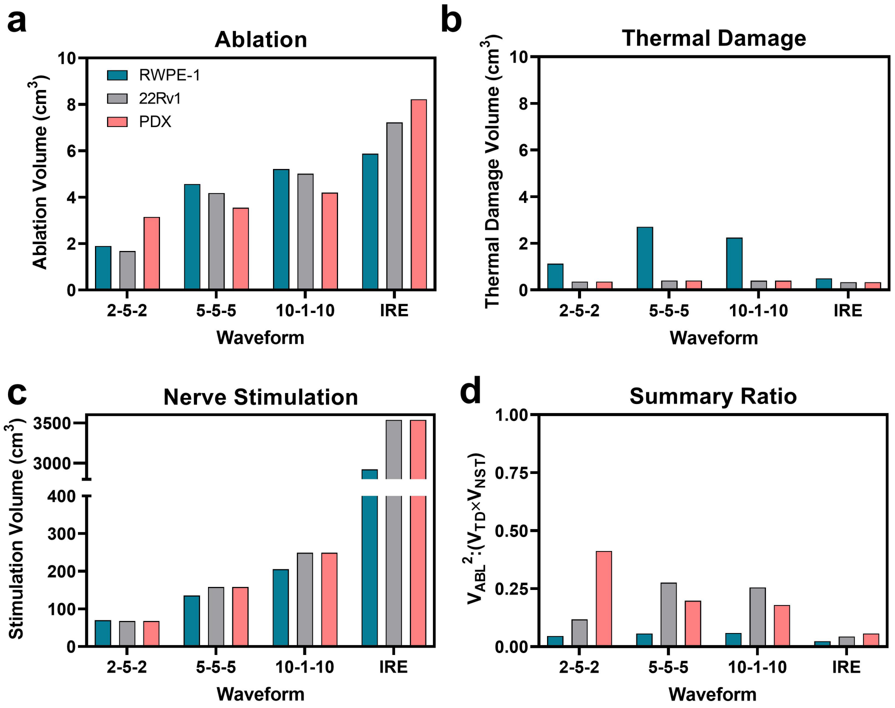

Figure 3.7 – Simulated results of a standard two needle clinical IRE procedure relative to identical dose-matched H-FIRE procedures. With the same applied voltage (3 kV) and repetition rate (60 ppm), numerically predicted volumes of (a) ablation, (b) thermal damage, and (c) nerve stimulation are shown for selected H-FIRE waveforms as well as IRE. These volumes are used to calculate a (d) summary ratio that represents the ablation size normalized to the volumes experiencing thermal damage or stimulation.

volume at the equivalent voltage is shown in **Figure 3.8b** and was less than 1.5% across all cases as seen in the near-identical ablation volumes achieved with different waveforms in each cell/tissue type **Figure 3.8c**. With these matched ablation sizes, thermal damage was strongly dependent upon applied pulse duration and somewhat dependent upon tissue type **Figure 3.8d**. Likewise, even with the high potentials applied with shorter H-FIRE waveforms, nerve stimulation trends retained their sharp reliance on pulse width **Figure 3.8e**. Overall, the 5–5–5 and 10–1–10 exhibited the strongest summary ratios, with the 2–5–2 in PDX tumor tissue again standing out as the most optimal case using this approach. For a given cell type, summary ratios for all H-FIRE waveforms outperformed those achieved with IRE **Figure 3.8f**.

3.4 – Discussion

H-FIRE is an electroporation-based technology with several potential benefits over conventional IRE and – owing to its non-thermal nature – is well-suited for focal ablation of prostate tumors. Despite its success in preliminary studies for other cancer types and in its first PCa trial in humans, the overall effect of different burst parameters on clinical outcomes is still poorly under- stood. Thus, in this study, we examined effects of H-FIRE treatment parameters on

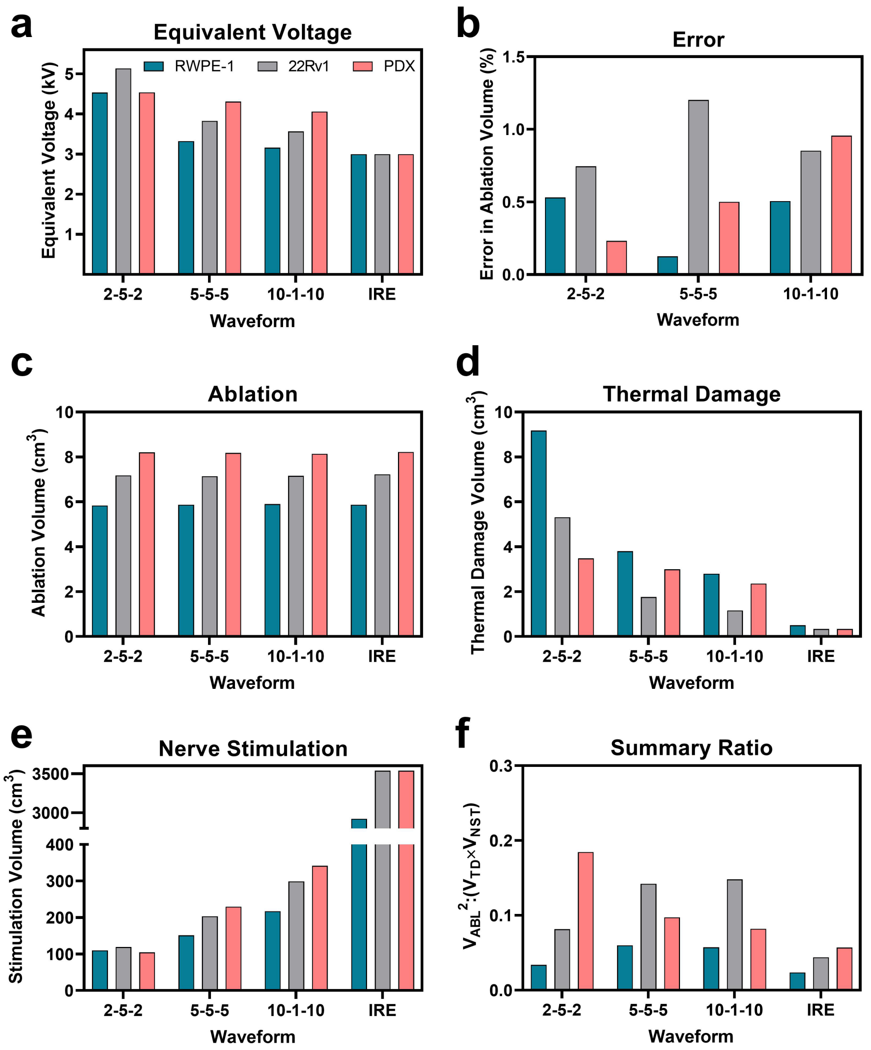

Figure 3.8 – Comparison of predicted clinical outcomes of IRE compared to H-FIRE waveforms with matched ablation sizes. After estimating the (a) equivalent voltage of each H-FIRE waveform using a parametric analysis, a final model was performed for each waveform using the determined voltage. The (b) difference (error) in ablation achieved with this voltage versus the targeted ablation size was under 1.5% for all cases. Thus, predicted (c) ablation volumes are identical for all waveforms using the given cell type's lethal threshold. With ablation volumes matched, anticipated (d) thermal damage and (e) nerve stimulation are shown, as well as the (f) summary ratio.

3D tumor mimics and compared them to traditional IRE. Immortalized prostate cell lines representative of non-neoplastic and malignant tissue were studied. Primary cells were also isolated from a patient-derived PCa xenograft to deter- mine the effects of these fields on a more physiologically relevant heterogenous sample. We used the experimental lethal EFT data to inform a clinically relevant numerical model to estimate the overall efficacy of different waveforms. This model was used to predict ablation volume, thermal damage, and nerve stimulation under standard settings. Subsequently, voltage was adjusted to match ablation volume across waveforms and side effects including thermal damage and nerve stimulation were analyzed, and a nondimensional parameter was used to objectively compare waveforms.

As expected, hydrogel lesion sizes increased and their corresponding EFTs were reduced with increasing pulse width, as has been described in prior works studying other cell and tissue types (Mercadal et al., 2020; Miklovic et al., 2017; B. Zhang et al., 2021). On the other hand, varying the interpulse delay from 1 to 10 μs had a minimal effect on lesion size, but is known to affect nerve stimulation thresholds (see **Chapter 4**) (Aycock et al., 2021; Casciola et al., 2019). Thus, shorter values of d_{ip} may provide the best balance of ablation size relative to nerve stimulation volume. It is also possible that wave- forms could be further optimized by varying the delay within each bipolar pulse and between subsequent bipolar pulses independently, but such a comprehensive study is outside the scope of this work.

While the dependence of electroporation on temperature has been documented for decades (Davalos et al., 2003; G. T. Martin et al., 2002; Weaver, 1993), it has recently been suggested that H-FIRE is a thermally mediated ablation modality, especially for short (~1 μs) pulse durations (Fesmire, Petrella, Kaufman, et al., 2020). In line with these results, we found that conventional IRE lethal EFTs did not change with variations in experimental temperature in non- neoplastic or malignant prostate cells. Further, H-FIRE treatment in non-neoplastic prostate cells was essentially unaffected by changing the ambient environment from room temperature to physiologic temperature. On the other hand, malignant (22Rv1) prostate cells were significantly more vulnerable to H-FIRE therapy when applied at 37 ºC versus 23 ºC, consistent with recent literature investigating malignant brain and pancreatic cells (Fesmire, Petrella, Kaufman, et al., 2020). Unlike trends reported for malignant astrocytes, however, we found that 2 µs duration waveforms were less temperature dependent than waveforms with pulse durations of 5 or 10 µs. This result suggests that with proper waveform selection, modulating local tissue temperature could offer an opportunity to selectively target malignant prostate cells without inflicting further damage on nearby non-neoplastic cells. This approach would require optimization to maximize H-FIRE induced ablative benefits without thermal damage. Finally, the high thresholds of non-malignant cells in the tumor periphery must be considered when planning for adequate treatment margins, as the high thresholds of peripheral non-neoplastic cells may require adjustments to the treatment voltage. Thus, future work is needed to elucidate the interplay of cell type, waveform selection, and local tissue temperature toward optimizing cell death outcomes for different applications.

At physiologic temperature, malignant cells (22Rv1 and PDX) consistently showed similar or lower EFTs than normal cells. PDX cells generally exhibited slightly lower EFTs than 22Rv1 cells, which were especially pronounced with 2 µs pulse durations. With pulse widths of 5 µs or longer, lethal EFTs were similar for PDX and immortalized 22Rv1 cell lines, despite the heterogenous nature of cells within PDX samples. These results suggest that immortalized cancer cell lines can be used in place of primary tumor cells for calculation of lethal EFTs in vitro. Using EFTs from these immortalized cells to numerically estimate clinical ablation sizes should thus represent the minimum ablation size likely to result from the modeled treatment. In practice, underestimation of ablation size is much more favorable than overestimation and may be beneficial to H-FIRE development by implicitly building in treatment margins.

Cell morphology is hypothesized to influence susceptibility to applied electric fields (Agarwal et al., 2007) depending on the waveform applied (Schoenbach et al., 2001). Cell size is thought to play a major role in electroporation particularly for longer pulse durations. However, capacitive and dielectric properties of the membrane vary (Zhuang et al., 2012) between cell lines and likely contribute substantially to lethal EFT values (Henslee et al., 2011). RWPE-1 cells were slightly larger than 22Rv1 cells and significantly larger than PDX cells (**Figure 3.4**). However, because EFTs were overall mostly higher in RWPE-1 cells, our data do not indicate that larger cells are more susceptible to IRE and H-FIRE, as seen in **Figure 3.6**. Nuclear area was similar across all cell types, but 22Rv1 and PDX cells displayed larger NCRs than RWPE-1 cells. NCR has been implicated as a mediator of selectivity, mostly for waveforms with extremely short pulse durations (Ivey et al., 2015), but it is possible that the higher NCR of PDX cells is contributing to their low EFT for waveforms with 2 μs pulse durations. These trends indicate that for shorter duration pulses, H-FIRE lethal thresholds may be dependent on NCR in addition to factors other than morphology (biochemical or biophysical) for higher frequency waveforms (Pakhomova et al., 2011).

Numerical simulation of a standard clinical ablation protocol demonstrated that pulse width is the dominant factor determining ablation size with different waveforms, as anticipated. For a given H-FIRE waveform, predicted ablation sizes were relatively consistent regardless of tissue or cell type. Because dynamic conductivity functions for each waveform have relatively unique profiles, anticipated ablation volumes for a given cell type and waveform did not directly correlate with the lethal EFT. For instance, the lethal EFTs for 22Rv1 cells treated with a 5–5–5 or 10–1–

10 were slightly lower than RWPE-1 cells treated with the same waveforms. However, models predict larger ablation volumes in non-neoplastic tissue with these waveforms, presumably due to changes in electrical conductivity which modulate electric field redistribution and can expand ablation sizes (**Figure 3.3**). Heat generation also causes increases in electrical conductivity, particularly near the electrodes, which may be contributing to the larger modeled ablations in non-neoplastic tissue. On the same note, normal prostate tissue is more conductive than neoplastic prostate, so it is also more vulnerable to thermal damage, as reflected in our models (**Figure 3.7b**). Because H-FIRE is intended to provide nonthermal ablation volumes, these results highlight the importance of ensuring pulse delivery does not produce thermally damaging temperatures, which can be achieved through thermal mitigation strategies, or by reducing the rate at which energy is delivered (Arena, Mahajan, et al., 2012; O'Brien, Lorenzo, et al., 2019; Sano et al., 2020; Y. Zhao & Davalos, 2020). Modeled nerve stimulation volumes were almost entirely dominated by waveform selection, suggesting tissue type is a negligible factor. Summary ratios were highest in models with low levels of thermal damage and nerve stimulation, so H-FIRE waveforms outperformed conventional IRE in all cases, and tumor tissue was especially favored.

Similar results were observed when the equivalent voltage method was used. As seen in **Figure 3.8a-c**, ablation volumes were successfully matched across waveforms by scaling voltage. As anticipated, in some cases this resulted in unacceptable levels of thermal damage (**Figure 3.8d**), especially when higher voltages were necessary in non-neoplastic tissue. Overall, nerve stimulation and summary ratio trends remained consistent, suggesting H-FIRE waveforms are more advantageous in terms of their ability to maximize ablation size relative to nerve stimulation and thermal injury. In particular, the 5–5–5 and 10–1–10 waveforms stood out due to their high summary ratios in both malignant cell types (**Figure 3.8f**).

This work provides a first step toward optimizing H-FIRE waveform selection in prostate cancer ablations, but it is important to point out limitations of our investigation. First, due to limited PDX tissue availability, some PDX datapoints provided in this paper contain only one or two replicates. Future analyses will be necessary to add relevance to these results and confirm reported trends. Second, the *in vitro* collagen hydrogel model is designed specifically to isolate electric field effects without thermal damage; while we assume that cell death behavior is similar between the *in vitro* model and the simulated *in vivo* cases, thermal dynamics are much different and could impact cell death behavior. Further, clinical simulations only considered three H-FIRE waveforms and IRE due to lack of experimental conductivity data. Thus, we did not model the full array of waveforms investigated experimentally, so it is possible that some waveform exhibits a unique conductivity and lethal EFT profile that make it even more ideally suited for prostate ablation than those included in this study. It is also worth noting that other pulse parameters and technologies can be implemented to reduce the high levels of thermal damage seen at the higher voltages needed in some models, but the goal of this study is to demonstrate the necessary increase in energy to achieve similar ablations across waveforms as a scaling factor, rather than tune each waveform independently. Finally, we acknowledge the importance of following this study with *in vivo* work seeking to validate trends reported herein and further optimize H-FIRE voltage waveforms.

3.5 – Conclusion

The effect of H-FIRE treatment with a variety of pulse widths and interpulse delays on 3D tumor mimics was examined in vitro. No differences between patient-derived and immortalized malignant cell lines were noticed, indicating the latter as a suitable replacement for complicated PDX models. Malignant cells were more significantly affected by variations in ambient temperature than their non-neoplastic counterparts, suggesting a potential window for selective exploitation. Among different H-FIRE wave- forms, pulse duration had the largest impact on EFT, while interpulse delay had a relatively ambiguous effect. In silico modeling was used to match ablation volumes to IRE, and nondimensional parameters were used to quantify the extent of thermal damage and nerve excitation relative to nonthermal ablation volumes. Among the waveforms under study, 5–10–5 and 10–1–10 were found to provide the largest nonthermal ablations relative to induced side effects.

4 – A Theoretical Argument for Extended Interpulse Delays in Therapeutic H-FIRE Treatments[3]

4.1 – Introduction

Electroporation is a biological phenomenon in which cells exhibit increased membrane permeability upon exposure to high amplitude electric fields. Increased permeabilization is presumably due to creation of defects in the cell membrane that increase transport of ionic species and macromolecules (Yarmush et al., 2014a). Depending upon characteristics of the applied field – such as amplitude and duration – these defects range in size from one to hundreds of nanometers, and can be tuned to target intracellular structures (Son et al., 2014; Tekle et al., 2001; Weaver et al., 2012). Electroporation can be implemented reversibly, whereby affected cells regain membrane integrity and recover following stimulus removal, or irreversibly, where cells die following treatment. Reversible electroporation has been used for decades to increase cellular uptake of poorly permeant or impermeant molecules, and to augment expression of specific genes by increasing transfection efficiency (Geboers et al., 2020; Yarmush et al., 2014a). The latter technique, known as irreversible electroporation (IRE), has recently emerged as a tissue ablation modality (Davalos et al., 2005a).

Unlike conventional ablative therapies in which temperature is manipulated to nonspecifically denature proteins, IRE directly affects cellular membranes without significant local heating, leaving the underlying tissue architecture intact. Due to this unique mechanism, IRE can be performed in cases where thermal ablation is contra-indicated by the presence of vasculature, ducts, or neural structures (X. Chen et al., 2015; Maor et al., 2007; Niessen et al., 2015). IRE also exhibits submillimeter precision and a sharp demarcation between untreated and

---

[3] Chapter 4 is adapted and reprinted with kind permission from the Institute for Electronics and Electrical Engineers. © 2021 IEEE. Aycock, K. N., Zhao, Y., Lorenzo, M. F., & Davalos, R. V. (2021). A Theoretical Argument for Extended Interpulse Delays in Therapeutic High-Frequency Irreversible Electroporation Treatments. *IEEE Transactions on Biomedical Engineering*, *68*(6), 1999–2010.

ablated tissue, both of which reduce the likelihood of overtreatment or off-target damage (Edd et al., 2006; van den Bos, de Bruin, et al., 2016). Despite these promising capabilities (Aycock & Davalos, 2019; R. C. G. Martin et al., 2015), management of patients receiving IRE can be difficult. The long (70-100 μs) pulses easily stimulate cardiac myocytes, pain receptors, and skeletal muscle fibers, resulting in muscle contractions and potential arrhythmias (Ball et al., 2010; Mali et al., 2008). To avoid such complications, a neuromuscular blockade is administered prior to treatment and pulses are delivered in synchronization with the absolute refractory period of the heart (Deodhar, Dickfeld, et al., 2011; R. C. Martin et al., 2015; Thomson et al., 2011). Thus, despite its benefits over thermal ablation, this anesthetic protocol can prevent IRE from being recommended in some cases (e.g. "awake surgeries" or outpatient procedures) (Yordanova et al., 2011).

To further extend clinical capabilities of IRE, an alternative pulse delivery scheme termed high-frequency IRE (H-FIRE) has recently been introduced (Arena, Sano, Rylander, et al., 2011; Dong, Wang, et al., 2018). H-FIRE replaces the long monopolar pulses with bursts of short (1-10 μs) bipolar pulses following a positive phase–interphase delay (d_1)–negative phase–interpulse delay (d_2) pattern (**Figure 4.1**) (Arena, Sano, Rossmeisl, et al., 2011; Arena, Sano, Rylander, et al., 2011). By changing the method of pulse delivery in this way, nerve excitation and muscle contractions are substantially reduced (Arena, Sano, Rossmeisl, et al., 2011; O'Brien, Passeri, et al., 2019; Partridge et al., 2020). This is due to the local repolarization that occurs with each negative phase prior to activation of the minimum number of voltage-gated sodium channels (VGSCs) required for excitation (Casciola et al., 2019; van den Honert & Mortimer, 1979). Additionally, the short bipolar pulses constitute a shift towards higher frequencies, which translates to more predictable ablation geometries and reduced likelihood of electrical arcing (S.

P. Bhonsle et al., 2015; Kaufman et al., 2020). A challenge that arises with H-FIRE waveforms is that lethal electric field thresholds (EFTs) are typically 1.5-3× higher than with IRE and are heavily dependent on the width of constitutive pulses (Dong, Yao, et al., 2018; Mercadal et al., 2020; O'Brien, Passeri, et al., 2019; Sano et al., 2017; Wasson et al., 2020). For this reason, higher voltages must be applied across the electrodes to achieve similar ablation volumes, which has consequences on the amount of heat produced.

A number of studies have explored non-pharmacological methods of lowering lethal EFTs for H-FIRE waveforms by modifying the delivery strategy or constitutive pulse width of burst waveforms. Sano *et al.* showed that with a fixed width of 2 μs, single bipolar pulses repeated at 25-100 Hz may exhibit lower EFTs than traditional bursts (Sano, Fesmire, et al., 2018). Additionally, reducing the width of alternate polarity pulses lowered the EFT to roughly half the value of corresponding symmetric bursts (Sano et al., 2017), but the charge imbalance caused muscle contractions similar to those resulting from IRE (Sano, Fan, et al., 2018).

Investigations have shown that cell permeability and survival are also closely linked to the delays within (interphase delay, d_1) and between (interpulse delay, d_2) bipolar pulses (**Figure 4.1c**) (Polajžer et al., 2020; Vižintin et al., 2020). This is presumably due to "bipolar cancellation" (BPC) mediated by assisted discharge, whereby the subsequent pulse of opposite polarity forces membrane repolarization rather than passively allowing the transmembrane potential to decay according to its time constant (τ_m) (Ibey et al., 2014; Pakhomov et al., 2014; Valdez et al., 2018). By increasing interphase and interpulse delays, the time the membrane is exposed to a critical transmembrane potential (usually ~ 1 V) is increased (Arena, Sano, Rossmeisl, et al., 2011). Thus, one might expect that longer delays would improve electroporation-based outcomes. On the other hand, it is known that increased interphase delays reduce the ability of anodic pulses to abolish action potentials elicited by the cathodic phase (Gorman & Mortimer, 1983; Reilly, 1988; van den Honert & Mortimer, 1979). Additionally, pores are created on the order of nanoseconds, but several microseconds are required for a sufficient number of VGSCs to open to cause nerve excitation, so while seemingly related, the mechanisms by which electroporation and stimulation are suppressed with bipolar pulses are not identical (Casciola et al., 2019). Further, recent reports suggest that a complex relationship exists between these delays and electroporation effects that cannot be fully explained by assisted discharge, and that extensions of the interpulse delay alone may enhance biophysical outcomes from treatment (Vižintin et al., 2020).

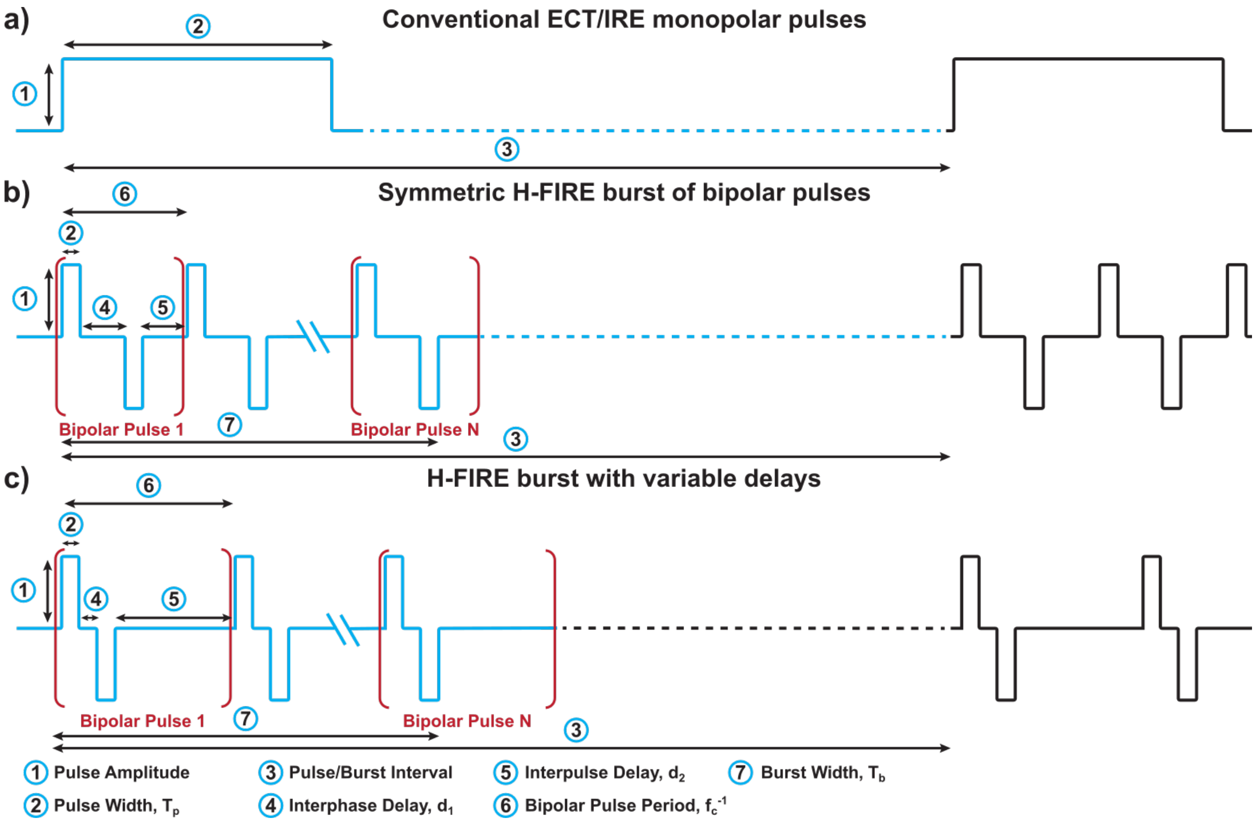

Figure 4.1 – Representative idealized voltage waveform of an a) IRE pulse, b) Symmetric H-FIRE burst, and c) Variable delay H-FIRE burst. Each IRE pulse is characterized by an amplitude (1) and pulse width (Tp; 2) and is repeated at a specific interval (3). Symmetric HFIRE bursts (b) are comprised of short bipolar pulses – each with a positive pulse of amplitude (1) and width (2), an interphase delay (d1; 4), and an identical negative pulse (i.e., ⑥=②+④+②+⑤). Each bipolar pulse is separated by an interpulse delay (d2; 5) equal to (4) and is repeated N times to achieve a desired "energized time." Variable delay H-FIRE bursts (c) are similar to (b) with the unique difference that (4) ≠ (5).

From a stimulation perspective, many studies have investigated methods to maximize efficiency of charge-balanced waveforms for functional stimulation purposes, offering insight into the effects of interphase gaps, multiple pulses in series, etc., but most of these investigations have been for much longer pulses than those we are interested in (Butikofer & Lawrence, 1978; BÜtikofer & Lawrence, 1979; Macherey et al., 2006). To our knowledge, modifications of the interphase and interpulse delays have not been investigated as a method to reduce excitation caused by clinical H-FIRE protocols, nor have the resulting biophysical effects been explicitly examined.

Here, we seek to determine the effects of integrating a variable delay approach into clinically relevant H-FIRE waveforms. As the transition to H-FIRE was in part motivated to mitigate tissue excitation, in this paper we further evaluate the relationship between interphase and interpulse delays within H-FIRE waveforms and resulting clinical outcomes, specifically nerve stimulation, electric field distribution, and resistive heating. After placing constraints on the range of delays that could realistically be implemented in clinical protocols – taking ECG synchronization and typically-employed repetition rates into account (see supplementary material) – we computationally evaluate the effect of modified burst waveforms on neural excitation. We then use the results from the nerve excitation study to inform the range of delays yielding desirable outcomes, and construct a numerical model to estimate ablation area, temperature rise, and thermal damage resulting from a typical treatment with a variety of modified waveforms. We demonstrate that extended interpulse delays increase excitation thresholds for bursts with constitutive pulse widths of 1 and 5 μs. We also show that the temperature increase due to Joule heating is lowered as the interpulse delay is extended from 100 ns to 1 ms, and that the field redistribution with longer interpulse delays may augment ablation size even in the absence of a reduced lethal EFT.

4.2 – Methods

4.2.1 – Modified SENN Model

To assess the response of a myelinated neuron to a temporally arbitrary electric field, we adopted the SENN framework introduced by Reilly *et al.* (Reilly et al., 1985), but replaced the Frankenhaeuser and Huxley current equations with Hodgkin-Huxley type formulations computed for mammalian neurons (McIntyre et al., 2002). This model can provide the nerve fiber response to any transient electric field with known spatial distribution. Because electroporation-based treatments are conventionally performed with needle electrodes, we chose to model a scenario representing a nerve terminus within the vicinity of the electrodes and in parallel with a given electric field contour, as originally proposed by Mercadal and colleagues (Mercadal et al., 2017). Thus, for each waveform under study, we calculated the electric field required to initiate an action potential in a short nerve segment with 6 nodes of Ranvier exposed to a uniform field. By assuming a nerve terminus is present at all points in a given domain, these thresholds can be extrapolated to estimate the amount of tissue exposed to fields capable of inducing action potentials irrespective of electrode geometry and stimulus amplitude (Mercadal et al., 2017). It is worth noting that peripheral motor neurons are excited at lower stimulus magnitudes than skeletal myocytes, so it is not necessary to consider direct stimulation of muscle cells themselves (Peckham & Knutson, 2005).

The equivalent circuit employed in this model, originally proposed by McNeal (McNeal, 1976), is given in **Figure 4.2**. The relative transmembrane potential at the n^{th} node is related to capacitive, ionic, and axial currents according to:

$$C_m \frac{dV_n}{dt} + I_{i,n} = G_a\big(V_{n-1} - 2V_n + V_{n+1} + V_{e,n-1} - 2V_{e,n} + V_{e,n+1}\big) \tag{4.1}$$

where C_m is the membrane capacitance of the node, V_n is the nodal transmembrane potential relative to the resting potential $\big(V_n = V_{i,n} - V_{e,n} - E_r\big)$, $I_{i,n}$ is the sum of ionic currents across the membrane at the node, G_a is the axoplasmic conductance, and $V_{e,n}$ is the extracellular voltage at the node. At the ends of the fiber, we assume no axial current (Mercadal et al., 2017), giving:

$$C_m \frac{dV_n}{dt} + I_{i,n} = G_a\big(-V_n + V_{n\pm1} - V_{e,n} + V_{e,n\pm1}\big) \tag{4.2}$$

In this equation, $\pm$ indicates that at node 1 and *N*, potentials at only the current and nearest neighboring node ($n+1$ and $n-1$, respectively) are considered. To determine the extracellular potential at each node, we employ the following equation, which describes the potential along a line in parallel to an applied electric field:

$$V_{e,n} = V_{e,1} + E \cdot L \cdot n \tag{4.3}$$

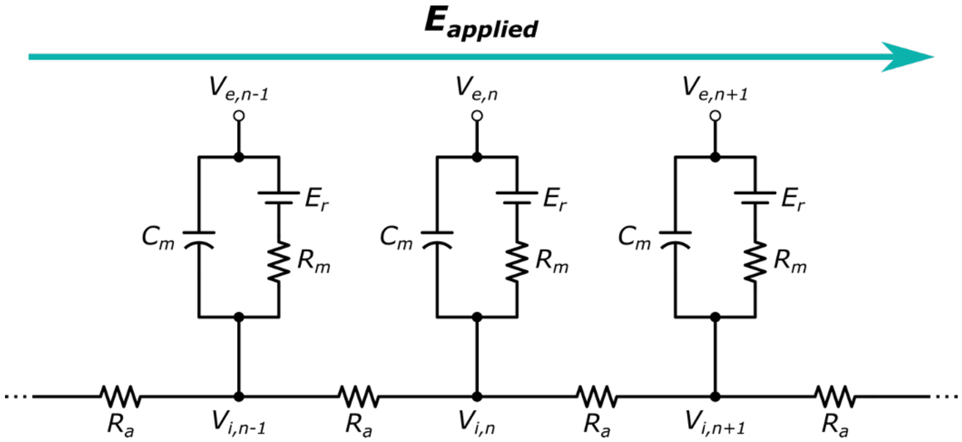

Figure 4.2 – Equivalent circuit model for myelinated nerve fiber. The membrane at each node of Ranvier can be described by a capacitance (C_m), resistance (R_m), and resting potential (E_r). Nodal transmembrane current is a function of the difference between local extracellular (V_e) and intracellular potential (V_i). Axial conduction is dependent upon internodal resistance (R_a). Teal line indicates direction of uniform field with respect to fiber.

where $V_{e,1}$ is a reference voltage at the terminal node nearest the cathode, E is the applied field, L is the internodal separation, and n is the node number. For convenience, $V_{e,1}$ was set to 0 as it has a negligible effect on the response (Reilly, 1989).

Ionic currents were calculated according to the Hodgkin-Huxley framework using the gating parameters introduced by McIntyre *et al.* for a mammalian myelinated nerve fiber at 36 ºC (McIntyre et al., 2002). Values of other parameters are given in **Table 4.1**. Voltage waveforms were created using a custom function in MATLAB vR2019a (MathWorks Inc., Natick, MA, US) with rise/fall times of 100 ns each. Waveforms were scaled to create time-varying extracellular potentials at each node according to equation (4.3). Equations (4.1) and (4.2) along with the nonlinear ionic current equations at each node were integrated implicitly and solved using a timestep of 2 ns. The applied field was increased stepwise in increments of 0.25% until an action potential was detected. In the ablation model, tissue exposed to fields equal to or above this threshold was considered to be excited (Mercadal et al., 2017).

4.2.2 – Determination of lethal EFTs in vitro

Lethal thresholds were characterized experimentally for each waveform given in **Table 4.3** using established methods (Arena, Szot, et al., 2012). Briefly, disk-shaped collagen type I hydrogel constructs were fabricated and seeded with hepatocellular carcinoma cell line Hep G2 (ATCC® HB-8065™) at a concentration of 10^6 cells/mL. Hydrogels were covered in culture media and incubated for 24 hours. Two needle electrodes (4 mm spacing, Ø = 0.9 mm) were used to treat gels with the given H-FIRE waveform or IRE in a mobile incubator maintained at 37 °C. Voltage (600 V), repetition rate (1 burst/s), energized time (100 μs), and number of bursts (100) were maintained constant. After treatment, media was replenished and cells were incubated for 24 hours prior to live/dead staining with calcein AM and propidium iodide, respectively. Finally, cells were imaged with a confocal microscope and ablation areas were measured in ImageJ (NIH). A 3D numerical model of treatment was constructed (Comsol Multiphysics v5.5) and a function relating electric field strength to area of exposure was created. Ablation areas were used as inputs to the function to estimate lethal EFTs.

Table 4.1 – Summary of parameters used in modified SENN model

Quantity	*Value*	*Units*	*Source*
Axoplasmic resistivity, ρ_i	70	$\Omega \cdot \mathrm{cm}$	McNeal, 1976
Membrane capacity, c_m	2	$\mu\mathrm{F}\ \mathrm{cm}^{-2}$	Mercadal et al., 2017
Fiber diameter, D	1	μm	Reilly et al., 1985
Nodal gap width, W	1	μm	Reilly et al., 1985
Axon diameter, d_a	0.7 D	μm	Mercadal et al., 2017
Nodal diameter, d_n	0.33 D	μm	Reilly et al., 1985
Internodal separation, L	1.15	mm	Reilly et al., 1985
Membrane capacitance	$c_m \pi d_n W$	$c_m \pi d_n W$	–
Membrane conductance	$\pi d_a^2/(4\rho_i L)$	$\pi d_a^2/(4\rho_i L)$	–
Rest potential, E_r	-88	mV	–

4.2.3 – Realistic In Vivo Ablation Model

To evaluate non-thermal ablation, temperature rise, and thermal damage resulting from treatment with symmetric and variable delay H-FIRE waveforms, a 2-D finite element model representative of a two-needle *in vivo* ablation was developed.

The steady-state electric potential ϕ in an electrically inhomogeneous medium was computed by solving a modified Laplace equation that considers local electrical conductivity σ:

$$\nabla \cdot (\sigma \cdot \nabla\phi) = 0 \tag{4.4}$$

The boundary conditions at the electrodes were Dirichlet in type and set to $\phi = V_0$ where the energized (leftmost) electrode meets tissue and $\phi = 0$ on the rightmost electrode boundaries. The exterior boundary was Neumann in type and electrically insulative, which confined all current to the domain and provided a worst-case scenario to temperature estimations. The tissue temperature rises during treatment according to the Joule heating term p, calculated as $\sigma|\nabla\phi|^2$. This term was scaled according to the energized time per burst (τ) and burst repetition rate (f), and added to the traditional Pennes bioheat equation to calculate the temperature distribution:

$$\rho c_p \frac{\partial T}{\partial t} = \nabla(k\nabla T) + \omega_b \rho_b c_b (T_a - T) + p\tau f \tag{4.5}$$

where ρ is the tissue density, c_p is the tissue heat capacity, T is the temperature, k is the tissue thermal conductivity, ω_b is the blood perfusion rate, ρ_b is the blood density, c_b is the heat capacity of blood, T_a is the arterial temperature, τ is the energized time per burst, and f is the burst repetition rate. Initially, the domain was set to a temperature of 37 °C and all boundaries, including electrodes, were considered adiabatic. Tissue metabolism was neglected as it contributes minimally to bulk temperature rise (Davalos et al., 2003).

Finally, an Arrhenius-type thermal dose equation was used to calculate the extent of thermal damage Ω:

$$\Omega = \int \xi e^{-E_a/RT}\, dt \tag{4.6}$$

where ξ is the frequency factor, E_a is the activation energy, and R is the universal gas constant (Thomsen & Pearce, 2011). To give a more intuitive description to the thermal damage arising from treatment, a probabilistic approach was used to estimate the percentage of cells P_Ω that would die upon reaching different values of Ω according to (Diller et al., 1983; Garcia et al., 2014):

$$P_\Omega = 100 \cdot (1 - e^{-\Omega}) \tag{4.7}$$

Using this approach, values of $\Omega = 1$ and $\Omega = 4.6$ correspond to 63% and 99% cell death due to thermal damage, respectively. To calculate the area where cells were killed due to heat, thermal damage was conservatively approximated as areas where tissue was exposed to $\Omega \geq 0.53$ (41%), as this has been noted as the onset of thermal damage (Garcia et al., 2014).

Tissue electrical conductivity exhibits complex behavior in response to applied electric fields (Corovic et al., 2013). This behavior is tissue specific and depends on the amplitude and duration of the applied field, as well as the number of pulses. Previous reports have shown that electroporation-induced conductivity changes can be represented by a sigmoidal curve that: (a) begins at a baseline conductivity σ_0 determined by the characteristic frequency of the waveform (Y. Zhao et al., 2018); (b) exhibits a transition range related to the reversible and irreversible ablation thresholds of the waveform (Sel et al., 2005); and (c) saturates to a final conductivity σ_f similar to the tissue's conductivity in the upper end of the β-dispersion frequency range (1 kHz – 100 MHz) (Neal et al., 2012, 2014a).

To consider these dynamic changes, we used the model introduced by Sel *et al.* (Sel et al., 2005), in which the dependence of σ on the local field is given by:

$$\sigma(\vec{E}) = \sigma_0 + \frac{\sigma_f - \sigma_0}{1 + D \cdot e^{-(|\vec{E}|-A)/B}} \tag{4.8}$$

where D is a fitting parameter, and A and B are related to the electroporation effects of the waveform. They are calculated as:

$$A = \frac{E_0 + E_1}{2} \qquad B = \frac{E_1 - E_0}{C} \tag{4.9}$$

where E_0 and E_1 are the electric field thresholds for reversible and irreversible electroporation, respectively, and C is a sigmoid fitting parameter. We used values of C and D of 8 and 10, respectively, which were previously determined for liver tissue (Sel et al., 2005). Baseline electrical conductivity $(\sigma_0)$was determined by evaluating a liver impedance model (Gabriel et al., 1996) at the characteristic frequency of each waveform, and electroporated conductivity (σ_f) was set to 0.32 S/m by evaluating the model at 10 MHz (**Table 4.3**).

Our experimental results showed no difference in lethal EFT as a function of d_2, so E_1 was set to 1,030 V/cm for all waveforms with 1 μs pulses, and 658 V/cm for waveforms made up of 5 μs pulses – the average across all values of d_2 for either constitutive pulse width. The reversible threshold (E_1) was characterized for the 5-1-5-1 protocol (453 V/cm) and assumed constant regardless of d_2 or T_p. Thresholds were also characterized for a conventional IRE protocol to provide a comparison. E_0 for the IRE protocol was set to 282 V/cm, which was computed by scaling our experimentally determined E_1 (429 V/cm) to the ratio of E_0/E_1 reported in (Sel et al., 2005).

We also considered the effect of temperature on local conductivity. Thus, the overall conductivity is given by:

$$\sigma(\vec{E},T) = \left[\sigma_0 + \frac{\sigma_f - \sigma_0}{1 + D \cdot e^{-(|\vec{E}|-A)/B}}\right]\left(1 + \alpha \cdot \left(T - T_{ref}\right)\right) \tag{4.10}$$

where α is the temperature coefficient of electrical conductivity and T_{ref} is a reference temperature at which the conductivity values were measured ($T_{ref} = T_a$ = 37 °C).

Table 4.2 – Material properties used in ablation model

Quantity	*Value*	*Units*	*Source*
Density, ρ	1,079	$\mathrm{kg\ m^{-3}}$	Hasgall et al., 2018
Heat capacity, c_p	3,540	$\mathrm{J\ kg^{-1}\ K^{-1}}$	Hasgall et al., 2018
Thermal conductivity, k	0.512	$\mathrm{W\ m^{-1}\ K^{-1}}$	Duck et al., 1990
Temperature coefficient, α	2	$\%\ \mathrm{K^{-1}}$	Duck et al., 1990
Blood perfusion, ω_b	9.27×10^{-3}	$\mathrm{s^{-1}}$	Cosman & Cosman, 2005
Blood density, ρ_b	1,050	$\mathrm{kg\ m^{-3}}$	Hasgall et al., 2018
Blood heat capacity, c_b	3,617	$\mathrm{J\ kg^{-1}\ K^{-1}}$	Hasgall et al., 2018
Frequency factor, ξ	2.08×10^{27}	$\mathrm{s^{-1}}$	Thomsen & Pearce, 2010
Activation energy, E_a	1.866×10^{5}	$\mathrm{J\ mol^{-1}}$	Thomsen & Pearce, 2010

COMSOL Multiphysics v5.5 (COMSOL Inc., Stockholm, Sweden) was used to construct the model and solve equations (4.4)-(4.10). Tissue was modeled as a circle with radius 20 cm to ensure boundary distortions would not play a role in the results. Two circles ($\emptyset = 1\ mm$) with center-to-center separation of 1 cm were used to represent the electrodes. For each waveform, a typical treatment consisting of 100 bursts was simulated with τ = 100 μs and f = 1 Hz. Thermal damage was computed 10 minutes after treatment ended, as thermal damage continues to accumulate until tissue temperature falls below approximately 43 ºC. The applied potential was set to 2,500 V in all simulations except those used to find the equivalent potential in **Figure 4.9**, in which case the voltage applied was varied until the area of excitation for the given variable delay waveform matched the area of excitation for the symmetric case. Material properties of liver tissue employed in the model can be found in **Table 4.2**. Burst parameters are summarized in **Table 4.3**. To ensure accuracy of the solution, the mesh was refined until less than a 1% difference was observed in the electric field distribution between refinements. The final mesh consisted of 226,499 vertices and 451,680 triangular elements. Simulations took place on a Dell OptiPlex 7071 with an 8-core Intel I9 processor and 32 GB of RAM.

4.2.4 – Determination of Maximum interpulse delay

To determine the range of reasonable values of d_2, we considered the fact that current H-FIRE protocols consist of 100-300 bursts delivered at a repetition rate of up to 1.5 Hz. To maximize clinical relevance, it is critical that the burst be amenable to incorporation into protocols in which ECG synchronization is desired and/or necessary. Considering that the absolute refractory period of cardiac myocytes is 250 – 300 ms, we placed an upper limit of 100 ms on the burst duration (Hall, 2011). This gives ample time for the R-wave to be detected and pulse delivery to be initiated. To find the maximum value of d2 that meets this constraint, the following equation giving the burst duration T_b was used:

Table 4.3 – Experimental matrix of burst waveforms examined in this study.

T_p (μs)	d_1 (μs)	d_2 (μs)	f_c (kHz)	σ_0 (mS cm^{-1})	T_b (ms)
1	1	0.1	322.6	1.5	0.15
1	1	1	250	1.3	0.20
1	1	10	76.9	0.81	0.64
1	1	100	9.71	0.53	5.1
1	1	1,000	0.997	0.41	49
5	1	0.1	90.1	0.84	0.11
5	1	1	83.3	0.82	0.12
5	1	10	47.6	0.72	0.20
5	1	100	9.01	0.53	1.0
5	1	1,000	0.989	0.41	9.1
100	N/A	N/A	10	0.535	0.1

$$T_b = N \cdot \left(2T_p + d_1 + d_2\right) - d_2 \tag{4.11}$$

Here, N is the number of bipolar pulses within the burst – chosen such that $2N \cdot T_p = 100$ μs. Waveforms with constitutive pulse widths of 1 μs require that $N = 50$, while 5 μs pulse bursts require $N = 10$. Thus, with the same delay structure, burst duration is inversely related to constitutive pulse width, so the maximum value of d_2 was determined by substituting 100 ms for T_b, 50 for N, and 1 μs for d_1 in (4.11), then solving for d_2. This gives a maximum interpulse delay of 2.04 ms, which was lowered to the nearest power of 10 for integration into our parametric analysis. It is worth noting that d_2 could theoretically be prolonged up to 11.1 ms while meeting the above constraints for bursts with constitutive pulse widths of 5 μs.

4.3 – Results

4.3.1 – Modified SENN Model Behavior and Validation

Figure 4.3 gives the strength/duration (S/D) curve for the modified SENN model employed here for single monopolar and bipolar pulses. The behavior of the model is in agreement with other published studies (Mercadal et al., 2017; Reilly, 1989; Rogers et al., 2004). Namely, on this log-log plot, a linear relationship is observed between threshold amplitude and pulse width for both monopolar and bipolar pulses with durations up to roughly 500 μs. Beyond this point, thresholds decrease minimally and are nearly identical for both monopolar and bipolar pulses. Comparison of the overall behavior of the model to experimental studies was obtained through a least-squares fit to the standard equation for excitation of an ideal linear membrane:

$$E_t = \left[1 - e^{-T_p/\tau_e}\right]^{-1} \tag{4.12}$$

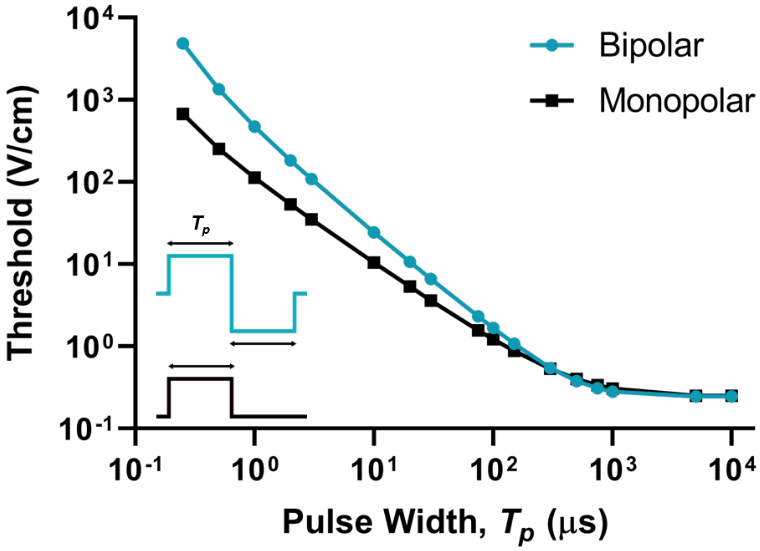

Figure 4.3 – Strength/duration curve for myelinated nerve fiber in response to single monopolar and bipolar pulsed fields.

in which E_t is the threshold field for a monopolar pulse of duration T_p and τ_e is an empirical S/D time constant. According to equation (4.12), the SENN model used here exhibits a time constant τ_e of 626 μs, which is in agreement with reported experimental values (Mogyoros et al., 1996; Reilly, 1988). Additionally, the threshold for a conventional IRE pulse (100 μs monopolar) was 1.2 V/cm - nearly identical to that reported by Rubinksy and Golberg (Golberg & Rubinsky, 2012).

4.3.2 – Effect of Pulse Width and Delays on Nerve Fiber Response

The neural response to varying interphase and interpulse delays is shown in **Figure 4.4**. Although intuitive given the body of literature demonstrating amplified excitability with prolonged interphase gaps for single biphasic pulses, here it is explicitly demonstrated that short interphase delays result in the greatest stimulation thresholds. For symmetric 1 μs pulse bursts, stimulation thresholds decreased 24% and 41% when the interphase delay was increased to 1 or 10 μs from 0. For 5 μs pulse bursts, this effect was not as pronounced, but thresholds fell 9% and 32% across the same delay increases.

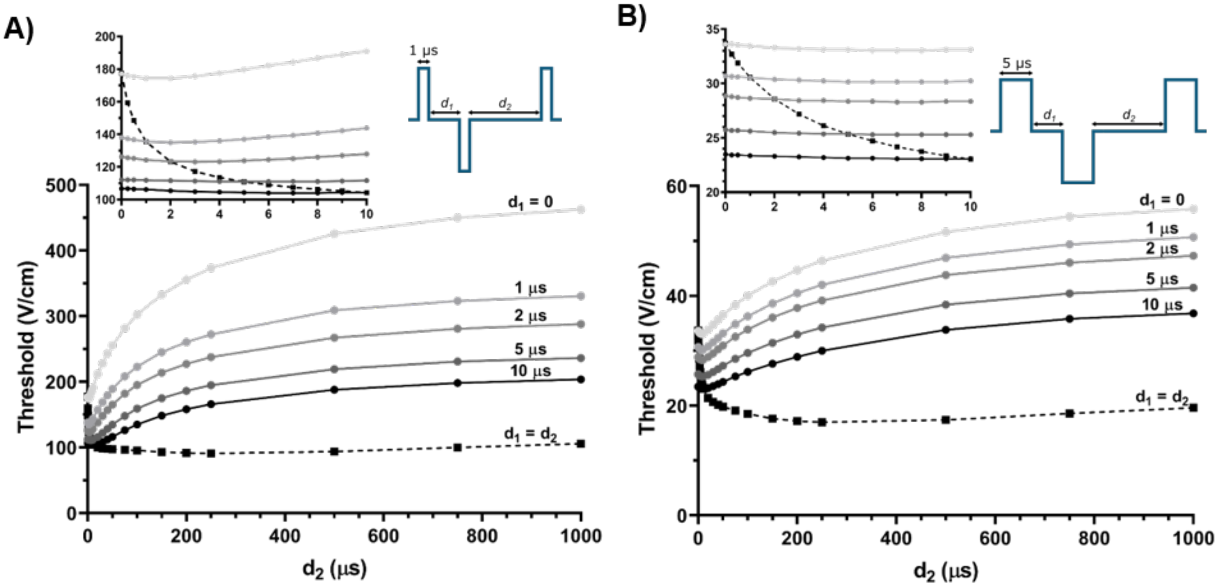

Figure 4.4 – Longer interpulse delays (d_2), but not interphase delays (d_1), increase thresholds required to elicit action potentials in the SENN model of a myelinated nerve fiber. Threshold electric fields required for stimulation for a) 1 μs pulse bursts and b) 5 μs pulse bursts. Note different ordinate scales. Thresholds calculated for single burst with energized time of 100 μs.

For bursts made up of 5 μs pulses, interpulse delays of 1 ms exhibited increased excitation thresholds approximately 60 % higher than with no interpulse delay, regardless of the interphase delay. Interestingly, for bursts with 1 μs constitutive pulse widths, holding the interphase delay to a minimum increases the relative gain in stimulation threshold that can be attained while lengthening the interphase delay. For example, a burst comprised of 1 μs pulses with d_1 of 1 μs and d_2 of 1,000 μs exhibits a threshold 2.44× that of a similar burst with d_2 maintained at 1 μs; extending d_1 to 10 μs reduces the gain that can be achieved with this modification in d_2 to 1.95×. Finally, the dashed curve in Fig. 4 indicates that symmetric increases in both delays cause a sharp decline in excitation threshold with a minimum near 250 μs and a gradual recovery with further symmetric increases in d_1/d_2. The trends observed here suggest the optimal strategy for reducing nerve stimulation is to minimize d_1 while maximizing d_2. In light of this observation, subsequent simulations were performed with d_1 fixed at 1 μs to examine the effects of d_2 independently. We chose to fix d_1 to 1 μs for practical reasons; most generators used in clinical and pre-clinical studies employ fully controlled solid-state switches (e.g. MOSFET, IGBT) which have a certain switching time, and when generating bipolar pulses, some time is required during polarity reversal to avoid shorting the DC power supply.

4.3.3 – Effect of Interpulse Delay on Physical Response

To assess the effect of the interpulse delay on ablation, temperature rise, and nerve excitation in a realistic clinical setting, we first characterized thresholds required to ablate liver cells in a 3D collagen hydrogel, which informed subsequent construction of a numerical model representative of *in vivo* treatment. In this model, we applied H-FIRE waveforms with pulse widths of 1 or 5 μs and fixed interphase delay of 1 μs, then varied the interpulse delay from 0.1 μs to 1,000 μs (**Table 4.3**).

Figure 4.5 illustrates the results of cell-laden hydrogel treatment with different variable delay H-FIRE waveforms. Due to generator limitations, the shortest interpulse delay used in experiments was 250 ns. A two-way ANOVA was performed to test the effect of pulse width and interpulse delay, and it was found that only pulse width contributed significantly ($p < 0.0001$) to different lethal EFTs. Due to this result, E_1 was set as the average of all protocols with a given constitutive pulse width, which was 1030 ± 182 V/cm for bursts with 1 µs pulses and 658 ± 116 V/cm for bursts made up of 5 µs pulses. See supplementary material for individual results.

In the model, lengthening the interpulse delay (d_2) reduced the effective baseline conductivity due to the lower characteristic frequency of the burst. This effect is especially prevalent in bursts with constitutive pulse widths of 1 µs but becomes less significant with pulse widths of 5 µs. As d_2 is extended to 100 µs or longer, the effective baseline conductivity becomes

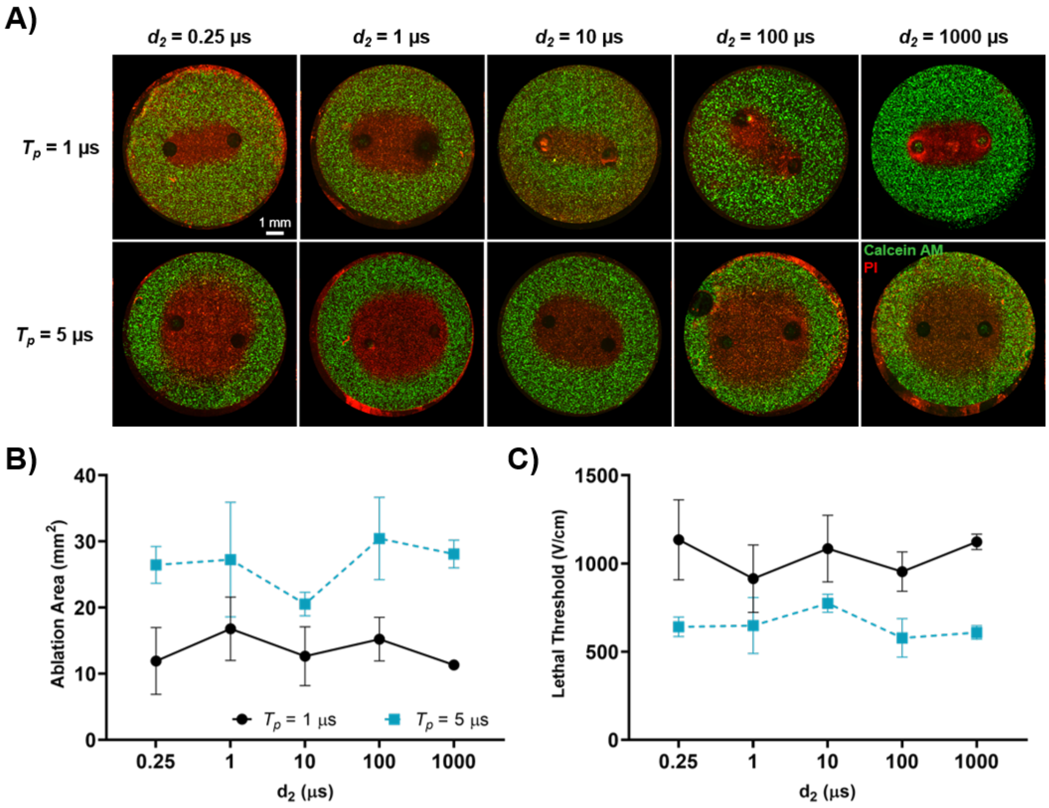

Figure 4.5 — Lethal thresholds are impacted by changes in pulse width but not interpulse delay. a) Representative confocal images of ablations produced by each combination of T_p and d_2 under study. Summarized ablation areas (b) and lethal thresholds (c) demonstrate differences due to T_p ($p < 0.0001$) but not d_2 ($p > 0.05$).

identical regardless of the constitutive pulse width of the burst (**Table 4.3**). Alternatively, the sigmoid transition range correlates with the relative difference between the reversible EFT and lethal EFT. At or above the lethal EFT, the conductivity of all burst waveforms with a given pulse width converges.

The electric field distribution during the last burst as a function of constitutive pulse width and interpulse delay is shown in **Figure 4.6**. As the electric field is a function of local conductivity, trends in the field distribution closely follow those of the conductivity as mentioned above. Of note is the increased vertical field exposure but slightly suppressed exposure moving horizontally outward from the electrodes with increased d_2. Panels (e) and (f) in **Figure 4.6** demonstrate the percent difference in amount of tissue exposed to varying electric fields compared to a symmetric burst with 1 μs interphase and interpulse delays. These curves were developed by calculating the area of tissue exposed to fields equal to or greater than each field given on the x-axis, then calculating the relative difference between each variable delay curve and the symmetric curve. Areas of exposure to fields of 10 to about 1,500 V/cm are increased with longer interpulse delays.

The exception to this trend occurs for a small range of fields near the midpoint of the transition zone in the dynamic conductivity curve for each waveform.

The intersection points between the vertical lines and the curve for each waveform indicate the relative difference in area of reversible (E_{rev}) and irreversible (E_{lethal}) electroporation compared to a symmetric burst with both delays set to 1 µs. Thus, 1 µs pulse bursts with d_2 = 1,000 µs give rise to a 17% and 4.9% increase in area of reversible and irreversible electroporation, respectively, while shortening d_2 to 0.1 µs reduces these areas by 2.7% and 0.6%, respectively.

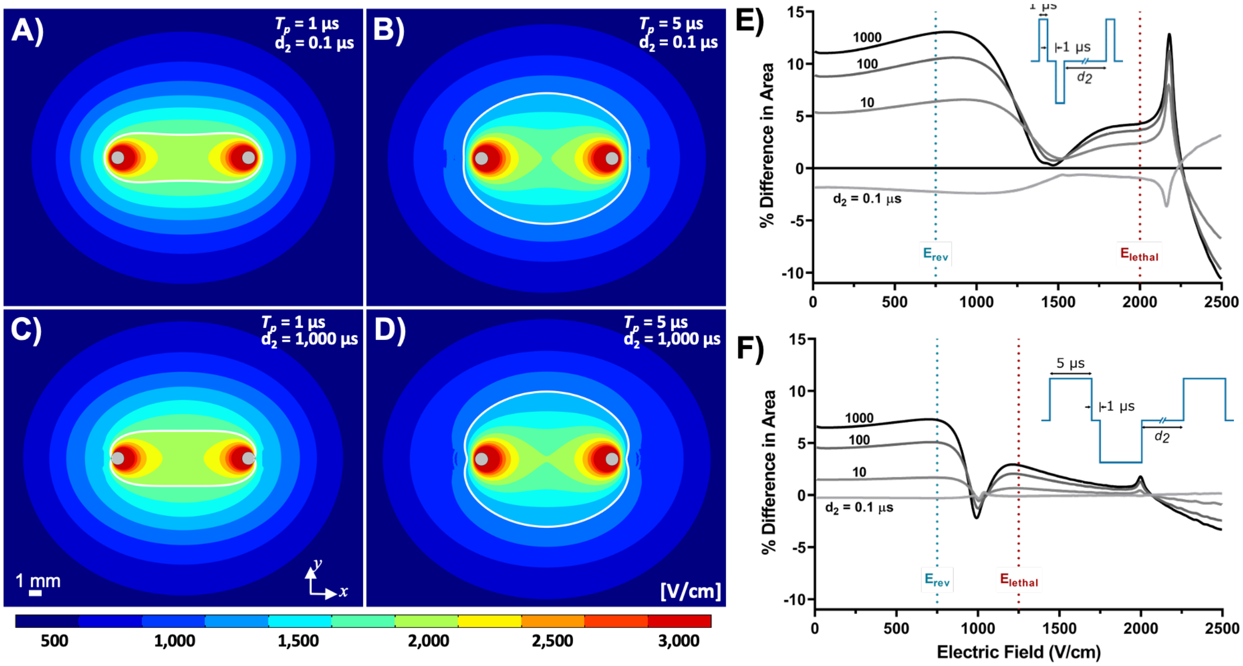

Figure 4.6 — Extended interpulse delays increase the area of exposure to therapeutic electric field strengths. a-d) Electric field contours for bursts with constitutive pulse widths of (a, c) 1 µs and (b, d) 5 µs and interpulse delays of 0.1 µs (a, b) and 1,000 µs (c, d) are shown during the final burst. The white line delineates the area of ablation due to IRE. e-f) Percent difference in exposure of tissue to therapeutic electric fields for each variable delay waveform versus a symmetric burst with d_1/d_2 set to 1 µs and pulse widths of e) 1 µs and f) 5 µs. It is worth noting that E_{rev} and E_{lethal} are dependent upon applied pulse characteristics and were determined experimentally in this study.

Bursts made up of 5 µs pulses exhibit similar trends, with increases in area of 7.6% and 3.2%, respectively, with d_2 = 1,000 µs versus the symmetric case. By shortening d_2 to 0.1 µs with a 5 µs pulse width, the area of reversible electroporation is reduced by 1% while the irreversibly electroporated region increases 2.3%.

Figure 4.7 illustrates the thermal damage distribution arising from treatment with different H-FIRE waveforms expressed as a percentage (P_{Ω}). For 1 μs pulse bursts, the area of thermal damage ($\Omega > 0.53$) is reduced from 38.7 mm^2 to 34.6 mm^2 as d$_2$ is extended from 0.1 to 1,000 μs. With the same extension in d$_2$, thermal damage resulting from treatment with 5 μs pulse bursts is reduced from 40.2 mm^2 to 39.3 mm^2. Additionally, the maximum value of Ω is inversely related to d$_2$. Bursts with constitutive pulse width of 1 μs exhibit maximum values of 5.7 and 4.1 for d$_2$ = 0.1 and 1,000 μs. Applying the same changes in d$_2$, 5 μs burst waveforms exhibit maxima of 6.1 and 5.8, respectively. This can be attributed to higher temperatures adjacent to the electrodes with shorter delays due to the increased electrical conductivity.

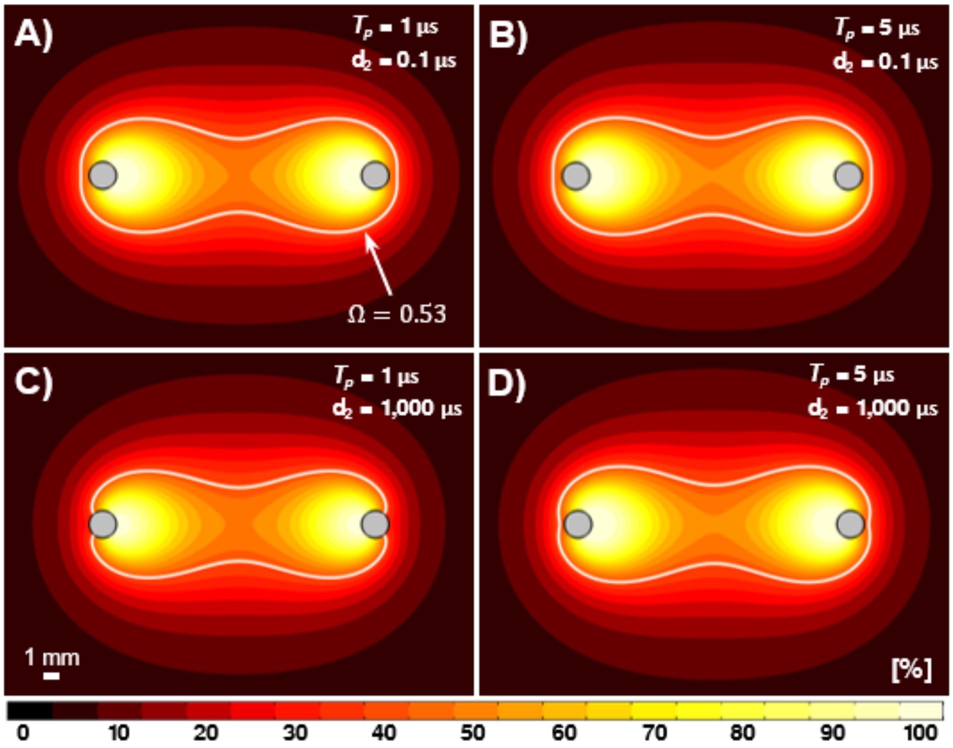

Figure 4.7 — Longer interpulse delays reduce thermal damage in therapeutic H-FIRE treatments. Thermal damage (%) contours for (a, c) 1 μs pulse bursts and (b, d) 5 μs pulse burst waveforms with interpulse delays of 0.1 and 1,000 μs, respectively. The white line indicates the onset of thermal damage.

4.3.4 – Effect of Interpulse Delay on Relative Efficacy

Next, we introduce a metric to define the relative efficacy of a given waveform:

$$\mathrm{R}_{eff} = \frac{A_{IRE}}{A_{TD}} \frac{A_{IRE}}{A_{EXC}} = \frac{A_{IRE}^2}{A_{TD} \cdot A_{EXC}} \tag{4.13}$$

where R_{eff} is a dimensionless quantity representative of the efficacy of the waveform and A_{IRE}, A_{TD}, and A_{EXC} are the areas of irreversible electroporation, thermal damage, and excitation. This value can be used to compare the ability of each waveform to create ablations while limiting the extent of thermal damage and nerve excitation.

Calculated values of A_{IRE}, A_{TD}, and A_{EXC} are shown in **Figure 4.8**. A minor increase in ablation area is observed with longer interpulse delays, while areas of excitation and thermal damage are reduced. Trends in R_{eff} versus d_2 are shown in **Figure 4.8c-d**. For visualization, R_{eff} for bursts with either constitutive pulse width was normalized to the case in which $d_2 = 1$ µs. Here,

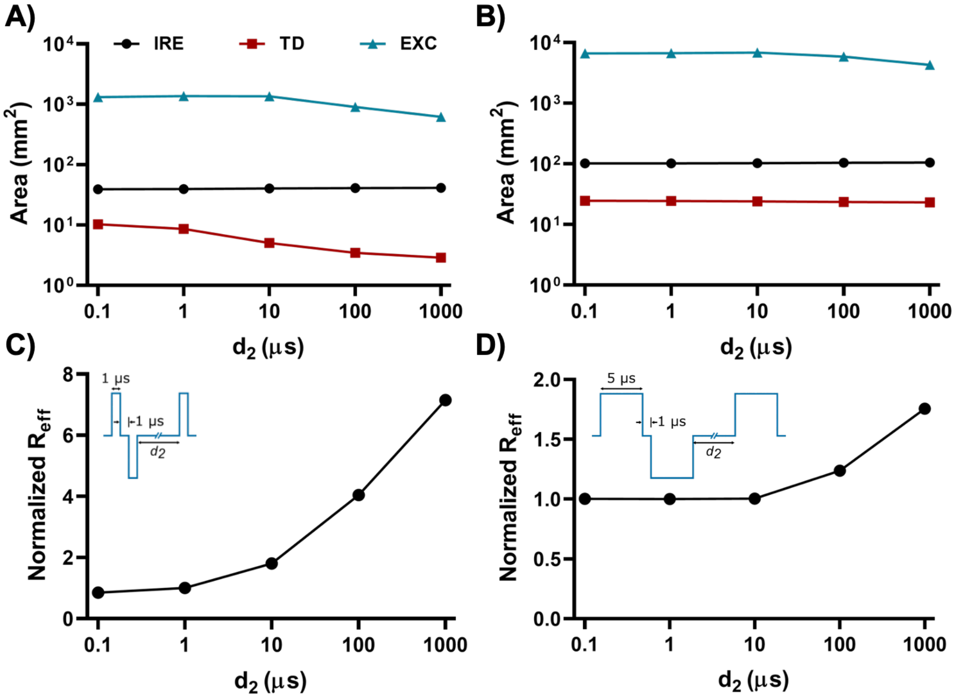

Figure 4.8 – Longer interpulse delays increase therapeutic efficacy of H-FIRE bursts. Areas of IRE, thermal damage, and excitation for 1 µs pulse bursts (a) and 5 µs pulse bursts (b) as a function of d_2. Right panel gives areas for a conventional IRE protocol. Normalized R_{eff} as a function of d_2 for 1 µs pulse bursts (c) and 5 µs pulse bursts (d). R_{eff} is normalized to value at $d_2 = 1$ µs (i.e., symmetric burst).

it can be seen that R_{eff} increases exponentially with d_2 on a log scale. This increase is continuous for 1 μs pulse bursts but is not obvious until d_2 reaches 100 μs for bursts with constitutive pulse widths of 5 μs. For 1 μs pulse bursts, increasing d_2 from 0.1 μs to 1,000 μs increased R_{eff} nearly 3-fold from 0.35 to 0.84. Similar modifications in d_2 for 5 μs pulse bursts increased R_{eff} from 0.23 to 0.36. For comparison, R_{eff} for the modeled conventional IRE protocol was 0.022 (not shown), which was mainly dominated by the large area of nerve stimulation.

Finally, a parametric analysis was performed for each variable delay waveform with extended d_2 to determine the maximum voltage that can be applied while maintaining the same excitation area as the case in which d_1/d_2 are symmetric and equal to 1 μs (**Figure 4.9**). For symmetric waveforms comprised of 1 μs and 5 μs pulse bursts, the standard treatment with 100 bursts at 2,500 V produced ablations of 130 mm^2 and 236 mm^2, respectively, and stimulation areas of 1,298 mm^2 and 6,341 mm^2. For 1 μs burst waveforms, extending d_2 to 10 μs, 100 μs, or 1,000 μs gave maximum voltages that could be applied of 2,422 V, 3,450 V, and 4,878 V, respectively, while maintaining a stimulation area of 1,298 mm^2. At these voltages, ablation areas are 127 mm^2, 123 mm^2, and 418 mm^2, respectively. Waveforms with 5 μs constitutive pulses exhibit maximum voltages of 2,116 V, 2,777 V, and 3,724 V when d_2 is 10 μs, 100 μs, or 1,000 μs, respectively.

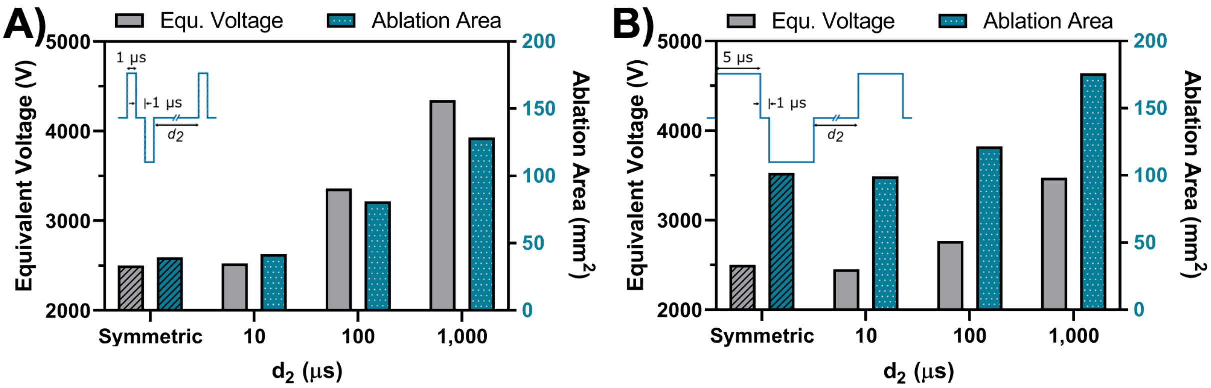

Figure 4.9 – Longer interpulse delays allow for higher applied voltages. Maximum voltages that can be applied while maintaining the same area of excitation as with symmetric interpulse delays (d_1/d_2 = 1 μs) are shown for bursts with a) 1 μs and b) 5 μs constitutive pulse widths. Also shown are the ablation areas resulting from treatment with the maximum voltage given for each waveform.

Applying bursts at these voltages gives ablation areas of 206 mm^2, 296 mm^2, and 472 mm^2, while maintaining a stimulation area of 6,341 mm^2.

4.4 – Discussion

In this study, we proposed that variable delays within H-FIRE bursts may be more clinically efficacious in terms of ablating tissue with reduced nerve excitation in comparison to current waveforms with symmetric delays. To evaluate the feasibility of such an approach, we analyzed the effects of variable delays on neural excitation for bursts with constitutive pulse widths of 1 μs and 5 μs. From these findings, we fixed the interphase delay to 1 μs and performed a parametric sweep of the interpulse delay in a realistic two-needle treatment model to quantify the extent of ablation, excitation, and thermal damage.

The results suggest that the largest clinical effect will be reduced nerve excitation with extended interpulse delays. For waveforms with short constitutive pulse widths near 1 μs, interpulse delay has a substantial influence on the characteristic frequency of the burst, and thus the effective baseline conductivity and Joule heating produced from treatment. This difference in baseline conductivity as a function of d_2 is dependent upon the slope of the tissue's impedance spectrum across the range of frequencies of interest. Thus, the effects of modifying the interpulse delay on electrical conductivity and Joule heating may vary between tissues.

As shown in **Figure 4.4**, prolonging d_2 yields a marked increase in the electric field required to stimulate a nerve fiber compared to a burst with short, symmetric delays. However, it should be noted that with longer burst durations, it is possible that a single burst will initiate multiple action potentials in excitable cells exposed to threshold stimuli or greater. This is because action potentials – and, in turn, refractory periods – in skeletal muscle and nerve are roughly 2 to 4 ms in duration. In the case that extremely long values of d_2 (250-1,000 μs) are not clinically efficacious, shorter delays that maintain a burst duration just below the absolute refractory period of muscle will likely still be desirable. For example, for a 5 μs pulse burst with 100 μs of energized time and d_1 set to 1 μs, d_2 can be extended to 146 μs assuming an absolute refractory period of 3 ms for muscle (see equation (4.11)). By maintaining a burst duration that can be delivered while the muscle is refractory, a single action potential would be generated in affected cells, mitigating synergistic effects such as frequency summation that might occur due to multiple action potentials firing in response to each burst. This approach has been taken for ECT protocols (8×100 μs pulses) and in an *in vivo* rat study, it was found that the number of contractions could be reduced from eight lighter contractions to a single stronger contraction by increasing the repetition rate to 100 Hz or more (Miklavčič et al., 2004). While further increases in frequency reduced the strength of the single contraction, this finding suggests that bursts with durations in the range of 70 ms will be feasible, but this relationship must be more rigorously explored to definitively place limits on d_2.

It is important to appreciate the mechanism by which prolonged values of d_2 suppress nerve fiber activation. Because these fibers are much longer than most cells in the tissue parenchyma, membrane charging occurs via a unique mechanism, relying on charge redistribution along the length of the fiber rather than the potential difference between the interior and exterior of the fiber at a given point (Cooper, 1995). As a result, while parenchymal cells exhibit charging constants on the order of 1 μs, membrane charging constants of nerve fibers are much longer, and are typically reported to be on the order of hundreds of microseconds (Kotnik & Pucihar, 2010; Mercadal et al., 2017; Panizza et al., 1994). Thus, extending d_2 to tens or hundreds of microseconds allows the nerve fiber membrane to discharge between subsequent bipolar pulses within the burst.

Excitation is also dependent on d_1, which must be shortened sufficiently for the negative phase of each bipolar pulse to adequately cancel VGSC activation by its corresponding positive phase (Casciola et al., 2019). Conversely, interphase delays on the order of the time constant of targeted cells increase time of exposure to a critical transmembrane potential, which has been shown to correlate with permeabilization (Kotnik et al., 2003). This implies an optimal value of d_1 exists that mitigates VGSC activation while also allowing passive discharge of targeted cellular membranes. In this study, we fixed d_1 to 1 μs ($\sim\tau_m$) to demonstrate theoretically that these mechanisms can be exploited to apply higher potentials without increased stimulation, which will allow for larger areas of ablation and permeabilization. In practice, this strategy will require optimization, and to achieve desirable results without substantial temperature increases, thermal mitigation strategies will be imperative (Arena et al., 2013; O'Brien et al., 2018; Sano et al., 2020).

In our *in vitro* study, we found that lethal EFTs were only a function of the width of constitutive pulses. Bursts with 1 μs pulse widths exhibited a threshold near 1 kV/cm, approximately 57% higher than those with 5 μs widths, indicative of the bipolar cancellation present with very short pulses. Recent experimental data have found that interphase and interpulse delays mediate permeabilization and lethality of high-frequency pulse bursts, with longer delays typically magnifying biological effects. For instance, Valdez and colleagues found that bipolar nanosecond pulses with interphase delays greater than 10 ms resulted in permeabilization comparable to that of energy-matched monopolar pulses (Valdez et al., 2018). And Polajzer and colleagues demonstrated that assisted discharge can explain cell viability trends resulting from symmetric increases in interphase and interpulse delay, but specific cases of cell permeabilization deviated from theoretical projections (Polajžer et al., 2020). Recently, increased cell death has also been achieved by independently lengthening the interpulse delay up to 1 ms for a single burst with

800 μs of energized time (Vižintin et al., 2020). Thus, while we did not find a significant impact of d_2 on lethal thresholds, it is possible that in other cell types or in bulk tissue, extended values of d_2 may exhibit lower thresholds than the symmetric bursts currently being used. Importantly, if this is realized clinically, R_{eff} will be further amplified as d_2 is prolonged.

Finally, it is important to acknowledge potential limitations of our approach. By assuming a constant perfusion rate, our simulations neglect to account for local disruptions in blood flow (Jarm et al., 2010), and may underestimate temperature rise. We assumed electrical properties of tissue exposed to sub-electroporative H-FIRE bursts could be defined by determining a discrete characteristic frequency at which the burst operates (S. Bhonsle et al., 2018; Yao, Dong, Zhao, Lv, et al., 2017; Y. Zhao et al., 2018). Next, we assumed this characteristic operating frequency f_c is defined as the inverse of the bipolar pulse period (**Figure 4.1**). This assumption has been employed previously, but not for high-frequency bipolar waveforms with variable delays as introduced here (Y. Zhao et al., 2018). Thus, it remains to be determined whether extensions in d_2 continuously generate reductions in f_c, or whether there is a limit to the influence of d_2 on f_c. Additionally, we calculated σ_f by assuming the β-dispersion of liver tissue plateaus at 10 MHz, which can be qualitatively concluded from the data reported in (Gabriel et al., 1996) and is consistent with theory (Grimnes & Martinsen, 2008; Schwan, 1957). Importantly, so long as each waveform saturates to the same conductivity, lengthening d_2 will produce the benefits reported in this paper regardless of the value of σ_f.

It is critical to note that the nerve excitation results are independent of the assumptions underlying the conductivity curves constructed in this study, and in their own right provide valuable information toward optimizing delays within H-FIRE waveforms. However, it is also important to recognize that the nerve stimulation model has limitations. To facilitate translation to the 2D ablation models, we chose to characterize thresholds for excitation at the terminus of a 6-node fiber. This truncated fiber model could introduce inaccuracies in terms of the current distribution that would not be present in a longer fiber. Additionally, the theoretical time constant of our model is high (τ_e = 626 µs) compared to the original SENN model (τ_e = 120 µs) exposed to uniform-field excitation, which reflects the small diameter and short length of the fiber modeled here; however, as previously mentioned, this falls within the range of experimental values for mammalian nerve (Reilly, 1988; Reilly et al., 1985). Finally, it is important to point out that areas given for excitation are areas in which a nerve terminus could be excited if aligned with a relatively constant field at threshold or higher. While these areas build intuition and facilitate comparison, they are not precisely indicative of the areas of tissue that will be stimulated, but surrogates that represent the relative magnitude of excitation (and thus, contraction). Thus, it will be critical to corroborate our findings with experimental results in the future.

4.5 – Conclusion

Irreversible electroporation is an emerging focal treatment modality for solid tumors and in cardiac ablation for treating atrial fibrillation (Maor et al., 2019; Ramirez et al., 2020). While promising results have been reported, adoption of IRE has been hindered by its complex anesthetic regimen and treatment protocols. H-FIRE has been introduced to overcome these limitations and drastically simplifies clinical procedures, but waveforms suffer from reduced ablation volumes compared to their IRE counterparts. For this reason, higher voltages are often desired during H-FIRE, but this increases the likelihood of thermal damage and muscle contractions. Here, we demonstrate that minor changes to the delays within H-FIRE burst waveforms may suppress neural excitation and Joule heating. It is also possible that these waveforms will increase ablation size by modulating local electrical conductivity. Modified waveforms can be readily implemented without generator hardware modifications or systemic changes to existing treatment protocols.

5 – Interphase and interpulse delays modulate cell death and nerve stimulation resulting from microsecond-duration pulsed electric field bursts

5.1 – Introduction

Electroporation (EP) is a biological phenomenon in which cell membrane permeability increases upon exposure to electric fields of sufficient magnitude and duration, presumably due to creation of nanoscale defects or "pores" (Geboers et al., 2020; Yarmush et al., 2014b). Depending upon characteristics of the applied field, electroporation exists in two regimes: reversible and irreversible. Reversible EP is a technique where transient permeabilization is induced to allow cellular uptake of otherwise impermeant molecules (e.g., large pharmaceuticals, proteins) (Geboers et al., 2020; Probst et al., 2018). It is primarily used in applications such as electrochemotherapy (ECT) and gene electrotransfer (GET). Irreversible electroporation (IRE), on the other hand, is a focal tissue ablation modality that exploits the increased membrane permeabilization to permanently disrupt cellular homeostasis, non-thermally destroying targeted cells (Davalos et al., 2005b).

The typical IRE procedure involves delivering a series (100-300) of monopolar pulses (1-3 kV/cm, 70-100 μs) directly to the tissue of interest through pairs of needle electrodes. Cells exposed to a sufficiently strong electric field are permeabilized to an extent that they cannot re-establish electrochemical homeostasis and die over the course of hours (Mercadal et al., 2020; Napotnik et al., 2021). This unique, non-thermal cell death mechanism allows IRE to be administered in cases where thermal techniques would be contraindicated such as for tumors adjacent to vascular, neural and/or ductal structures. IRE has been used successfully in the treatment of nearly 10 thousand patients with unresectable pancreatic, liver, and prostate tumors (Aycock & Davalos, 2019); it is also gaining attention for non-thermal cardiac ablation (Maor et al., 2019; Sugrue et al., 2019).

While IRE has clearly demonstrated its utility in the clinic, it is well understood that conventional monopolar pulses may not be optimal for every application requiring pulsed field ablation. For instance, these pulses easily stimulate excitable cells (i.e., peripheral nerves, skeletal muscle cells, cardiomyocytes), requiring general anesthesia and neuromuscular blocking agents to prevent skeletal muscle contractions. Pulses must also be ECG synchronized to mitigate the risk of arrhythmia (Ball et al., 2010; Deodhar, Dickfeld, et al., 2011). Further, studies have reported that the electric field distribution arising from IRE pulses can be vulnerable to distortions, especially when administered in heterogeneous tissues (Arena, Sano, Rylander, et al., 2011; Murovec et al., 2016; Yao, Zhao, Mi, et al., 2017). This has led to several preclinical investigations into the use of high-frequency bipolar and monopolar burst waveforms that seek to mitigate muscle contractions and/or improve the predictability of the field distribution. While there is a general understanding of the relationship between the duration of constitutive pulses within the burst and the resulting ablation size, little is known about how manipulating the latent periods (i.e., repetition frequency) affects ablation. Moreover, the connection between burst polarity, pulse duration, and these delays remains to be characterized.

In this work, we seek to make progress toward filling this gap in knowledge. We use an *in vitro* three-dimensional culture platform to characterize the electric field required to ablate human brain and liver cancer cells with monopolar and bipolar burst waveforms across a range of constitutive pulse durations and delays. We pair these experiments with mathematical modeling of nerve stimulation thresholds for each waveform. We report trends demonstrating how pulse polarity, constitutive pulse duration, and delays can be tuned to generate different levels of ablation relative to nerve stimulation.

5.2 – Methods

5.2.1 – Cell Culture

Human hepatocellular carcinoma (HepG2, ATCC HB-8065, Manassas, VA) cells were cultured in Eagle's Minimum Essential Medium (EMEM, ATCC) and human glioblastoma (U-251, Sigma-Aldrich 09063001, St. Louis, MO) cells were cultured in Dulbecco's Modified Eagle Medium (DMEM, ATCC); each were supplemented with 10% FBS (Fisher Scientific, Hampton, NH) and 1% penicillin-streptomycin (Fisher Scientific). Cells were incubated at 37°C with 5% CO_2 and subcultured regularly at ~80% confluency.

5.2.2 – Hydrogel Fabrication

Cell-laden collagen hydrogels were constructed as previously described (Arena, Szot, et al., 2012). Briefly, commercial rat tail collagen type I (Corning, Corning, NY) was neutralized with a solution of 10× DMEM (10% total volume, Sigma), 1 N NaOH, (2% collagen volume, Sigma-Aldrich), and 1× culture medium to a final concentration of 5 mg/mL. Cells were detached from flasks with 0.25% trypsin-EDTA (Fisher Scientific) and added to the collagen mixture at a final concentration of 10^6 cells/mL. The solution was thoroughly mixed on ice and dispensed into each well of a 12-well culture plate to achieve a thickness of ~1 mm. Plates were incubated for 20 min at 37°C to polymerize scaffolds. Culture media was then added to each well and plates were incubated overnight prior to treatment.

5.2.3 – Pulsed Electric Field Treatments

Approximately 24 hours after seeding, media was removed from scaffolds. A custom-made ring and pin electrode ($Ø_{pin}$ = 1.85 mm; $Ø_{ring}$ = 18 mm) was inserted into each well (Fig. 1B). Bursts with an amplitude of 500 V were applied with a custom high-voltage generator (VoltMed Inc., Blacksburg, VA). All waveforms were adjusted to achieve 100 µs of energized time, and 100 bursts were delivered to each well at a frequency of 1 burst per second. Warm culture media was replenished immediately after treatment. All experiments were performed within a humidified benchtop incubator maintained at 37°C.

5.2.4 – Confocal Imaging – Live/Dead

Approximately 24 hours after treatment, wells were incubated with a solution containing 22.4 μM propidium iodide (Thermo Fisher, Waltham, MA) and 2.5 μM Calcein AM (Thermo Fisher) in phosphate buffered saline (PBS) for 30 minutes. Wells were then rinsed twice with PBS and imaged with an inverted confocal microscope (DMI 6000B, Leica Microsystems, Wetzlar, Germany) with a 5× objective.

5.2.5 – Lethal Threshold Calculation

Images of each well were imported into ImageJ (NIH, Bethesda, MD). Two diameter measurements (horizontal and vertical) as well as two area measurements were taken and averaged. The average diameter and area were correlated with the electric field distribution to determine the electric field required to achieve the ablated dimension. Calculated electric fields were then averaged to determine the overall lethal electric field threshold (EFT) for a given lesion. Thus, for a given EFT, four measurements were considered, and each waveform was performed a minimum of n=3 times.

5.2.6 – Confocal Imaging – Cellular Morphology

Morphological analysis was performed with the same approach described in **Chapter 3.2.5**. Briefly, after preparing as described above, hydrogels were incubated for 24 hours then fixed with 10% neutral buffered formalin, incubated with 0.5% Triton X-100 for 10 minutes and blocked with 1% bovine serum albumin (BSA) for 60 minutes. Alexa Fluor^{TM} 568 Phalloidin (ThermoFisher Scientific) was used to mark F-actin and DAPI (ThermoFisher Scientific) was used to stain nuclei. Cell morphology was visualized with an inverted confocal microscope (DMI 6000B, Leica Microsystems, Wetzlar, Germany) fitted with a 40× objective.

5.2.7 – Computational Investigation of Nerve Stimulation

We used a spatially extended nonlinear node model to represent exposure of a short segment of a myelinated nerve fiber to an external electric field as previously described (McNeal,

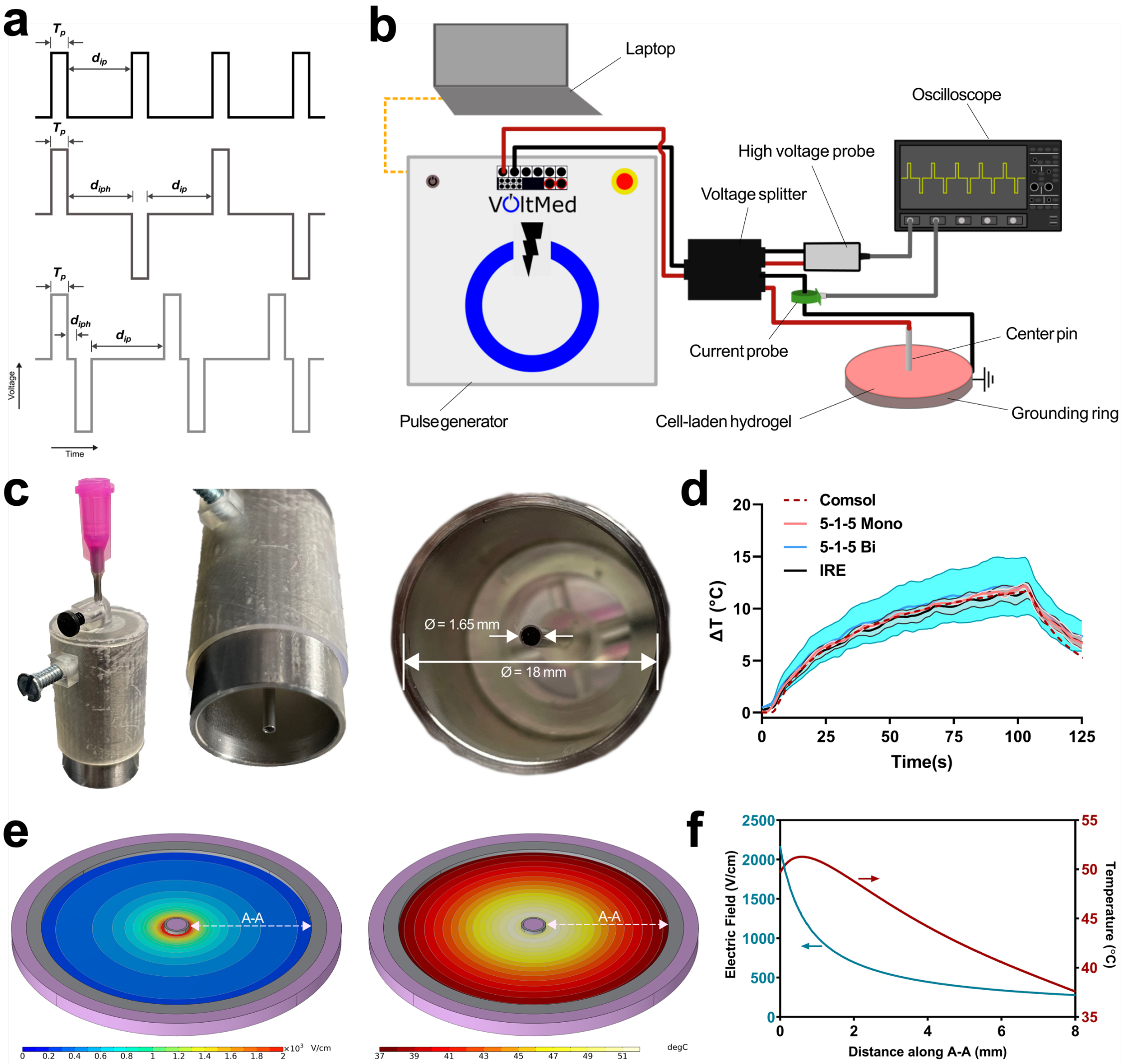

Figure 5.1 – Overview of experimental and numerical approach for determining lethal electric field thresholds. Idealized representations of pulsed voltage waveforms are shown in (a). (b) illustrates the electrical connections and equipment used to treat cell-laden collagen hydrogels with the (c) custom concentric cylinder electrode setup. Representative experimental and numerically computed temperature profiles for different voltage waveforms are shown in (d), establishing model validation. Also shown are the computed (e) electric field and temperature profiles within the hydrogel. The radial dependence of the field (blue) and temperature (red) are also plotted in (f).

1976; Mercadal et al., 2017; Reilly, 1988). Briefly, we assumed the terminus of a 10 μm fiber containing 6 nodes of Ranvier was positioned in parallel to a uniform electric field. Ionic current was carried by fast and persistent sodium channels as well as a slow potassium channel, each of which was based on dynamics of human nerve at 36 °C (McIntyre et al., 2002). A leak current was also considered. The timing characteristics and directionality of the field were controlled by a custom Matlab (Mathworks, Inc., Natick, MA) script with a maximum step size of 10 ns. The system of equations – including the transmembrane potential and rate functions for channel gating – was solved using an implicit Euler technique. For a given waveform, the electric field was serially increased in steps of 0.25% and transmembrane potential of the fiber at each node was monitored until an action potential was observed.

5.2.8 – Statistical Analysis

Details regarding sample size and statistical significance of results are given in each figure and its respective caption. All statistical analyses were performed using Prism version 9 (GraphPad Inc., San Diego, CA). In each figure, experimental data are presented as mean ± SEM. A p value of 0.05 or below was considered statistically significant.

5.3 – Results

5.3.1 – Symmetric delays mediate efficiency of monopolar and bipolar bursts

Representative images of HepG2 cells treated with monopolar and bipolar bursts with different delays can be seen in **Figure 5.2**. Regions of red represent areas of PI uptake, while green regions represent live cells. It can be seen that ablation size increases as the delays are extended within bipolar bursts (top row), but that the opposite occurs when monopolar bursts are used (bottom row).

This result is quantified in terms of the lethal electric field threshold which is detailed comprehensively in **Figure 5.2**. In all cases, pulse duration exhibited a strong effect on lethal EFT. This trend was most obvious within bipolar bursts and was weakest for monopolar bursts with short delays. It can be seen that with shorter pulse durations, EFTs increased for both cell lines when delays were increased within monopolar bursts (**Figure 5.3a-b**). When bipolar bursts were used, EFT varied inversely with interphase/interpulse delay (**Figure 5.3c-d**). This trend was relatively weak for HepG2 cells (**Figure 5.3c**) but was quite apparent within the U251 cell line (**Figure 5.3d**). To quantify the influence of the pulse polarity itself, we calculated the ratio of the bipolar EFT to the monopolar EFT for all pulse width and delay combinations (**Figure 5.3e-f**).

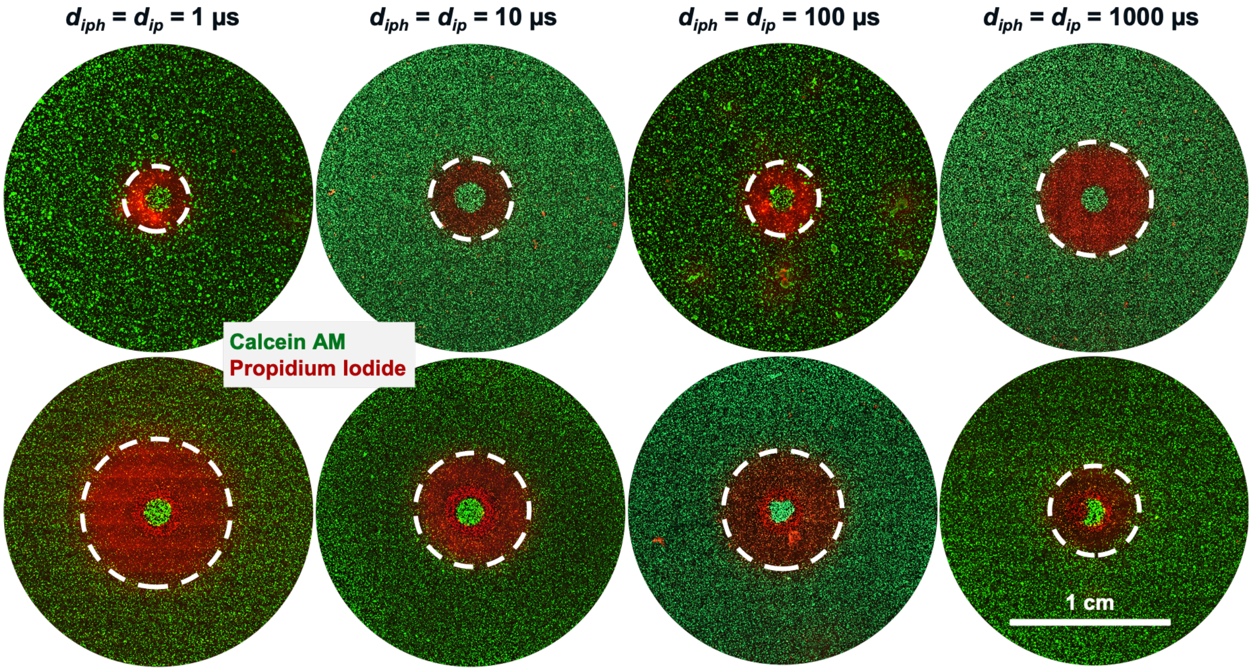

Figure 5.2 – Representative live/dead fluorescent images of ablation regions created with bipolar (top row) and monopolar (bottom row) waveforms in HepG2 hydrogels. In all images, the pulse duration was fixed at 2 µs and cells wells were treated with 100 bursts of a symmetric waveform with the indicated delays and polarity.

With shorter pulse durations and short delays (< ~10 µs), this ratio was heightened to 1.5 or above in both cell lines, with U251 cells exhibiting the highest ratios. Certain bursts in which polarity is alternated required up to a 140% increase in electric field to generate cell death versus their monopolar counterparts. With extended delays of 100 μs or more, the ratio approached unity, meaning that the polarity was no longer playing a role in the lethality of a given waveform. Ratios computed for HepG2 cells were more resistant to waveform modifications (**Figure 5.3e**), whereas ratios for U251 cells were heavily impacted by pulse waveform manipulations (**Figure 5.3f**).

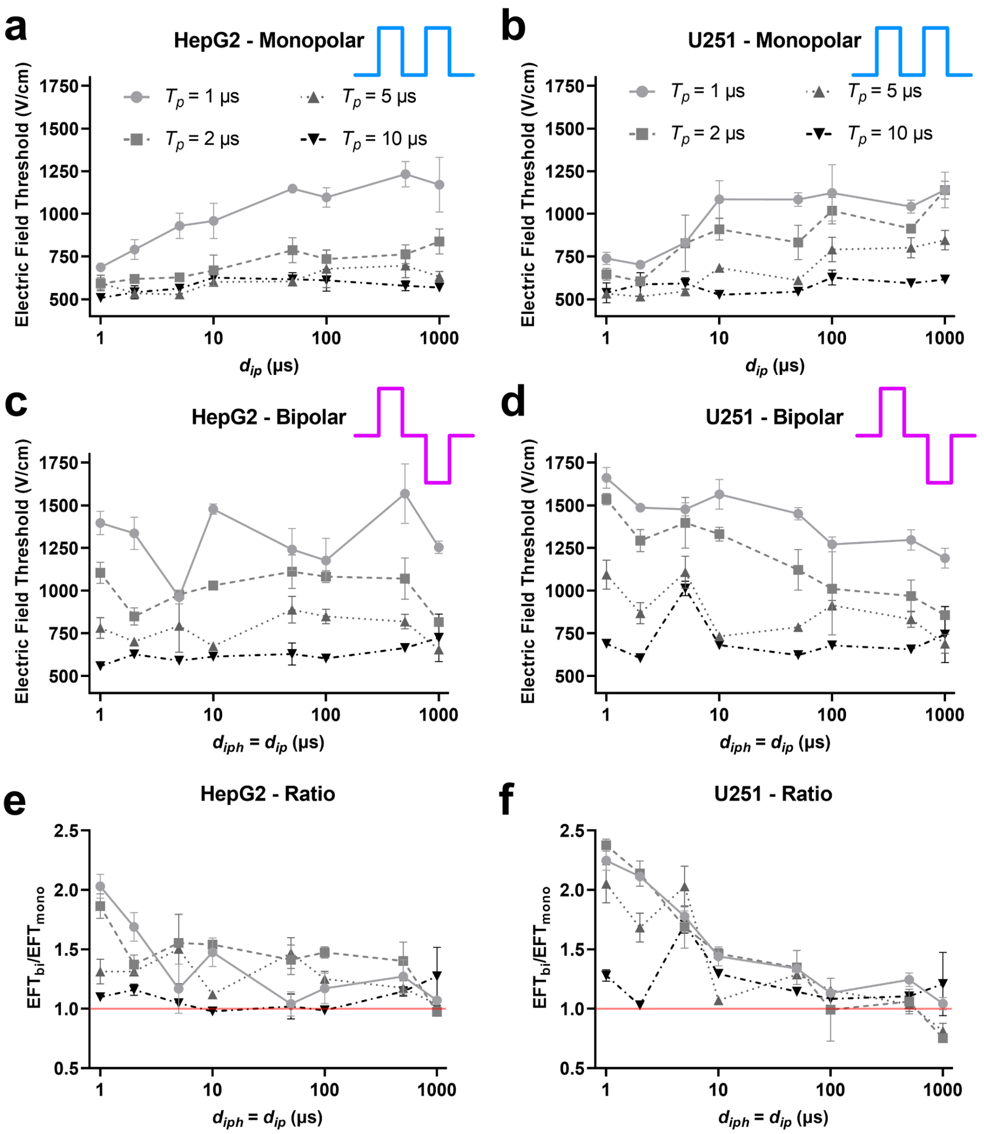

Figure 5.3 – Latent periods modulate lethality of both monopolar and bipolar bursts. Two cell lines were exposed to pulsed field treatment with (a-b) monopolar and (c-d) bipolar burst waveforms containing 100 μs of energized time each. Constitutive pulse widths of 1 μs, 2 μs, 5 μs, and 10 μs were used. Within monopolar bursts, the interpulse delay was varied from 1 μs to 1,000 μs. Within bipolar bursts, the interphase and interpulse delay were varied symmetrically from 1 μs to 1,000 μs. We also report the (e-f) ratio of the bipolar to monopolar lethal threshold for waveforms with identical time characteristics.

5.3.2 – *Effects of burst parameter choices on computed nerve stimulation thresholds*

For all the waveforms tested *in vitro*, we also computed the theoretical threshold electric field necessary to elicit an action potential in a myelinated human nerve. These thresholds correlate with the likelihood of different waveforms to cause pain and/or muscle contractions. Model-estimated thresholds are shown in **Figure 5.4**. Within monopolar bursts, pulse duration had almost no effect on nerve stimulation threshold until the interpulse delay was extended to ~50 µs or beyond, whereafter significant divergence was observed for waveforms with different constitutive pulse durations (**Figure 5.4a**). In contrast, for bipolar waveforms, simulated thresholds exhibited a strong dependence on pulse duration, which can be seen by the vertical distance between each curve in **Figure 5.4b**. The effect of increasing the delay within bipolar bursts was not immediately intuitive. Stimulation thresholds fell initially until a delay of ~200 µs was reached. After a small plateau up to ~400 µs, thresholds increased and plateaued once again at a delay of ~1,000 µs, reaching ~80 % of their maximum value. Finally, we computed the ratio of the thresholds from a given bipolar burst to the threshold of a monopolar burst with the same timing characteristics (**Figure 5.4c**). Threshold ratios were maximized with pulse durations and short delays. For instance, a bipolar burst with a 1 µs constitutive pulse duration and 1 µs delays has a threshold 86 times higher than a monopolar burst with the same pulse width and delays. Increasing only the pulse duration to 2 µs or 5 µs, the ratio falls to 51.4 and 23.8, respectively. As the delay increased, threshold ratios dropped exponentially, reaching a plateau with a delay of ~100 µs.

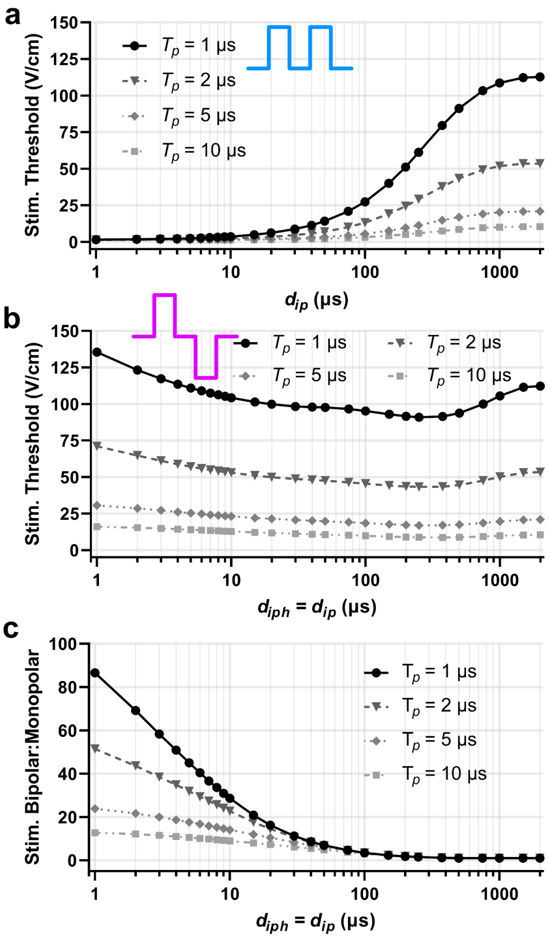

Figure 5.4 – Nerve stimulation thresholds for monopolar and bipolar burst waveforms. Threshold electric fields needed to generate an action potential in the SENN model were computed for (a) monopolar and (b) bipolar bursts with different pulse durations and delays. The (c) ratio of the bipolar stimulation threshold to monopolar threshold is also shown.

5.3.3 – Influence of polarity, constitutive pulse duration, and delays on ablation relative to nerve stimulation

Calculated lethal EFTs and corresponding nerve stimulation thresholds were used to evaluate the extent of ablation relative to nerve stimulation likely to arise from each waveform (**Figure 5.5**). Overall, E_{lethal}:E_{stim} ratios were much higher for monopolar bursts (**Figure 5.5a**) as compared to bipolar bursts (**Figure 5.5c-d**). With monopolar bursts, ratios were highest when delays were short, and with these short delays, pulse duration was relatively unimportant, especially for HepG2 cells (**Figure 5.5a**). With moderate delays (10-100 µs), the effect of pulse duration became more apparent, with shorter pulses exhibiting lower thresholds. With delays >

100 μs, ratios were minimized and converged once again. Ratios computed for bipolar bursts exhibited a relatively straightforward trend. Shorter pulse duration consistently resulted in lower thresholds. The influence of the delays was pronounced for bursts with longer pulse durations and extending the delay resulted in a relatively linear increase in the ratio.

5.4 – Discussion

The current study was performed to comprehensively characterize the effect of burst waveform modifications on lethality and nerve stimulation with pulsed electric fields. To our knowledge, this is the first investigation directly comparing the advantages and drawbacks of

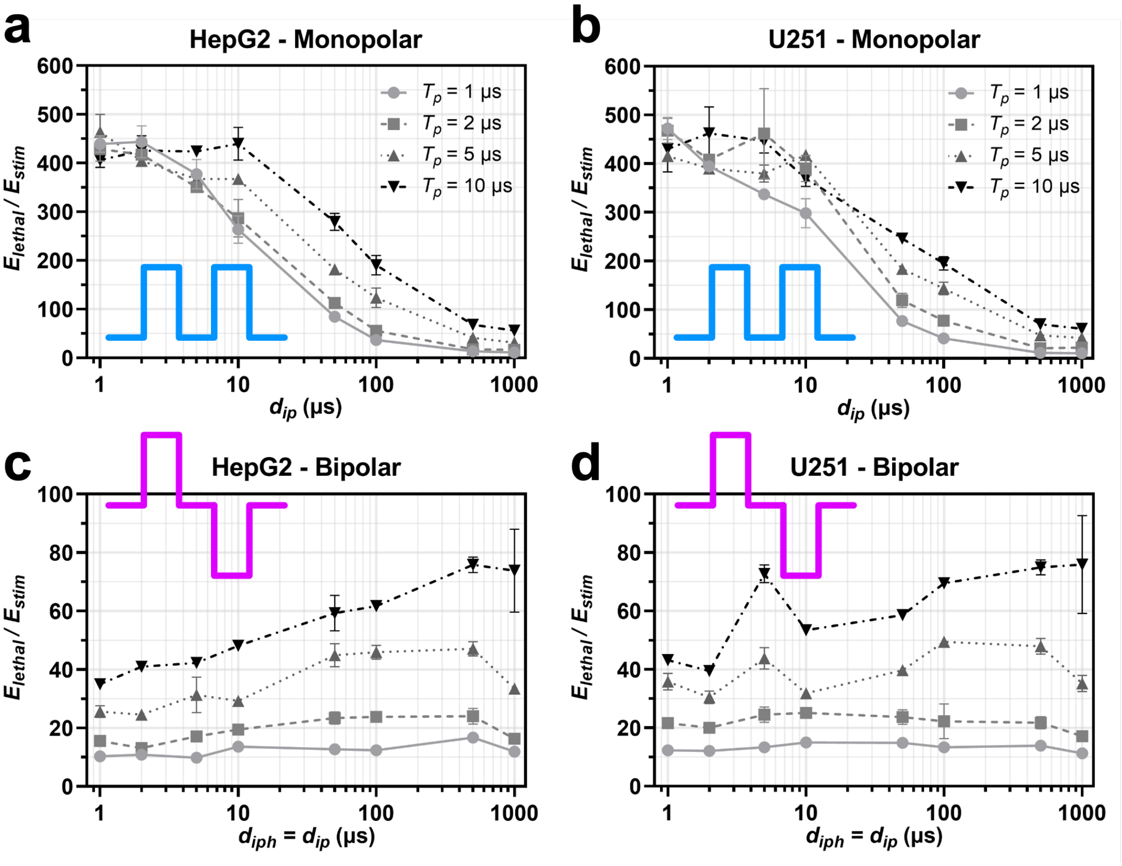

Figure 5.5 – Lethal electric field thresholds (E_{lethal}) normalized to stimulation thresholds (E_{stim}) for all waveforms under consideration. A lower threshold indicates a stronger ability to generate ablation without contraction, whereas a higher threshold indicates more stimulation will occur with less cellular ablation. Ratios were computed for (a-b) monopolar and (c-d) bipolar waveforms in both (a, c) HepG2 and (b, d) U251 cells. Note different y-axis scales for (a-b) versus (c-d).

manipulating pulse polarity and delays across a broad range to modulate cell death and/or stimulation.

Long (≥100 μs) monopolar pulses have been conventionally used for decades in the context of electroporation for nearly every application. And while monopolar burst waveforms are commonly used with nanosecond pulses (Sözer et al., 2021), little attention has been given to the use of μs-duration monopolar burst waveforms. In the few studies that have examined these bursts, only very short pulse durations and delays have been employed (Gudvangen et al., 2022; Yao, Zhao, Mi, et al., 2017). In this work, we show that with proper tuning of pulse duration and delays, monopolar bursts can achieve E_{lethal}:E_{stim} ratios on par with those typical of bipolar bursts.

It is typically assumed that bipolar bursts are inherently less efficient in terms of cellular ablation than their monopolar counterparts. However, our data demonstrate that the relative efficiency with different polarities is nuanced and depends heavily on both the pulse duration and delays. This is illustrated clearly in terms of the computed EFT ratios which are presented in **Figure 5.3e-f**. Here, it can be seen that with short pulse durations and delays (i.e., high duty cycles), bipolar bursts are significantly less lethal than monopolar bursts. The obvious explanation for this difference is that the transmembrane potential continues to rise with each pulse within a monopolar burst given that the delay between subsequent pulses is similar to or below the membrane charging constant (Sözer et al., 2021). In contrast, within a bipolar burst, the alternating polarity not only prevents the TMP from continuously increasing but can actively force the TMP to decline rapidly (Arena, Sano, Rossmeisl, et al., 2011). In contrast, with long delays, EFTs were similar for both polarities even with 1 μs pulse durations. It is also worth highlighting that with a constitutive pulse duration of 10 μs, polarity was almost completely inconsequential even with 1 μs delays.

The lethal EFT data collected in this study presented significant, but speculative, insight into the mechanics of electroporation and cell death. For most mammalian cell lines, the membrane charging constant is on the order of 1 μs, and it has been empirically determined that delays around 5 μs are long enough to mitigate the forced membrane discharge within bipolar bursts described above (Polajžer et al., 2020). However, we found that EFTs were strongly dependent upon delay, and trends were relatively consistent across the entire range of delays considered, especially when shorter pulses were used (**Figure 5.3**). Theoretically, once the delay is beyond 5-10 μs, it should cease to influence the development of the transmembrane potential (TMP). This leads us to speculate that the changing EFTs even with delays of 100 μs or more can be ascribed to underlying dynamics of pore formation, coalescence, and resealing. It is also worth mentioning that most similar studies have done so using cell suspensions, in which cells are uniformly round and somewhat compact, which lowers their effective charging constant and can "shield" them from TMP development.

We chose to expose two different cell lines to each of the waveforms under study. The primary reason for this was to understand whether cells with different characteristic morphologies reacted differently to waveform parameter manipulations. **Figure 5.6** shows representative 2D projections of Z-stack collected on both cell lines in 3-dimensional culture. It can be seen that the HepG2 cells are consistently small and round with relatively large nuclei (**Figure 5.6a-d**). U251 cells exhibited notable heterogeneity. They were often elongated and sometimes multinucleated, but relative nuclear volume was qualitatively low compared to HepG2 cells (**Figure 5.6e-h**). The increased size and elongation of U251 cells likely means these cells require longer time periods to charge and discharge relative to HepG2 cells. This could explain why pulse duration and delay both seemed to have a heightened effect in U251s.

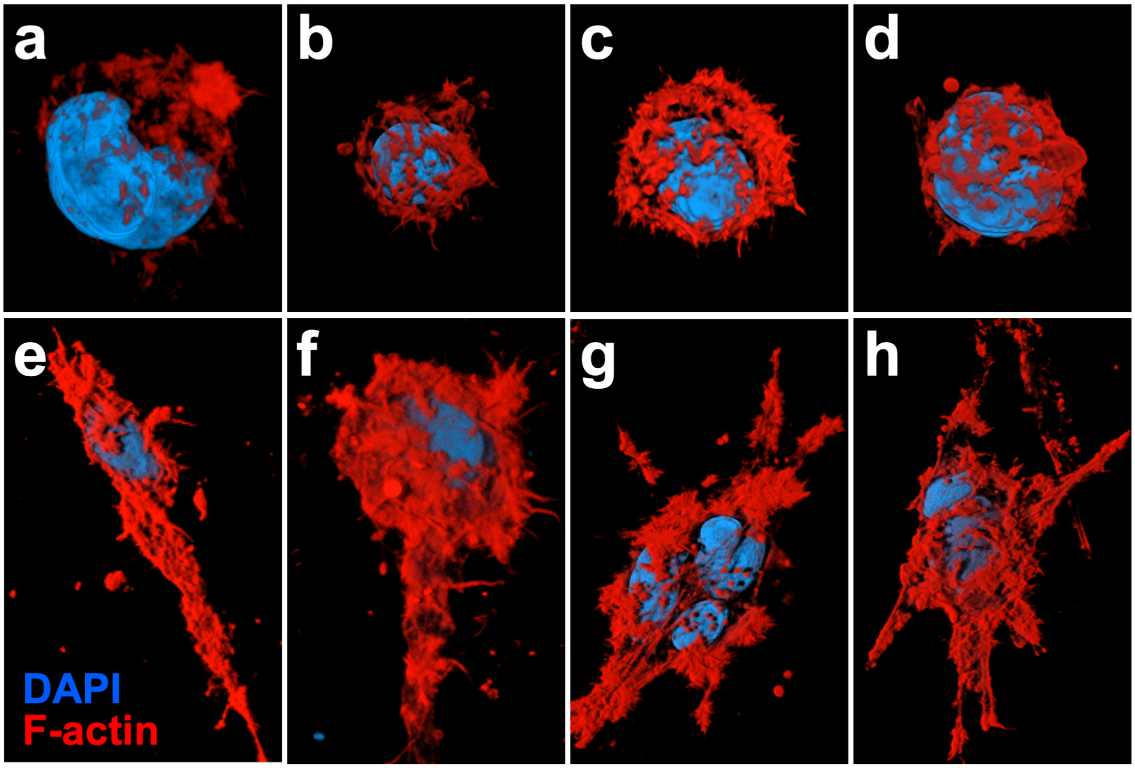

Figure 5.6 – Representative confocal images of cells in 3-dimensional culture. Each panel shows a 2D projection of serial confocal images in a Z-stack containing a single cell. All waveforms were tested on both (a-d) human hepatocellular carcinoma [HepG2] cells as well as (e-h) human malignant glioma [U251] cells. Each cell line clearly exhibits unique morphological characteristics – HepG2 cells were consistently spherical and similar in size, while U251 cells exhibited significant heterogeneity. In general, U251 cells were elongated and, in many cases, multinucleated.

5.5 – *Conclusion*

Burst waveforms have become a popular option for generation of bioeffects with pulsed electric fields. Depending upon the application, the desired amount of targeted cellular ablation relative to nerve stimulation can differ greatly. In this work, we performed a parametric analysis to study the effect of burst polarity, constitutive pulse duration, and delays (i.e., duty cycle) within burst waveforms for therapeutic applications. We demonstrate that each parameter plays an important role in the ability of burst waveforms to ablate human brain and liver cancer cells. We also show computationally that nerve stimulation can vary significantly within both bipolar and monopolar bursts, and that there are certain parameter choices with either polarity that result in very little or significant stimulation. The work presented herein provides a framework by which to design burst waveforms for different therapeutic applications such as irreversible electroporation, reversible electroporation, and peripheral nerve stimulation.

6 – A Comparative Modeling Study of Engineered Thermal Mitigation Strategies in Electroporation-Based Therapies[4]

6.1 – Introduction

Irreversible electroporation (IRE), or non-thermal pulsed field ablation (PFA), is a focal tissue ablation modality used to treat solid tumors and arrhythmogenic cardiac tissue (Geboers et al., 2020; Maor et al., 2019). IRE is performed by applying a series of short (1-100 μs), high intensity (1-3 kV/cm) electrical pulses to elevate the transmembrane potential (TMP) of cells within the targeted region beyond a threshold value (~1 V). Once this threshold is exceeded, nanoscale defects – or "pores" – appear in the cellular membrane (Weaver et al., 2012; Yarmush et al., 2014a). When several pulses of sufficient magnitude are applied, formation of large, long-lived pores leads to disruption of cellular homeostasis, eventually causing death through various pathways (Brock et al., 2020; Geboers et al., 2020; Napotnik et al., 2021). Due to cell death relying solely on the induced TMP, IRE is considered a non-thermal ablation modality; thus, it can be employed in various scenarios where thermal ablation is contraindicated (W. Li et al., 2011; Maor et al., 2007). This includes deep-seated tumors situated near vascular and/or neural structures (Narayanan et al., 2014; Vogel et al., 2016), as well as sensitive myocardial tissue in which thermal ablation is associated with numerous side effects (Muthalaly et al., 2018).

In oncology, IRE is administered through two (or more) needle electrodes inserted directly into the targeted region containing the tumor prior to pulse delivery. In select instances, a single-insertion bipolar probe (two electrodes integrated within the same cylindrical shaft) is used (R. C. G. Martin et al., 2015; Narayanan et al., 2012). For each treatment, the type and number of electrodes, as well as their spacing and exposure, are carefully selected to ensure the targeted

---

[4] Chapter 6 is adapted and reprinted with kind permission from the American Society of Mechanical Engineers. © 2022 by ASME. Aycock, K. N., Campelo, S. N., & Davalos, R. V. (2022). A Comparative Modeling Study of Thermal Mitigation Strategies in Irreversible Electroporation Treatments. *Journal of Heat Transfer*, *144*(3), 1–10.

region is exposed to an electric field of sufficient strength to induce cell death. Although IRE relies on a non-thermal mechanism, ablating the desired treatment region with zero thermal damage can sometimes be challenging (**Figure 6.1**).

The first modeling study on IRE showed that ablation and thermal effects can be mutually exclusive phenomena within certain constraints, and although countless follow-up studies have determined optimal parameters for ablation in different settings, undesired side effects due to temperature development remain the foremost factor limiting the size of IRE ablations (Cindric et al., 2021; Davalos et al., 2005a; Garcia et al., 2011). Clinically, differences in institutional pulse administration protocols and clinician experience can generate varying degrees of thermal tissue injury, which are likely somewhat responsible for the range of complication rates and oncological outcomes reported in the literature (Agnass et al., 2020; Ansari et al., 2017; R. C. G. Martin et al., 2015; Philips et al., 2013). Even with moderate voltages, the steep potential gradient at the electrode boundaries can produce relatively high electric fields (and thus, temperatures), leading

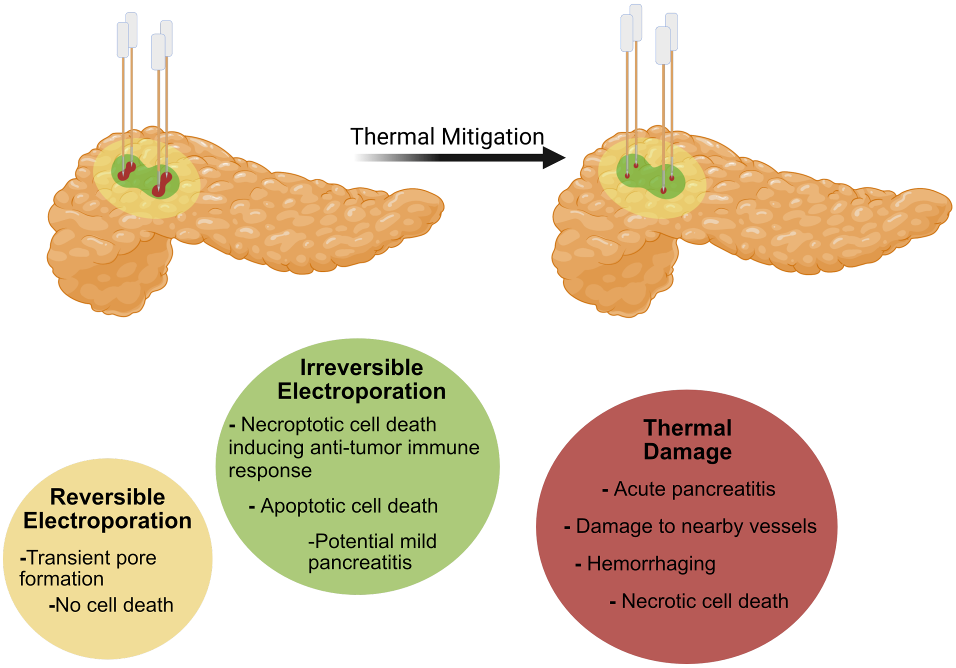

Figure 6.1 – If not actively considered in treatment planning and delivery, irreversible electroporation can result in thermal damage, which can cause undesirable side effects. The use of thermal mitigation strategies reduces the likelihood of thermal damage, minimizing the risk of adverse effects and improving control over expected cell death mechanisms.

to effects such as tissue coagulation, denaturation of extracellular proteins, and hemorrhage (Dunki-Jacobs et al., 2014). In rare cases, significant increases in electrical current due to heating can pose the risk of electrical arcing (Buist et al., 2021; Wandel et al., 2016).

Despite these concerns, existing clinical pulsing protocols do not actively consider temperature rise during IRE procedures. In the absence of real-time feedback during pulse delivery, the risk of thermal damage can vary widely between patients depending upon the tissue being treated, electrode configuration and pulsing paradigm, as well as patient-specific tissue properties (O'Brien, Lorenzo, et al., 2019; Ren et al., 2019). For example, a recent study estimated that approximately 30% of the average IRE ablation volume experiences mild hyperthermia (40 - 50 °C), with 5% being exposed to temperatures in excess of 50 °C (Agnass et al., 2020). As clinicians and researchers continually seek to expand ablation volumes toward treating larger tumors, maintaining the non-thermal aspects of IRE will be increasingly difficult (Yang et al., 2018). Additionally, recent work suggests that even when thermal damage is unlikely, reducing mild-to-moderate thermal effects could promote better immune activation (Brock et al., 2020; Shao et al., 2019b), which could enhance long-term treatment efficacy and lead to improved patient outcomes (Beitel-White et al., 2019; J. Zhao et al., 2019). Thus, solutions to mitigate and/or control thermal effects in the vicinity of the electrodes are paramount to optimizing IRE and other pulsed electric field (PEF)-based ablation modalities for more widespread clinical adoption.

Several approaches to limit temperature rise during PEF therapies – termed thermal mitigation (TM) strategies – have been considered. These include innovative probe designs that integrate heat-dissipating technologies as well as pulse paradigm adjustments that allow tissue perfusion to disperse heat between consecutive pulses. Prior work has examined the feasibility of actively perfusing a cooling solution through a bipolar probe (O'Brien et al., 2018), integrating phase change materials (PCMs) (Arena et al., 2013; Arena, Mahajan, et al., 2012) or an endothermic reaction (Y. Zhao & Davalos, 2020) within the core of monopolar probes, and distributing applied energy into "cycles" where a subset of pulses is delivered across each electrode pair repeatedly until the total number of pulses is reached (O'Brien, Lorenzo, et al., 2019). A summary of these strategies, along with advantages and drawbacks of each, can be found in **Table 6.1**.

Notably, each of these prior investigations was performed independently, so it remains relatively unknown how different TM strategies compare to one another. In this study, we numerically compare the utility of two engineered TM strategies that have been introduced and examined experimentally, as these are the technologies most likely to be adopted in medical practice. To build a more comprehensive understanding of how these TM technologies may perform in clinical scenarios, we determine treatment conditions where thermal mitigation approaches are necessary, then assess design and performance characteristics that may affect the efficacy of either technology.

Table 6.1 – Summary of previously introduced thermal mitigation strategies

Modality	*Config.*	*Mode of action*	*Advantages*	*Drawbacks*	*Ref.*
Active Cooling (AC)	Bipolar	Applicator is cooled internally with water perfusion	- Efficient reduction of tissue temperature	- Cumbersome electrode - Requires external equipment - May require more fixation devices	a
Phase Change Material (PCM)	Monopolar	Heat absorbed due to phase change of embedded material	- Moderate reduction in temperature - No change to clinical procedure	- Limited by choice of PCM - Finite duration in which heat is absorbed	b, c
Cycled Pulsing	Monopolar	Reduced number of contiguous pulses across a single electrode pair	- Simple change to pulsing paradigm that can limit temperature rise due to cumulative pulses	- Only applicable to multi-electrode experiments -Potential increase in procedure duration	d
Endothermic Reaction	Monopolar	Heat absorbed due to endothermic processes	- No changes to clinical procedure - Efficient reduction in temperature rise for a short time	- Not reduced to practice - Potentially complicated to design/implement	e

a – (O'Brien et al., 2019); b – (Arena et al., 2012); c – (Arena et al., 2013); d – (O'Brien et al., 2019b); e – (Zhao et al., 2020)

6.2 – Methods

6.2.1 – General Model Construction

Numerical simulations were performed in COMSOL Multiphysics 5.6 (Comsol Inc., Stockholm, Sweden) to determine the electric field and temperature distributions arising from a clinical procedure performed with various electrode types. For simulations considering a single bipolar probe, a 2D axisymmetric model was used to reduce computation time. For all other simulations, a 3D model was used. In all cases, pancreatic tissue was represented by an ellipsoid with dimensions of 15 cm x 15 cm x 25 cm. These dimensions were chosen to prevent boundary effects while also allowing for an identical modeling domain between 2D axisymmetric and 3D simulations. Electrical field distribution and thermal effects were computed using common techniques (Davalos & Rubinsky, 2008; Garcia et al., 2014). Briefly, the electric potential distribution at the end of a given pulse was calculated using a modified Laplace equation under the electro-quasistatic approximation (equation (6.1)), and the resulting electric field distribution with equation (6.2):

$$-\nabla \cdot (\sigma(|E|, T)\nabla\Phi) = 0 \tag{6.1}$$

$$\vec{E} = -\nabla\Phi \tag{6.2}$$

where σ is the electrical conductivity which depends on both the local field magnitude $|E|$ and temperature T, and Φ is the local electric potential. Equation (6.1) is valid given that the pulse width is much longer than the charging time constant of cell membranes (~1 μs). One electrode boundary was set to $\Phi = V_0$ and the other set to $\Phi = 0$. External boundaries were considered insulating to provide a worst-case approximation to thermal effects. After computing the field distribution, tissue temperature was calculated using the traditional Pennes bioheat equation with the addition of a Joule heating term Q_J:

$$\rho c_p \frac{\partial T}{\partial t} = \nabla \cdot (k(T)\nabla T) + \rho_b c_{p,b} \omega_b (T_b - T) + Q_J \quad (6.3)$$

Here, ρ and c_p are the tissue density and heat capacity, respectively, and ρ_b and $c_{p,b}$ are the same for blood; ω_b is the blood perfusion rate; T_b is the temperature of blood (37 °C); tissue thermal conductivity, $k(T)$, was taken to have a linear dependence on local temperature and computed as:

$$k(T) = a \cdot T + b \quad (6.4)$$

where a and b are empirically-determined fitting coefficients (Mohammadi et al., 2021). Initially, all domains were set to physiologic temperature (37 °C), and all external boundaries were considered adiabatic unless otherwise indicated. The Joule heating term was calculated in all domains as:

$$Q_J = \sigma|E|^2 \quad (6.5)$$

and was scaled by the duty cycle – the product of pulse duration and pulse frequency – as previously described (Garcia et al., 2012). Electroporation results in a field-dependent increase in electrical conductivity due to intra- and extracellular exchange of ions, and thermal effects cause further increases at a rate of ~1-2 %/°C. These effects are captured through the following expression:

$$\sigma(|E|,T) = \left[\sigma_0 + \frac{\sigma_f - \sigma_0}{1 + e^{-A\cdot(|E|-E_{del})}}\right]\left(1 + \alpha(T - T_0)\right) \quad (6.6)$$

where σ_0 is the baseline electrical conductivity, σ_f is the maximum (electroporated) conductivity, A is a fitting parameter determining how quickly the conductivity transitions from its native state to fully electroporated, E_{del} is the midpoint of the transition, α is the thermal coefficient of conductivity, and T_0 is the baseline temperature at which σ_0 was determined.

Finally, thermal damage in the tissue domain was calculated with an Arrhenius-type dose equation based on the temperature over time at each point:

$$\Omega = \int \xi e^{-E_a/(R \cdot T(t))}\, dt \tag{6.7}$$

where Ω is the Arrhenius damage integral, ξ is the frequency factor, E_a is the activation energy, R is the gas constant, and $T(t)$ is the temperature at time t. Tissue exposed to Ω values of 0.53 or greater was assumed to be thermally damaged, as this has been empirically estimated as the onset of irreversible thermal damage in blood-perfused skin (Diller & Hayes, 1983).

Unless otherwise indicated, tissue was modeled as pancreas and assigned previously published dynamic electrical conductivity parameters (Beitel-White et al., 2020). Properties assigned to each domain can be found in **Table 6.2**.

6.2.2 – Phase Change Material

Latent heat storage systems rely on PCMs to store thermal energy for various applications. Due to their high latent heat of fusion, PCMs absorb energy as they transition from solid (*s*) to liquid (*l*) while maintaining a nearly constant temperature. In other words, when heated to their melting point, PCMs require further energy to change phases, and until this phase transition is complete, temperature remains stagnant.

Mathematically, heat absorption during the phase change was modeled with the effective heat capacity $\left(c_{p,eq}\right)$ method by including the latent heat of fusion (λ) in the volume average of the specific heat capacity at constant pressure (Arena et al., 2013):

$$c_{p,eq} = \Theta\left(c_{p,s} + \lambda\Pi\right) + (1 - \Theta)\left(c_{p,l} + \lambda\Pi\right) \tag{6.8}$$

where Θ is the volume fraction of solid PCM, computed as:

$$\Theta = 1 - flc2hs[(T - T_m), T_R] \tag{6.9}$$

in which $flc2hs$ is a Heaviside function centered about the melting temperature (T_M) and stepping from 1 to 0 over the transition range T_R. This function approximates the solid-to-liquid *(s-l)* transition as a smooth step with a continuous second derivative, reducing computational burden associated with true logical steps. In equation (6.8), Π is a normalized pulse occurring about T_M, calculated by taking the derivative of Θ with respect to T. In the PCM domain, the temperature distribution was calculated in a similar manner to that of the tissue domain but without perfusion (equation (6.10)), and by using the volume averages of either phase to calculate density (ρ_{eq}) and thermal conductivity (k_{eq}):

$$\left(\rho c_p\right)_{eq}\frac{\partial T}{\partial t} = \nabla\cdot\left(k_{eq}\nabla T\right) + Q_J \tag{6.10}$$

$$\rho_{eq} = \Theta\rho_s + (1-\Theta)\rho_l \tag{6.11}$$

$$k_{eq} = \Theta k_s + (1-\Theta)k_l \tag{6.12}$$

Unless explicitly stated, material properties of the PCM were taken from (Arena, Mahajan, et al., 2012) and are listed in **Table 6.3**.

6.2.3 – Active Cooling

Active cooling is a technology commonly integrated within the core of delivery devices used for thermal ablation to limit tissue charring immediately adjacent to the probe. The core of the device contains two concentric cylinders such that fluid flows in through the innermost cylinder before exiting via the outer cylinder (**Figure 6.4**). This allows for convective transfer of thermal energy from adjacent tissue to the perfusate, limiting temperature rise near the probe edge.

From a computational perspective, the core of the probe was taken to be hollow, and a convective heat flux was assigned to the perfusion channel boundary within the probe:

$$-k\cdot\nabla T = h\cdot(T - T_{ext}) \tag{6.13}$$

where h is the heat transfer coefficient, T is the electrode temperature at the boundary, and T_{ext} is the perfusate temperature. The convective heat transfer coefficient was computed as previously described and was found to be similar to values reported in prior works with comparable channel geometries and flow characteristics (D. Liu & Yu, 2010; O'brien, 2019). Briefly, the user-defined volumetric flow rate, along with the diameter (D) of the perfusion inlet, was used to compute the fluid velocity within the electrode shaft $\left(V = {}^{Q}/_{A}\right)$. Next, assuming material properties of water, Reynolds (Re) and Prandtl (Pr) number were computed (equations (6.14)-(6.15)). Nusselt number (Nu) for laminar flow within a pipe (Re < 2100) was then calculated using equation (6.16), and from this h was determined (equation (6.17)).

Table 6.2 – Material properties used in each modeling domain for solid-core electrodes

Material	*Symbol*	*Description*	*Value*	*Units*	*Ref.*
Stainless Steel					
	ρ	Mass density	7900	$\mathrm{kg\,m^{-3}}$	(O'Brien et al., 2019)
	σ	Electrical conductivity	2.22×10^{6}	$\mathrm{S\,m^{-1}}$	(O'Brien et al., 2019)
	k	Thermal conductivity	15	$\mathrm{W\,m^{-1}\,K^{-1}}$	(O'Brien et al., 2019)
	c_p	Heat capacity	500	$\mathrm{J\,kg^{-1}\,K^{-1}}$	(O'Brien et al., 2019)
Insulation					
	ρ	Mass density	2329	$\mathrm{kg\,m^{-3}}$	(O'Brien et al., 2019)
	σ	Electrical conductivity	1×10^{-12}	$\mathrm{S\,m^{-1}}$	(O'Brien et al., 2019)
	k	Thermal conductivity	0.2	$\mathrm{W\,m^{-1}\,K^{-1}}$	(Ngo et al., 2016)
	c_p	Heat capacity	700	$\mathrm{J\,kg^{-1}\,K^{-1}}$	(O'Brien et al., 2019)
Pancreatic Tissue					
	ρ	Mass density	1087	$\mathrm{kg\,m^{-3}}$	(Hasgall et al., 2018)
	σ_0	Baseline electrical conductivity	0.118	$\mathrm{S\,m^{-1}}$	(Beitel-White et al., 2020)
	σ_f	Final electrical conductivity	0.268	$\mathrm{S\,m^{-1}}$	(Beitel-White et al., 2020)
	A	Fitting parameter	2.5×10^{-3}	$\mathrm{cm\,V^{-1}}$	(Beitel-White et al., 2020)
	E_{del}	Transition zone midpoint	1738	$\mathrm{V\,cm^{-1}}$	(Beitel-White et al., 2020)
	α	Conductivity thermal coefficient	0.02	$\mathrm{{}^{\circ}C^{-1}}$	(Beitel-White et al., 2020)
	a	Linear fitting parameter	5.7×10^{-4}	$\mathrm{W\,m^{-1}\,K^{-2}}$	(Mohammadi et al., 2021)
	b	Baseline thermal conductivity	0.506	$\mathrm{W\,m^{-1}\,K^{-1}}$	(Mohammadi et al., 2021)
	c_p	Heat capacity	3164	$\mathrm{J\,kg^{-1}\,K^{-1}}$	(Hasgall et al., 2018)
	ω_b	Average blood perfusion rate	1.39×10^{-2}	$\mathrm{s^{-1}}$	(Hasgall et al., 2018)
	ρ_b	Blood density	1050	$\mathrm{kg\,m^{-3}}$	(Hasgall et al., 2018)
	$c_{p,b}$	Blood heat capacity	3617	$\mathrm{J\,kg^{-1}\,K^{-1}}$	(Hasgall et al., 2018)

$$Re = \frac{\rho \cdot V \cdot D}{\mu} \tag{6.14}$$

$$Pr = \frac{c_p \cdot \mu}{k} \tag{6.15}$$

$$Nu = 1.86 \cdot Re^{1/3} \cdot Pr^{1/3} \cdot \left(\frac{D}{L}\right)^{1/3} \left(\frac{\mu_b}{\mu_w}\right)^{0.14} \tag{6.16}$$

$$h = \frac{Nu \cdot k}{D} \tag{6.17}$$

In the above equations, $\rho, \mu, c_p,$ and k are the density, dynamic viscosity, heat capacity, and thermal conductivity of water, respectively; L is the length of the probe, and μ_b and μ_w are the bulk and wall viscosity of the perfusate. In the present work, μ_b/μ_w was assumed to be unity given the relatively low temperatures involved. Perfusate characteristics are given in **Table 6.3**.

Table 6.3 – Material properties used in each modeling domain for solid-core electrodes

Strategy	*Symbol*	*Description*	*Value*	*Units*	*Ref.*
Phase Change Material					
	ρ	Mass density	1520/1450	$\mathrm{kg\,m^{-3}}$	(Arena et al., 2012)
	σ	Electrical conductivity	1.0/1.0	$\mathrm{S\,m^{-1}}$	(Arena et al., 2012)
	k	Thermal conductivity	1/0.6	$\mathrm{W\,m^{-1}\,K^{-1}}$	(Arena et al., 2012)
	c_p	Heat capacity	1960/3430	$\mathrm{J\,kg^{-1}\,K^{-1}}$	(Arena et al., 2012)
	λ	Mass density	266	$\mathrm{kJ\,kg^{-1}}$	(Arena et al., 2012)
	T_m	Electrical conductivity	43	℃	–
	dT	Thermal conductivity	2	℃	–
Active Cooling					
	h	Mass density	0.381	$\mathrm{W\,cm^{-2}\,K^{-1}}$	(Liu & Yu, 2010)
	T_{ext}	Blood heat capacity	37	℃	–

6.2.4 – Modeling Approach

In both models a voltage-to-distance ratio of 1500 V/cm was applied across either the bipolar or monopolar configuration (**Figure 6.4**). Unless otherwise specified, simulated treatments consisted of 100 pulses, each with a duration of 100 µs, delivered at a rate of 1 pulse per second. Except where explicitly noted, probes were modeled after existing clinical devices (Jourabchi et al., 2014). The bipolar probe was assigned a diameter of 1.65 mm, a wall thickness of 0.2 mm, an electrode exposure of 7 mm (each), and an insulation height of 8 mm. Monopolar probes were given the same diameter and wall thick – ness, but the exposure was set to 1 mm to coincide with demarcations on commercially available devices.

First, clinically relevant variables expected to impact temperature rise were swept to determine the performance of different integrated TM technologies under these conditions. To illustrate this, pulse rate was selected, as it fluctuates from patient to patient depending on their heart rate and plays a major role in temperature development. Next, geometric parameters were assessed to determine impact of probe geometry on performance. Finally, we parametrically studied the effects of different PCM material properties and active cooling flow characteristics.

Initially, the mesh was refined until less than a 1% difference in electric field distribution along the x-axis was achieved, which resulted in COMSOL's default "extra fine" meshing option. All models were computed on a Dell Optiplex 7071 with 8 cores, an Intel Core i9 processor, and 32 GB of RAM. Bipolar models (2D axisymmetric) solved in ~ 2.5 minutes while dual monopolar geometries (3D) required ~ 250 minutes to solve.

6.2.5 – *Model Validation*

Prior to performing the current study, phase change models were validated by reproducing the modeling results of Arena et al., 2012. Model construction was performed using the previously described methodology, with all parameters and material properties taken from (Arena, Mahajan,

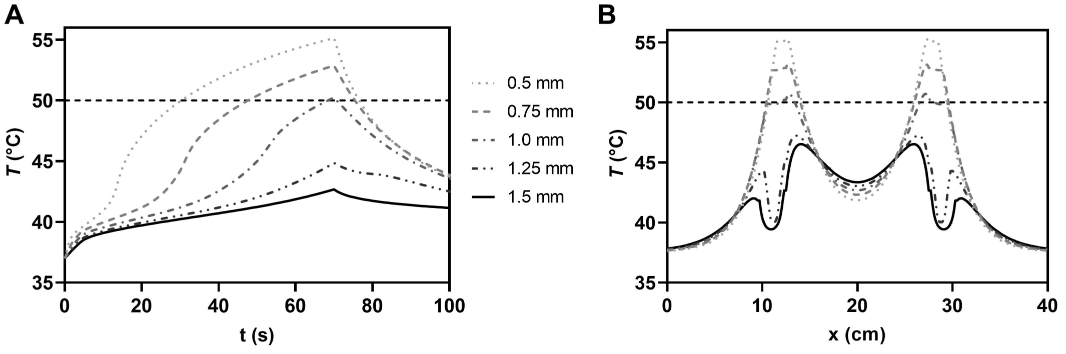

Figure 6.2 – Previous PCM core modeling results were recreated to validate the current work prior to predictive modeling. Temperature versus time (a) is shown for a two-needle model of PCM core electrodes during administration of 70 pulses, each with 90 µs duration applied at 2000 V/cm. Also shown is the (b) temperature along the x-axis through the center of the monopolar electrodes. Probe radius was swept from 0.5 mm to 1.5 mm to validate the developed model against that introduced by Arena and colleagues.

et al., 2012). The model consists of two monopolar probes spaced 1.5 cm apart. Treatment was simulated as 70 pulses of 90 µs duration, and probe diameter was varied from 0.5 mm to 1.5 mm. The temperature at the electrode boundary as a function of time is plotted in **Figure 6.2a**. Additionally, temperature along the x-axis passing through the center of the monopolar probes during the last pulse is shown in **Figure 6.2b**. The results of the model developed herein match the previously published results almost identically, confirming the validity of the numerical techniques used in the current work.

Actively cooled models were validated by comparing the model-predicted temperature to experimentally determined temperature values. Agar tissue mimics were constructed (1% w/v) by dissolving powdered agar (Thermo Fisher Scientific, Suwanee, GA) in deionized water. Sodium chloride (Sigma-Aldrich, St. Louis, MO) was added until the electrical conductivity reached 0.2 S/m to resemble the properties of liver. Samples were briefly brought to a boil and allowed to solidify at room temperature overnight in 250 mL Erlenmeyer flasks. An actively cooled bipolar probe (Angiodynamics, Inc, Latham, NY) with fiber optic temperature sensors (LumaSense Technologies, Santa Clara, CA) affixed to the top of one electrode and center of the insulation (see inset in **Figure 6.3**) was inserted into the center of each mimic. After approximately 10 seconds, a peristaltic pump was turned on and set to the desired flow rate. Approximately 15 seconds after

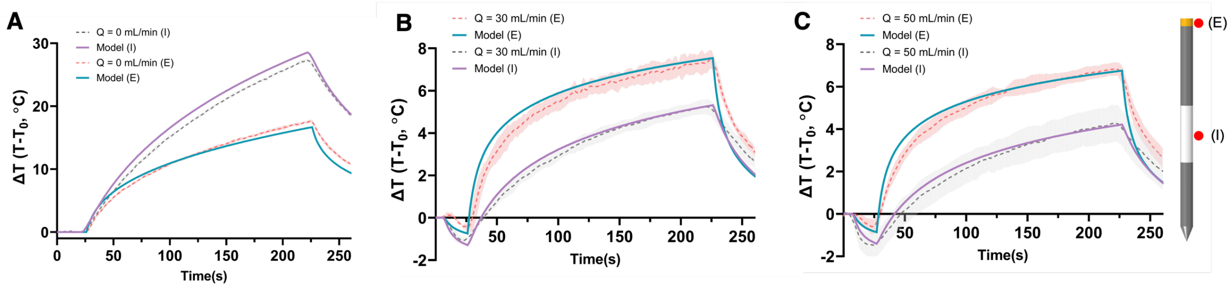

Figure 6.3 – Comparison of model-predicted versus experimentally measured temperature for actively cooled probes with various flow rates. Temperature is plotted at the points indicated in the inset for flow rates of (a) 0 mL/min, (b) 30 mL/min, and (c) 50 mL/min. Treatment consisted of 200 pulses with an applied voltage-to-distance ratio of 1500 V/cm. Experiments were conducted by applying pulses within an agar tissue mimic (n=3). Note different y-axis scales on (a) versus (b, c).

turning on flow, a series of 200 monopolar pulses (100 μs duration) were applied with a voltage-to-distance ratio of 1500 V/cm at a rate of 1 Hz. Alongside experiments, an actively cooled model was developed (as described in Methods) to represent the agar phantom domain. Electrical conductivity was assigned as 0.2 S/m and the initial temperature was set to 23 °C. A comparison of experimentally determined temperature profiles versus those computed numerically is shown in **Figure 6.3** for different flow rates. Model-predicted temperatures matched closely with experimental temperatures, verifying the approach used in this manuscript for prediction of thermal effects with actively cooled electrodes.

6.3 – *Results*

The temperature distribution during the final pulse of a standard clinical protocol is shown in Fig. 3. Peak temperatures for the bipolar probe are located adjacent to the probe body alongside either electrode, with the distal electrode experiencing marginally more thermal effects than the proximal electrode (**Figure 6.5a**). Similarly, the monopolar setup exhibited maximum temperatures within the vicinity of the tapered tip, with slightly less thermal damage than corresponding bipolar cases (**Figure 6.5b**). It is easily observed that probes with integrated TM

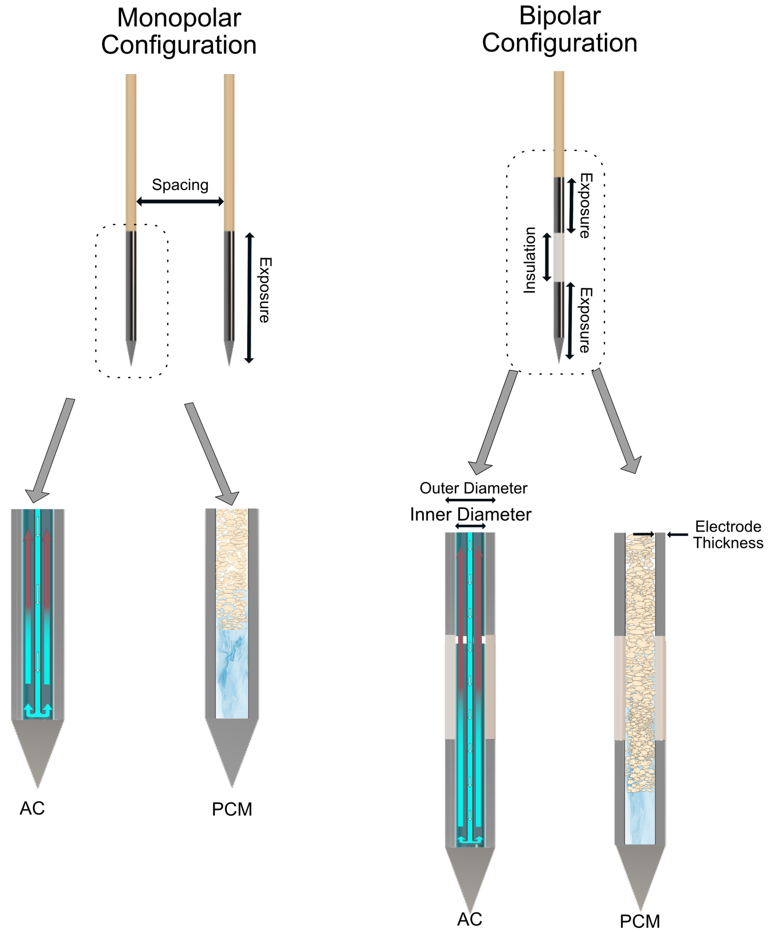

Figure 6.4 – Schematic diagram of (left) monopolar and right (bipolar) probe geometries employed in numerical models. In standard simulations, center-to-center spacing was 1.5 cm, probe diameter was 1.65 mm, and wall thickness was 0.2 mm for either configuration. For the bipolar configuration, electrode exposure was 7 mm and insulation height was 8 mm. For monopolar simulations, electrode exposure was 1 cm. A preliminary modeling study was used to ensure that either configuration resulted in similar volumetric exposure to electric fields of 0 to 2500 V/cm along with similar ablation volumes (data not shown).

technologies have reduced thermal damage (blue contour) compared to those without, and that active cooling is more effective than PCM (**Figure 6.5c-f**) under these pulse conditions.

To evaluate the significance of pulse delivery rate on performance of PCM or active cooling, a parametric study was performed in which the delivery rate was varied from 1 pulse every 2 seconds (0.5 Hz) to 2 pulses per second (2 Hz) (**Figure 6.6**). For solid core probes, increasing the delivery rate from 0.5 Hz to 2 Hz correspondingly increased peak temperature at the probe boundary by ~15 °C (**Figure 6.6a-b**). In the case of PCM-core probes, as temperature approached 43 °C, the integrated PCM absorbed heat, reducing temperature rise by 2 - 4 °C

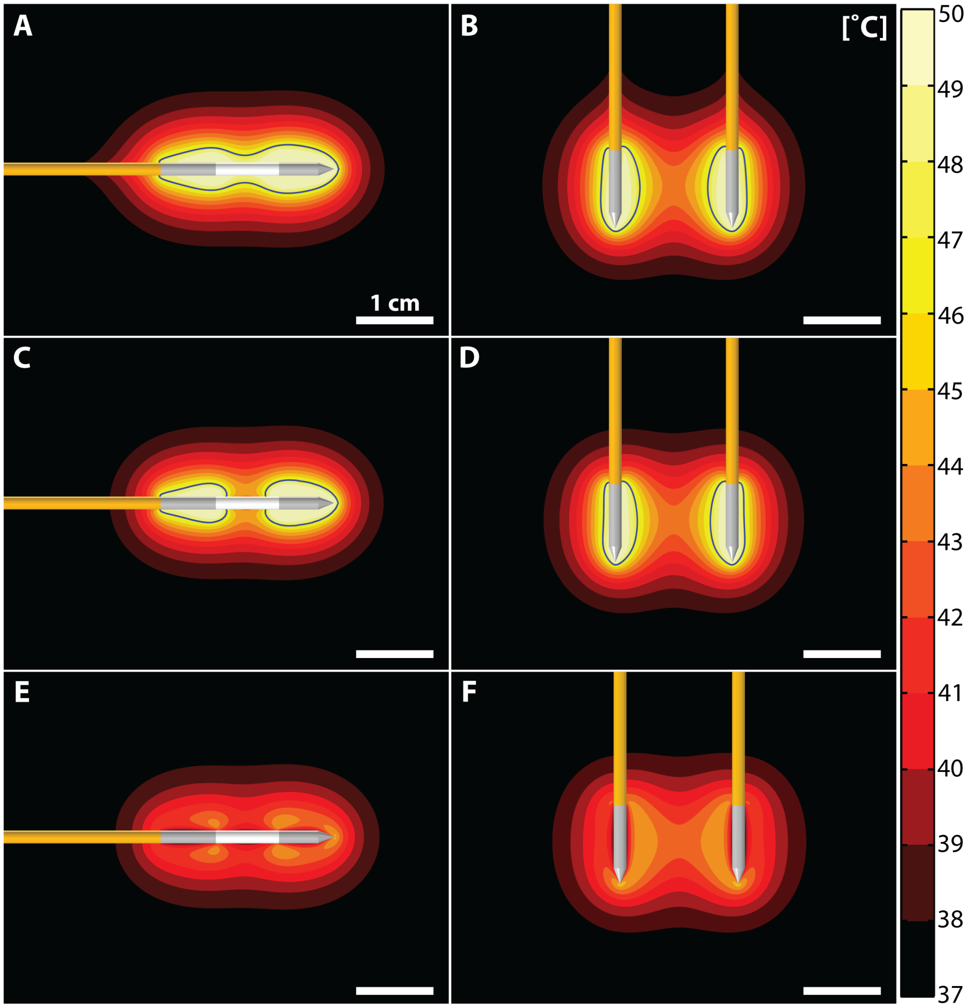

Figure 6.5 – Temperature distribution at the end of IRE treatment with various probe types and geometries. The left column represents a bipolar probe with a a) solid core, c) PCM-filled core, and e) actively cooled core. The right columns illustrate the same for monopolar probes with b) solid cores, d) PCM-filled cores, and f) actively cooled cores. In panels a-d, blue line indicates thermal damage ($\Omega > 0.53$), taken 2 minutes after treatment completion.

throughout the treatment duration in both the bipolar (**Figure 6.6c**) and monopolar (**Figure 6.6d**) arrangements, resulting in ~2 °C lower peak temperatures compared to the solid probes (**Figure 6.6a-b**). In comparison to the other probes modeled, temperature in the vicinity of actively cooled probes was relatively unaffected by pulse rate and rose only modestly during treatment; with pulses delivered at 2 Hz, temperature rise was nearly 20 °C less with actively cooled probes relative to the solid counterpart, and other active cooling cases exhibited even less significant thermal effects. These observations are further reflected by the extent of thermal damage. Across all cases, thermal damage volume was reduced by ~40% with PCM-filled probes compared to solid probes, while actively cooled probes prevented thermal damage altogether (**Figure 6.6g**).

Next, we examined probe geometry to determine the extent to which design choices might impact the performance of either TM technology. Within either probe type, outer wall thickness was varied from 0.05 mm to 0.3 mm, and diameter from 1 mm to 2.5 mm. For small diameters (1-1.5 mm), there was almost no effect of incorporating PCM into the probe core for either arrangement (**Figure 6.7**). Conversely, temperature reductions appeared when the probe diameter

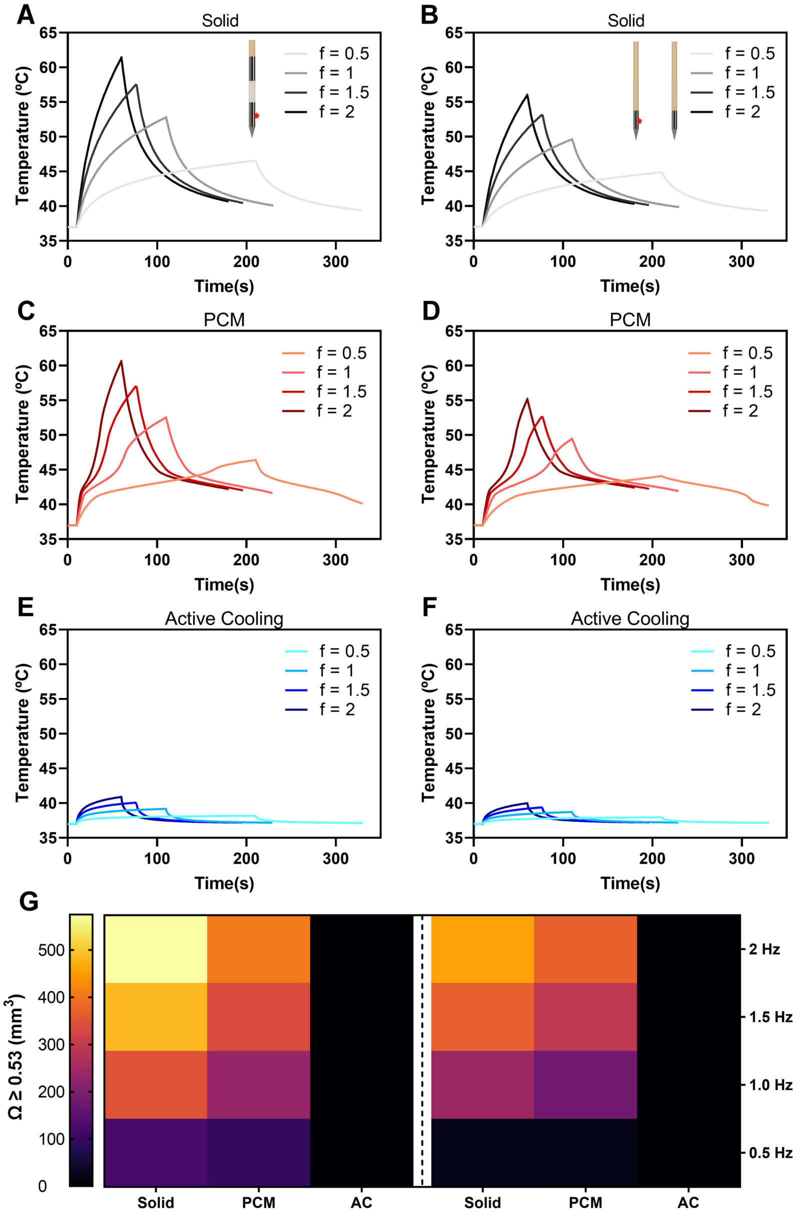

Figure 6.6 – Impact of pulse delivery rate on temperature rise and thermal damage. Temperature (a-f) at the tissue-electrode boundary is shown for solid (a-b), PCM-filled (c-d), and actively cooled (e-f) probes in either a bipolar (a, c, e) or monopolar (b, d, f) electrode configuration. Also shown is the (g) volume of thermal damage for each case.

was adjusted to 2 mm, with 2.5 mm offering the most significant benefit. When considering the actively cooled probes, there was not a strong dependence on geometry and in all cases, temperature was highest ~1 mm from the probe edge with a slight decay thereafter (**Figure 6.7**). Importantly, it appears that integrated TM technologies can impact temperature within ~4 mm of the edge of bipolar probes and ~3 mm for monopolar probes, with little change in temperature relative to solid probes thereafter (**Figure 6.7**). In addition to probe diameter, outer wall thickness also played a role in the efficiency of PCM-core probes (**Figure 6.8**), but not actively cooled probes (data not shown). Specifically, wall thickness was especially important for bipolar probes with moderate radii (0.75 to 1 mm), with thinner walls leading to less thermal damage (**Figure 6.8a,c**). In monopolar simulations, probe radius dominated effectiveness of PCM-core electrodes, and wall thickness was not as significant (**Figure 6.8b,d**).

Finally, we investigated engineering and user-defined parameters that may impact the effectiveness of thermal mitigation strategies (**Figure 6.9**). Because bipolar probes generally resulted in higher temperatures, only this configuration was examined. Additionally, since performance of the PCM-core probes was heavily dependent upon geometry, probe radius for

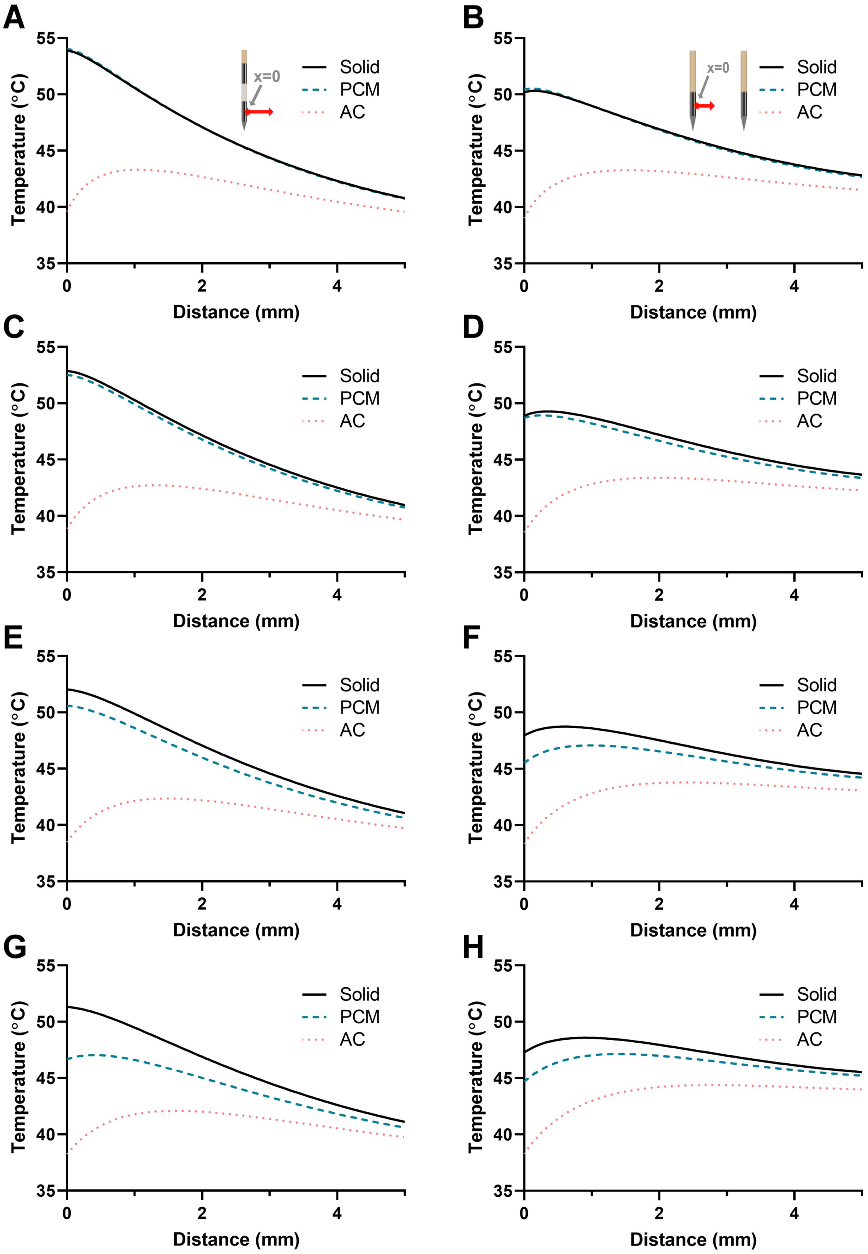

Figure 6.7 – Probe design affects the performance of PCM-filled probes but not actively cooled probes. Temperature along a line moving radially outward from the electrode edge (a-h) is shown for (a, c, e, g) bipolar probes and (b, d, f, h) monopolar probes with radii of (a-b) 0.5 mm, (c-d) 0.75 mm, (e-f) 1 mm, and (g-h) 1.25 mm. Center-to-center separation was 1.5 cm for either probe configuration.

PCM probes was increased to 1 cm, while wall thickness was maintained at 0.2 cm. The standard geometry was employed for actively cooled probes. **Figure 6.9a-c** demonstrates that changes to PCM material properties impact its ability to absorb heat during pulse delivery. With a relatively low heat of fusion (**Figure 6.9a**), tissue temperature is nearly identical regardless of k_{eq}. On the other hand, increasing λ (**Figure 6.9a-c**) has the strongest effect on temperature rise, while k_{eq} had a clear impact when paired with higher values of λ. Of further note, the effect of k_{eq} appeared to plateau once it reached its standard value. For actively cooled probes (**Figure 6.9d-f**) with very low flow rates (i.e., $h/100$), T_{ext} was insignificant (**Figure 6.9d**). However, by increasing the heat transfer coefficient to $h/10$ (**Figure 6.9e**), tissue temperature peaked at ~20 - 30 °C above T_{ext}. With h set to its baseline value (corresponding to ~35 mL/min (**Figure 6.9f**)), tissue temperature

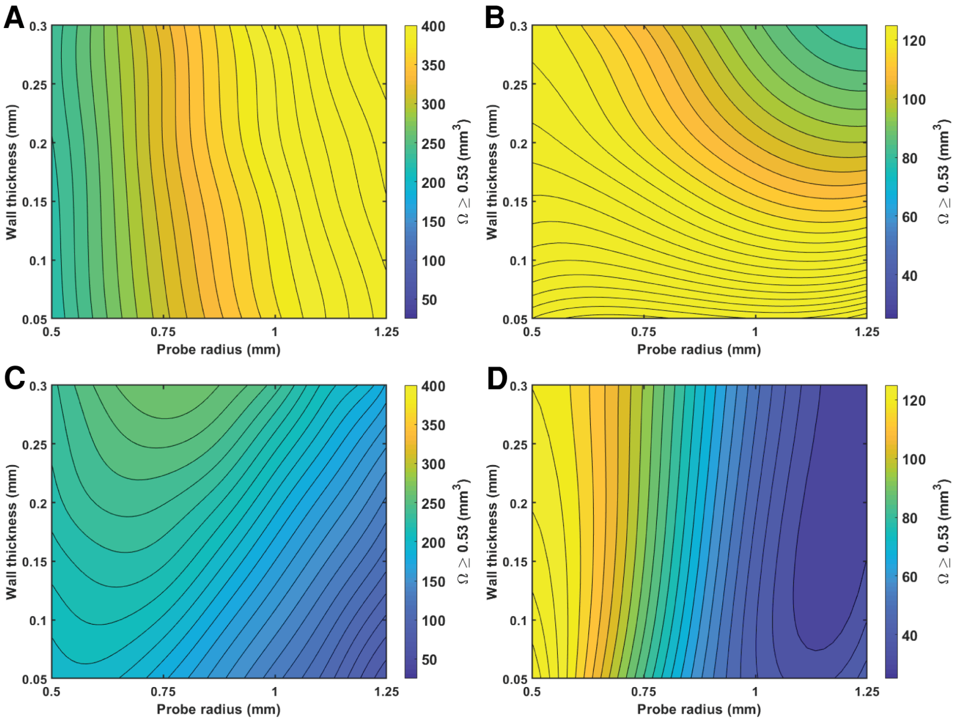

Figure 6.8 – Impact of probe diameter and wall thickness on thermal damage accumulation for PCM-filled probes relative to solid probes. Volume of tissue undergoing thermal damage ($\Omega \geq 0.53$) 2 minutes after treatment completion is shown for (a-b) solid probes and (c-d) PCM-filled probes in either a (a, c) bipolar or (b, d) monopolar configuration. Note different y-axis scales for (a, c) bipolar versus (b, d) monopolar cases.

rapidly approached T_{ext} prior to the onset of pulse application and increased less than 5 °C during treatment.

6.4 – *Discussion*

This work modeled and directly compared the theoretical ability of actively cooled and PCM-core electrodes to limit thermal effects during IRE treatment. In addition to IRE, the benefits of integrated TM technologies will translate to other PEF-based ablative and non-ablative modalities such as electrochemotherapy (ECT) and electrogene transfer (EGT). Our data demonstrate that the PCM approach was successful in reducing the risk of thermal damage/necrosis, while the actively cooled approach markedly reduced the risk of thermal damage compared to both existing IRE electrodes and PCM-core probes. It is worth mentioning that another engineered strategy, where an endothermic reaction takes place within the probe core

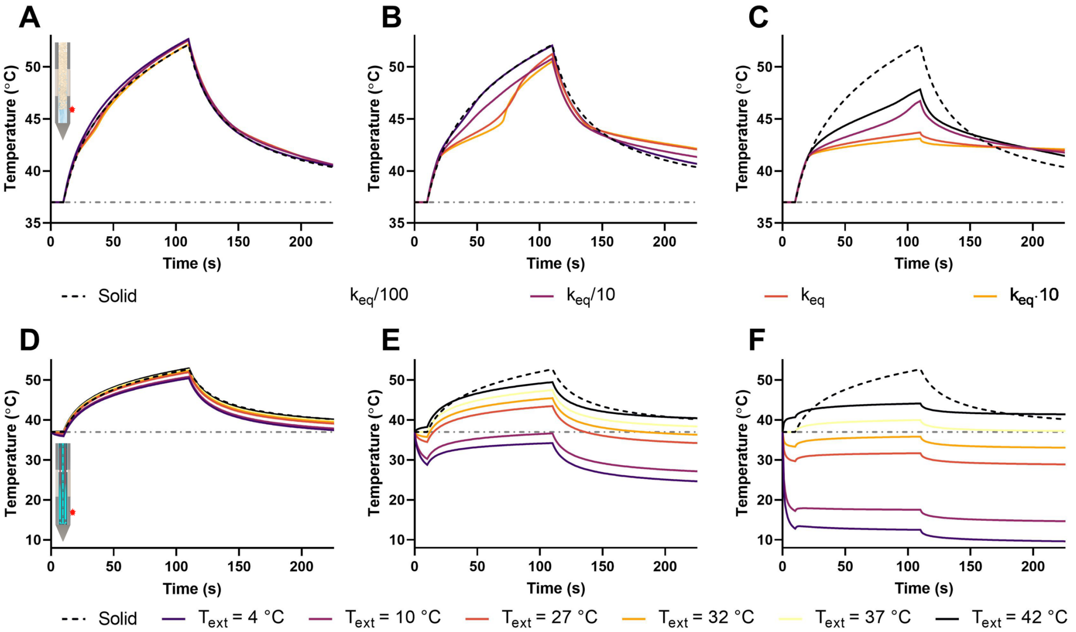

Figure 6.9 – Performance of PCM-core and actively cooled probes depends upon material properties and user-defined settings. Temperature development during and after pulsing at the vertical midpoint of the distal electrode boundary is shown for (A-C) a PCM-core and (D-F) actively cooled bipolar probe. For PCM-core models, the latent heat of fusion was set to (A) $\lambda/10$, (B) λ, and (C) $\lambda \cdot 10$, respectively, with each curve corresponding to a different effective thermal conductivity (k_{eq}). For actively cooled models, the heat transfer coefficient was varied between $h/100$, $h/10$, and h, respectively. For PCM-core probes, $\emptyset$ was set to 2 mm while $\emptyset$ = 1.65 mm was used for actively cooled probes.

during treatment, has been proposed (Y. Zhao & Davalos, 2020). This design could potentially offer similar or improved performance relative to PCM-core probes within the same platform. However, the endothermic probe has not been fabricated or studied experimentally, and it is not trivial to separate the reactants prior to dissolution. Thus, we chose to omit the endothermic probe from the current study.

Throughout this work, actively cooled probes were effective in preventing substantial temperature rise in the vicinity of the electrodes in essentially every case, and no thermal damage was seen except when perfusate temperature was elevated above physiological (body) temperature. This suggests that active cooling is highly efficacious regardless of the probe geometry and pulsing protocol employed. Extrapolating these data implies that tissue conductivity plays only a minor role on the effectiveness of actively cooled probes. Thus, for applications where temperature control and thermal mitigation is an absolute requirement, actively cooled electrodes should be considered. These probes may also be warranted in specific clinical settings during which large ablation volumes are targeted, or when inexperienced users are becoming familiar with IRE and more prone to overtreating. They could also be useful for maintaining tissue temperature at predetermined values during treatment. For instance, perfusate temperature could be held a few degrees above physiologic temperature, as moderate heating has been shown to elicit magnified biophysical effects during certain PEF-based therapies (Edelblute et al., 2017; Sano et al., 2020). In contrast, with higher flow rates and low perfusate temperatures, although thermal damage becomes a non-issue, ablation size could be negatively affected. Our models predict that with h = 0.381 W cm^{-2} K^{-1} and T_{ext} = 4°C, ablation volume would be reduced by 30% versus solid probes (data not shown). Thus, future efforts should be devoted to quantifying ablative effects of actively cooled probes under the influence of relevant parameters.

Despite the apparent advantages of actively cooled electrodes, this technology is not without limitation. For example, using an actively cooled electrode system requires an external peristaltic pump to circulate perfusate through the probe and the ability to regulate perfusate temperature if desired. Additionally, the probes are heavier and more cumbersome due to the need for external tubing, so additional fixation devices may be necessary to hold the probe(s) in place. In specific instances such as prostate ablation, this may be less concerning since a brachytherapy grid is used to precisely place the IRE probes, stabilizers are already in use for ultrasound transducer positioning, and the probes only need to be inserted a few centimeters (Baur et al., 2017). In addition, actively cooled probes may offer further advantages since the prostate is highly conductive (i.e. increased thermal effects) and dense with sensitive vasculature and neural components (Campelo et al., 2017; Checcucci et al., 2019; Neal et al., 2014b). For other deep-seated or less conductive tumors in which a small amount of thermal damage is acceptable, PCM-core probes might be the preferred option.

Probes with integrated PCM within the core acted to only moderately limit temperature rise as compared to solid electrodes. This effect was heavily dependent upon both the chosen pulse parameters and the probe geometry. With high pulse rates, the PCM completely melted, and temperature increased faster than in the solid case for a few seconds shortly thereafter. Thus, if possible, treatment should be completed prior to PCMs completely undergoing their phase transition. Intuitively, the most effective probe geometries were those that maximized PCM volume (i.e., large radius and thin wall). Probes with diameters of 2 mm or more obviously reduced the peak temperature at the end of treatment by 2-3 °C. Interestingly, despite these seemingly modest effects, the cumulative suppression of temperature development over the course of treatment resulted in substantial reductions of thermal damage (by 40% or more). Because thermal damage depends not only on temperature but also time of exposure, the steady 1-5 °C reduction in temperature over the course of 100 seconds played a major role in mitigating thermal injury (**Figure 6.6** and **Figure 6.8**).

For comparative purposes, we chose a salt hydrate PCM as originally modeled by Arena and colleagues (Arena, Mahajan, et al., 2012). However, a wide array of materials could be selected as the PCM within probes used for IRE, with each exhibiting a unique melting point, thermal conductivity, density, and heat of fusion. Each of these characteristics contributes to the behavior of the PCM and its ability to prevent temperature development in different scenarios. For IRE and PEF-based applications, the ideal PCM would have a high density and latent heat of storage to allow the PCM to absorb as much heat as possible given the limited volume of material that can be stored within a needle electrode. Finally, a high thermal conductivity would allow the PCM to conduct heat from the distal region of the probe through the shaft, dispersing the thermal energy among the entire volume of PCM and increasing its effectiveness. Ideally, the phase transition should be initiated as early as possible during treatment, but not completed prior to treatment cessation. This could be tuned by selecting a PCM with an optimal melting temperature. For long duration or high amplitude treatments, the ideal T_m is likely to be 5-10 °C above physiologic temperature. For non-ablative treatments such as ECT and EGT, T_m should be just above 37 °C since only a few pulses are administered. For treatment of superficial tissues where probe bodies are not inserted deeply, it may be ideal for T_m to lie near the midpoint of physiological and room temperature. Attractive PCMs include salt hydrates (as studied here) or metallic PCMs, but some eutectics may also be desirable. A number of works comprehensively summarize PCMs available for different applications (Jankowski & McCluskey, 2014; Su et al., 2015; Zalba et al., 2003).

This paper is intended to directly compare engineered thermal mitigation strategies, but it is important to highlight limitations to the approach employed. First, a 3D model was used to simulate the monopolar configuration, whereas a 2D axisymmetric numerical model was employed to simulate bipolar probes. While this approach significantly reduced computation time, minor differences may exist in the element shape and number between the bipolar and monopolar models, which could have a small impact on the calculated thermal effects. Additionally, we assumed the electrical and thermal properties of pancreatic tissue for this study since IRE is commonly employed for the treatment of unresectable pancreatic adenocarcinoma and the pancreas is highly sensitive to thermal damage. Thus, while the trends reported in this paper are likely similar for other tissue types, the degree of temperature development for other organ systems will depend upon tissue-specific characteristics such as electrical conductivity, heat capacity, thermal conductivity, and extent of blood perfusion. It is also important to reiterate that TM strategies help reduce the risk of thermal injury within the immediate vicinity of the electrodes. However, certain scenarios may arise where more Joule heating occurs outside the region of influence of either integrated TM strategy. This is conceivable particularly for electrode setups designed to expose large tissue volumes to elevated field strengths (Kaufman et al., 2020; Y. Zhao et al., 2021).

6.5 – Conclusion

Irreversible electroporation is a focal tissue ablation modality used to treat a variety of solid tumors and cardiac arrhythmias. Though cell death occurs predominantly via non-thermal processes, Joule heating can arise in the vicinity of electrodes due to the nonlinear electric field distribution. Integrated thermal mitigation strategies including active cooling and phase change materials have been introduced to limit thermal effects. Here, we numerically studied different clinical and engineered parameters that can affect the performance of thermal mitigation modalities. Our data indicate that probes with either technology will limit thermal damage. Performance of probes with PCM cores is highly dependent upon the properties of the PCM, applied pulse parameters, and probe design choices. Conversely, active cooling efficiently mitigates thermal damage regardless of probe size or applied pulse parameters and can be tuned to maintain tissue temperature at a predetermined value. Because PCM-core probes are less cumbersome and likely more cost-effective compared to actively cooled probes, it is important to consider the relative to the benefits of each system compared to existing IRE probes for specific case use.

7 – Toward Large Hepatic Ablations with Single-Insertion High-Frequency Irreversible Electroporation: In Vivo Pilot Study

7.1 – Introduction

Liver cancer is the leading cause of cancer-related death worldwide and, unlike most other malignancies at the top of this list, is increasing in incidence (Anwanwan et al., 2020). Hepatocellular carcinoma (HCC) is the most common form of liver cancer (~90% of cases) and accounts for nearly 1 million deaths annually (Siegel et al., 2022). The liver is also a common site of metastasis from primary neoplasms of the gastrointestinal tract – approximately 50% of colorectal cancer (CRC) patients will develop liver metastases – as well as the breast, lungs, and skin, further exacerbating the burden of disease (Che-Lok Chow & Siu-Ho Chok, 2019).

A major factor contributing to the high mortality of liver cancer is the lack of effective treatment options. Surgical intervention (partial hepatectomy or liver transplant) is a definitive first-line therapy, but only 5-15% of patients are candidates due to compromised liver function or an inability to meet transplant criteria (Anwanwan et al., 2020). Focal ablation is a third choice that can be used with curative intent or as a downstaging technique. It has been well documented that ablative therapy can be just as effective as hepatectomy for both HCC and CRC metastases with the added benefit of fewer complications (M. S. Chen et al., 2006; Y. Fang et al., 2014; M. Zhang et al., 2017b). Several energy-based and chemical approaches have been introduced for focal liver ablation (Llovet et al., 2021; Niemeyer et al., 2014b), but radiofrequency (RFA) and microwave ablation (MWA) are by far the most clinically employed techniques, with MWA becoming the therapy of choice in recent years (Izzo et al., 2019; Mrudula Glassberg et al., 2019).

Though thermal therapy has become a mainstay within the multidisciplinary treatment of liver cancer, it is not without limitation. Because tissue destruction is indiscriminate, both cellular and acellular components within the ablation zone are destroyed, posing a risk of non-tumor tissue loss and damage to nearby critical structures (Imajo et al., 2020; Ohmoto et al., 2009). Tumors near vasculature and bile ducts are particularly difficult to treat with RFA and MWA, which precludes many patients from therapy and increases the risk of local recurrence for those who are treated (Chiang et al., 2016). RFA suffers from the heat-sink effect, where the convective cooling of larger vessels (> 3 mm) prevents tissue from reaching target coagulation temperatures (Z.-Y. Lin et al., 2016). In contrast, the rapid, diffuse temperature rise from MWA can lead to thrombosis of smaller (≤ 3 mm) vessels and ducts (Chiang et al., 2014, 2017).

Irreversible electroporation (IRE) is a non-thermal ablation modality capable of overcoming several of the technical challenges associated with RFA/MWA, including sparing of vascular and biliary integrity (Narayanan et al., 2013; Ueshima et al., 2018). IRE employs high-voltage pulsed electric fields to destroy targeted cells through the creation of long-lived nanoscale defects – or pores – in the lipid bilayer (Geboers et al., 2020; Jiang et al., 2015). IRE has shown success for the treatment of primary and metastatic liver tumors up to 3 cm in diameter and can be used even when tumors are adjacent to vessels and nerves (Koethe et al., 2022; Sutter et al., 2017).

Though IRE provides an option to eradicate otherwise untreatable neoplasms, clinical implementation has been somewhat limited due to the complexity of treatment. IRE pulses must be synchronized to the cardiac rhythm and intraoperative paralytics must be administered to prevent cardiac asynchrony and severe muscle contractions (Ball et al., 2010; O'Neill & Martin, 2020). Additionally, existing IRE procedures require the placement of 2 to 6 needle electrodes with precise positioning relative to the target, but also at the same depth, in parallel to one another, and with accurate spacing. Thus, probe placement can be quite time consuming (and sometimes erroneous (Mathy et al., 2020)) leading to increased intraoperative time for IRE relative to RFA/MWA.

High-frequency irreversible electroporation (H-FIRE) is an emerging technology that was introduced to offer the benefits of IRE while removing these disadvantages. H-FIRE utilizes shorter pulses (1-10 µs) of alternating polarity that can minimize the extent of nerve excitation and obviate the need for cardiac synchronization (Arena, Sano, Rossmeisl, et al., 2011). H-FIRE may also produce more predictable electric field distributions than IRE (S. P. Bhonsle et al., 2015; Murovec et al., 2016). Preclinical studies have demonstrated the safety and feasibility of H-FIRE within normal and neoplastic liver (Siddiqui et al., 2016, 2017). Investigations have also shown successful treatment delivery with single-needle devices that further simplify the procedure (DeWitt et al., 2019; Partridge et al., 2020; Sano, DeWitt, et al., 2018). H-FIRE clearly provides several advantages over conventional IRE in terms of treatment administration, but the size of ablations that can be generated with H-FIRE remains unknown. Thus, the goal of the current study was to examine the upper limit to ablation size achievable with H-FIRE administered via a single-needle device, and to characterize the resulting biological and immune response.

7.2 – Methods

7.2.1 – Analysis of Electrical Arcing

Agar tissue phantoms were prepared by dissolving 1% (w/v) agar and 0.1% (w/v) NaCl in deionized water and briefly boiling the solution. Warm agar (~50 °C) was poured into plastic cups and allowed to cool to room temperature overnight. For each waveform, a bipolar electrode capable of internal cooling was carefully inserted to a depth of 4 cm into the agar. Once inserted, 10 bursts of the specified waveform, each with 100 µs of on-time, were delivered at a rate of 1 Hz by a custom generator as described below. The applied voltage was sequentially increased 100 V and 10 more bursts delivered until arcing was detected visually and confirmed through current measurements. Once arcing was detected, voltage was reduced by 50 V and pulse delivery attempted again. The maximum voltage at which all 10 bursts were successfully delivered was recorded. Equipment layout was similar for this experiment as well as the *in vivo* tests (**Figure 7.1a**), albeit without accelerometry.

7.2.2 – Assurances

Five female Yorkshire pigs (46 ± 2 kg) were used for the current study (Palmetto Research Swine, Reeseville, South Carolina). All experiments were approved by the Institutional Animal Care and Use Committee (Atrium Health Carolinas Medical Center, Charlotte, NC) and conformed to the Guide for Animal Care and Use of Laboratory Animals (National Institutes of Health, Bethesda, MD).

7.2.3 – Surgical Procedures

Animals were fasted overnight and anesthesia was induced with Xylazine (2 mg/kg, i.m.), Telazol (5 mg/kg, i.m.), and sodium thiopental (20 mg/kg, i.v.). The animals were intubated and surgical anesthesia was maintained with inhaled isoflurane. Vitals were continuously monitored using telemetry and pulse oximetry. A midline incision (~15 cm) was made and a Balfour retractor was placed to provide access to the liver. A 3-axis accelerometer (ADXL337, Analog Devices, Norwood, MA) was affixed approximately 5 cm lateral to the caudal end of the incision and connected to an Arduino UNO based data acquisition unit to monitor potential muscle contractions resulting from treatment. For each ablation, a single 18-gauge internally cooled bipolar applicator (AngioDynamics, Inc., Latham, NY) (**Figure 7.1b**) was inserted distally within the targeted lobe and advanced toward the hilum until an insertion depth of 4-5 cm was achieved. A fiber optic temperature sensor (Luxtron Series, Advanced Energy, Denver, CO) was affixed to the surface of the probe approximately 1 mm proximal to the in-line electrode (**Figure 7.1b**) and connected to a

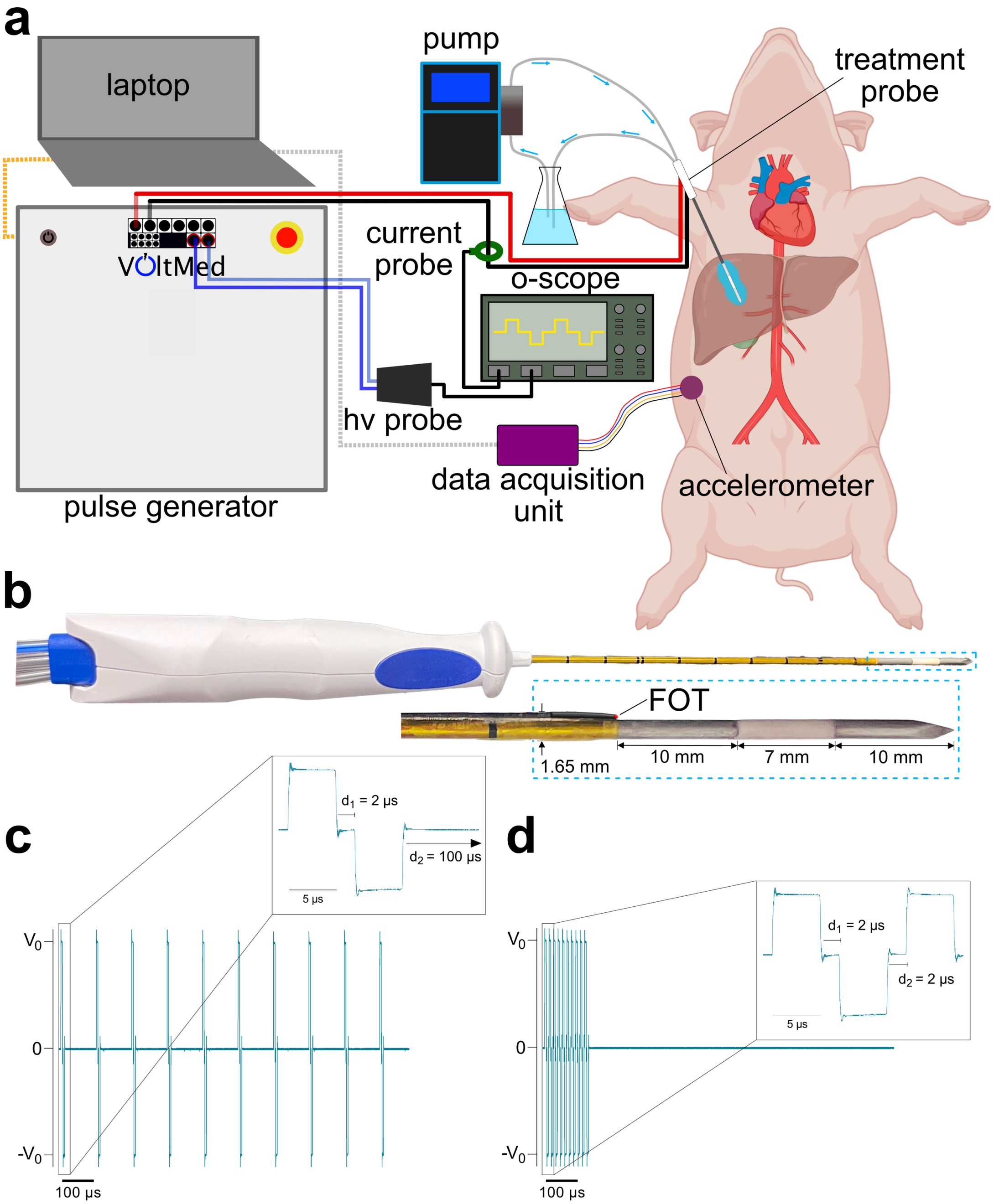

Figure 7.1 – Overview of approach used for in vivo hepatic ablations and benchtop arc testing. (a) Schematic of equipment setup used for in vivo experiments. In agar trials, the setup was the same except probe was inserted ~ 4 cm into a vessel filled with 1% (w/v) agar and 1% (w/v) NaCl. (b) The bipolar electrode capable of internal cooling used in the current study. In certain animal trials, a fiber optic temperature sensor was affixed to the probe (inset) to record temperature. Representative voltage traces are shown for the (c) modified H-FIRE waveform and (d) traditional H-FIRE waveform used in in vivo experiments.

data acquisition unit. Temperature was recorded at a rate of 2 Hz in at least two replicates per treatment condition during the study. Once probe placement was complete, pulse delivery was commenced as described below. Six ablations were performed in each animal, with care taken to make sure each treatment was separated by > 5 cm from neighboring ablations.

7.2.4 – Pulse Delivery

H-FIRE bursts were delivered through a high-voltage generator (Voltmed Inc., Blacksburg, VA) capable of producing pulse trains with potentials up to 5 kV and currents up to 100 A. Seven different pulse delivery protocols were used in the current study (**Table 7.1**). Applied waveform, voltage, and use of internal cooling were varied among the protocols, and protocols were randomly distributed across the five animals. In all cases, 300 bursts of the prescribed waveform – each containing 100 µs of energized time – were delivered at a rate of 1 Hz without cardiac synchronization. Prior to treatment delivery, a sequence of 3 bursts was delivered beginning at 1000 V and incrementing by 250 V each step until the target voltage was reached to collect tissue property information and confirm the absence of arcing. For treatments in which internal cooling was used, probe perfusion was commenced after completion of this "voltage ramp" to ensure that coolant flow did not modify local tissue temperature. During pre-treatment characterizations and treatment, delivered voltage and current waveforms were monitored with a 1000× attenuation high-voltage probe (BTX Enhancer 3000, Harvard Apparatus, Holliston, MA) and 10× attenuation

Table 7.1 – Summary of treatment groups used to generate ablations *in vivo*

Treatment Group	*Waveform*	*Voltage (V)*	*Cooling*	*Bursts*	*Delivery Rate (Hz).*	*n*
1C	5-2-5-2	2250	No	300	1	4
1M	5-2-5-100	2250	No	300	1	4
2C	5-2-5-2	2250	Yes	300	1	5
2M	5-2-5-100	2250	Yes	300	1	4
3C	5-2-5-2	3000	Yes	300	1	3
3M	5-2-5-100	3000	Yes	300	1	5
4M	5-2-5-100	3300	Yes	300	1	4

passive current probe (2877, Pearson Electronics, Palo Alto, CA), respectively, each of which were connected to an oscilloscope (3024z, Teledyne LeCroy, Chestnut Ridge, NY).

7.2.5 – Sacrifice /Excision

Animals were anesthetized as previously described 24 hours after the last ablation, and the surgical incision was reopened. B-mode ultrasound was performed to take axial and radial sonograms of each ablation. Animals were then euthanized (12 mL EUTHASOL) and livers were removed. Longitudinal (along the electrode insertion path) and transverse sections were taken, and paired sections were photographed. Samples were then placed in 1.5% (w/v) 2,3,5-triphenyltetrazolium chloride (TTC) in phosphate buffered saline (PBS) for approximately 10 minutes at 20 °C. Samples were rinsed with DI water, patted dry, and imaged again. Samples were then fixed in 10% (v/v) neutral buffered formalin overnight, rinsed, dried, and imaged a final time.

7.2.6 – Histological analysis

Following fixation, samples were embedded in paraffin, sectioned with a thickness of 4 μm, and mounted on slides. Standard staining with hematoxylin and eosin (H&E) was used to visualize regions of ablation and check for the presence of thermal damage. We also used H&E to confirm ablation dimensions. Immunohistochemistry (IHC) using an antibody against cleaved caspase 3 (ab4051 [1:200], Abcam, Waltham, MA) was performed to examine the extent and location(s) of apoptotic cell death within each ablation. Dual IHC with antibodies against CD4 and CD68 (ab133616 [1:100], ab125212 [1:200], Abcam, Waltham, MA) was used to characterize infiltration of T lymphocytes and macrophages, respectively. Anti-caspase 3 samples were counterstained with Mayer's hematoxylin while dual IHC samples were counterstained with methyl green. Analysis of all IHC markers was performed using QuPath v0.4.1.

7.2.7 – Computational Modeling

Numerical simulations were executed in COMSOL Multiphysics v6.0 (COMSOL AB, Stockholm, Sweden) to compare the electric field distribution and thermal effects of the different treatment groups, as well as to compute lethal electric field thresholds. Due to the radially symmetric probe employed in this study, a 2D axisymmetric modeling domain was used. Liver tissue was modeled as an ellipsoid with radii of 7.5 cm in the radial direction and 5 cm in the axial direction. The hollow bipolar probe was centered in the domain and given dimensions as shown in **Figure 7.1b** including a hollow inner channel with wall thickness of 0.2 mm. Electroporation-dependent conductivity behavior was characterized for each waveform by matching model-predicted electrical current to current measured *in vivo* across a range of applied voltages as previously described (O'Brien, Passeri, et al., 2019; Partridge et al., 2020). Thermal effects of Joule heating were considered as previously described, and temperature changes were assumed to increase local electrical conductivity at a rate of 1.2 %/°C (Beitel-White et al., 2020; Davalos & Rubinsky, 2008). For each model, we assigned the relevant voltage and simulated the full 300 burst treatment to compute the electric field distribution. Measured ablation width and length, as well as the estimated ablation volume, were used to compute the electric field threshold (EFT) corresponding to ablation for each protocol under study.

7.2.8 – Statistical Analysis

Statistical analyses were performed with JMP Pro v16.0 (SAS Institute, Cary, NC) or Prism v9.3.1 (GraphPad, San Diego, CA). To evaluate the relative contribution of the applied voltage, treatment waveform, and use of internally cooling on the resulting ablation dimensions, a least squares parametric fit was performed. A one-way ANOVA followed by post-hoc Tukey's test, where applicable, was used to test the effect of the treatment group on primary and secondary outcomes. Statistical significance was defined as $p \leq 0.05$. All data are presented as mean ± SEM unless otherwise indicated.

7.3 – Results

7.3.1 – Analysis of factors affecting electrical arcing with a bipolar electrode in agar phantoms

A pilot study was performed to gain an understanding of how waveform parameters affect electrical arcing and to inform the selection of waveforms for use *in vivo*. We investigated the effect of pulse duration as well as symmetrically or asymmetrically varying the interphase and interpulse delays (**Figure 7.2**). Our data show that, in general, waveforms with lower duty cycles tend to require higher voltages to generate arcing (**Figure 7.2b, d**). We also found that shorter pulse widths increase the risk of arcing for traditional H-FIRE waveforms containing symmetric delays until a critical delay threshold (~30 μs) is met, whereafter the trend reverses and shorter pulse durations become preferable (**Figure 7.2a**). We also investigated the effect of lengthening the interpulse delay with a fixed pulse duration (**Figure 7.2c**), as studies have begun to suggest that this approach could improve treatment efficacy and reduce muscle stimulation. We found that, as expected, maximum voltage varied inversely with duty cycle regardless of the delays chosen (**Figure 7.2d**). The results of this study were used to justify the maximum voltages attempted with the control waveform (3000 V) as well as the modified waveform, in which this voltage was increased by 10% (3300 V).

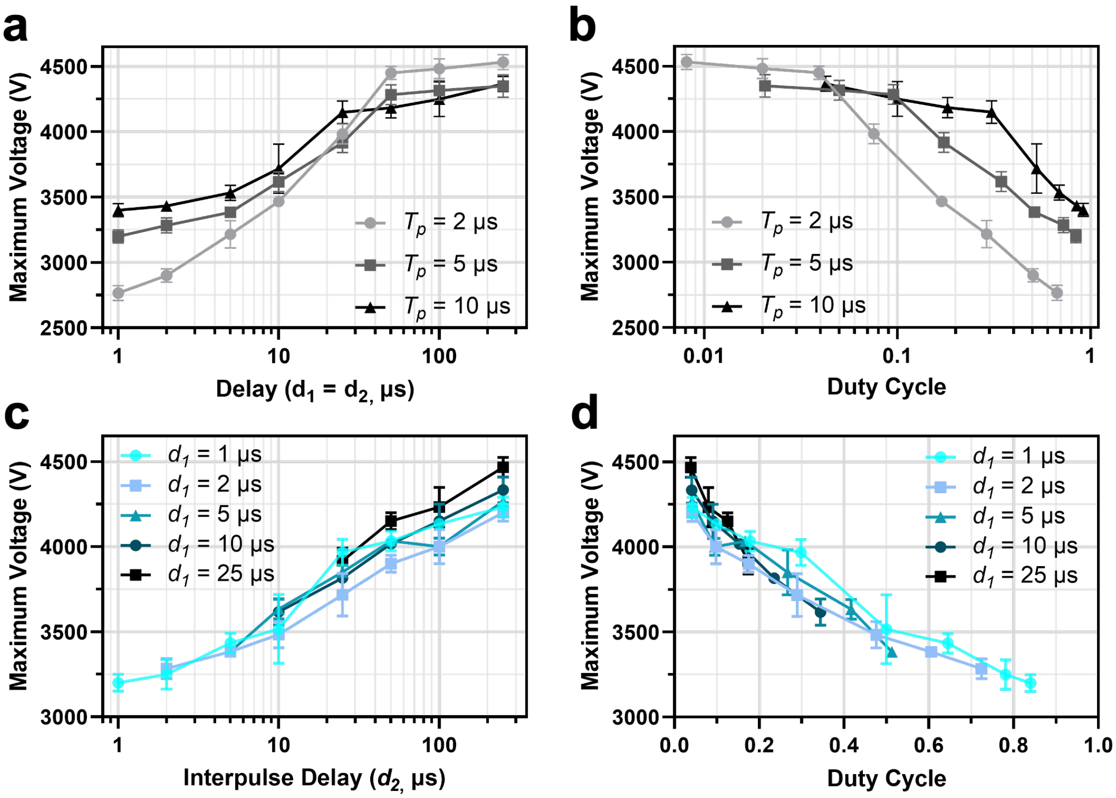

Figure 7.2 – Factors affecting electrical arcing with an internally cooled bipolar electrode. A parametric analysis shows the maximum safe voltage for biphasic waveforms with (a-b) symmetric delays and 3 different pulse widths, as well as (c-d) long interpulse delays with a fixed pulse width of 5 µs and varying interphase delay. For each waveform, a series of 10 bursts was applied at increasing voltages within an agar tissue phantom until arcing was detected visually and confirmed through oscilloscope recordings.

7.3.2 – In vivo H-FIRE – Treatment success and intraoperative observations

All H-FIRE procedures were technically successful. Probe insertion time was approximately 1 minute while treatment duration was 5 minutes in all cases. During treatment, no cardiac abnormalities were detected. Mild, innocuous muscle twitching was observed in some cases and seemed related to the distance between the probe and the diaphragm. With the conventional 5-2-5-2 waveform, arcing was detected in 3 of 6 replicates (50%) during the voltage ramp stage at 3000 V before beginning treatment. In these scenarios, the planned treatment group was substituted with a different group containing a lower voltage or the modified waveform. Arcing was not a limiting factor to treatment success with the 5-2-5-100 (9/9 planned treatments (100%) were successfully delivered at 3000 V and 3300 V).

7.3.3 – Gross analysis of tissue ablations

Single-needle H-FIRE treatment resulted in ellipsoidal and sometimes peanut-shaped ablations depending upon the treatment group (**Figure 7.3a**). After TTC staining and overnight fixation, ablation regions presented with a darker core region of ablation outlined by a slightly lighter rim (**Figure 7.3a**). Ablation volume (**Figure 7.3b**) was calculated from the ablation width (**Figure 7.3c**) and length (**Figure 7.3d**) assuming the lesions were elliptical. Also reported are the measured transverse ablation area (**Figure 7.3e**) and longitudinal area (**Figure 7.3f**). Ablation size in general and especially the volume was affected primarily by the applied voltage ($p<0.001$), as anticipated. The use of internal cooling slightly reduced ablation volume, but this was not significant ($p=0.14$). Between the two waveforms, ablation volumes were consistently larger with the modified 5-2-5-100 as compared to the control 5-2-5-2 ($p=0.002$). Of particular note is that the ability to increase the applied potential to 3300 V with the 5-2-5-100 allowed for moderate increases in ablation length and width, resulting in a substantial volume increase that was nearly double the size of those achieved with 3000 V (**Figure 7.3b**).

7.3.4 – Comparison of Lesion Sizes measured Grossly and through Ultrasound

In addition to measuring single-needle H-FIRE dimensions grossly, ultrasound was used to visualize and measure lesions immediately before euthanasia and necropsy (**Figure 7.4**). Ultrasound, metabolic staining, and histological examination all revealed qualitatively similar lesions (**Figure 7.4a-c**). Lesions visualized on ultrasound were characterized by a hypoechoic core with a narrow hyperechoic rim (**Figure 7.4a**). We quantitatively assessed the correlation between

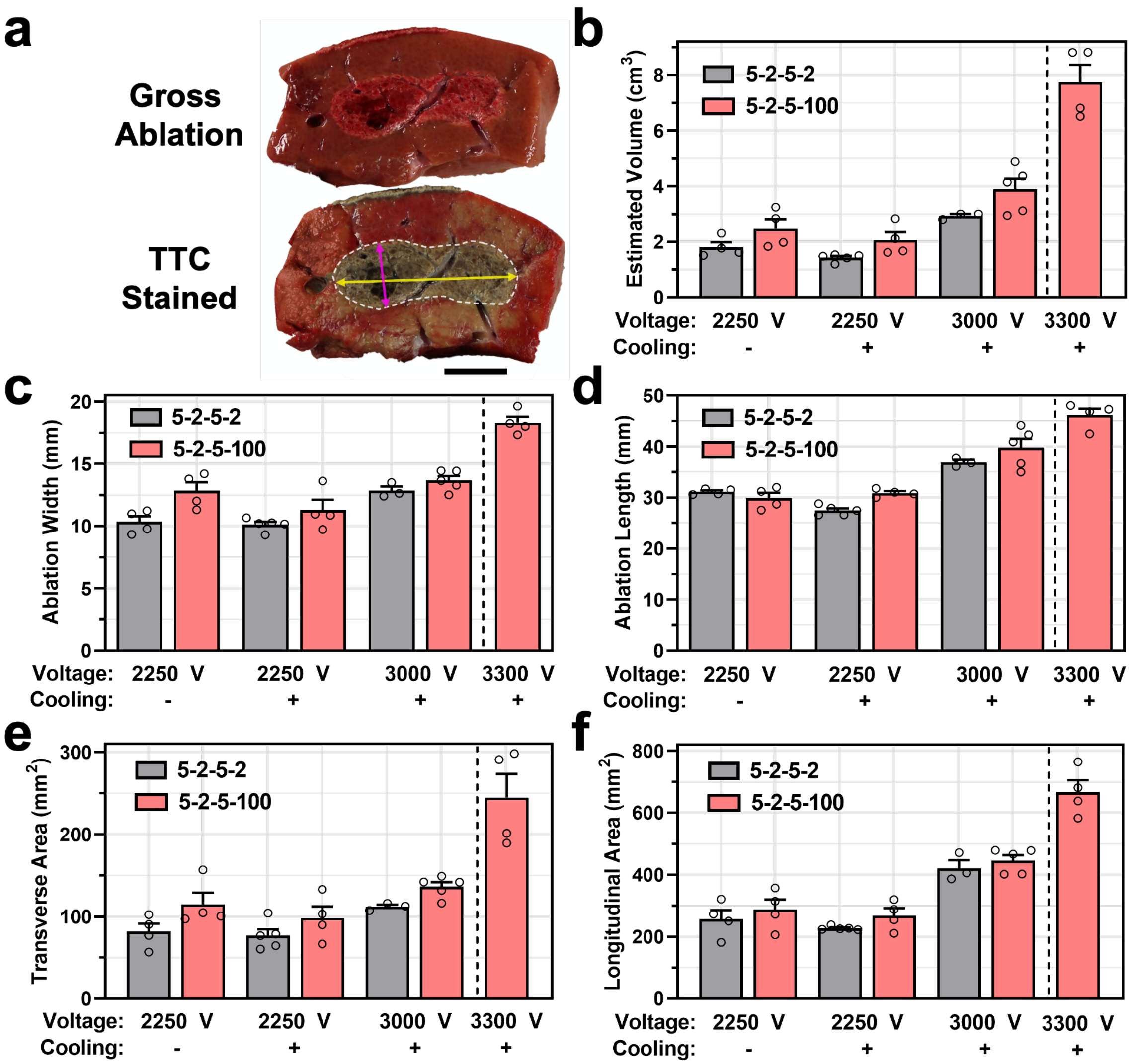

Figure 7.3 – Comparison of single needle H-FIRE ablation measurements from gross tissue samples. Necropsied tissue was stained with TTC for ~10 min prior to overnight fixation in formalin. Representative images of an ablation before and after staining and fixation are shown in (a) with the width (pink line), length (yellow line), and longitudinal area (white dashed line) indicated. Estimated ablation volumes (b) were generated from measured lesion widths (c) and lengths (d) assuming the volume was ellipsoidal. We also measured the ablation area in the transverse (e) and longitudinal planes (f). Scale bar = 1 cm.

the area contained within the outer edge of this hyperechoic rim and the region of ablation measured grossly (**Figure 7.4d-e**). Both the longitudinal (**Figure 7.4d**) and the cross-sectional (**Figure 7.4e**) area measurements agreed ($R^2 = 0.87$). Gross longitudinal areas tended to be slightly larger than those measured with ultrasound (**Figure 7.4d**), while the trend flipped for transverse areas in all cases except the highest energy groups (**Figure 7.4e**). Within the range of ablation sizes reported in this work, the predicted difference in ablation area did not exceed 9%.

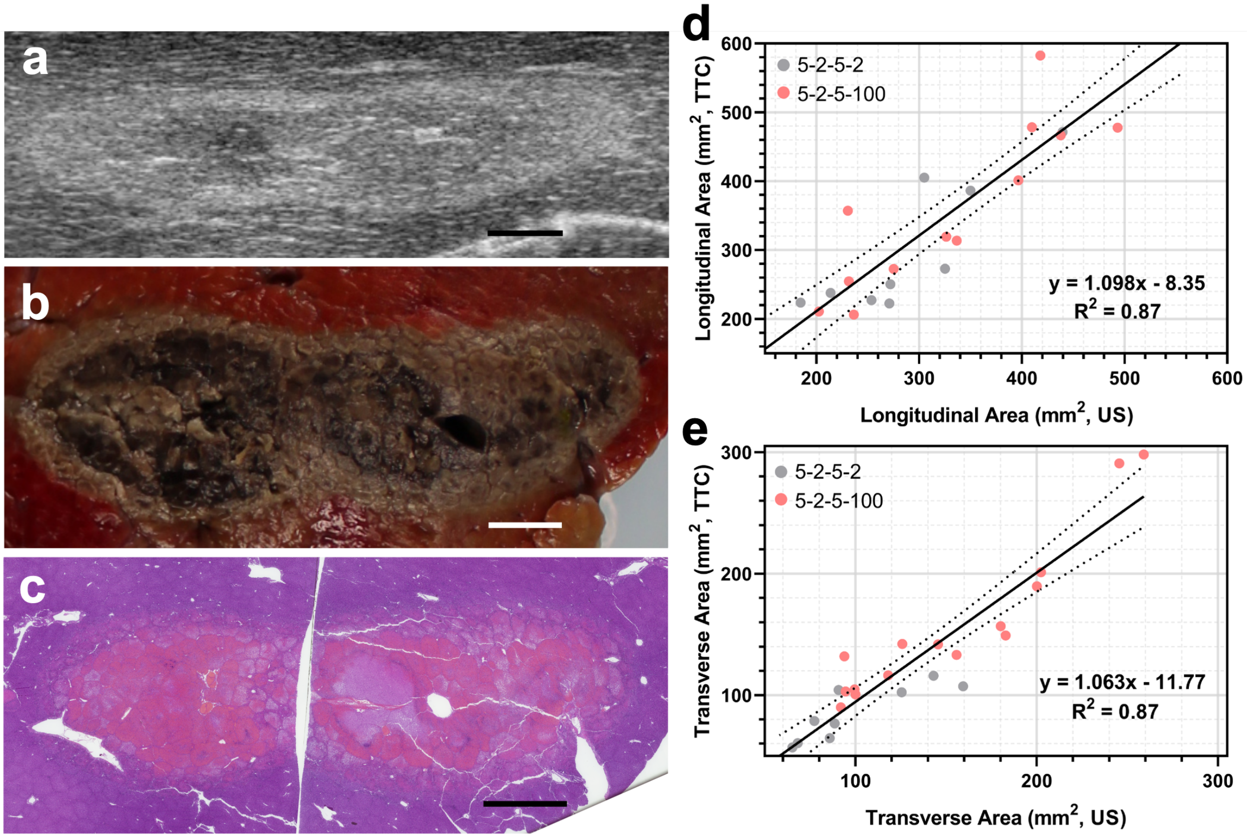

Figure 7.4 – H-FIRE ablations were similar in size and shape across measurement modalities. (a-c) Representative lesion images as obtained by (a) Ultrasound, (b) Gross metabolic staining with TTC, and (c) Histological examination with H&E. Ultrasound and gross lesion areas were measured in both the (d) longitudinal and (e) transverse planes and agreement between measurements was quantified via linear fitting. Scale bar = 5 mm.

7.3.5 – Analysis of Thermal Effects

Gross samples were inspected for tissue whitening, which is typically considered indicative of thermal damage. Other than a couple of ~ 1 mm sections observed in groups 1C and 1M, we did not observe tissue whitening in any instances. The lack of thermal damage was further confirmed by measuring temperature (**Figure 7.5**) near the edge of the proximal electrode on the probe with a fiber optic sensor as shown in **Figure 7.1b**. Measured temperature rise was weakly dependent on the applied waveform, with the 5-2-5-2 showing slightly higher temperatures across comparable groups. Treatments applied without internal cooling at 2250 V resulted in measured temperature increases of up to 12 °C (**Figure 7.5a**). Treatments delivered with internal cooling at 2250 V (**Figure 7.5b**) did not produce a notable temperature change, and temperature rise plateaued at a maximum of ~ 3 °C during cooled treatments applied at 3000 V (**Figure 7.5c**). With the highest energy group, measured temperature rise was 5 °C ± 2 °C (**Figure 7.5d**). Further examination of any potential thermal damage was performed by assessing the structure of small hepatic vessels histologically. **Figure 7.6** shows a representative ablation produced with the 5-2-5-100 at 3,000 V. Each inset depicts a high-magnification image of a portal triad in different regions including untreated liver (**Figure 7.6b**), ablated liver near the boundary (**Figure 7.6c**), and ablated liver near the center (**Figure 7.6d**). In panels **7.6c** and **7.6d**, it can be seen that the structural integrity of the portal triad is preserved despite decimation of cells in the hepatic parenchyma surrounding it.

7.3.6 – Histological Examination and Immunohistochemistry

Histological and IHC analyses were performed to provide deeper insights into the type and extent of cell and tissue damage occurring in the ablated regions, to investigate immune infiltration, and to confirm the absence of thermal damage. Regions of ablation as visualized by routine H&E as well as IHC are shown in **Figure 7.7**. Compared to the area of cell depletion as visualized by H&E (**Figure 7.7a-c**), areas of apoptotic cell death were localized to the periphery of the ablation (**Figure 7.7d-f**). Generally, infiltrating immune cells also seemed localized to these areas (**Figure 7.7g-i**). However, upon close examination, it can be seen that at the cell level, $CD4^+$ cells correlate extremely well with apoptotic cells, while $CD68^+$ cells seemed to be located even more peripherally than cells undergoing caspase cleavage. Additionally, immune infiltrates tended to follow vascular tracks closely, while apoptotic cells were discovered more diffusely throughout hepatic lobules.

7.3.7 – Electrical Properties and Computational Modeling

"Voltage ramps" were performed after probe insertion and prior to treatment delivery. These consisted of a stepwise increase in applied electrical potential with concurrent recording of voltage and current across the tissue. Recorded electrical current at each voltage level can be seen in **Figure 7.8a**. The dynamic electrical conductivity functions constructed for either waveform are shown in **Figure 7.8b**. For both waveforms, and as expected, current increase was slightly nonlinear, consistent with the notion that increased current pathways arise at increased field strengths due to membrane electroporation, as reflected in the numerically predicted conductivity functions (**Figure 7.8b**). Measured current was almost always higher for the 5-2-5-2 waveform in comparison to the 5-2-5-100, which resulted in a slightly higher baseline conductivity (0.22 S/m vs. 0.20 S/m) and a more significant increase in the electroporated conductivity (0.53 S/m vs. 0.45 S/m). The sigmoidal curves took on similar transition field strengths and slopes during the transition were also similar, suggesting that the onset of electroporation and its dynamics were similar between the two waveforms. Once tissue characterization was completed, transient numerical models were employed to estimate the electric field distribution (**Figure 7.8c**) and lethal threshold (**Figure 7.8d**) for each treatment group. In all cases, the lethal threshold was slightly lower for the modified waveform as compared to the control waveform, but this was statistically significant only for the 3,000 V group (879 ± 72 V/cm vs. 1024 ± 20 V/cm, p = 0.016). In the highest energy group (4M), the lethal threshold was computed to be 633 ± 101 V/cm, significantly lower than that of any other group under test.

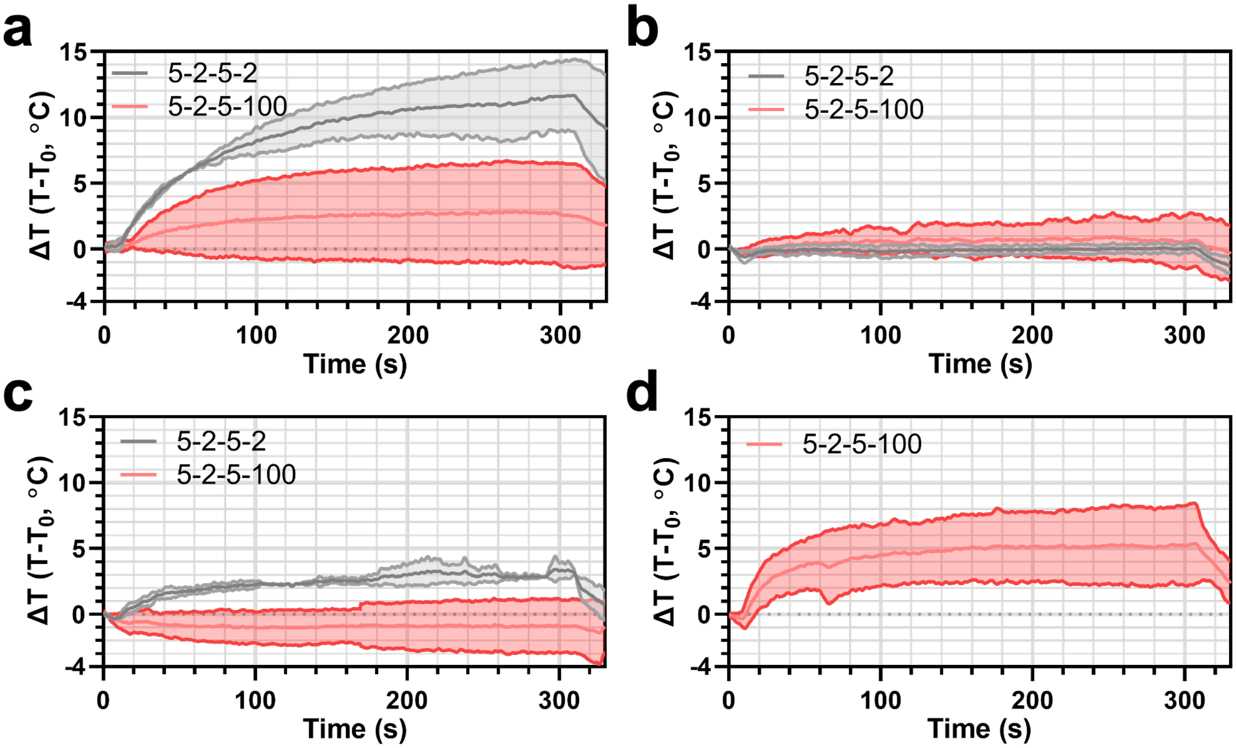

Figure 7.5 – Temperature recordings confirm non-thermal nature of ablations performed in the current study. A fiber optic temperature probe was used to record temperature rise in at least 2 separate experiments with each treatment condition. Shown are the mean ± SD contours for both waveforms when performed at (a) 2250 V with no cooling, (b) 2250 V with cooling, (c) 3000 V with cooling, and (d) 3300 V with cooling.

7.4 – Discussion

The primary goal of the current study was to evaluate the size of non-thermal ablations possible with single-needle H-FIRE. To initiate this investigation, we first sought to determine the maximum voltage that could be applied with a bipolar electrode, as pulse duration and voltage are the foremost factors regulating ablation size. Our preliminary data suggested that electrical arcing would limit the extent to which applied voltage could be increased with this electrode geometry

(Aycock, Campelo, et al., 2022). Arcing is also a limiting factor in IRE treatments and has been observed even with a multi-needle geometry (Guenther et al., 2015; Kaufman et al., 2020). Thus, we used an agar-based tissue phantom designed to mimic liver tissue to investigate the voltage at which electrical arcing would occur with various H-FIRE waveforms. We hypothesized that duty cycle was the primary driving force behind the risk of arcing. While this was mostly true, our results suggest the mechanism is more nuanced (**Figure 7.2b**). For instance, at low duty cycles, bursts with the shortest pulse duration required the highest applied potential to generate an arc. However, at higher duty cycles, longer pulse durations required higher applied potentials for arcing. While we performed this investigation purely to understand waveform parameters allowing for the highest voltages *in vivo*, we suspect the observed trends are the result of electrolysis creating hydrogen bubbles around the electrodes. Thus, we speculate that a more rigorous investigation into bubble production, coalescence, and cavitation during the burst would mechanistically explain our results.

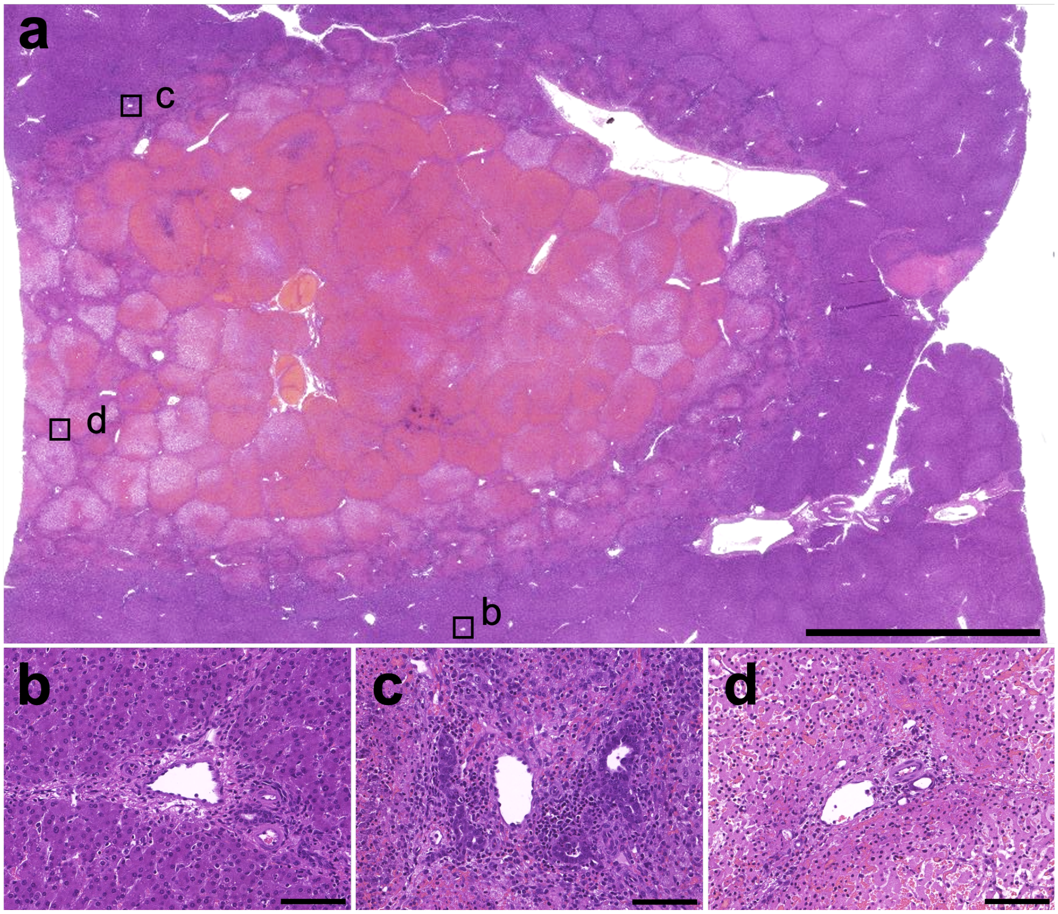

Figure 7.6 – Hepatic vasculature and biliary structures were preserved even in high energy ablation zones. (a-d) Representative H&E photomicrographs demonstrate intact portal triads within H-FIRE ablations. Three regions of a treatment performed with internal cooling at 3000 V are marked in the (a) whole-slide ablation image representing the hepatic parenchyma that was untreated (b), within the ablation at the peripheral boundary (c), and in the center of the hemorrhagic ablation (d). High-magnification micrographs of the portal triad at each location show intact portal venules, hepatic arteries, and bile duct branches. Scale bar = 5 mm (a), 100 μm (b-d).

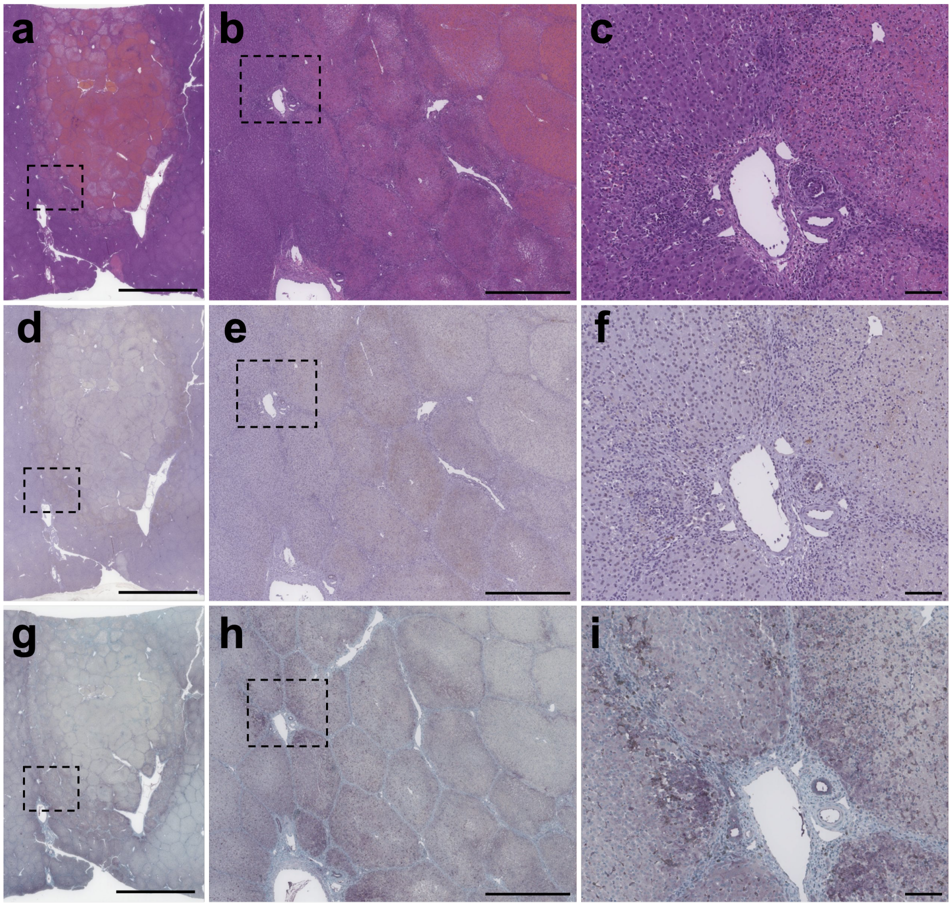

Figure 7.7 – Histological and immunohistochemical characterization of ablation regions. Representative low, medium, and high-magnification images are shown for an ablation produced with group 3M (5-2-5-100, 3000 V, internal cooling). Standard staining with H&E shows the (a) whole-slide image, (b) 2.3X magnification image of the ablation boundary, and (c) 10X image of the ablation boundary. Also shown are the (d-f) same regions stained with an antibody against cleaved caspase 3 (brown) and the (g-i) dual-staining results with antibodies against CD4 (T lymphocytes, brown) and CD68 (macrophages, violet). Scale bars = 5 mm (a,d,g); 1 mm (b,e,h); 100 µm (c,f,i).

Notably, the modified waveforms we previously introduced to help mitigate muscle contractions – those with long interpulse delays ($d_{ip} \geq \sim 100$ µs) – were also found to reduce the risk of electrical arcing. Compared to a typical 5-2-5-2, the 5-2-5-100 allowed for the delivery of therapy with an increase in applied potential of more than 750 V (a 23% increase). This allowed us to deliver more energy *in vivo*, significantly improving ablation dimensions and volumes relative to our controls. Volumes were also significantly than those published in prior studies, in which only up to 2,250 V has been applied with this electrode geometry (O'Brien, Passeri, et al., 2019; Partridge et al., 2020; Passeri et al., 2018). The use of internal electrode cooling limited temperature rise, maintaining the non-thermal aspects of H-FIRE.

It has been reported that neoplastic tissue tends to be more susceptible to damage from pulsed fields in comparison to non-neoplastic tissue (Aycock et al., 2022; Ivey et al., 2015; Partridge et al., 2020). With this in mind, ablation dimensions reported in this study should be considered conservative. In fact, estimating the lethal thresholds of liver tumors based on the relationship between non-neoplastic/neoplastic tissue reported by *Partridge et al.*, computational modeling suggests that with the highest energy group reported in this study, it would be possible to achieve ablation volumes of 10.9 cm^3 with a minimum dimension of approximately 2.1 cm (Partridge et al., 2020).

Though our study contributes important findings to the field of non-thermal ablation using pulsed electric fields, some limitations must be considered. First, we chose to employ an open approach to make sure that several ablations could be performed without overlap in each animal. While this was convenient for our experimental protocol, it is not representative of how similar procedures would occur clinically, where an ultrasound-guided transcutaneous approach would more than likely be implemented. Additionally, as a precaution, we used neuromuscular blocking agents in this study. This was done to avoid the possibility of muscle contractions limiting our ability to place ablations immediately adjacent to the diaphragm and so that arcing would be the only factor limiting our applied voltage. While we anticipate that muscle contractions would not be of concern with the waveforms used in this study, particularly the modified waveform, future work will be required to demonstrate that this holds true even at the elevated potentials applied here.

The bipolar probe geometry employed in this work is not the only type of single-insertion device that has been used for delivery of pulsed electric fields. Before beginning the current study, we compared the maximum applied voltage achievable with 1) a monopolar probe with a distant grounding pad (M+GP) and 2) a single bipolar probe, each of which have unique limiting factors. The M+GP geometry is attractive due to its ability to produce relatively spherical electric field distributions (DeWitt et al., 2019; Sano, DeWitt, et al., 2018). In a preliminary study, we compared muscle contractions resulting from the M+GP with three different GP locations: the outside of hind limb, the medial mid-lower back, and the medial abdomen cranial to the hip socket. We found

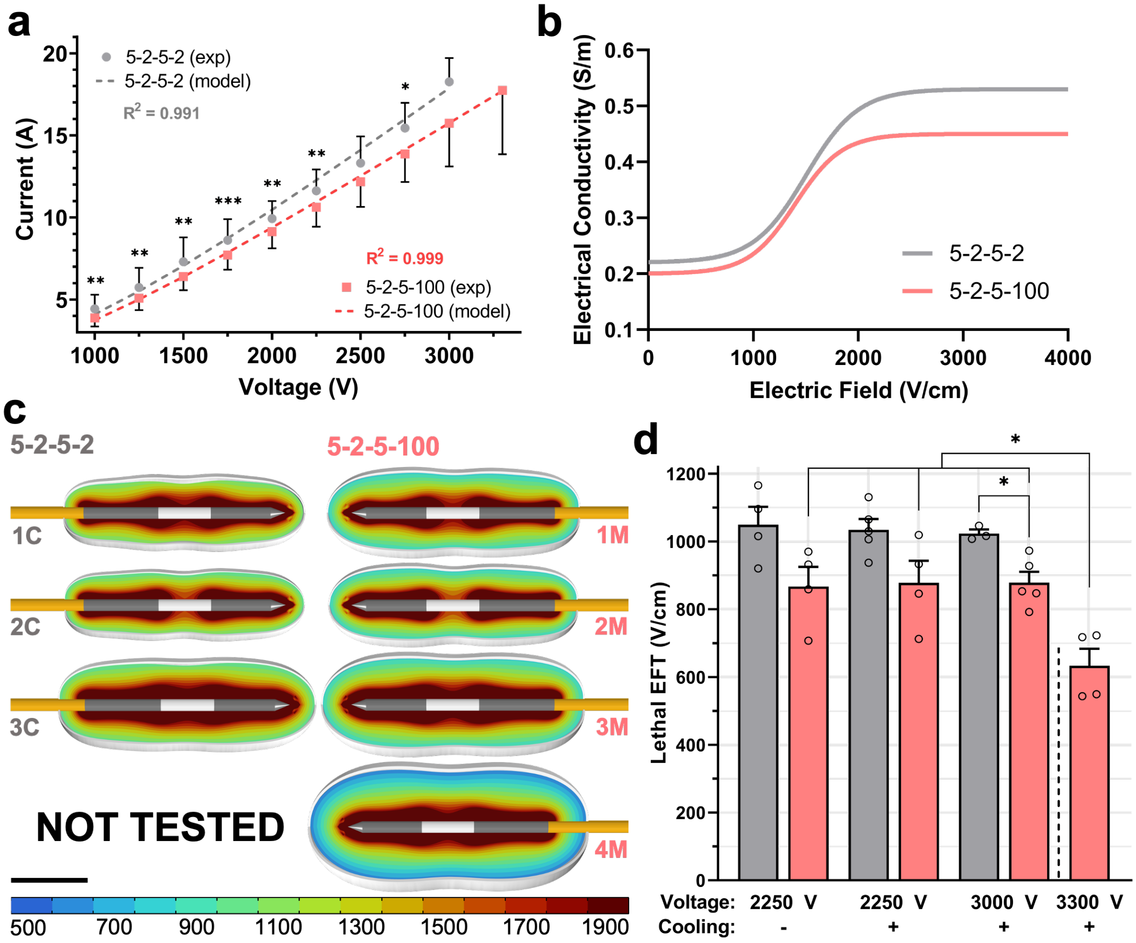

Figure 7.8 – Characterization of electrical behavior and computational modeling of single-needle H-FIRE ablations. (a) Electrical current was recorded in 250 V increments beginning at 1000 V and ending at the treatment voltage in all experiments. These data were used to construct a (b) dynamic conductivity function for each waveform for use in numerical models. The (c) electric field distribution [V/cm] is shown for each treatment group, along with the simulated ablation region (white outline). These contours were used to compute the (d) lethal electric field threshold for all protocols. Scale bar = 1 cm.

that muscle contractions were minimized when the GP was placed on the lower abdomen, but that even with neuromuscular blocking agents, significant contractions (~9 m/s^2) precluded the applied voltage from being elevated beyond 1,000 V (data not shown). Based on this finding, we proceeded to conduct the current study with a bipolar electrode.

7.5 – Conclusion

H-FIRE is an emerging non-thermal ablation modality with the potential to supersede conventional IRE due to its advantages such as reduced risk for arrhythmia and muscle contractions and improved predictability of electric field distributions. However, H-FIRE ablation dimensions have remained small. In this work, we present solutions to technical challenges that have limited the ability to generate considerable ablation volumes with H-FIRE. Using an internally cooled, single-insertion electrode, we report the ability of H-FIRE to rapidly (5 minutes) produce ablations of ~ 2 cm x 4.5 cm with volumes up to 8 cm^3. We demonstrate that ablation volumes were non-thermal in nature and resulted in significant immune infiltration 24 hours following the procedure. This study provides a foundation for future work seeking to optimize devices and waveforms toward enabling H-FIRE to rapidly treat 3 cm neoplasms.

8 – Treatment of Spontaneous Hepatocellular Carcinoma in Canines with High-Frequency Irreversible Electroporation

8.1 – Introduction

The work leading up to this point has been devoted primarily to improving pulse parameters to expand the capabilities of non-thermal ablation with pulsed electric fields. While improvements in pulsed field delivery and devices are the main focus of this dissertation, it is equally critical to understand the fundamental response of tissues of interest following treatment with H-FIRE.

Past work has suggested that H-FIRE exhibits selectivity toward malignant cell phenotypes, but this hypothesis has only been evaluated in highly controlled *in vitro* experiments (Ivey et al., 2015; Partridge et al., 2020). Thus, in this chapter, we sought to understand whether early observations would hold true *in vivo*, where several factors beyond the individual cellular biophysics also contribute to ablation development such as local perfusion and immune cell invasion (Neal et al., 2013; Ringel-Scaia et al., 2019).

This dissertation culminates in the use of H-FIRE to treat veterinary patients with primary hepatocellular carcinoma (HCC) at the VA-MD College of Veterinary Medicine. We used H-FIRE to treat HCC and non-neoplastic liver with an identical geometry and pulsing regimen as reported by (Partridge et al., 2020) to investigate whether H-FIRE selectively targets neoplastic cells. Because the inability to effectively target infiltrative malignant cells beyond the tumor boundary is a major contributor to both local and distant recurrence, we hope these findings present a small step toward overcoming this major clinical burden.

8.2 – Methods

8.2.1 – Canine Patients

Client-owned dogs diagnosed with HCC were recruited to the Animal Cancer Care and Research Center at the Virginia-Maryland College of Veterinary Medicine. Patients were screened for inclusion with a complete blood count (CBC), serum chemistry, urinalysis, prothrombin time, and partial thromboplastin time. Candidates were staged with thoracic and abdominal triple phase computed tomography (CT). Ultrasound-guided needle core biopsies were also collected from the suspicious mass prior to enrollment. Owner-informed consent was provided prior to enrollment, and the study was approved by the Virginia Tech Institutional Animal Care and Use Committee.

8.2.2 – CT Imaging

All images were obtained using an Aquilion 64 (Toshiba, Tokyo, Japan) whole body CT scanner. Patients were anesthetized via inhaled isoflurane with a breath hold during the scan. Pre-contrast, immediate, 1-minute, and 3-minute delay sequences were acquired. Following the pre-contrast scan, iopromide contrast agent (Ultravist, Bayer, Whippany, NJ) was administered with a pressure injector (Medrad Stellant, Bayer, Whippany, NJ). Images were examined in the Horos image viewer and with 3D Slicer (an open-source medical image analysis software). CT images were collected prior to surgery, and when possible post-H-FIRE images were obtained ~1 day, ~4 days and ~30 days after surgery. Ablation regions visualized on CT were independently measured by three skilled users and averaged to obtain ablation length, width, and volume for each patient.

8.2.3 – Pre-Treatment Planning

Prior surgery, pre-treatment CT scans were imported into 3D Slicer for segmentation of the relevant anatomical features including the liver, tumor(s), hepatic vasculature, gallbladder, ribs, and other nearby anatomy as needed. Three-dimensional segments were exported to stereolithography (.stl) files and imported into 3Matic (Materialise, Leuven, Belgium). Here, all segments were wrapped and smooth, interfaces were sealed, and a non-manifold assembly was created for volumetric meshing. The mesh was imported into Comsol Multiphysics v5.6 (COMSOL AB, Stockholm, Sweden). The desired electrode(s) were constructed and placed in the tumor in the region to be treated. The electrode geometry was empirically chosen based on discussions among an interdisciplinary team of veterinarians and engineers with consideration given to the volume of liver to be treated as well as the proximity to critical structures. Numerical simulations were performed as previously described (Latouche et al., 2017; Partridge et al., 2020). Electroporation and temperature-dependent changes in tumor electrical conductivity were

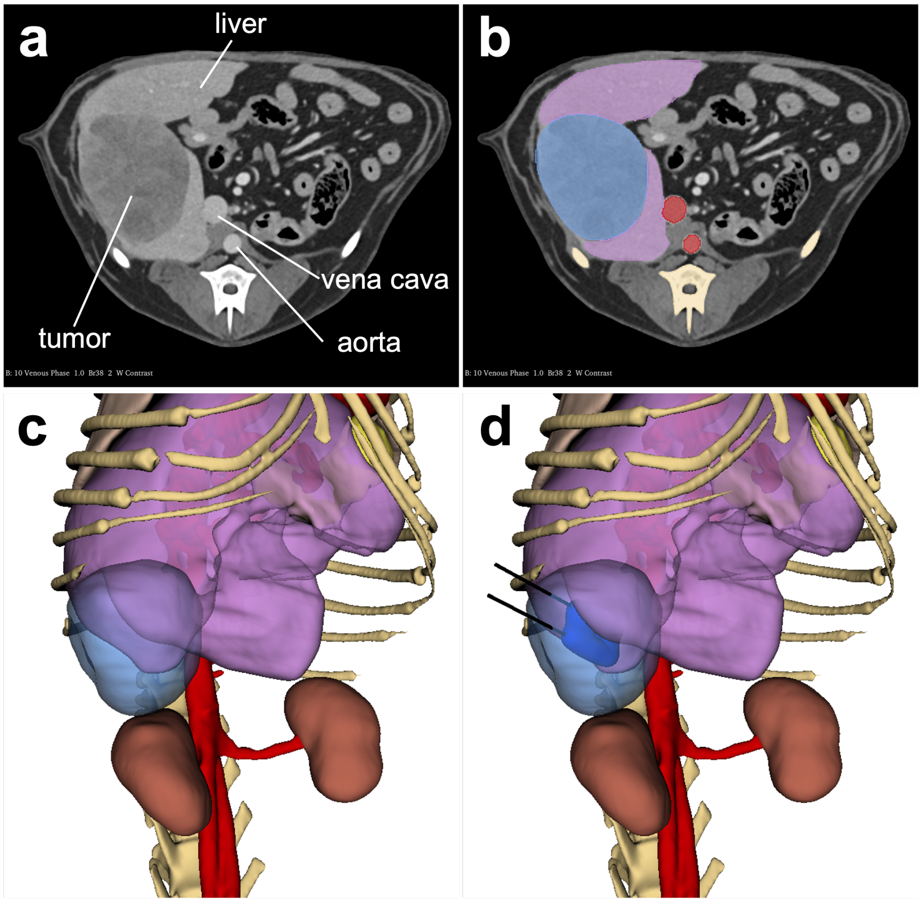

Figure 8.1 – Treatment planning pipeline for canine HCC tumors. (a) A representative post-contrast CT scan showing a large, hypoattenuating mass in the caudal right liver. (b) Relevant anatomical features including the liver, tumor, nearby vasculature, and landmark features such as kidneys and bones were segmented using an open-source medical image analysis software. (c) 3D reconstruction was performed, and segments were imported into Comsol Multiphysics for simulation of the (d) estimated ablation volume and insertion approach.

included in simulations of the electric field distribution. Simulations were performed to estimate the treatment volume and dimensions and to ensure the absence of relevant thermal effects.

8.2.4 – Surgical Procedures

Canines were placed under inhalation anesthesia for H-FIRE ablation and surgery. A routine ventral abdominal approach was used to access the affected liver lobe(s). Once the target lesion was identified, the lobe was isolated for H-FIRE treatment. In most cases, one or two bipolar probes were used. In the case of dual probes, a custom 3D printed electrode holder was used to maintain the desired spacing. When possible, a small portion of non-neoplastic liver was treated in addition to the tumor ablations. In these cases, a single bipolar probe was used. Probe(s) were advanced into the target lesion approximately 4-5 cm, and treatment was initiated immediately after placement was confirmed. When possible, tumors were resected following H-FIRE. Non-neoplastic tissue was not resected.

8.2.5 – H-FIRE Treatment

H-FIRE bursts were delivered with a custom high-voltage generator (VoltMed Inc., Blacksburg, VA). In all cases, treatment was administered at an applied voltage-to-distance ratio of 1,500 V/cm. The voltage waveform consisted of 2 μs bipolar pulses, with each subsequent pulse

Table 8.1 – Summary of treatment configurations and data collected from canine patients

Patient #[a]	Tumor Treatment	Non-neoplastic Treatment	Follow-Up CT	Ablation Vol. Data (T/NN)[b]
1	Single bipolar	–	4d	T
2	Single bipolar	–	4d	T
3	Single bipolar	–	4d	T
4	Dual bipolar	Single bipolar	1d, 4d	T*/NN
5	Dual monopolar	Single bipolar	1d, 4d	T*/NN
6	Single bipolar	Single bipolar	1d, 4d	NN
7	Single bipolar	Single bipolar	1d, 4d	NN
8	Dual/single bipolar[c]	–		

[a]Patients 1-3 from *Partridge et al., 2020*; [b]T – tumor, NN – Non-neoplastic; [c]3 dual and 2 single bipolar treatments
*ablation size cannot be directly compared within this patient due to probe geometry mismatch

separated by a 5 μs delay. Bipolar pulses were repeated 25 times to achieve 100 μs of energized time per burst. For single bipolar probe treatments, 200 bursts were delivered in total. Bursts were split into 4 sets of 50 with a 30 second delay after each set to minimize thermal effects. When dual bipolar probes were used, 100 total bursts were delivered across each of 4 electrode pairs in sets of 25. A 30 second delay was implemented after every other set. **Figure 8.2** illustrates the pulse sequencing strategy. In all cases, a pre-treatment "voltage ramp" was performed to characterize the electrical properties malignant and non-neoplastic canine liver, as well as to ensure the absence of muscle contractions. This procedure involved the delivery of 3 bursts at a sub-electroporative voltage (25 V), then at incrementally increasing voltages until the treatment voltage was reached. At each step, delivered voltage and current were measured with an Enhancer 3000 (Harvard Apparatus, Cambridge, MA) high-voltage probe and a passive current monitor (3972, Pearson Electronics, Palo Alto, CA), respectively, each of which were connected to an oscilloscope (3024z, Teledyne LeCroy, Thousand Oaks, CA). The resulting voltage and current data were used to fit

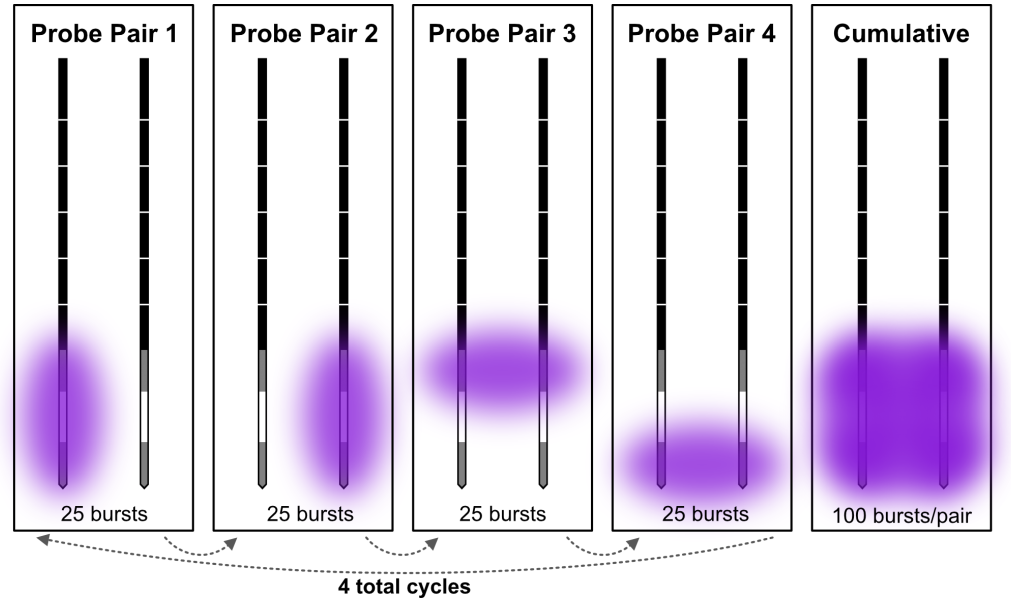

Figure 8.2 – Pulse sequencing strategy used to treat HCC patients with dual bipolar electrodes. To maximize treatment volume in neoplastic liver, a dual bipolar electrode geometry was employed. Four probe pairs were each individually pulsed with 25 bursts as shown. This sequence was repeated three more times to achieve a total of 100 bursts per pair. In non-neoplastic tissue, only a single bipolar electrode was used, and 200 bursts were delivered as 4 sets of 50 with 30 second delays after each set.

curves describing the electroporation-dependent electrical conductivity to tumor and non-neoplastic tissue in each patient. The sigmoidal function describing the local electrical conductivity, σ, as a function of the local field magnitude, $|\vec{E}|$, is given by:

$$\sigma(|\vec{E}|) = \sigma_0 \left(1 + A \cdot flc2hs(|\vec{E}| - E_{del}, E_{range})\right) \tag{8.1}$$

where σ_0 is the baseline electrical conductivity prior to electroporation, A is a conductivity multiplier describing the fold-change in conductivity due to electroporation effects, E_{del} is the field at which σ is at the midpoint between its minimum and maximum value, and E_{range} represents half the span of the transition zone.

8.2.6 – Statistical methods

All statistical analyses were performed in GraphPad Prism v9.5 (GraphPad Software LLC, San Diego, CA). For comparison of ablation dimensions and electrical behavior between non-neoplastic and malignant liver, unpaired students' t-tests were used with α set to 0.05. Data are presented as mean ± SD unless otherwise stated.

8.3 – Results

8.3.1 – Treatment Delivery and Intraoperative Monitoring

In all canine patients, H-FIRE therapy was successfully delivered. Neuroparalytics were not used in any of the clinical cases reported herein, and the target VDR of 1500 V/cm was achieved in all treatments in the absence of notable muscle contractions. As these treatments were delivered using an open approach, mild twitching of the abdominal wall was observed in some cases. Anecdotally, this effect seemed related to 1) the distance between the activated probe pair and the abdominal wall, and 2) the presence of fluid and/or seemingly necrotic tissue between the probes, which could have provided a current pathway to the abdominal muscles. In two patients, cardiac synchronization was used as a safety precaution. In all other patients, bursts were delivered at 1 Hz. Neither cardiac interference nor arrhythmia were observed in any of these cases. Thus, though not rigorously examined in a dedicated study, H-FIRE appeared to be safe to deliver to HCC and non-neoplastic liver without concern for cardiac complications.

8.3.2 – Comparison of Ablation Size in Malignant and Non-neoplastic liver

The first goal of the current study was to determine whether the purported "selective targeting" of H-FIRE can be realized in a clinical setting. To this end, H-FIRE therapy was administered to 4 canine patients with spontaneous HCC with identical treatment parameters as reported by Partridge and colleagues (Partridge et al., 2020). H-FIRE ablations of HCC resulting from treatment in their study are shown in **Figure 8.3**. In the present work, non-neoplastic H-FIRE ablations in 4 canines were monitored via triple phase, contrast enhanced CT 24 hours and 4 days after treatment. CT images of the lesions resulting from treatment at each timepoint are shown in **Figure 8.4**. One day after treatment (**Figure 8.4a-d**), lesions visualized on CT were characterized by a peanut-shaped region of hypoattenuation surrounded by a thin hyperattenuating rim. Lesion

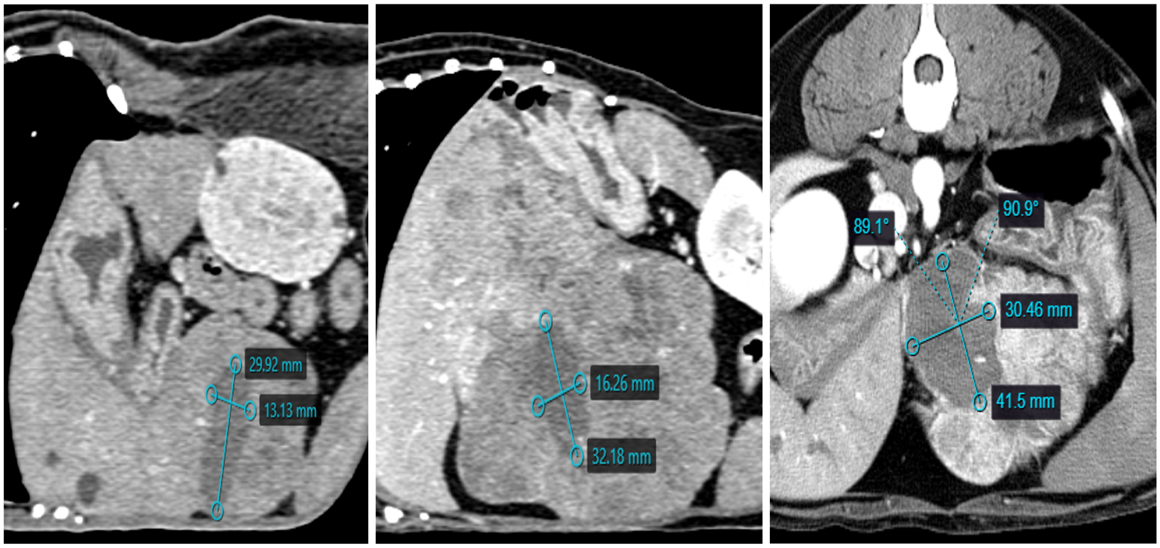

Figure 8.3 – CT images acquired 4 days following H-FIRE ablation of canine HCC with a single-insertion bipolar electrode (Partridge et al., 2020). Ablations were characterized by a relatively uniform, ellipse-shaped region of hypoattenuation. Ablation length (along axis of probe insertion) and width (orthogonal to probe insertion) measurements are highlighted.

length and width measured 21.6 ± 1.2 mm and 7.9 ± 2.1mm, respectively. By four days (**Figure 8.4e-h**), the hyperattenuating rim was no longer visible, and the region of hypoattenuation was markedly reduced. At this point, length and width were 16.9 ± 4.8 mm and 5.8 ± 1.3 mm, respectively. Comparing measurements 4 days following treatment in the present work to those reported in the Partridge study (also 4 days), we found that ablation length (p = 0.008) and width (p = 0.03) were both significantly smaller in non-neoplastic liver, leading to a striking difference in ablation volume between the two (**Figure 8.5a**). Serial CT imaging of the H-FIRE lesions in non-neoplastic liver showed that not only were the lesions small in size, but also recovered on a rapid timeline. Ablation volume was reduced by 53% ± 11.6% on scans acquired 4 days after therapy in comparison to those acquired only 24 hours after treatment (**Figure 8.5b**). Images were also obtained 30 days after H-FIRE therapy in non-neoplastic liver in one patient, and the region of ablation was completely indiscernible (not shown).

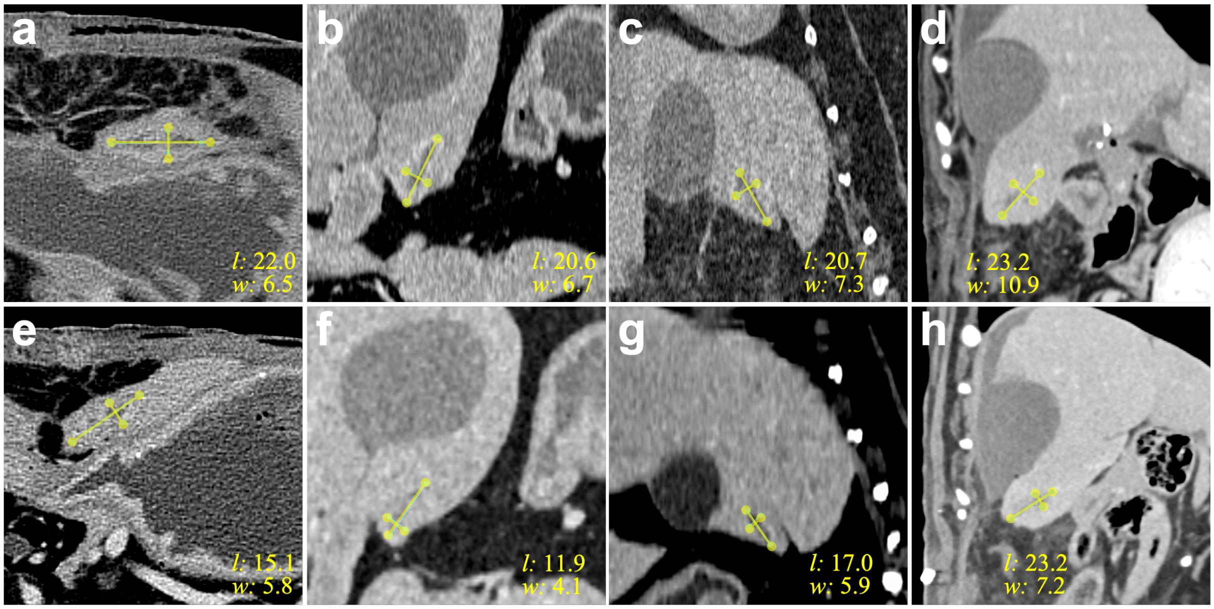

Figure 8.4 – Non-neoplastic liver is resistant to H-FIRE ablation and recovers rapidly. Post-contrast CT images are shown for 4 patients (a-d) 24 hours after therapy and (e-h) 4 days after therapy. At 24 hours, ablations are characterized by a hypoattenuating core surrounded by a thin hyperattenuating rim. By 4 days, the ablation is smaller and the hyperattenuating rim is no longer present. In each panel, the length (longitudinal to probe insertion) and width (orthogonal to probe insertion) are indicated and their measurements given in millimeters.

8.3.3 – Electrical properties of malignant and non-neoplastic liver

Two methods were used to characterize electrical behavior of cancerous and non-malignant canine liver. Before and after H-FIRE therapy, we applied low-voltage diagnostic pulses to gain insight into how the native electrical impedance of the tissue responded to treatment. Before treatment, but after the aforementioned diagnostic pulse, we also applied a "voltage ramp" in which the electrical impedance of the tissue was examined at a range of sub-electroporative and electroporative voltages, providing insight into the susceptibility of the tissue to electroporation.

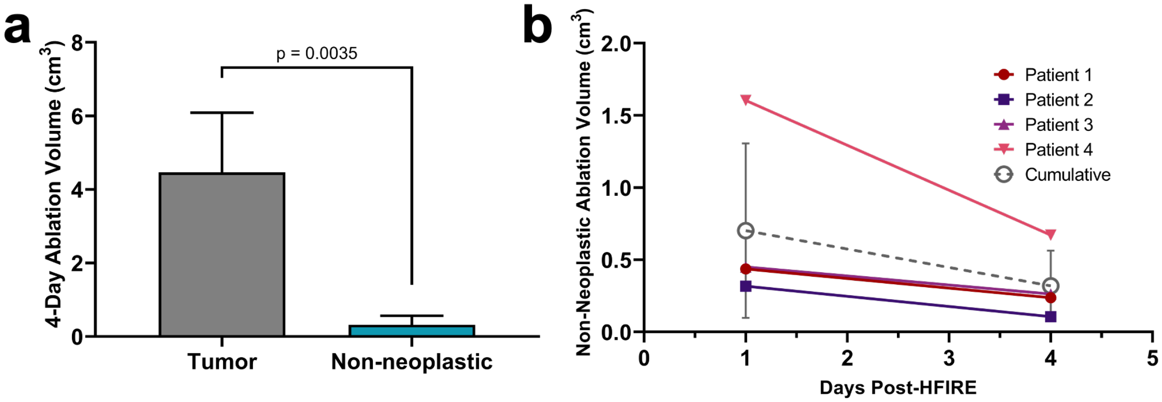

Figure 8.5 – Malignant liver is more susceptible to H-FIRE therapy than non-neoplastic liver. (a) Quantitative comparison between ablation volumes from malignant and non-neoplastic liver treated with H-FIRE based on CT images acquired 4 days after therapy. (b) Volume of ablation in non-neoplastic liver over time from 1 to 4 days post-treatment.

The resulting impedance measurement from the first method are given in **Figure 8.6**.Native electrical impedance before H-FIRE treatment was similar (705 ± 171 Ω vs. 646 ± 101 Ω, p = 0.38) between the two tissue types prior to administering H-FIRE (**Figure 8.6a**). After treatment, liver tumors were significantly less electrically resistant than non-neoplastic liver (408 ± 63 Ω vs. 536 ± 65 Ω, p = 0.0003). This is further reflected in the relative change in resistance for both tissue types quantified on a patient-specific basis (**Figure 8.6b**). In all patients, relative change in low-voltage resistance of tumor tissue was significantly greater than in non-neoplastic tissue. Within each patient, tumor impedance change of tumor tissue was more than double that of non-neoplastic liver ($p \leq 0.0012$ in all cases). Lumping all patients, tumor impedance dropped by 40 ± 10% while non-neoplastic liver fell only 16 ± 6% ($p = 0.025$).

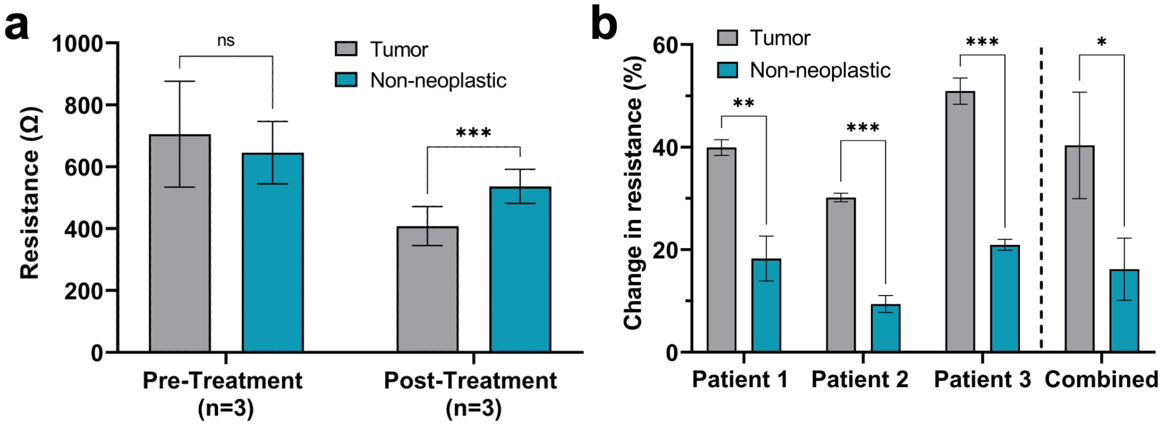

Figure 8.6 – Electrical behavior of neoplastic liver changes more significantly following H-FIRE treatment than non-neoplastic liver. Low-voltage impedance was measured before and immediately after H-FIRE therapy using sub-electroporative, diagnostic electrical pulses. (a) Pre- and post-treatment resistance recorded in 3 canine patients. (b) Change in resistance is shown for 3 individual patients and the overall population (n=3). *p<0.05; ***p<0.001; ****p<0.0001.

As mentioned above, the second method of electrical behavior characterization involved describing the electroporation-dependent conductivity for tumor and non-neoplastic liver for each patient treated in the current study. The dynamic ellipsoidal curves we fitted to voltage and current data are tabulated in **Table 8.2** and illustrated in **Figure 8.7**. Consistent with the low-voltage impedance data, we found that baseline electrical conductivity (σ_0) was similar across both tissue

Table 8.2 – Dynamic electrical property parameters found for HCC and non-neoplastic liver

Patient	Tissue	σ_0 [S/m]	A [-]	E_{del} [V/cm]	E_{range} [V/cm]	R^2
1	HCC	0.116	1.05	800	850	0.9999
2	HCC	0.183	1.2	1100	1100	0.9996
3	HCC	0.104	2.54	800	650	0.9981
Average	HCC	0.134	1.6	900	867	–
1	Non-neoplastic	0.127	0.75	950	550	0.9987
2	Non-neoplastic	0.160	1.2	1600	700	0.9999
3	Non-neoplastic	0.128	1.1	1000	1400	0.9991
Average	Non-neoplastic	0.138	1.02	1183	883	–

types. The change in conductivity due to electroporation was more significant in liver tumors, while the field required to initiate this change (E_{del}) was lower in neoplastic liver.

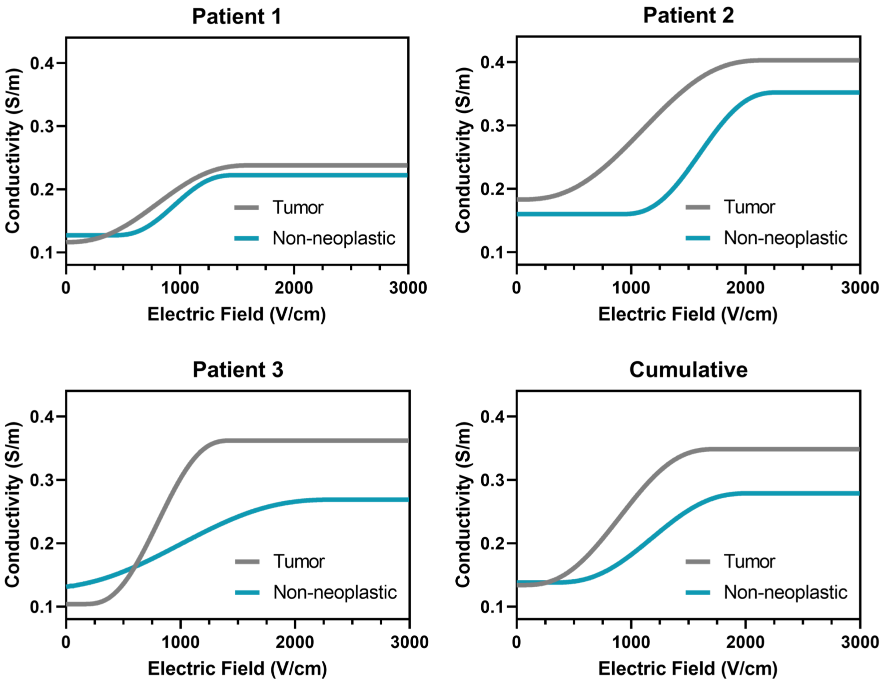

Figure 8.7 – Dynamic electrical conductivity of cancerous liver is distinct from non-neoplastic liver. In each panel, dynamic conductivity curves computed from voltage ramp data are shown for tumor and non-neoplastic tissue. The bottom right panel shows the average curve computed for both tissue types.

8.4 – Discussion

The present study adds significant insight into the ability of H-FIRE to selectively target malignant phenotypes. This effect has been suggested in prior work *in vitro* work, and comparisons have been made between ablations in canine HCC and porcine liver. The current work expands on these investigations by demonstrating selective ablation in a cohort of 4 canines, each of which had background liver cancer. To our knowledge, this is the most robust analysis comparing malignant and non-malignant H-FIRE ablation to date.

H-FIRE treatment in non-neoplastic liver resulted in small, quickly resolving ablations in all four of the trials performed. The largest non-neoplastic ablation observed 4 days after treatment

($0.67\ cm^3$) was 75% smaller than the smallest HCC ablation ($2.72\ cm^3$) observed at the same timepoint. Though we expected to observe smaller ablations in non-malignant liver, the magnitude of the difference we observed was surprising.

It is important to highlight the potential implications of selective targeting. First, this means H-FIRE could provide the opportunity to eradicate infiltrative neoplastic cells while sparing normal hepatocytes at the tumor boundary. In the case of human HCC, the vast majority of patients present with concomitant cirrhosis and liver disease (Llovet et al., 2021). Thus, being able to successfully eliminate neoplastic cells while sparing functional cells could mitigate the risk of liver decompensation following therapy (Kong et al., 2009). Secondly, if the differential response to pulsed electric fields between tumor/non-neoplastic tissue reported here also extends to more sensitive organ systems such as the pancreas and/or brain, drastic improvements in therapeutic outcome relevant to current standard-of-care would be expected. Finally, it is worth highlighting that in some instances, selective ablation could be considered a drawback. For example, it is well known that immune cells within the tumor microenvironment are reprogrammed to promote immune evasion. Thus, in some applications it will inevitably be desirable to ablate a large margin of “non-tumor” parenchymal and stromal cells, and the use of a selective ablation modality could limit the efficacy of creating such a margin.

As mentioned, the preferential killing of cancer cells with H-FIRE has been suggested in prior efforts. However, the mechanism has not been fully described. Theoretically, the effective capacitance of the cell membrane is reduced as waveform frequency is increased, meaning more charge is delivered within the cell rather than polarizing the membrane. This is thought to cause an increase in the potential imposed on the nuclear envelope, since it is the largest intracellular organelle (Kotnik & Miklavčič, 2006). Based on this assumption, the enlarged nuclei typical of neoplastic cells could predispose them to nuclear damage during H-FIRE (Ivey et al., 2015, 2017). Due to the clinical nature of the present study, we did not obtain detailed analyses of the cell size or morphology between the non-neoplastic hepatocytes and the HCC cells, but it has been reported that HCC cells exhibit increased nucleocytoplasmic ratios, which would corroborate this theory (Watanabe et al., 1983).

In addition to comparing ablation outcomes, we investigated potential differences in electrical behavior of HCC and non-malignant liver. We found that the native electrical properties of tumor tissue changed more drastically following H-FIRE than non-neoplastic liver did. This change in low-voltage impedance seen following treatment is likely the result of long-lasting pores that are still present when the post-treatment diagnostic pulses are applied. In non-neoplastic liver, the moderate change in low-voltage impedance suggests that pulses had less of an electroporative effect, or that membrane resealing in the majority of affected cells occurred rapidly after delivery of the last high-voltage pulses. It is also possible that the differences in low-voltage impedance are due to discrepancies in the extent of immediate cell death. While a significant portion of cell damage from H-FIRE occurs on the course of hours to days, there is a population of cells that dies almost instantly due to their exposure to the highest local fields (Brock et al., 2020; Mercadal et al., 2020). It is also worth noting that local temperature increases can account for a reduction in tissue impedance. Because we delivered similar amounts of energy (at a similar rate) within both tissue types, we believe that it is unlikely that thermal effects varied substantially across treatments. However, it is worth considering that the highly heterogeneous electrical environment present in tumors could have caused localized high-field regions.

In addition to the low-voltage impedance changes, tumor tissue was also characterized by an increased susceptibility to electroporation as observed in the dynamic conductivity curves.

These data provide more direct evidence that the membrane effects of H-FIRE are more significant in cancer cells (in addition to the hypothesized nuclear effects). From a utilitarian perspective, these data provide insight into how the electrical signature of HCC tumors changes after H-FIRE therapy, which could be used in the future to define a therapeutic endpoint. The conductivity data can be used to inform treatment plans for electroporation-based therapies by providing material property inputs for tumor tissue as well as surrounding non-neoplastic tissue, both of which are required to provide a complete description of the tissue response to therapy.

Though this work provides compelling evidence demonstrating that H-FIRE selectively ablates malignant phenotypes, there are some limitations to the current study. First, unfortunately we have not had the ability to perform identical therapeutic regimens in both tissue types within the same patient. This is mainly due to the fact that canine patients nearly always present with large HCC tumors that are borderline resectable. The decision to resect or leave the tumor *in situ* is made during surgery, so it is always critical to treat as large of a tumor volume as possible. Though this is obviously beneficial for the canine patients (and their owners) it presents two issues with respect to study design. First, we typically perform multiple H-FIRE ablations in the neoplasm, and to maximize efficiency, we use a dual bipolar probe geometry. This means that if the tumor remains *in situ*, we cannot directly compare the non-neoplastic and neoplastic ablations observed on CT. Secondly, if the tumor is determined to be resectable following H-FIRE therapy, it is immediately removed. This prevents us from obtaining volumetric data, as H-FIRE ablations require approximately 24 hours to fully resolve (Mercadal et al., 2020).

Finally, it is worth noting that it is difficult to ascertain whether the non-neoplastic tissue was injured to the same extent as neoplastic liver and recovered more quickly, if it was more resistant to injury, or if a combination of both was occurring. The ability of neoplastic cells to repair their membranes is likely much lower than that of normal hepatocytes. In fact, though normally quiescent, mammalian hepatocytes (including canine) possess a remarkable ability to undergo compensatory hyperplasia following injury (Kruitwagen et al., 2014; Schotanus et al., 2013). In rats, it has been shown that it takes ~10 days following partial hepatectomy of two-thirds of the liver for the remaining cells to regenerate the liver back to its original mass (Alison et al., 2009). However, in this study, if regeneration alone were to be responsible for the discrepancy in ablation size, we would anticipate that we'd see similar ablations between the non-neoplastic liver at 1 day and the neoplastic liver at 4 days. However, even only 1 day after treatment, the non-neoplastic ablation volumes were significantly smaller than any of the ablations seen in the HCC tissue. Thus, we suspect the main differentiating factor is the resilience of non-neoplastic cells to injury rather than their rapid recovery.

8.5 – Conclusion

We treated peripheral non-neoplastic liver in 4 canines diagnosed with HCC. Our results were compared to ablations resulting from identical H-FIRE therapy administered in 3 canine HCC tumors. The data reported in this chapter demonstrate that H-FIRE ablations were significantly smaller in non-neoplastic tissue as compared to HCC tumors. Ablations in non-neoplastic tissue also recovered rapidly over the course of days. Differential lesion sizes resulting from pulsed electric fields were corroborated by tissue electrical behavior. We found that electrical resistance of malignant tissue changed more significantly after therapy. Increases in electrical conductivity due to electroporation were also more notable in cancerous tissue. These data collectively suggest that electroporation is more efficient in malignant liver, and that non-neoplastic cells are resistant to electropermeabilization and cell death following treatment with high-frequency pulsed fields.

9 – Conclusions and Future directions

9.1 – Overall Conclusions

H-FIRE is a promising non-thermal option for focal tissue ablation. When tuned properly, H-FIRE is capable of offering the same advantages as conventional IRE while obviating the need for intraoperative paralytics and neuromuscular blocking agents. Other potential advantages of H-FIRE that have been demonstrated in preliminary studies include improved predictability of electric field distributions and selective targeting of neoplastic cell phenotypes.

In practice, it has been difficult to realize the postulated benefits of H-FIRE without making sacrifices in terms of ablation size. This is due to the fact that ablation efficiency is a direct function of constitutive pulse duration. With the short pulse durations of 1-2 μs that mitigate muscle stimulation and increase the effective frequency of the waveform, lethal electric field thresholds are ~2× those of IRE, limiting the region of cell death. In this dissertation, we rigorously investigate several different strategies for manipulating burst waveforms toward generating relevant ablation volumes with reduced stimulation of excitable cells.

Our initial work laid the foundation, showing that the overall efficacy of H-FIRE is improved relative to IRE. We then performed two follow-up studies to 1) parametrically investigate the effect of interphase and interpulse delays within bipolar bursts, and 2) compare the advantages and disadvantages of bipolar versus monopolar burst waveforms with varying pulse durations and latent periods. We discovered that manipulating the delays within the burst can drastically change the relationship between nerve stimulation and ablation, both for monopolar and bipolar waveforms.

Our results culminated in the discovery that bipolar pulses with short interphase, but long interpulse delays achieve the most optimal ratio of ablation to stimulation. These waveforms allow for increased constitutive pulse durations with reduced muscle contractions, meaning improved ablation volumes can be achieved. We further demonstrated that modified burst waveforms reduce the risk of electrical arcing, allowing clinicians to increase the applied potential to maximize the treatment region. We confirmed this finding *in vivo* by using a single-insertion electrode to rapidly produce the largest H-FIRE ablations reported to date. Finally, we treated several canine patients with spontaneous liver cancer to 1) evaluate the efficacy of H-FIRE and 2) compare ablation efficacy in non-neoplastic liver and HCC. In this work, we show a stark difference in the lethality of H-FIRE in tumor and non-tumor liver within a clinical setting.

9.2 – Opportunities for future work

This dissertation provides a framework for systematic optimization of microsecond-duration bursts for the generation of targeted cellular damage. Though this work describes significant advancements in our understanding of burst parameters, this constitutes only a small step toward establishing H-FIRE as a first-line therapeutic for the treatment of unresectable cancer.

In the future, H-FIRE could provide a safe, simple, point-of-care option for focal tumor ablation. Ideally, H-FIRE would be performed in an outpatient setting with only mild sedation, expanding the number of candidate patients, and maximizing recovery following therapy. For this to be realized, future work must show that H-FIRE can consistently produce ablations of ~3 cm in the absence of notable muscle stimulation. Further optimization of the burst waveform and clever pulse delivery strategies will likely make this possible in the coming years. It is also imperative that future studies investigate the development of novel applicators capable of expanding the radial dimension of the ablation, as this is what ultimately limits the size of neoplastic lesion that can be targeted. Finally, dedicated safety studies rigorously evaluating the claim that arrhythmias are unlikely with H-FIRE must be carried out to evaluate the risk posed by different waveforms and electrode configurations. It will also be important to determine the minimum proximity between applicator electrodes and the heart to be certain that H-FIRE is implemented safely.

Lastly, we must consider than ablative therapy is only one component of a multifaceted, interdisciplinary approach to cancer care. Thus, H-FIRE will not need to completely eradicate cancer cells on its own in every oncological application. In fact, for many cancer types, this would be considered a wishful fantasy. There is a growing appreciation that a key component of any successful cancer therapy is the stimulation of a strong antitumor immune response (Gotwals et al., 2017). While H-FIRE elicits such a response on its own (Ringel-Scaia et al., 2019), future iterations of the therapy will likely contain a combinatorial strategy of focal biophysical damage to initiate antigen release, alongside a systemic regimen such as immune checkpoint inhibitor therapy. With this in mind, future work describing changes in immune cell populations within the tumor microenvironment for various malignancies will be necessary. In addition to this, because H-FIRE also produces a region of permeabilized cells in the periphery of the ablation zone, it is uniquely positioned to be used alongside chemotherapeutic or biologic adjuvants. For instance, pro-inflammatory plasmids such as IL-12 could be delivered to peripheral cells following H-FIRE ablation with the use of a secondary electrophoretic pulsing paradigm (S. Li et al., 2002).

References

Abidor, I. G., Arakelyan, V. B., Chernomordik, L. V., Chizmadzhev, Y. A., Pastushenko, V. F., & Tarasevich, M. P. (1979). Electric breakdown of bilayer lipid membranes. I. The main experimental facts and their qualitative discussion. *Bioelectrochemistry and Bioenergetics*, *6*, 37–52.

Agarwal, A., Zudans, I., Weber, E. A., Olofsson, J., Orwar, O., & Weber, S. G. (2007). Effect of cell size and shape on single-cell electroporation. *Analytical Chemistry*, *79*(10), 3589–3596.

Agnass, P., van Veldhuisen, E., van Gemert, M. J. C., van der Geld, C. W. M., van Lienden, K. P., van Gulik, T. M., Meijerink, M. R., Besselink, M. G., Kok, H. P., & Crezee, J. (2020). Mathematical modeling of the thermal effects of irreversible electroporation for in vitro, in vivo, and clinical use: a systematic review. *International Journal of Hyperthermia*, *37*(1), 486–505.

Akinlaja, J., & Sachs, F. (1998). The breakdown of cell membranes by electrical and mechanical stress. *Biophysical Journal*, *75*(1), 247–254.

Akinwande, O., Ahmad, S. S., Van Meter, T., Schulz, B., & Martin, R. C. G. (2015). CT Findings of Patients Treated with Irreversible Electroporation for Locally Advanced Pancreatic Cancer. *Journal of Oncology*, *2015*, 1–8.

Alison, M. R., Islam, S., & Lim, S. (2009). Stem cells in liver regeneration, fibrosis and cancer: the good, the bad and the ugly. *Journal of Pathology J Pathol*, *217*, 282–298.

Alnaggar, M., Qaid, A. M., Chen, J., Niu, L., & Xu, K. (2018). Electroporation of malignant liver tumors: Effect on laboratory values. *Oncology Letters*, *16*(3), 3881–3888.

Al-Sakere, B., André, F., Bernat, C., Connault, E., Opolon, P., Davalos, R. V., Rubinsky, B., & Mir, L. M. (2007). Tumor ablation with irreversible electroporation. *PLoS ONE*, *2*(11), e1135.

Al-Sakere, B., Bernat, C., André, F., Connault, E., Opolon, P., Davalos, R. V., & Mir, L. M. (2007). A study of the immunological response to tumor ablation with irreversible electroporation. *Technology in Cancer Research and Treatment*, *6*(4), 301–305.

Altekruse, S. F., Henley, S. J., Cucinelli, J. E., & McGlynn, K. A. (2014). Changing hepatocellular carcinoma incidence and liver cancer mortality rates in the United States. *American Journal of Gastroenterology*, *109*(4), 542–553.

Ansari, D., Kristoffersson, S., Andersson, R., & Bergenfeldt, M. (2017). The role of irreversible electroporation (IRE) for locally advanced pancreatic cancer: a systematic review of safety and efficacy. *Scandinavian Journal of Gastroenterology*, *52*(11), 1165–1171.

Anwanwan, D., Singh, S. K., Singh, S., Saikam, V., & Singh, R. (2020). Challenges in liver cancer and possible treatment approaches. *Biochimica et Biophysica Acta - Reviews on Cancer*, *1873*(1).

Appelbaum, L., Ben-David, E., Faroja, M., Nissenbaum, Y., Sosna, J., & Goldberg, S. N. (2014). Irreversible electroporation ablation: Creation of large-volume ablation zones in in vivo porcine liver with four-electrode arrays. *Radiology*, *270*(2), 416–424.

Arena, C. B., Garcia, P. a., Sano, M. B., Olson, J. D., Rogers-Cotrone, T., Rossmeisl, J. H., & Davalos, R. V. (2014). Focal blood-brain-barrier disruption with high-frequency pulsed electric fields. *Technology*, *2*(3), 1–8.

Arena, C. B., Mahajan, R. L., Nichole Rylander, M., & Davalos, R. V. (2013). An Experimental and Numerical Investigation of Phase Change Electrodes for Therapeutic Irreversible Electroporation. *Journal of Biomechanical Engineering*, *135*(11), 111009.

Arena, C. B., Mahajan, R. L., Rylander, M. N., & Davalos, R. V. (2012). Towards the development of latent heat storage electrodes for electroporation-based therapies. *Applied Physics Letters*, *101*(8), 83902.

Arena, C. B., Sano, M. B., Rossmeisl, J. H., Caldwell, J. L., Garcia, P. A., Rylander, M. N., & Davalos, R. v. (2011). High-frequency irreversible electroporation (H-FIRE) for non-thermal ablation without muscle contraction. *BioMedical Engineering OnLine*, *10*(102), 1–20.

Arena, C. B., Sano, M. B., Rylander, M. N., & Davalos, R. v. (2011). Theoretical Considerations of Tissue Electroporation With High-Frequency Bipolar Pulses. *IEEE Transactions on Biomedical Engineering*, *58*(5), 1474–1482.

Arena, C. B., Szot, C. S., Garcia, P. A., Rylander, M. N., & Davalos, R. V. (2012). A three-dimensional in vitro tumor platform for modeling therapeutic irreversible electroporation. *Biophysical Journal*, *103*(9), 2033–2042.

Aycock, K. N., Campelo, S. N., Salameh, Z. S., Vadlamani, R. A., Lorenzo, M. F., & Davalos, R. v. (2022). Extended interpulse delays improve therapeutic efficacy of microsecond-duration pulsed electric fields. *Proceedings of the Annual International Conference of the IEEE Engineering in Medicine and Biology Society, EMBS*, *2022-July*, 5021–5024.

Aycock, K. N., & Davalos, R. v. (2019). Irreversible Electroporation: Background, Theory, and Review of Recent Developments in Clinical Oncology. *Bioelectricity*, *1*(4), 214–234.

Aycock, K. N., Vadlamani, R. A., Jacobs, E. J., Imran, K. M., Verbridge, S. S., Allen, I. C., Manuchehrabadi, N., & Davalos, R. v. (2022). Experimental and Numerical Investigation of Parameters Affecting High-Frequency Irreversible Electroporation for Prostate Cancer Ablation. *Journal of Biomechanical Engineering*, *144*(6), 1–11.

Aycock, K. N., Zhao, Y., Lorenzo, M. F., & Davalos, R. V. (2021). A Theoretical Argument for Extended Interpulse Delays in Therapeutic High-Frequency Irreversible Electroporation Treatments. *IEEE Transactions on Biomedical Engineering*, *68*(6), 1999–2010.

Ball, C., Thomson, K. R., & Kavnoudias, H. (2010). Irreversible electroporation: A new challenge in "out of operating theater" anesthesia. *Anesthesia and Analgesia*, *110*(5), 1305–1309.

Baur, A. D. J., Collettini, F., Enders, J., Maxeiner, A., Schreiter, V., Stephan, C., Gebauer, B., Hamm, B., & Fischer, T. (2017). MRI-TRUS fusion for electrode positioning during irreversible electroporation for treatment of prostate cancer. *Diagnostic and Interventional Radiology*, *23*(4), 321–325.

Beitel-White, N., Lorenzo, M. F., Zhao, Y., Aycock, K. N., Manuchehrabadi, N. M., Brock, R. M., Coutermarsh-Ott, S., Imran, K. M., Allen, I. C., & Davalos, R. V. (2022). Comparison of analysis methods for determination of dynamic tissue conductivity during microseconds-long pulsed electric fields. *Biomedical Signal Processing and Control*, *72*, 103305.

Beitel-White, N., Lorenzo, M. F., Zhao, Y., Brock, R., Coutermarsh-Ott, S., Allen, I. C., Manuchehrabadi, N., & Davalos, R. v. (2020). Multi-tissue Analysis on the Impact of Electroporation on Electrical and Thermal Properties. *IEEE Transactions on Biomedical Engineering*, *1*.

Beitel-White, N., Martin, R. C. G., Li, Y., Brock, R. M., Allen, I. C., & Davalos, R. V. (2019). Real-time prediction of patient immune cell modulation during irreversible electroporation therapy. *Scientific Reports*, *9*(1).

Belfiore, G., Belfiore, M. P., Reginelli, A., Capasso, R., Romano, F., Ianniello, G. Pietro, Cappabianca, S., & Brunese, L. (2017). Concurrent chemotherapy alone versus irreversible electroporation followed by chemotherapy on survival in patients with locally advanced pancreatic cancer. *Medical Oncology*, 34–38.

Bhonsle, S., Lorenzo, M. F., Safaai-jazi, A., & Davalos, R. V. (2018). Characterization of nonlinearity and dispersion in tissue impedance during high-frequency electroporation. *IEEE Transactions on Biomedical Engineering*, *65*(10), 2190–2201.

Bhonsle, S. P., Arena, C. B., Sweeney, D. C., & Davalos, R. v. (2015). Mitigation of impedance changes due to electroporation therapy using bursts of high-frequency bipolar pulses. *Biomedical Engineering*, *14*(Suppl 3), 1–14.

Bhutiani, N., Philips, P., Scoggins, C. R., McMasters, K. M., Potts, M. H., & Martin, R. C. G. (2016). Evaluation of tolerability and efficacy of irreversible electroporation (IRE) in treatment of Child-Pugh B (7/8) hepatocellular carcinoma (HCC). *Hpb*, *18*(7), 593–599.

Böckmann, R. A., De Groot, B. L., Kakorin, S., Neumann, E., & Grubmüller, H. (2008). Kinetics, statistics, and energetics of lipid membrane electroporation studied by molecular dynamics simulations. *Biophysical Journal*, *95*(4), 1837–1850.

Bower, M., Sherwood, L., Li, Y., & Martin, R. (2011). Irreversible electroporation of the pancreas: Definitive local therapy without systemic effects. *Journal of Surgical Oncology*, *104*(1), 22–28.

Brock, R. M., Beitel-White, N., Davalos, R. v, & Allen, I. C. (2020). Starting a Fire Without Flame: The Induction of Cell Death and Inflammation in Electroporation-Based Tumor Ablation Strategies. *Frontiers in Oncology*, *10*(1235).

Buist, T. J., Groen, M. H. A., Wittkampf, F. H. M., Loh, P., Doevendans, P. A. F. M., Van Es, R., & Elvan, A. (2021). Efficacy of multi-electrode linear irreversible electroporation. *Europace*, *23*(3), 464–468.

Bulvik, B. E., Rozenblum, N., Gourevich, S., Ahmed, M., Andriyanov, A. V., Galun, E., & Nahum Goldberg, S. (2016). Irreversible electroporation versus radiofrequency ablation: A Comparison of Local and Systemic Effects in a Small-Animal Model. *Radiology*, *280*(2), 413–424.

Butikofer, R., & Lawrence, P. D. (1978). Electrocutaneous Nerve Stimulation–I: Model and Experiment. *IEEE Transactions on Biomedical Engineering*, *BME-25*(6), 526–531.

BÜtikofer, R., & Lawrence, P. D. (1979). Electrocutaneous Nerve Stimulation—II: Stimulus Waveform Selection. *IEEE Transactions on Biomedical Engineering*, *BME-26*(2), 69–75.

Campelo, S., Valerio, M., Ahmed, H. U., Hu, Y., Arena, S. L., Neal, R. E., Emberton, M., & Arena, C. B. (2017). An evaluation of irreversible electroporation thresholds in human prostate cancer and potential correlations to physiological measurements. *APL Bioengineering*, *1*(1), 016101.

Cancer, P., Services, U. S. P., & Force, T. (2012). PreventiveServicesTaskForce. Screeningforprostatecancer:U.S.Preventive Services Task Force recommendation statement. *Annals of Internal Medicine*, *157*(2), 120–134.

Cannon, R., Ellis, S., Hayes, D., Narayanan, G., & Martin, R. C. G. (2013). Safety and early efficacy of irreversible electroporation for hepatic tumors in proximity to vital structures. *Journal of Surgical Oncology*, *107*(5), 544–549.

Casciola, M., Xiao, S., Apollonio, F., Paffi, A., Liberti, M., Muratori, C., & Pakhomov, A. G. (2019). Cancellation of nerve excitation by the reversal of nanosecond stimulus polarity and its relevance to the gating time of sodium channels. *Cellular and Molecular Life Sciences*, *76*, 4539–4550.

Charpentier, K. P., Wolf, F., Noble, L., Winn, B., Resnick, M., & Dupuy, D. E. (2010). Irreversible electroporation of the pancreas in swine: A pilot study. *Hpb*, *12*(5), 348–351.

Checcucci, E., Amparore, D., De Luca, S., Autorino, R., Fiori, C., & Porpiglia, F. (2019). Precision prostate cancer surgery: An overview of new technologies and techniques. *Minerva Urologica e Nefrologica*, *71*(5), 487–501.

Che-Lok Chow, F., & Siu-Ho Chok, K. (2019). Colorectal liver metastases: An update on multidisciplinary approach ORCID number: Conflict-of-interest statement. *World J Hepatol*, *11*(2), 150–172.

Chen, C., Smye, S. W., Robinson, M. P., & Evans, J. A. (2006). Membrane electroporation theories: A review. *Medical and Biological Engineering and Computing*, *44*(1–2), 5–14.

Chen, M. S., Li, J. Q., Zheng, Y., Guo, R. P., Liang, H. H., Zhang, Y. Q., Lin, X. J., & Lau, W. Y. (2006). A prospective randomized trial comparing percutaneous local ablative therapy and partial hepatectomy for small hepatocellular carcinoma. *Annals of Surgery*, *243*(3), 321–328.

Chen, W., Zhongsheng, Z., & Lee, R. C. (2006). Supramembrane potential-induced electroconformational changes in sodium channel proteins: A potential mechanism involved in electric injury. *Burns*, *32*(1), 52–59.

Chen, X., Ren, Z., Zhu, T., Zhang, X., Peng, Z., Xie, H., Zhou, L., Yin, S., Sun, J., & Zheng, S. (2015). Electric Ablation with Irreversible Electroporation (IRE) in Vital Hepatic Structures and Follow-up Investigation. *Scientific Reports*, *5*.

Chiang, J., Cristescu, M., Lee, M. H., Moreland, A., Hinshaw, J. L., Lee, F. T., & Brace, C. L. (2016). Effects of Microwave ablation on arterial and Venous Vasculature after Treatment of hepatocellular carcinoma. *Radiology*, *281*(2), 617–624.

Chiang, J., Nickel, K., Kimple, R. J., & Brace, C. L. (2017). Potential Mechanisms of Vascular Thrombosis after Microwave Ablation in an in Vivo Liver. *Journal of Vascular and Interventional Radiology*, *28*(7), 1053–1058.

Chiang, J., Willey, B. J., del Rio, A. M., Hinshaw, J. L., Lee, F. T., & Brace, C. L. (2014). Predictors of Thrombosis in Hepatic Vasculature during Microwave Tumor Ablation of an In Vivo Porcine Model. *Journal of Vascular and Interventional Radiology*, *25*(12), 1965-1971.e2.

Cindric, H., Mariappan, P., Beyer, L., Wiggermann, P., Moche, M., Miklavcic, D., & Kos, B. (2021). Retrospective study for validation and improvement of numerical treatment planning of irreversible electroporation ablation for treatment of liver tumors. *IEEE Transactions on Biomedical Engineering*, *X*(X).

Clausen, T., & Gissel, H. (2005). Role of Na+,K+ pumps in restoring contractility following loss of cell membrane integrity in rat skeletal muscle. *Acta Physiologica Scandinavica*, *183*(3), 263–271.

Cooper, M. S. (1995). Membrane potential perturbations induced in tissue cells by pulsed electric fields. *Bioelectromagnetics*, *16*(4), 255–262.

Cornelis, F. H., Cindrič, H., Kos, B., Fujimori, M., Petre, E. N., Miklavčič, D., Solomon, S. B., & Srimathveeravalli, G. (2019). Peri-tumoral Metallic Implants Reduce the Efficacy of Irreversible Electroporation for the Ablation of Colorectal Liver Metastases. *CardioVascular and Interventional Radiology*.

Corovic, S., Lackovic, I., Sustaric, P., Sustar, T., Rodic, T., & Miklavcic, D. (2013). Modeling of electric field distribution in tissues during electroporation. *BioMedical Engineering Online*, *12*(1), 1–27.

Davalos, R. V., Mir, L. M., & Rubinsky, B. (2005a). Tissue ablation with irreversible electroporation. *Annals of Biomedical Engineering*, *33*(2), 223–231.

Davalos, R. V, Mir, L. M., & Rubinsky, B. (2005b). Tissue Ablation with Irreversible Electroporation. *Annals of Biomedical Engineering*, *33*(2), 223–231.

Davalos, R. v, & Rubinsky, B. (2008). Temperature considerations during irreversible electroporation. *International Journal of Heat and Mass Transfer*, *51*, 5617–5622.

Davalos, R. V., Rubinsky, B., & Mir, L. M. (2003). Theoretical analysis of the thermal effects during in vivo tissue electroporation. *Bioelectrochemistry*, *61*(1–2), 99–107.

Deamer, D. W., & Bramhall, J. (1986). Permeability of lipid bilayers to water and ionic solutes. *Chemistry and Physics of Lipids*, *40*(2–4), 167–188.

Debruin, K. A., & Krassowska, W. (1998). Electroporation and shock-induced transmembrane potential in a cardiac fiber during defibrillation strength shocks. *Annals of Biomedical Engineering*, *26*(4), 584–596.

Debruin, K. A., & Krassowska, W. (1999). Modeling Electroporation in a Single Cell. I. Effects of Field Strength and Rest Potential. *Biophysical Journal*, *77*(Sep), 1213–1224.

Deodhar, A., Dickfeld, T., Single, G. W., Hamilton, W. C., Thornton, R. H., Sofocleous, C. T., Maybody, M., Gónen, M., Rubinsky, B., Solomon, S. B., Solomon, S. B., & Deodhar, A. (2011). Irreversible Electroporation Near the Heart: Ventricular Arrhythmias Can Be Prevented With ECG Synchronization. *AJR Am J Roentgenol*, *196*(3), 330–335.

Deodhar, A., Monette, S., Single, G. W., Hamilton, W. C., Thornton, R. H., Sofocleous, C. T., Maybody, M., & Solomon, S. B. (2011). Percutaneous irreversible electroporation lung ablation: Preliminary results in a porcine model. *CardioVascular and Interventional Radiology*, *34*(6), 1278–1287.

DeWitt, M. R., McKillop, I., Davalos, R. v., Sano, M., Lattouche, E., Kaufman, J. D., Fesmire, C. C., Swet, J., Kirks, R., Baker, E., Vrochides, D., & Iannitti, D. (2019). Simplified Non-Thermal Tissue Ablation With A Single Insertion Device Enabled By Bipolar High-Frequency Pulses. *IEEE Transactions on Biomedical Engineering*, 1–1.

Diller, K. R., & Hayes, L. J. (1983). A finite element model of burn injury in blood–perfused skin. *Journal of Biomechanical Engineering*, *105*(3), 300–307.

Diller, K. R., Hayes, L. J., Dilier, K. R., & Hayes, L. J. (1983). A finite element model of burn injury in blood–perfused skin. *Journal of Biomechanical Engineering*, *105*(3), 300–307.

Dollinger, M., Müller-Wille, R., Zeman, F., Haimerl, M., Niessen, C., Beyer, L. P., Lang, S. A., Teufel, A., Stroszczynski, C., & Wiggermann, P. (2015). Irreversible electroporation of malignant hepatic tumors - Alterations in venous structures at subacute follow-up and evolution at mid-term follow-up. *PLoS ONE*, *10*(8), e0135773.

Dong, S., Wang, H., Zhao, Y., Sun, Y., & Yao, C. (2018). First human trial of high-frequency irreversible electroporation therapy for prostate cancer. *Technology in Cancer Research and Treatment*, *17*, 1–9.

Dong, S., Yao, C., Zhao, Y., Lv, Y., & Liu, H. (2018). Parameters optimization of bipolar high frequency pulses on tissue ablation and inhibiting muscle contraction. *IEEE Transactions on Dielectrics and Electrical Insulation*, *25*(1), 207–216.

Dunki-Jacobs, E. M., Philips, P., & Martin, R. C. G. (2014). Evaluation of thermal injury to liver, pancreas and kidney during irreversible electroporation in an in vivo experimental model. *British Journal of Surgery*, *101*(9), 1113–1121.

Dupuy, D. E., Aswad, B., & Ng, T. (2011). Irreversible electroporation in a swine lung model. *CardioVascular and Interventional Radiology*, *34*(2), 391–395.

Edd, J. F., Horowitz, L., Davalos, R. V., Mir, L. M., & Rubinsky, B. (2006). In vivo results of a new focal tissue ablation technique: Irreversible electroporation. *IEEE Transactions on Biomedical Engineering*, *53*(7), 1409–1415.

Edelblute, C. M., Hornef, J., Burcus, N. I., Norman, T., Beebe, S. J., Schoenbach, K., Heller, R., Jiang, C., & Guo, S. (2017). Controllable Moderate Heating Enhances the Therapeutic Efficacy of Irreversible Electroporation for Pancreatic Cancer. *Scientific Reports*, *7*(1).

Ellis, T. L., Garcia, P. A., Rossmeisl, J. H., Henao-Guerrero, N., Robertson, J., & Davalos, R. V. (2011). Nonthermal irreversible electroporation for intracranial surgical applications: Laboratory investigation. *Journal of Neurosurgery*, *114*(3), 681–688.

Fang, Y., Chen, W., Liang, X., Li, D., Lou, H., Chen, R., Wang, K., & Pan, H. (2014). Comparison of long-term effectiveness and complications of radiofrequency ablation with hepatectomy for small hepatocellular carcinoma. *Journal of Gastroenterology and Hepatology (Australia)*, *29*(1), 193–200.

Fang, Z., Chen, L., Moser, M. A. J., Zhang, W., Qin, Z., & Zhang, B. (2021). Electroporation-Based Therapy for Brain Tumors: A Review. *Journal of Biomechanical Engineering*, *143*(10).

Fenton, J. J., Weyrich, M. S., Durbin, S., Liu, Y., Bang, H., & Melnikow, J. (2018). Prostate-specific antigen-based screening for prostate cancer evidence report and systematic review for the us preventive services task force. *JAMA - Journal of the American Medical Association*, *319*(18), 1914–1931.

Ferrer, M., Guedea, F., Suárez, J. F., De Paula, B., Macías, V., Mariño, A., Hervás, A., Herruzo, I., Ortiz, M. J., Ponce De León, J., Sancho, G., Boladeras, A., Ayala, A., Craven-Bratle, J., Ávila, M., Cunillera, O., Pardo, Y., Alonso, J., & Aguiló, F. (2013). Quality of life impact of treatments for localized prostate cancer: Cohort study with a 5 year follow-up. *Radiotherapy and Oncology*, *108*(2), 306–313.

Fesmire, C. C., Petrella, R. A., Fogle, C. A., Gerber, D. A., Xing, L., & Sano, M. B. (2020). Temperature Dependence of High Frequency Irreversible Electroporation Evaluated in a 3D Tumor Model. *Annals of Biomedical Engineering*.

Fesmire, C. C., Petrella, R. A., Kaufman, J. D., Topasna, N., & Sano, M. B. (2020). Irreversible electroporation is a thermally mediated ablation modality for pulses on the order of one microsecond. *Bioelectrochemistry (Amsterdam, Netherlands)*, *135*, 107544.

Flak, R. V., Stender, M. T., Jensen, T. M., Andersen, K. L., Henriksen, S. D., Mortensen, P. B., Sall, M., & Thorlacius-Ussing, O. (2019). Treatment of locally advanced pancreatic cancer with irreversible electroporation–a Danish single center study of safety and feasibility. *Scandinavian Journal of Gastroenterology*, *54*(2), 252–258.

Frandsen, S. K., Gissel, H., Hojman, P., Tramm, T., Eriksen, J., & Gehl, J. (2012). Direct therapeutic applications of calcium electroporation to effectively induce tumor necrosis. *Cancer Research*, *72*(6), 1336–1341.

Fusco, R., Di Bernardo, E., D'Alessio, V., Salati, S., & Cadossi, M. (2021). Reduction of muscle contraction and pain in electroporation-based treatments: An overview. *World Journal of Clinical Oncology*, *12*(5), 367–381.

Gabriel, S., Lau, R. W., & Gabriel, C. (1996). The dielectric properties of biological tissues: III. Parametric models for the dielectric spectrum of tissues. *Physics in Medicine and Biology*, *41*(11), 2271–2293.

Garcia, P. A., Davalos, R. V, & Miklavcic, D. (2014). A numerical investigation of the electric and thermal cell kill distributions in electroporation-based therapies in tissue. *PLoS ONE*, *9*(8), 103083.

Garcia, P. A., Neal, R. E., Rossmeisl, J. H., & Davalos, R. V. (2010). Non-thermal irreversible electroporation for deep intracranial disorders. *32nd Annual International Conference of the IEEE Engineering in Medicine and Biology Society*, 2743–2746.

Garcia, P. A., Pearce, J. A., & Davalos, R. V. (2012). A comparison between the pulsed and duty cycle approaches used to capture the thermal response of tissue during electroporation-based therapies. *ASME 2012 Summer Bioengineering Conference, SBC 2012*, 945–946.

Garcia, P. A., Rossmeisl, J. H., Neal, R. E., Ellis, T. L., & Davalos, R. V. (2011). A parametric study delineating irreversible electroporation from thermal damage based on a minimally invasive intracranial procedure. *BioMedical Engineering Online*, *10*(April), 34.

Garcia, P. A., Rossmeisl, J. H., Neal, R. E., Ellis, T. L., Olson, J. D., Henao-Guerrero, N., Robertson, J., & Davalos, R. V. (2010). Intracranial nonthermal irreversible electroporation: In vivo analysis. *Journal of Membrane Biology*, *236*(1), 127–136.

Garcia, P. A., Rossmeisl, J. H., Robertson, J., Ellis, T. L., & Davalos, R. V. (2009). Pilot study of irreversible electroporation for intracranial surgery. *31st Annual International Conference of the IEEE Engineering in Medicine and Biology Society*, 6513–6516.

Geboers, B., Scheffer, H. J., Graybill, P. M., Ruarus, A. H., Nieuwenhuizen, S., Puijk, R. S., van den Tol, P. M., Davalos, R. v., Rubinsky, B., de Gruijl, T. D., Miklavčič, D., & Meijerink, M. R. (2020). High-Voltage Electrical Pulses in Oncology: Irreversible Electroporation, Electrochemotherapy, Gene Electrotransfer, Electrofusion, and Electroimmunotherapy. *Radiology*, *295*(2), 192190.

Gissel, H., Lee, R. C., & Gehl, J. (2011). Electroporation and Cellular Physiology. In S. et al Kee (Ed.), *Clinical Aspects of Electroporation* (pp. 9–17). Springer.

Glaser, R. W., Leikin, S. L., Chernomordik, L. V., Pastushenko, V. F., & Sokirko, A. I. (1988). Reversible electrical breakdown of lipid bilayers: formation and evolution of pores. *BBA - Biomembranes*, *940*(2), 275–287.

Golberg, A., & Rubinsky, B. (2012). Towards electroporation based treatment planning considering electric field induced muscle contractions. *Technology in Cancer Research and Treatment*, *11*(2), 189–201.

Gorman, P. H., & Mortimer, J. T. (1983). The Effect of Stimulus Parameters on the Recruitment Characteristics of Direct Nerve Stimulation. *IEEE Transactions on Biomedical Engineering*, *BME-30*(7), 407–414.

Goswami, I., Coutermarsh-Ott, S., Morrison, R. G., Allen, I. C., Davalos, R. V., Verbridge, S. S., & Bickford, L. R. (2017). Irreversible electroporation inhibits pro-cancer inflammatory signaling in triple negative breast cancer cells. *Bioelectrochemistry*, *113*, 42–50.

Gotwals, P., Cameron, S., Cipolletta, D., Cremasco, V., Crystal, A., Hewes, B., Mueller, B., Quaratino, S., Sabatos-Peyton, C., Petruzzelli, L., Engelman, J. A., & Dranoff, G. (2017). Prospects for combining targeted and conventional cancer therapy with immunotherapy. *Nature Reviews Cancer 2017 17:5*, *17*(5), 286–301.

Grimnes, S., & Martinsen, O. G. (2008). *Bioimpedance and Bioelectricity Basics* (2nd ed.). Academic Press.

Gudvangen, E., Kim, V., Novickij, V., Battista, F., & Pakhomov, A. G. (2022). Electroporation and cell killing by milli-to nanosecond pulses and avoiding neuromuscular stimulation in cancer ablation. *Scientific Reports*, *12*, 1763.

Guenther, E., Klein, N., Mikus, P., Stehling, M. K., & Rubinsky, B. (2015). Electrical breakdown in tissue electroporation. *Biochemical and Biophysical Research Communications*, *467*(4), 736–741.

Guenther, E., Klein, N., Zapf, S., Weil, S., Schlosser, C., Rubinsky, B., & Stehling, M. K. (2019). Prostate cancer treatment with Irreversible Electroporation (IRE): Safety, efficacy and clinical experience in 471 treatments. *PLoS ONE*, *14*(4), e0215093.

Hall, J. E. (2011). *Guyton and Hall Textbook of Medical Physiology* (12th ed.). Saunders Elsevier.

He, C., Wang, J., Sun, S., Zhang, Y., & Li, S. (2019). Immunomodulatory Effect after Irreversible Electroporation in Patients with Locally Advanced Pancreatic Cancer. *Journal of Oncology*, *2019*, 1–13.

Heidenreich, A., Bolla, M., Joniau, S., Van Der Kwast, T. H., Matveev, V., Mason, M. D., Mottet, N., Schmid, H.-P., Wiegel, T., & Zattoni, F. (2008). Guidelines on prostate cancer. *European Urology*, *53*(1), 68–80.

Henslee, B. E., Morss, A., Hu, X., Lafyatis, G. P., & Lee, L. J. (2011). Electroporation dependence on cell size: Optical tweezers study. *Analytical Chemistry*, *83*(11), 3998–4003.

Howlader, N., Noone, A., Krapcho, M., Miller, D., Brest, A., Yu, M., Ruhl, J., Tatalovich, Z., Mariotto, A., Lewis, D., Chen, H., Feuer, E., & Cronin, K. (2018). *SEER Cancer Statistics Review, 1975-2016*.

Iavarone, M., & Colombo, M. (2014). Management of hepatocellular carcinoma. *Gastroenterology & Hepatology*, *10*(3), 544–551.

Ibey, B. L., Ullery, J. C., Pakhomova, O. N., Roth, C. C., Semenov, I., Beier, H. T., Tarango, M., Xiao, S., Schoenbach, K. H., & Pakhomov, A. G. (2014). Bipolar nanosecond electric pulses are less efficient at electropermeabilization and killing cells than monopolar pulses. *Biochemical and Biophysical Research Communications*, *443*, 568–573.

Imajo, K., Ogawa, Y., Yoneda, M., Saito, · Satoru, & Nakajima, A. (2020). A review of conventional and newer generation microwave ablation systems for hepatocellular carcinoma. *Journal of Medical Ultrasonics*, *47*, 265–277.

Ivey, J. W., Latouche, E. L., Richards, M. L., Lesser, G. J., Debinski, W., Davalos, R. v., & Verbridge, S. S. (2017). Enhancing Irreversible Electroporation by Manipulating Cellular Biophysics with a Molecular Adjuvant. *Biophysical Journal*, *113*(2), 472–480.

Ivey, J. W., Latouche, E. L., Sano, M. B., Rossmeisl, J. H., Davalos, R. v., & Verbridge, S. S. (2015). Targeted cellular ablation based on the morphology of malignant cells. *Scientific Reports*, *5*, 1–17.

Ivey, J. W., Wasson, E. M., Alinezhadbalalami, N., Kanitkar, A., Debinski, W., Sheng, Z., Davalos, R. V., & Verbridge, S. S. (2019). Characterization of Ablation Thresholds for 3D-Cultured Patient-Derived Glioma Stem Cells in Response to High-Frequency Irreversible Electroporation. *Research*, *2019*, 1–14.

Izzo, F., Granata, V., Grassi, R., Fusco, R., Palaia, R., Delrio, P., Carrafiello, G., Azoulay, D., Petrillo, A., & Curley, S. A. (2019). Radiofrequency Ablation and Microwave Ablation in Liver Tumors: An Update. *The Oncologist*, *24*, e990–e1005.

Jankowski, N. R., & McCluskey, F. P. (2014). A review of phase change materials for vehicle component thermal buffering. *Applied Energy*, *113*, 1525–1561.

Jansen, M., & Blume, A. (1995). A comparative study of diffusive and osmotic water permeation across bilayers composed of phospholipids with different head groups and fatty acyl chains. *Biophysical Journal*, *68*(3), 997–1008.

Jarm, T., Cemazar, M., Miklavcic, D., & Sersa, G. (2010). Antivascular effects of electrochemotherapy: Implications in treatment of bleeding metastases. *Expert Review of Anticancer Therapy*, *10*(5), 729–746.

Jemal, A., Culp, M. B. B., Ma, J., Islami, F., & Fedewa, S. A. (2021). Prostate cancer incidence 5 years after us preventive services task force recommendations against screening. *Journal of the National Cancer Institute*, *113*(1), 64–71.

Jiang, C., Davalos, R. v., & Bischof, J. C. (2015). A review of basic to clinical studies of irreversible electroporation therapy. *IEEE Transactions on Biomedical Engineering*, *62*(1), 4–20.

Jourabchi, N., Beroukhim, K., Tafti, B. A., Kee, S. T., & Lee, E. W. (2014). Irreversible electroporation (NanoKnife) in cancer treatment. *Gastrointestinal Intervention*, *3*(1), 8–18.

Kanthou, C., Kranjc, S., Sersa, G., Tozer, G., Zupanic, A., & Cemazar, M. (2006). The endothelial cytoskeleton as a target of electroporation-based therapies. *Molecular Cancer Therapeutics*, *5*(12), 3145–3152.

Kaufman, J. D., Fesmire, C. C., Petrella, R. A., Fogle, C. A., Xing, L., Gerber, D., & Sano, M. B. (2020). High-Frequency Irreversible Electroporation Using 5,000-V Waveforms to Create Reproducible 2- and 4-cm Ablation Zones—A Laboratory Investigation Using Mechanically Perfused Liver. *Journal of Vascular and Interventional Radiology*, *31*(1), 162–168.

Kim, K. R., & Thomas, S. (2014). Complications of image-guided thermal ablation of liver and kidney neoplasms. *Seminars in Interventional Radiology*, *31*(2), 138–148.

Kingham, T. P., Karkar, A. M., D'Angelica, M. I., Allen, P. J., Dematteo, R. P., Getrajdman, G. I., Sofocleous, C. T., Solomon, S. B., Jarnagin, W. R., & Fong, Y. (2012). Ablation of perivascular hepatic malignant tumors with irreversible electroporation. *Journal of the American College of Surgeons*, *215*(3), 379–387.

Kinosita, K., & Tsong, T. Y. (1977a). Formation and resealing of pores of controlled sizes in human erythrocyte membrane. *Nature*, *268*, 438–441.

Kinosita, K., & Tsong, T. Y. (1977b). Hemolysis of human erythrocytes by a transient electric field. *Proceedings of the National Academy of Sciences*, *74*(5), 1923–1927.

Kinosita, K., & Tsong, T. Y. (1978). Survival of sucrose-loaded erythrocytes in the circulation. *Nature*, *272*, 258–260.

Kinosita, K., & Tsong, T. Y. (1979). Voltage-induced conductance in human erythrocyte membranes. *Biochimica et Biophysica Acta*, *554*, 479–497.

Koethe, Y., Wilson, N., & Narayanan, G. (2022). Irreversible electroporation for colorectal cancer liver metastasis: a review. In *International Journal of Hyperthermia* (Vol. 39, Issue 1, pp. 682–687). Taylor and Francis Ltd.

Kong, W.-T., Zhang, W.-W., Qiu, Y.-D., Zhou, T., Qiu, J.-L., Zhang, W., Ding Wen-Tao Kong, Y.-T., & Ding, Y.-T. (2009). Major complications after radiofrequency ablation for liver tumors: Analysis of 255 patients. *World J Gastroenterol*, *15*(21), 2651–2656.

Kos, B., Voigt, P., Miklavcic, D., & Moche, M. (2015). Careful treatment planning enables safe ablation of liver tumors adjacent to major blood vessels by percutaneous irreversible electroporation (IRE). *Radiology and Oncology*, *49*(3), 234–241.

Kotnik, T., Kramar, P., Pucihar, G., Miklavčič, D., & Tarek, M. (2012). Cell membrane electroporation - Part 1: The phenomenon. *IEEE Electrical Insulation Magazine*, *28*(5), 14–23.

Kotnik, T., & Miklavčič, D. (2006). Theoretical evaluation of voltage inducement on internal membranes of biological cells exposed to electric fields. *Biophysical Journal*, *90*(2), 480–491.

Kotnik, T., & Pucihar, G. (2010). Induced transmembrane voltage - theory, modeling, and experiments. In D. Miklavčič, A. Pakhomov, & M. Markov (Eds.), *Advanced Electroporation Techniques in Biology and Medicine* (pp. 51–70). CRC Press.

Kotnik, T., Pucihar, G., Reberšek, M., Miklavčič, D., & Mir, L. M. (2003). Role of pulse shape in cell membrane electropermeabilization. *Biochimica et Biophysica Acta - Biomembranes*, *1614*(2), 193–200.

Kramar, P., Delemotte, L., Lebar, A. M., Kotulska, M., Tarek, M., & Miklavčič, D. (2012). Molecular-level characterization of lipid membrane electroporation using linearly rising current. *Journal of Membrane Biology*, *245*(10), 651–659.

Kruitwagen, H. S., Spee, B., & Schotanus, B. A. (2014). Hepatic progenitor cells in canine and feline medicine: potential for regenerative strategies. *BMC Veterinary Research*, *10*(137), 1–15.

Latouche, E. L., Arena, C. B., Ivey, J. W., Garcia, P. A., Pancotto, T. E., Pavlisko, N., Verbridge, S. S., Davalos, R. V., & Rossmeisl, J. H. (2018). High-Frequency Irreversible Electroporation for Intracranial Meningioma: A Feasibility Study in a Spontaneous Canine Tumor Model. *Technology in Cancer Research & Treatment*, *17*, 1–10.

Latouche, E. L., Sano, M. B., Lorenzo, M. F., Davalos, R. v., & Martin, R. C. G. (2017). Irreversible electroporation for the ablation of pancreatic malignancies: A patient-specific methodology. *Journal of Surgical Oncology*, *115*(6), 711–717.

Lavee, J., Onik, G., Mikus, P., & Rubinsky, B. (2007). A novel nonthermal energy source for surgical epicardial atrial ablation: Irreversible electroporation. *Heart Surgery Forum*, *10*(2), 96–101.

Lee, E. W., Loh, C. T., & Kee, S. T. (2007). Imaging guided percutaneous irreversible electroporation: Ultrasound and immunohistological correlation. *Technology in Cancer Research and Treatment*, *6*(4), 287–293.

Lee, E. W., Wong, D., Tafti, B. A., Prieto, V., Totonchy, M., Hilton, J., Dry, S., Cho, S., Loh, C. T., & Kee, S. T. (2012). Irreversible electroporation in eradication of rabbit VX2 liver tumor. *Journal of Vascular and Interventional Radiology*, *23*(6), 833–840.

Lee, R. C., Zhang, D., & Hannig, J. (2000). Biophysical Injury Mechanisms in Electrical Shock Trauma. *Annual Review of Biomedical Engineering*, *2*(1), 477–509.

Leen, E., Picard, J., Stebbing, J., Abel, M., Dhillon, T., & Wasan, H. (2018). Percutaneous irreversible electroporation with systemic treatment for locally advanced pancreatic adenocarcinoma. *Journal of Gastrointestinal Oncology*, *9*(2), 275–281.

Levine, Z. A., & Vernier, P. T. (2010). Life cycle of an electropore: Field-dependent and field-independent steps in pore creation and annihilation. *Journal of Membrane Biology*, *236*(1), 27–36.

Li, J., Djenaba, J. A., Soman, A., Rim, S. H., & Master, V. A. (2012). Recent Trends in Prostate Cancer Incidence by Age, Cancer Stage, and Grade, the United States, 2001–2007. *Prostate Cancer*, *2012*, 1–8.

Li, S., Zhang, X., & Xia, X. (2002). Regression of Tumor Growth and Induction of Long-Term Antitumor Memory by Interleukin 12 Electro-Gene Therapy. *Journal of the National Cancer Institute*, *94*(10), 762–768.

Li, W., Fan, Q., Ji, Z., Qiu, X., & Li, Z. (2011). The effects of irreversible electroporation (IRE) on nerves. *PLoS ONE*, *6*(4), e18831.

Li, X., Xu, K., Li, W., Qiu, X., Ma, B., Fan, Q., & Li, Z. (2012). Immunologic response to tumor ablation with irreversible electroporation. *PloS One*, *7*(11), e48749.

Lin, M., Alnaggar, M., Liang, S., Wang, X., Liang, Y., Zhang, M., Chen, J., Niu, L., & Xu, K. (2017). An important discovery on combination of irreversible electroporation and allogeneic natural killer cell immunotherapy for unresectable pancreatic cancer. In *Oncotarget* (Vol. 8, Issue 60).

Lin, Z.-Y., Li, G.-L., Chen, J., Chen, Z.-W., Chen, Y.-P., & Lin, S.-Z. (2016). Effect of heat sink on the recurrence of small malignant hepatic tumors after radiofrequency ablation. *Journal of Cancer Research and Therapeutics*, *12*, C153–C158.

Litwin, M. S., & Tan, H. J. (2017). The diagnosis and treatment of prostate cancer: A review. *JAMA - Journal of the American Medical Association*, *317*(24), 2532–2542.

Liu, D., & Yu, L. (2010). Experimental investigation of single-phase convective heat transfer of nanofluids in a minichannel. *Proceedings of the 14th International Heat Transfer Conference*, 1–12.

Liu, H., Yao, C., Zhao, Y., Chen, X., Dong, S., Wang, L., & Davalos, R. V. (2021). In Vitro Experimental and Numerical Studies on the Preferential Ablation of Chemo-Resistant Tumor Cells Induced by High-Voltage Nanosecond Pulsed Electric Fields. *IEEE Transactions on Biomedical Engineering*, *68*(8), 2400–2411.

Liu, X., Krawczyk, E., Suprynowicz, F. A., Palechor-Ceron, N., Yuan, H., Dakic, A., Simic, V., Zheng, Y. L., Sripadhan, P., Chen, C., Lu, J., Hou, T. W., Choudhury, S., Kallakury, B., Tang, D., Darling, T., Thangapazham, R., Timofeeva, O., Dritschilo, A., … Schlegel, R. (2017). Conditional reprogramming and long-term expansion of normal and tumor cells from human biospecimens. *Nature Protocols*, *12*(2), 439–451.

Livia, C., Sugrue, A., Witt, T., Polkinghorne, M. D., Maor, E., Kapa, S., Lehmann, H. I., DeSimone, C. V., Behfar, A., Asirvatham, S. J., & McLeod, C. J. (2018). Elimination of purkinje fibers by electroporation reduces ventricular fibrillation vulnerability. *Journal of the American Heart Association*, *7*(15), e009070.

Llovet, J. M., Kelley, R. K., Villanueva, A., Singal, A. G., Pikarsky, E., Roayaie, S., Lencioni, R., Koike, K., Zucman-Rossi, J., & Finn, R. (2021). Hepatocellular carcinoma. *Nature Reviews Disease Primers*, *7*(6).

Macherey, O., Van Wieringen, A., Carlyon, R. P., Deeks, J. M., & Wouters, J. (2006). Asymmetric pulses in cochlear implants: Effects of pulse shape, polarity, and rate. *JARO - Journal of the Association for Research in Otolaryngology*, *7*(3), 253–266.

Mafeld, S., Wong, J. J., Kibriya, N., Stenberg, B., Manas, D., Bassett, P., Aslam, T., Evans, J., & Littler, P. (2019). Percutaneous Irreversible Electroporation (IRE) of Hepatic Malignancy: A Bi-institutional Analysis of Safety and Outcomes. *CardioVascular and Interventional Radiology*, *42*(4), 577–583.

Mali, B., Jarm, T., Corovic, S., Paulin-Kosir, M. S., Cemazar, M., Sersa, G., & Miklavcic, D. (2008). The effect of electroporation pulses on functioning of the heart. *Medical and Biological Engineering and Computing*, *46*(8), 745–757.

Månsson, C., Brahmstaedt, R., Nilsson, A., Nygren, P., & Karlson, B. M. (2016). Percutaneous irreversible electroporation for treatment of locally advanced pancreatic cancer following chemotherapy or radiochemotherapy. *European Journal of Surgical Oncology*, *42*(9), 1401–1406.

Maor, E., Ivorra, A., Leor, J., & Rubinsky, B. (2007). The effect of irreversible electroporation on blood vessels. *Technology in Cancer Research and Treatment*, *6*(4), 307–312.

Maor, E., Ivorra, A., Leor, J., & Rubinsky, B. (2008). Irreversible electroporation attenuates neointimal formation after angioplasty. *IEEE Transactions on Biomedical Engineering*, *55*(9), 2268–2274.

Maor, E., Ivorra, A., Mitchell, J. J., & Rubinsky, B. (2010). Vascular smooth muscle cells ablation with endovascular nonthermal irreversible electroporation. *Journal of Vascular and Interventional Radiology*, *21*(11), 1708–1715.

Maor, E., Ivorra, A., & Rubinsky, B. (2009). Non Thermal Irreversible Electroporation: Novel Technology for Vascular Smooth Muscle Cells Ablation. *PLoS ONE*, *4*(3), e4757.

Maor, E., Phillips, M., Maor, E., & Rubinsky, B. (2010). Nonthermal Irreversible Electroporation for Tissue Decellularization. *Journal of Biomechanical Engineering*, *132*(9), 0910031–0910038.

Maor, E., & Rubinsky, B. (2010). Endovascular nonthermal irreversible electroporation: A finite element analysis. *Journal of Biomechanical Engineering*, *132*(3), 013008.

Maor, E., Sugrue, A., Witt, C., Vaidya, V. R., DeSimone, C. V., Asirvatham, S. J., & Kapa, S. (2019). Pulsed electric fields for cardiac ablation and beyond: A state-of-the-art review. *Heart Rhythm*, *16*(7), 1112–1120.

Martin, G. T., Pliquett, U. F., & Weaver, J. C. (2002). Theoretical analysis of localized heating in human skin subjected to high voltage pulses. *Bioelectrochemistry*, *57*(1), 55–64.

Martin, R. C. G., Kwon, D., Chalikonda, S., Sellers, M., Kotz, E., Scoggins, C., McMasters, K. M., & Watkins, K. (2015). Treatment of 200 locally advanced (Stage III) pancreatic adenocarcinoma patients with irreversible electroporation safety and efficacy. *Annals of Surgery*, *262*(3), 486–492.

Martin, R. C. G., McFarland, K., Ellis, S., & Velanovich, V. (2012). Irreversible electroporation therapy in the management of locally advanced pancreatic adenocarcinoma. *Journal of the American College of Surgeons*, *215*(3), 361–369.

Martin, R. C. G., McFarland, K., Ellis, S., & Velanovich, V. (2013). Irreversible electroporation in locally advanced pancreatic cancer: Potential improved overall survival. *Annals of Surgical Oncology*, *20*(3 SUPPL.), 443–449.

Martin, R. CG., Schwartz, E., Adams, J., Farah, I., & Derhake, B. M. (2015). Intra-operative Anesthesia Management in Patients Undergoing Surgical Irreversible Electroporation of the Pancreas, Liver, Kidney, and Retroperitoneal Tumors. *Anesthesiology and Pain Medicine*, *5*(2), 22786.

Mathy, R. M., Tinoush, P., da Florencia, R. D., Braun, A., Ghamarnejad, O., Radeleff, B., Kauczor, H. U., & Chang, D. H. (2020). Impact of needle positioning on ablation success of irreversible electroporation: a unicentric retrospective analysis. *Scientific Reports*, *10*(1).

McIntyre, C. C., Richardson, A. G., & Grill, W. M. (2002). Modeling the excitability of mammalian nerve fibers: Influence of afterpotentials on the recovery cycle. *Journal of Neurophysiology*, *87*(2), 995–1006.

McNeal, D. R. (1976). Analysis of a Model for Excitation of Myelinated Nerve. *IEEE Transactions on Biomedical Engineering*, *23*(4), 329–337.

Mercadal, B., Arena, C. B., Davalos, R. v., & Ivorra, A. (2017). Avoiding nerve stimulation in irreversible electroporation: A numerical modeling study. *Physics in Medicine and Biology*, *62*(20), 8060–8079.

Mercadal, B., Beitel-White, N., Aycock, K. N., Castellví, Q., Davalos, R. v., & Ivorra, A. (2020). Dynamics of Cell Death After Conventional IRE and H-FIRE Treatments. *Annals of Biomedical Engineering*, *48*(5), 1451–1462.

Miklavčič, D., Pucihar, G., Pavlovec, M., Ribaric, S., Mali, M., Macek-Lebar, A., Petkovsek, M., Nastran, J., Kranjc, S., Cemazar, M., & Serša, G. (2004). The effect of high frequency electric pulses on muscle contractions and antitumor efficiency in vivo for a potential use in clinical electrochemotherapy. *Bioelectrochemistry*, *65*, 121–128.

Miklavcic, D., Šel, D., Cukjati, D., Batiuskaite, D., Slivnik, T., Mir, L. M., Sel, D., Cukjati, D., Batiuskaite, D., Slivnik, T., Mir, L. M., & Miklavcic, D. (2005). Sequential finite element model of tissue electropermeabilization. *Ieee Transactions on Biomedical Engineering*, *52*(5), 816–827.

Miklovic, T., Latouche, E. L., DeWitt, M. R., Davalos, R. V., & Sano, M. B. (2017). A Comprehensive Characterization of Parameters Affecting High-Frequency Irreversible Electroporation Lesions. *Annals of Biomedical Engineering*, *45*(11), 2524–2534.

Mir, L. M., Orlowski, S., Belehradek, J., & Paoletti, C. (1991). Electrochemotherapy potentiation of antitumour effect of bleomycin by local electric pulses. *European Journal of Cancer and Clinical Oncology*, *27*(1), 68–72.

Mogyoros, I., Kiernan, M. C., & Burke, D. (1996). Strength-duration properties of human peripheral nerve. In *Brain* (Vol. 119, Issue 2).

Mohammadi, A., Bianchi, L., Asadi, S., & Saccomandi, P. (2021). Measurement of ex vivo liver, brain and pancreas thermal properties as function of temperature. *Sensors*, *21*(12).

Mrudula Glassberg, T. B., Ghosh, S., Clymer, J. W., Qadeer, R. A., Ferko, N. C., Sadeghirad, B., Wright, G. W., & Amaral, J. F. (2019). Microwave ablation compared with radiofrequency ablation for treatment of hepatocellular carcinoma and liver metastases: a systematic review and meta-analysis. *OncoTargets and Therapy*, *12*, 6407–6438.

Murovec, T., Sweeney, D. C., Latouche, E., Davalos, R. v., & Brosseau, C. (2016). Modeling of Transmembrane Potential in Realistic Multicellular Structures before Electroporation. *Biophysical Journal*, *111*(10), 2286–2295.

Muthalaly, R. G., John, R. M., Schaeffer, B., Tanigawa, S., Nakamura, T., Kapur, S., Zei, P. C., Epstein, L. M., Tedrow, U. B., Michaud, G. F., Stevenson, W. G., & Koplan, B. A. (2018). Temporal trends in safety and complication rates of catheter ablation for atrial fibrillation. *Journal of Cardiovascular Electrophysiology*, *29*(6), 854–860.

Nam, R. K., Cheung, P., Herschorn, S., Saskin, R., Su, J., Klotz, L. H., Chang, M., Kulkarni, G. S., Lee, Y., Kodama, R. T., & Narod, S. A. (2014). Incidence of complications other than urinary incontinence or erectile dysfunction after radical prostatectomy or radiotherapy for prostate cancer: A population-based cohort study. *The Lancet Oncology*, *15*(2), 223–231.

Napotnik, T. B., Polajžer, T., & Miklavčič, D. (2021). Cell death due to electroporation – A review. *Bioelectrochemistry*, *141*, 10871.

Narayanan, G., Bhatia, S., Echenique, A., Suthar, R., Barbery, K., & Yrizarry, J. (2014). Vessel Patency Post Irreversible Electroporation. *CardioVascular and Interventional Radiology*, *37*(6), 1523–1529.

Narayanan, G., Froud, T., Suthar, R., & Barbery, K. (2013). Irreversible electroporation of hepatic malignancy. *Seminars in Interventional Radiology*, *30*(1), 67–73.

Narayanan, G., Hosein, P. J., Arora, G., Barbery, K. J., Froud, T., Livingstone, A. S., Franceschi, D., Rocha Lima, C. M., & Yrizarry, J. (2012). Percutaneous irreversible electroporation for downstaging and control of unresectable pancreatic adenocarcinoma. *Journal of Vascular and Interventional Radiology*, *23*(12), 1613–1621.

Neal, R. E., Garcia, P. A., Robertson, J. L., Davalos, R. V., II, R. E. N., Garcia, P. A., Robertson, J. L., Davalos, R. V., Neal, R. E., Garcia, P. A., Robertson, J. L., & Davalos, R. V. (2012). Experimental characterization and numerical modeling of tissue electrical conductivity during pulsed electric fields for irreversible electroporation treatment planning. *IEEE Transactions on Biomedical Engineering*, *59*(4), 1076–1085.

Neal, R. E., Millar, J. L., Kavnoudias, H., Royce, P., Rosenfeldt, F., Pham, A., Smith, R., Davalos, R. V., & Thomson, K. R. (2014a). In vivo characterization and numerical simulation of prostate properties for non-thermal irreversible electroporation ablation. *Prostate*, *74*(5), 458–468.

Neal, R. E., Millar, J. L., Kavnoudias, H., Royce, P., Rosenfeldt, F., Pham, A., Smith, R., Davalos, R. V., & Thomson, K. R. (2014b). In vivo characterization and numerical simulation of prostate properties for non-thermal irreversible electroporation ablation. *Prostate*, *74*(5), 458–468.

Neal, R. E., Rossmeisl, J. H., Robertson, J. L., Arena, C. B., Davis, E. M., Singh, R. N., Stallings, J., & Davalos, R. v. (2013). Improved Local and Systemic Anti-Tumor Efficacy for Irreversible Electroporation in Immunocompetent versus Immunodeficient Mice. *PLoS ONE*, *8*(5), e64559.

Neu, J. C., & Krassowska, W. (1999). Asymptotic model of electroporation. *Physical Review E*, *59*(3), 3471–3482.

Neumann, E., & Rosenheck, K. (1972). Permeability Changes Induced by Electric Impulses in Vesicular Membranes. *J. Membrane Biol*, *10*, 279–290.

Neumann, E., Schaefer-Ridder, M., Wang, Y., & Hofschneider, P. H. (1982). Gene transfer into mouse lyoma cells by electroporation in high electric fields. *The EMBO Journal*, *1*(7), 841–845.

Neven, K., Van Driel, V., Van Wessel, H., Van Es, R., Doevendans, P. A., & Wittkampf, F. (2014). Myocardial Lesion Size After Epicardial Electroporation Catheter Ablation After Subxiphoid Puncture. *Circulation: Arrhythmia and Electrophysiology*, *7*(4), 728–733.

Niemeyer, D. J., Simo, K. A., Iannitti, D. A., & McKillop, I. H. (2014a). Ablation therapy for hepatocellular carcinoma: past, present and future perspectives. *Hepatic Oncology*, *1*(1), 67–79.

Niemeyer, D. J., Simo, K. A., Iannitti, D. A., & McKillop, I. H. (2014b). Ablation therapy for hepatocellular carcinoma: past, present and future perspectives. *Hepatic Oncology*, *1*(1), 67–79.

Niessen, C., Igl, J., Pregler, B., Beyer, L., Noeva, E., Dollinger, M., Schreyer, A. G., Jung, E. M., Stroszczynski, C., & Wiggermann, P. (2015). Factors associated with short-term local recurrence of liver cancer after percutaneous ablation using irreversible electroporation: A prospective single-center study. *Journal of Vascular and Interventional Radiology*, *26*(5), 694–702.

O'brien, T. J. (2019). *An Investigation of Thermal Mitigation Strategies for Electroporation-Based Therapies*. Virginia Tech.

O'Brien, T. J., Arena, C. B., & Davalos, R. V. (2017). Thermal Considerations with Tissue Electroporation. In F. A. Kulacki (Ed.), *Handbook of Thermal Science and Engineering* (pp. 1–31). Springer Inter.

O'Brien, T. J., Bonakdar, M., Bhonsle, S., Neal, R. E., Aardema, C. H., Robertson, J. L., Goldberg, S. N., & Davalos, R. V. (2018). Effects of internal electrode cooling on irreversible electroporation using a perfused organ model. *International Journal of Hyperthermia*, *35*(1), 44–55.

O'Brien, T. J., Lorenzo, M. F., Zhao, Y., Neal, R. E., Robertson, J. L., Goldberg, S. N., Davalos, R. V., Neal II, R. E., Robertson, J. L., Goldberg, S. N., & Davalos, R. V. (2019). Cycled pulsing to mitigate thermal damage for multi-electrode irreversible electroporation therapy. *International Journal of Hyperthermia*, *36*(1), 953–963.

O'Brien, T. J., Passeri, M., Lorenzo, M. F., Sulzer, J. K., Lyman, W. B., Swet, J. H., Vrochides, D., Baker, E. H., Iannitti, D. A., Davalos, R. v., & McKillop, I. H. (2019). Experimental High-Frequency Irreversible Electroporation Using a Single-Needle Delivery Approach for Nonthermal Pancreatic Ablation In Vivo. *Journal of Vascular and Interventional Radiology*, *30*(6), 854-862.e7.

Ohmoto, K., Yoshioka, N., Tomiyama, Y., Shibata, N., Kawase, T., Yoshida, K., Kuboki, M., & Yamamoto, S. (2009). Comparison of therapeutic effects between radiofrequency ablation and percutaneous microwave coagulation therapy for small hepatocellular carcinomas. *Journal of Gastroenterology and Hepatology*, *24*(2), 223–227.

Okino, M., & Mohri, H. (1987). Effects of a high-voltage electrical impulse and an anticancer drug on in vivo growing tumors. *Japanese Journal of Cancer Research*, *78*(12), 1319–1321.

O'Neill, C. H., & Martin, R. C. G. (2020). Cardiac synchronization and arrhythmia during irreversible electroporation. *Journal of Surgical Oncology*, *May*, 1–5.

Onik, G., Mikus, P., & Rubinsky, B. (2007). Irreversible electroporation: Implications for prostate ablation. *Technology in Cancer Research and Treatment*, *6*(4), 295–300.

Onik, G., & Rubinsky, B. (2010). Irreversible Electroporation: First Patient Experience Focal Therapy of Prostate Cancer. In J. Nagel (Ed.), *Irreversible Electroporation* (pp. 235–247). Springer Berlin Heidelberg.

Paiella, S., De Pastena, M., D'Onofrio, M., Crinò, S. F., Pan, T. L., De Robertis, R., Elio, G., Martone, E., Bassi, C., & Salvia, R. (2018). Palliative therapy in pancreatic cancer—interventional treatment with radiofrequency ablation/irreversible electroporation. *Translational Gastroenterology and Hepatology*, *3*, 80–80.

Pakhomov, A. G., Semenov, I., Xiao, S., Pakhomova, O. N., Gregory, B., Schoenbach, K. H., Ullery, J. C., Beier, H. T., Rajulapati, S. R., & Ibey, B. L. (2014). Cancellation of cellular responses to nanoelectroporation by reversing the stimulus polarity. *Cellular and Molecular Life Sciences*, *71*(22), 4431–4441.

Pakhomova, O. N., Gregory, B. W., Khorokhorina, V. A., Bowman, A. M., Xiao, S., & Pakhomov, A. G. (2011). Electroporation-induced electrosensitization. *PLoS ONE*, *6*(2), 36–38.

Pandya, G. J., & Shelat, V. G. (2015). Radiofrequency ablation of pancreatic ductal adenocarcinoma: The past, the present and the future. *World Journal of Gastrointestinal Oncology*, *7*(2), 6–11.

Panizza, M., Nilsson, J., Roth, B. J., Rothwell, J., & Hallett, M. (1994). The time constants of motor and sensory peripheral nerve fibers measured with the method of latent addition. *Electroencephalography and Clinical Neurophysiology*, *93*, 147–154.

Partridge, B. R., O'Brien, T. J., Lorenzo, M. F., Coutermarsh-Ott, S. L., Barry, S. L., Stadler, K., Muro, N., Meyerhoeffer, M., Allen, I. C., Davalos, R. v., & Dervisis, N. G. (2020). High-Frequency Irreversible Electroporation for Treatment of Primary Liver Cancer: A Proof-of-Principle Study in Canine Hepatocellular Carcinoma. *Journal of Vascular and Interventional Radiology*, *31*(3), 482-491.e4.

Passeri, M., O'Brien, T. J., Lorenzo, M. F., Lyman, W., Swet, J. H., Neal, R. E., Vrochides, D., Baker, E. H., Davalos, R. v, Iannitti, D. A., & Mckillop, I. H. (2018). Evaluating a single needle high-frequency irreversible electroporation (H-FIRE) probe for pancreatic ablation in vivo. *HPB*, *20*, S40.

Pastushenko, V., Chizmadzhev, Y., & Arakelyan, V. B. (1979). 247 - Electrical breakdown of bilayer lipid membranes II. Calculation of the membrane lifetime in the steady-state diffusion approximation. *Bioelectrochemistry*, *6*(1), 53–62.

Pavlin, M., & Miklavčič, D. (2008). Theoretical and experimental analysis of conductivity, ion diffusion and molecular transport during cell electroporation - Relation between short-lived and long-lived pores. *Bioelectrochemistry*, *74*(1), 38–46.

Pech, M., Janitzky, A., Wendler, J. J., Strang, C., Blaschke, S., Dudeck, O., Ricke, J., & Liehr, U. B. (2011). Irreversible electroporation of renal cell carcinoma: A first-in-man phase i clinical study. *CardioVascular and Interventional Radiology*, *34*(1), 132–138.

Peckham, P. H., & Knutson, J. S. (2005). Functional electrical stimulation for neuromuscular applications. *Annual Review of Biomedical Engineering*, *7*, 327–360.

Pei, Y., Moore, C. E., Wang, J., Tewari, A. K., Eroshkin, A., Cho, Y. J., Witt, H., Korshunov, A., Read, T. A., Sun, J. L., Schmitt, E. M., Miller, C. R., Buckley, A. F., McLendon, R. E., Westbrook, T. F., Northcott, P. A., Taylor, M. D., Pfister, S. M., Febbo, P. G., & Wechsler-Reya, R. J. (2012). An Animal Model of MYC-Driven Medulloblastoma. *Cancer Cell*, *21*(2), 155–167.

Perera, M., Krishnananthan, N., Lindner, U., & Lawrentschuk, N. (2016). An update on focal therapy for prostate cancer. *Nature Reviews Urology*, *13*(11), 641–653.

Philips, P., Hays, D., & Martin, R. C. G. (2013). Irreversible electroporation ablation (IRE) of unresectable soft tissue tumors: Learning curve evaluation in the first 150 patients treated. *PLoS ONE*, *8*(11), e76260.

Polajžer, T., Dermol-Černe, J., Reberšek, M., O'Connor, R., & Miklavčič, D. (2020). Cancellation effect is present in high-frequency reversible and irreversible electroporation. *Bioelectrochemistry*, *132*.

Probst, U., Fuhrmann, I., Beyer, L., & Wiggermann, P. (2018). Electrochemotherapy as a new modality in interventional oncology: A review. *Technology in Cancer Research and Treatment*, *17*.

Rajan, N., Habermehl, J., Coté, M. F., Doillon, C. J., & Mantovani, D. (2007). Preparation of ready-to-use, storable and reconstituted type I collagen from rat tail tendon for tissue engineering applications. *Nature Protocols*, *1*(6), 2753–2758.

Ramirez, F. D., Reddy, V. Y., Viswanathan, R., Hocini, M., & Jais, P. (2020). Emerging Technologies for Pulmonary Vein Isolation. *Circulation Research*, *127*(1), 170–183.

Reddy, V. Y., Koruth, J., Jais, P., Petru, J., Timko, F., Skalsky, I., Hebeler, R., Labrousse, L., Barandon, L., Kralovec, S., Funosako, M., Mannuva, B. B., Sediva, L., & Neuzil, P. (2018). Ablation of Atrial Fibrillation With Pulsed Electric Fields: An Ultra-Rapid, Tissue-Selective Modality for Cardiac Ablation. *JACC: Clinical Electrophysiology*, *4*(8), 987–995.

Reilly, J. P. (1988). Electrical Models for Neural Excitation Studies. *John Hopkins APL Technical Digest*, *9*(1), 44–59.

Reilly, J. P. (1989). Peripheral nerve stimulation by induced electric currents: exposure to time-varying magnetic fields. *Medical and Biological Engineering and Computing*, *27*, 101–110.

Reilly, J. P., Freeman, V. T., & Larkin, W. D. (1985). Sensory Effects of Transient Electrical Stimulation—Evaluation with a Neuroelectric Model. *IEEE Transactions on Biomedical Engineering*, *BME-32*(12), 1001–1011.

Ren, F., Li, Q., Gao, X., Zhu, K., Zhang, J., Chen, X., Yan, X., Chu, D., Hu, L., Gao, Z., Wu, Z., Wu, R., & Lv, Y. (2019). Electrical and thermal analyses of catheter-based irreversible electroporation of digestive tract. *International Journal of Hyperthermia*, *36*(1), 854–867.

Ringel-Scaia, V. M., Beitel-White, N., Lorenzo, M. F., Brock, R. M., Huie, K. E., Coutermarsh-Ott, S., Eden, K., McDaniel, D. K., Verbridge, S. S., Rossmeisl, J. H., Oestreich, K. J., Davalos, R. v., & Allen, I. C. (2019). High-frequency irreversible electroporation is an effective tumor ablation strategy that induces immunologic cell death and promotes systemic anti-tumor immunity. *EBioMedicine*, *44*(1), 112–125.

Roberts, C. B., Jang, T. L., Shao, Y. H., Kabadi, S., Moore, D. F., & Lu-Yao, G. L. (2011). Treatment profile and complications associated with cryotherapy for localized prostate cancer: A population-based study. *Prostate Cancer and Prostatic Diseases*, *14*(4), 313–319.

Rogers, W. R., Merritt, J. H., Comeaux, J. A., Kuhnel, C. T., Moreland, D. F., Teltschik, D. G., Lucas, J. H., & Murphy, M. R. (2004). Strength-duration curve an electrically excitable tissue extended down to near 1 nanosecond. *IEEE Transactions on Plasma Science*, *32*(4 II), 1587–1599.

Rolong, A., Schmelz, E. M., & Davalos, R. V. (2017). High-frequency irreversible electroporation targets resilient tumor-initiating cells in ovarian cancer. *Integrative Biology*, *9*, 979–987.

Rubinsky, B., Onik, G., & Mikus, P. (2007). Irreversible electroporation: A new ablation modality - Clinical implications. *Technology in Cancer Research and Treatment*, *6*(1), 37–48.

Rubinsky, J., Onik, G., Mikus, P., & Rubinsky, B. (2008). Optimal Parameters for the Destruction of Prostate Cancer Using Irreversible Electroporation. *Journal of Urology*, *180*(6), 2668–2674.

Rubinsky, L., Guenther, E., Mikus, P., Stehling, M., & Rubinsky, B. (2016). Electrolytic Effects During Tissue Ablation by Electroporation. *Technology in Cancer Research and Treatment*, *15*(5), NP95–NP103.

Sale, A., & Hamilton, W. (1967). Effects of high electric fields on microorganisms: I. Killing of bacteria and yeasts. *Biochimica et Biophysica Acta*, *148*, 781–788.

Sano, M. B., DeWitt, M. R., Teeter, S. D., & Xing, L. (2018). Optimization of a single insertion electrode array for the creation of clinically relevant ablations using high-frequency irreversible electroporation. *Computers in Biology and Medicine*, *95*(December 2017), 107–117.

Sano, M. B., Fan, R. E., Cheng, K., Saenz, Y., Sonn, G. A., Hwang, G. L., & Xing, L. (2018). Reduction of Muscle Contractions during Irreversible Electroporation Therapy Using High-Frequency Bursts of Alternating Polarity Pulses: A Laboratory Investigation in an Ex Vivo Swine Model. *Journal of Vascular and Interventional Radiology*, *29*(6), 893-898.e4.

Sano, M. B., Fan, R. E., & Xing, L. (2017). Asymmetric Waveforms Decrease Lethal Thresholds in High Frequency Irreversible Electroporation Therapies. *Scientific Reports*, *7*.

Sano, M. B., Fesmire, C. C., Dewitt, M. R., & Xing, L. (2018). Burst and continuous high frequency irreversible electroporation protocols evaluated in a 3D tumor model. *Physics in Medicine and Biology*, *63*(13).

Sano, M. B., Fesmire, C. C., & Petrella, R. A. (2020). Electro-Thermal Therapy Algorithms and Active Internal Electrode Cooling Reduce Thermal Injury in High Frequency Pulsed Electric Field Cancer Therapies. *Annals of Biomedical Engineering*, *49*(1), 191–202.

Sano, M. B., Neal, R. E., Garcia, P. A., Gerber, D., Robertson, J., & Davalos, R. V. (2010). Towards the creation of decellularized organ constructs using irreversible electroporation and active mechanical perfusion. *BioMedical Engineering Online*, *9*(1), 83.

Scheffer, H. J., Nielsen, K., De Jong, M. C., Van Tilborg, A. A. J. M., Vieveen, J. M., Bouwman, A., Meijer, S., Van Kuijk, C., Van Den Tol, P., & Meijerink, M. R. (2014). Irreversible electroporation for nonthermal tumor ablation in the clinical setting: A systematic review of safety and efficacy. *Journal of Vascular and Interventional Radiology*, *25*(7), 997–1011.

Scheffer, H. J., Stam, A. G. M., Geboers, B., Vroomen, L. G. P. H., Ruarus, A., De Bruijn, B., Petrousjka Van Den Tol, M., Kazemier, G., Meijerink, M. R., De, T. D., & De Gruijl, T. D. (2019). Irreversible electroporation of locally advanced pancreatic cancer transiently alleviates immune suppression and creates a window for antitumor T cell activation. *Oncoimmunology*, *8*(11), e1652532.

Schicho, A., Niessen, C., Haimerl, M., Wiesinger, I., Stroszczynski, C., Beyer, L. P., & Wiggermann, P. (2019). Long-term survival after percutaneous irreversible electroporation of inoperable colorectal liver metastases. *Cancer Management and Research*, *11*, 317–322.

Schmid, F. A., Schindele, D., Mortezavi, A., Spitznagel, T., Sulser, T., Schostak, M., & Eberli, D. (2020). Prospective multicentre study using high intensity focused ultrasound (HIFU) for the focal treatment of prostate cancer: Safety outcomes and complications. *Urologic Oncology: Seminars and Original Investigations*, *38*(4), 225–230.

Schoenbach, K. H., Beebe, S. J., & Buescher, E. S. (2001). Intracellular effect of ultrashort electrical pulses. *Bioelectromagnetics*, *22*(6), 440–448.

Schotanus, B. A., Penning, L. C., & Spee, B. (2013). Potential of regenerative medicine techniques in canine hepatology. *Veterinary Quarterly*, *33*(4), 207–216.

Schwan, H. P. (1957). Electrical Properties of Tissue and Cell Suspensions. *Advances in Biological and Medical Physics*, *5*, 147–209.

Sel, D., Cukjati, D., Batiuskaite, D., Slivnik, T., Mir, L. M., & Miklavcic, D. (2005). Sequential finite element model of tissue electropermeabilization. *Ieee Transactions on Biomedical Engineering*, *52*(5), 816–827.

Seraphin, T. P., Joko-Fru, W. Y., Hämmerl, L., Griesel, M., Mezger, N. C. S., Feuchtner, J. C., Adoubi, I., Egué, M. D. D., Okerosi, N., Wabinga, H., Hansen, R., Vuma, S., Lorenzoni, C., Coulibaly, B., Odzebe, S. W., Buziba, N. G., Aynalem, A., Liu, B., Medenwald, D., … Kantelhardt, E. J. (2021). Presentation, patterns of care, and outcomes of patients with prostate cancer in sub-Saharan Africa: A population-based registry study. *Cancer*, *127*(22), 4221–4232.

Sersa, G., Miklavcic, D., Cemazar, M., Rudolf, Z., Pucihar, G., & Snoj, M. (2008). Electrochemotherapy in treatment of tumours. *European Journal of Surgical Oncology*, *34*(2), 232–240.

Shao, Q., O'Flanagan, S., Lam, T., Roy, P., Pelaez, F., Burbach, B. J., Azarin, S. M., Shimizu, Y., & Bischof, J. C. (2019a). Engineering T cell response to cancer antigens by choice of focal therapeutic conditions. *International Journal of Hyperthermia*, *36*(1), 130–138.

Shao, Q., O'Flanagan, S., Lam, T., Roy, P., Pelaez, F., Burbach, B. J., Azarin, S. M., Shimizu, Y., & Bischof, J. C. (2019b). Engineering T cell response to cancer antigens by choice of focal therapeutic conditions. *International Journal of Hyperthermia*, *36*(1), 130–138.

Siddiqui, I. A., Kirks, R. C., Latouche, E. L., DeWitt, M. R., Swet, J. H., Baker, E. H., Vrochides, D., Iannitti, D. A., Davalos, R. v., & McKillop, I. H. (2017). High-Frequency Irreversible Electroporation: Safety and Efficacy of Next-Generation Irreversible Electroporation Adjacent to Critical Hepatic Structures. *Surgical Innovation*, *24*(3), 276–283.

Siddiqui, I. A., Latouche, E. L., DeWitt, M. R., Swet, J. H., Kirks, R. C., Baker, E. H., Iannitti, D. A., Vrochides, D., Davalos, R. v., & McKillop, I. H. (2016). Induction of rapid, reproducible hepatic ablations using next-generation, high frequency irreversible electroporation (H-FIRE) in vivo. *HPB*, *18*(9), 726–734.

Siegel, R. L., Miller, K. D., Fuchs, H. E., & Jemal, A. (2021). Cancer Statistics, 2021. *CA: A Cancer Journal for Clinicians*, *71*(1), 7–33.

Siegel, R. L., Miller, K. D., Fuchs, H. E., & Jemal, A. (2022). Cancer Statistics, 2022. *CA: A Cancer Journal for Clinicians*, *72*, 7–33.

Siegel, R. L., Miller, K. D., & Jemal, A. (2019). Cancer statistics, 2019. *CA: A Cancer Journal for Clinicians*, *69*(1), 7–34.

Silk, M. T., Wimmer, T., Lee, K. S., Srimathveeravalli, G., Brown, K. T., Kingham, P. T., Fong, Y., Durack, J. C., Sofocleous, C. T., & Solomon, S. B. (2014). Percutaneous ablation of peribiliary tumors with irreversible electroporation. *Journal of Vascular and Interventional Radiology*, *25*(1), 112–118.

Son, R. S., Smith, K. C., Gowrishankar, T. R., Vernier, P. T., & Weaver, J. C. (2014). Basic Features of a Cell Electroporation Model: Illustrative Behavior for Two Very Different Pulses. *Journal of Membrane Biology*, *247*(12), 1209–1228.

Sözer, E. B., Pakhomov, A. G., Semenov, I., Casciola, M., Kim, V., Vernier, P. T., & Zemlin, C. W. (2021). Analysis of electrostimulation and electroporation by high repetition rate bursts of nanosecond stimuli. *Bioelectrochemistry*, *140*.

Stampfli, R. (1958). Reversible electrical breakdown of the excitable membrane of a Ranvier Node. *Anais Da Academia Brasileira de Ciências*, *30*, 57–63.

Stampfli, R., & Willi, M. (1957). Membrane potential of a Ranvier node measured after electrical destruction of its membrane. *Experientia*, *13*(7), 297–298.

Su, W., Darkwa, J., & Kokogiannakis, G. (2015). Review of solid-liquid phase change materials and their encapsulation technologies. *Renewable and Sustainable Energy Reviews*, *48*, 373–391.

Sugrue, A., Vaidya, V., Witt, C., DeSimone, C. V., Yasin, O., Maor, E., Killu, A. M., Kapa, S., McLeod, C. J., Miklavčič, D., & Asirvatham, S. J. (2019). Irreversible electroporation for catheter-based cardiac ablation: a systematic review of the preclinical experience. *Journal of Interventional Cardiac Electrophysiology*, *55*(1), 251–265.

Sutter, O., Calvo, J., N'Kontchou, G., Nault, J. C., Ourabia, R., Nahon, P., Ganne-Carrié, N., Bourcier, V., Zentar, N., Bouhafs, F., Sellier, N., Diallo, A., & Seror, O. (2017). Safety and efficacy of irreversible electroporation for the treatment of hepatocellular carcinoma not amenable to thermal ablation techniques: A retrospective single-center case series. *Radiology*, *284*(3), 877–886.

Tekle, E., Astumian, R. D., Friauf, W. A., & Chock, P. B. (2001). Asymmetric pore distribution and loss of membrane lipid in electroporated DOPC vesicles. *Biophysical Journal*, *81*(2), 960–968.

Thomsen, S., & Pearce, J. A. (2011). Thermal Damage and Rate Processes in Biologic Tissues. In *Optical-Thermal Response of Laser-Irradiated Tissue* (pp. 487–549).

Thomson, K. R., Cheung, W., Ellis, S. J., Federman, D., Kavnoudias, H., Loader-Oliver, D., Roberts, S., Evans, P., Ball, C., & Haydon, A. (2011). Investigation of the safety of irreversible electroporation in humans. *Journal of Vascular and Interventional Radiology*, *22*(5), 611–621.

Tieleman, D. P. (2004). The molecular basis of electroporation. *BMC Biochemistry*, *5*(1), 10.

Tokman, M., Lee, J. H. J., Levine, Z. A., Ho, M. C., Colvin, M. E., & Vernier, P. T. (2013). Electric Field-Driven Water Dipoles: Nanoscale Architecture of Electroporation. *PLoS ONE*, *8*(4), e61111.

Tsivian, M., & Polascik, T. J. (2013). Bilateral focal ablation of prostate tissue using low-energy direct current (LEDC): A preclinical canine study. *BJU International*, *112*(4), 526–530.

Ueshima, E., Schattner, M., Mendelsohn, R., Gerdes, H., Monette, S., Takaki, H., Durack, J. C., Solomon, S. B., & Srimathveeravalli, G. (2018). Transmural ablation of the normal porcine common bile duct with catheter-directed irreversible electroporation is feasible and does not affect duct patency. *Gastrointestinal Endoscopy*, *87*(1), 300.e1-300.e6.

Valdez, C. M., Barnes, R., Roth, C. C., Moen, E., & Ibey, B. (2018). The interphase interval within a bipolar nanosecond electric pulse modulates bipolar cancellation. *Bioelectromagnetics*, *39*(6), 441–450.

Valerio, M., Stricker, P. D., Ahmed, H. U., Dickinson, L., Ponsky, L., Shnier, R., Allen, C., & Emberton, M. (2014). Initial assessment of safety and clinical feasibility of irreversible electroporation in the focal treatment of prostate cancer. *Prostate Cancer and Prostatic Diseases*, *17*(4), 343–347.

van den Bos, W., de Bruin, D. M., Jurhill, R. R., Savci-Heijink, C. D., Muller, B. G., Varkarakis, I. M., Skolarikos, A., Zondervan, P. J., Laguna-Pes, M. P., Wijkstra, H., de Reijke, T. M., & de la Rosette, J. J. M. C. H. (2016). The correlation between the electrode configuration and histopathology of irreversible electroporation ablations in prostate cancer patients. *World Journal of Urology*, *34*(5), 657–664.

van den Bos, W., de Bruin, D. M., Veelo, D., Postema, A. W., Muller, B. G., Varkarakis, I. M., Skolarikos, A., Zondervan, P. J., Laguna-Pes, M. P., Savci-Heijink, C., Wijkstra, H., de Reijke, T. M., & de la Rosette, J. J. M. C. H. (2015). Quality of Life and Safety Outcomes

Following Irreversible Electroporation Treatment for Prostate Cancer: Results from a Phase I-Ii Study. *Journal of Cancer Science & Therapy*, *7*(10), 312–321.

van den Bos, W., Jurhill, R. R., de Bruin, D. M., Savci-Heijink, C. D., Postema, A. W., Wagstaff, P. G. K., Muller, B. G., Varkarakis, I. M., Skolarikos, A., Zondervan, P. J., Laguna Pes, M. P., de Reijke, T. M., & de la Rosette, J. J. M. C. H. (2016). Histopathological Outcomes after Irreversible Electroporation for Prostate Cancer: Results of an Ablate and Resect Study. *Journal of Urology*, *196*(2), 552–559.

van den Bos, W., Scheltema, M. J., Siriwardana, A. R., Kalsbeek, A. M. F., Thompson, J. E., Ting, F., Böhm, M., Haynes, A. M., Shnier, R., Delprado, W., & Stricker, P. D. (2018). Focal irreversible electroporation as primary treatment for localized prostate cancer. *BJU International*, *121*(5), 716–724.

van den Honert, C., & Mortimer, J. T. (1979). The response of the myelinated nerve fiber to short duration biphasic stimulating currents. *Annals of Biomedical Engineering*, *7*(2), 117–125.

Van Driel, V. J. H. M., Neven, K. G. E. J., Van Wessel, H., Du Pré, B. C., Vink, A., Doevendans, P. A. F. M., & Wittkampf, F. H. M. (2014). Pulmonary vein stenosis after catheter ablation: electroporation versus radiofrequency. *Circulation: Arrhythmia and Electrophysiology*, *7*(4), 734–738.

Verloh, N., Jensch, I., Lürken, L., Haimerl, M., Dollinger, M., Renner, P., Wiggermann, P., Werner, J. M., Zeman, F., Stroszczynski, C., & Beyer, L. P. (2019). Similar complication rates for irreversible electroporation and thermal ablation in patients with hepatocellular tumors. *Radiology and Oncology*, *53*(1), 116–122.

Verma, A., Asivatham, S. J., Deneke, T., Castellvi, Q., & Neal, R. E. (2021). Primer on Pulsed Electrical Field Ablation: Understanding the Benefits and Limitations. *Circulation: Arrhythmia and Electrophysiology*, *September*, 1–16.

Vižintin, A., Vidmar, J., Ščančar, J., & Miklavčič, D. (2020). Effect of interphase and interpulse delay in high-frequency irreversible electroporation pulses on cell survival, membrane permeabilization and electrode material release. *Bioelectrochemistry*, *134*.

Vogel, J. A., Van Veldhuisen, E., Agnass, P., Crezee, J., Dijk, F., Verheij, J., Van Gulik, T. M., Meijerink, M. R., Vroomen, L. G., Van Lienden, K. P., & Besselink, M. G. (2016). Time-dependent impact of irreversible electroporation on pancreas, liver, blood vessels and nerves: A systematic review of experimental studies. *PLoS ONE*, *11*(11), e0166987.

Wandel, A., Ben-David, E., Ulusoy, B. S., Neal, R., Faruja, M., Nissenbaum, I., Gourovich, S., & Goldberg, S. N. (2016). Optimizing Irreversible Electroporation Ablation with a Bipolar Electrode. *Journal of Vascular and Interventional Radiology*, *27*(9), 1441-1450.e2.

Wasson, E. M., Alinezhadbalalami, N., Brock, R. M., Allen, I. C., Verbridge, S. S., & Davalos, R. V. (2020). Understanding the role of calcium-mediated cell death in high-frequency irreversible electroporation. *Bioelectrochemistry*, *131*(107369).

Watanabe, S., Okita, K., Harada, T., Kodama, T., Numa, Y., Takemoto, T., & Takahashi, T. (1983). Morphologic studies of the liver cell dysplasia. *Cancer*, *51*, 2197–2205.

Weaver, J. C. (1993). Electroporation: A general phenomenon for manipulating cells and tissues. *Journal of Cellular Biochemistry*, *51*(4), 426–435.

Weaver, J. C., & Chizmadzhev, Y. A. (1996). Theory of electroporation: A review. *Bioelectrochemistry and Bioenergetics*, *41*(2), 135–160.

Weaver, J. C., Smith, K. C., Esser, A. T., Son, R. S., & Gowrishankar, T. R. (2012). A brief overview of electroporation pulse strength-duration space: A region where additional intracellular effects are expected. *Bioelectrochemistry*, *87*, 236–243.

Wei, Z. L., Ogawa, R., Takasaki, I., Zhao, Q. L., Zheng, H. C., Ahmed, K., Hassan, M. A., & Kondo, T. (2010). Mild hyperthermia prior to electroporation increases transfection efficiency in HCT 116, HeLa S3 and SGC 7901 cells. *Biotechnology Letters*, *32*(3), 367–371.

Weir, H. K., Anderson, R. N., King, S. M. C., Soman, A., Thompson, T. D., Hong, Y., Moller, B., & Leadbetter, S. (2019). Heart Disease and Cancer Deaths — Trends and Projections in the United States, 1969–2020. *Preventing Chronic Disease*, *13*.

Witt, C. M., Sugrue, A., Padmanabhan, D., Vaidya, V., Gruba, S., Rohl, J., DeSimone, C. V., Killu, A. M., Naksuk, N., Pederson, J., Suddendorf, S., Ladewig, D. J., Maor, E., Holmes, D. R., Kapa, S., & Asirvatham, S. J. (2018). Intrapulmonary vein ablation without stenosis: A novel balloon-based direct current electroporation approach. *Journal of the American Heart Association*, *7*(14), e009575.

Wittkampf, F. H., Van Driel, V. J., Van Wessel, H., Vink, A., Hof, I. E., GrÜndeman, P. F., Hauer, R. N., & Loh, P. (2011). Feasibility of electroporation for the creation of pulmonary vein ostial lesions. *Journal of Cardiovascular Electrophysiology*, *22*(3), 302–309.

Yang, Y., Moser, M., Zhang, E., Zhang, W., & Zhang, B. (2018). Optimization of Electrode Configuration and Pulse Strength in Irreversible Electroporation for Large Ablation Volumes

Without Thermal Damage. *Journal of Engineering and Science in Medical Diagnostics and Therapy*, *1*(2).

Yang, Y., Qin, Z., Du, D., Wu, Y., Qiu, S., Mu, F., Xu, K., & Chen, J. (2019). Safety and Short-Term Efficacy of Irreversible Electroporation and Allogenic Natural Killer Cell Immunotherapy Combination in the Treatment of Patients with Unresectable Primary Liver Cancer. *CardioVascular and Interventional Radiology*, *42*(1), 48–59.

Yao, C., Dong, S., Zhao, Y., Lv, Y., Liu, H., Gong, L., Ma, J., Wang, H., & Sun, Y. (2017). Bipolar Microsecond Pulses and Insulated Needle Electrodes for Reducing Muscle Contractions during Irreversible Electroporation. *IEEE Transactions on Biomedical Engineering*, *64*(12), 2924–2937.

Yao, C., Liu, H., Zhao, Y., Mi, Y., Dong, S., & Lv, Y. (2017). Analysis of dynamic processes in single-cell electroporation and their effects on parameter selection based on the finite-element model. *IEEE Transactions on Plasma Science*, *45*(5), 889–900.

Yao, C., Zhao, Y., Liu, H., Dong, S., Lv, Y., & Ma, J. (2017). Dielectric variations of potato induced by irreversible electroporation under different pulses based on the cole-cole model. *IEEE Transactions on Dielectrics and Electrical Insulation*, *24*(4), 2225–2233.

Yao, C., Zhao, Y., Mi, Y., Dong, S., Lv, Y., Liu, H., Wang, X., & Tang, L. (2017). Comparative Study of the Biological Responses to Conventional Pulse and High-Frequency Monopolar Pulse Bursts. *IEEE Transactions on Plasma Science*, *45*(10), 2629–2638.

Yarmush, M. L., Golberg, A., Serša, G., Kotnik, T., & Miklavčič, D. (2014a). Electroporation-Based Technologies for Medicine: Principles, Applications, and Challenges. *Annual Review of Biomedical Engineering*, *16*(1), 295–320.

Yarmush, M. L., Golberg, A., Serša, G., Kotnik, T., & Miklavčič, D. (2014b). Electroporation-Based Technologies for Medicine: Principles, Applications, and Challenges. *Annual Review of Biomedical Engineering*, *16*(1), 295–320.

Yordanova, Y., Moritz-Gasser, S., & Duffau, H. (2011). Awake surgery for WHO Grade II gliomas within "noneloquent" areas in the left dominant hemisphere: toward a "supratotal" resection. *Journal of Neurosurgery*, *115*(2), 232–239.

Zalba, B., Marin, J. M., Cabeza, L. F., & Mehling, H. (2003). Review on thermal energy storage with phase change: materials, heat transfer analysis and applications. *Applied Thermal Engineering*, *23*, 251–283.

Zhang, B., Liu, F., Fang, Z., Ding, L., Moser, M. A. J., & Zhang, W. (2021). An in vivo study of a custom-made high-frequency irreversible electroporation generator on different tissues for clinically relevant ablation zones. *International Journal of Hyperthermia*, *38*(1), 593–603.

Zhang, M., Ma, H., Zhang, J., He, L., Ye, X., & Li, X. (2017a). Comparison of microwave ablation and hepatic resection for hepatocellular carcinoma: A meta-analysis. *OncoTargets and Therapy*, *10*, 4829–4839.

Zhang, M., Ma, H., Zhang, J., He, L., Ye, X., & Li, X. (2017b). Comparison of microwave ablation and hepatic resection for hepatocellular carcinoma: A meta-analysis. *OncoTargets and Therapy*, *10*, 4829–4839.

Zhao, J., Wen, X., Tian, L., Li, T., Xu, C., Wen, X., Melancon, M. P., Gupta, S., Shen, B., Peng, W., & Li, C. (2019). Irreversible electroporation reverses resistance to immune checkpoint blockade in pancreatic cancer. *Nature Communications*, *10*(1), 899.

Zhao, Y., Bhonsle, S., Dong, S., Lv, Y., Liu, H., Safaai-Jazi, A., Davalos, R. V., & Yao, C. (2018). Characterization of conductivity changes during high-frequency irreversible electroporation for treatment planning. *IEEE Transactions on Biomedical Engineering*, *65*(8), 1810–1819.

Zhao, Y., & Davalos, R. V. (2020). Development of an endothermic electrode for electroporation-based therapies: A simulation study. *Applied Physics Letters*, *117*(143702), 0–5.

Zhao, Y., McKillop, I. H., & Davalos, R. V. (2021). Modeling of a single bipolar electrode with tines for irreversible electroporation delivery. *Computers in Biology and Medicine*, 104870.

Zhuang, J., Ren, W., Jing, Y., & Kolb, J. F. (2012). Dielectric evolution of mammalian cell membranes after exposure to pulsed electric fields. *IEEE Transactions on Dielectrics and Electrical Insulation*, *19*(2), 609–622.